

Structural- and Spectroscopic-Reactivity Relationships of
Nonheme Oxoiron(IV) Complexes

A THESIS SUBMITTED TO THE FACULTY OF THE
UNIVERSITY OF MINNESOTA
BY

Waqas Rasheed

IN PARTIAL FULFILLMENT OF THE REQUIREMENTS
FOR THE DEGREE OF
DOCTOR OF PHILOSOPHY

Prof. Lawrence Que, Jr., Advisor

May 2019

Acknowledgments

There have been at least 30 Que group members who I overlapped with during my time in the lab, and the support of every one of them in one way or the other has been instrumental in my development as a scientist and as a person in general. The graduate school journey has also made me learn to be true to myself, and to others. However, I'm not perfect, and I likely inadvertently upset people too. So, I want to not only thank them in general, but also acknowledge them for being patient with me.

First and foremost, I want to acknowledge Larry for instilling general curiosity about chemistry. He treats it like art, discusses it eloquently, and writes it meticulously. He is both obsessed with perfecting our figures as well as our stories and ensuring that we are clear in communicating about it. He is genuinely interested in unraveling Nature's secrets and comes up with creative and rigorous ways to test hypotheses. I really enjoyed working with Larry in my time here and am humbled by this experience.

Secondly, I want to thank my continuous mentor Mayank Puri, who I got to know before I even arrived in the United States! Mayank and Nirja even picked me up at the airport and have both been a major source of support throughout my time in graduate school. They've both been the kindest people I know, and words cannot truly capture how thankful I am for their support in science and in life.

I also want to thank my lab mates in the Que lab who brought different experiences and cultural backgrounds and taught me about how their world interfaced with chemistry, and I am thankful to all of them for telling me the tales about not only about science but also things not science.

I want to thank Scott Kleespies for teaching me the ways of the lab and introducing me to the Que lab. I want to thank all the postdocs in the lab over the years, particularly Caleb Allpress and Seesaw Ching, who not only honed my chemistry skills, but also pulled me out of my chemistry hole. I will cherish the fun times playing Resistance, the

Castle of the Devil and other games, and I am grateful to have had the company of Seesaw when we visited the Yosemite National Park. I want to thank Ang Zhou for his very helpful nature, and his help in navigation of my graduate school journey and for just being a fun person you could relate with.

I also want to thank Dr Apparao Draksharapu for his mentorship outside and inside the lab. While he was a Raman expert to the rest of the lab, he taught me how to obtain oxoiron(IV) complex crystal structures at a time when there were less than ten of them out there. I was able to almost double that number, and in all his techniques, this became a standard way for me to generate and isolate many of my oxoiron(IV) complexes. In addition, he was also my neighbor for almost two years, and I am glad to have had his support even outside of lab.

I also want to thank Saikat Banerjee for all the times in the lab, and his resilience and persistence with me. He has been the closest person who I worked with in the lab. We have both shared frustrations and joys with low-temperature NMR spectroscopy, where we kept trying to get better data, and pushed each other to the limits and highest standards. Outside of lab, I'm glad to have known him, and his ruminations of what he wanted to do in life made me respect him that much more. I am grateful to Shuangning Xu for really everything, because I can't think of just one way he has been a source of support for me. I want to thank Anna Komor and Andy Jasniewski for their mentorship and advice.

Many people in the department provided technical and administrative assistance throughout my graduate school journey. These include Mollie Dunlap, Chuck Tomlinson and Nancy Thao for all things grad school related, Ben Geisbauer for his improvisation, and Rick Finger for coordinating over 50 shipments. Thank you!

I am also indebted to people in the Lipscomb, the Lu and the Tolman labs. JT helped me navigate the screw axes from a distance in Pakistan; Courtney, Nicole, Debanjan and Ben from the Tolman labs for various things related to research and outside of research, for example SciMentors; and Rahul and Melanie for their willingness to help in every possible way a biochemist could help.

Last but not the least, I want to thank my family and friends. My family has been thousands of miles away, but their well wishes were likely with me throughout my time in the United States. As I venture into my next endeavor, I hope to have their constant support and understanding. I also want to thank friends outside of chemistry department, starting with Talha Ahmed for his help in emergencies, Imran Saeed for his generosity and Huda Zahid for her agility and brilliance (oh wait, she is a chemist). I must also acknowledge Colleen Meyers, a great friend and a teacher. In case the message got lost above, thank you all once again to all the people who were part of my life in graduate school.

Dedication

This thesis is dedicated to all the future, current and past Que group members, to all my friends and family, to different operating systems, to a future pet I might have, and to the reader who fell asleep while reading it.

Abstract

Non-heme oxoiron(IV) motifs have been identified as key intermediates that activate strong C—H bonds. Unlike the enzymatic intermediates however, most oxoiron(IV) complexes in synthetic chemistry have a triplet ground spin state and thus differ in their functional and electronic properties from the $S = 2$ units characterized in the enzymes. One striking exception is the complex $[\text{Fe}^{\text{IV}}(\text{O})(\text{TQA})(\text{L})]^{2+}$, where TQA = tris(2-quinolylmethyl)amine, which has Mössbauer parameters that closely resemble those of TauD-**J**, an enzymatic intermediate that has been relatively well-characterized. This oxoiron(IV) complex contains quinoline donors, and its thermal instability precludes its structural characterization (half-life = 15 minutes at 233 K). In this dissertation, several oxoiron(IV) complexes supported by pentadentate and tetradentate ligands are characterized, and examined for their reactivity and spectroscopic features. Crystallographic characterization of a few of these molecules is also reported. The structurally characterized oxoiron(IV) complexes along with some previously reported oxoiron(IV) complexes are used to set up structure-reactivity and spectroscopic-reactivity relationships, and show linear correlations with increasing isomer shifts, λ_{max} values as well as metal-ligand distances. In addition, this thesis also uses ^1H -NMR spectroscopy as an effective tool to identify solution-state structure as well the spin state of oxoiron(IV) complexes. We also characterize the first example of a spin crossover oxoiron(IV) complex, examples of which are only seen in iron(II) and iron(III) complexes.

Table of Contents

List of Tables

List of Figures and Schemes

Abbreviations

<i>Chapter 1: Oxoiron(IV) Complexes Supported by Various Ligand Frameworks and Their NMR Signatures</i>	1
1.1 Scope and Aim of this Thesis	2
1.2 Oxoiron(IV) Intermediates in Non-Heme Iron Enzymes.....	3
1.3 Synthetic Nonheme Oxoiron(IV) Complexes	5
1.4 Oxoiron(IV) Complexes Supported by Modified N4Py-Based Ligands	9
1.5 Oxoiron(IV) Complexes Supported by Modified BnTPEN-Based Ligands....	11
1.6 Solution-State NMR Spectroscopic Studies of Oxoiron(IV) Complexes	13
1.7 References	16
 <i>Chapter 2: Oxoiron(IV) Complexes Supported by N4Py-Based Ligands</i>	20
2.1 Introduction.....	21
2.2 Experimental Section.....	28
2.2.1 Synthesis of the ligands and complexes.....	29
2.2.2 ESI-MS of complexes 2 and 3	36
2.2.3 UV-Visible spectroscopy and thermal stability of the complexes	36
2.2.4 Vibrational spectroscopy.....	38
2.2.5 Mössbauer Spectroscopy	41
2.2.6 High-Frequency and -Field EPR (HF-EPR) and FIRMS spectroscopy	44
2.2.7 X-Ray Crystallography.....	50
2.3 Comparisons of Crystallographic and Spectroscopic Data	55
2.3.1 Discussion of crystal structures:	57
2.3.2 Inequivalence of pyridine heterocycles on N4Py	59
2.4 Reactivity and kinetic studies for 2 and 3	62

2.4.1 Second-order rate constants of complex 3	63
2.4.2 DFT-optimized structures & spin-state splitting energies of 1, 2 and 3.....	69
2.5 Correlation of reactivity with structural data	70
2.6 Acknowledgments	82
2.8 References	83

Chapter 3: Oxoiron(IV) Complexes Supported by BnTPEN-Based Ligands..... 88

3.1 Introduction.....	89
3.2 Results.....	94
3.2.1 Thermal Stability of the Ferryl Complexes	96
3.2.2 Structural Characterization of Ferryl Complexes	99
3.2.3 Spectroscopic Characterization of Ferryl Complexes	101
3.2.3.1 UV-visible Spectroscopy	101
3.2.3.2 Vibrational Spectroscopy	103
3.2.3.3 Mössbauer Spectroscopy	104
3.2.4 Computed Spin State Splitting Energies of Ferryl Complexes.....	106
3.2.5 Reactivity of Ferryl Complexes	109
3.3. Discussion	114
3.3.1 Correlation of Structure and Reactivity	123
3.3.2 Correlation of Spectroscopy and Reactivity	125
3.4 Conclusion.....	127
3.5 Experimental Section.....	128
3.5.1 Syntheses and Characterization.....	129
3.5.1.1 Synthesis of ligands.....	129
3.5.1.2 Syntheses of Iron(II) Complexes	140
3.5.1.3 Synthesis and Generation of Oxoiron(IV) Complexes	143
3.5.2 Crystallographic Details for 0 and 1-B	144
3.5.3 Oxidative Reactivity and Kinetics of Oxoiron(IV) Complexes.....	147
3.6 Acknowledgments	171
3.7 References	172

<i>Chapter 4: Use of NMR Spectroscopy to Characterize Oxoiron(IV) Complexes and their Spin States</i>	174
4.1 Introduction.....	175
4.2 Results.....	179
4.2.1 Generation of oxoiron(IV) complexes and their thermal stability.....	179
4.2.2 Mössbauer and Absorption Spectroscopy of Ferryl Complexes	179
4.2.3 NMR spectroscopy of Oxoiron(IV) Complexes	182
4.2.3.1 NMR Assignment of $S = 1$ complexes 0, 1 and 1a	182
4.2.3.2 NMR Peak Assignment for $S = 2$ complexes 3, 3a, 3b and 2	193
4.2.3 Computed NMR Chemical Shifts for Oxoiron(IV) Complexes.....	199
4.2.4 Reactivity of Oxoiron(IV) Complexes	200
4.3 Discussion	202
4.4 Conclusion.....	203
4.5 Experimental Section.....	204
4.5.1 Syntheses and Characterization.....	205
4.5.2 Preparation of NMR Samples and Characterization	205
4.5.3 Reactivity and Kinetics of Oxoiron(IV) Complexes	207
4.6 Acknowledgments	219
4.7 References	220
 <i>Chapter 5: Conclusions and Perspectives</i>	 223
5.1 Introduction.....	224
5.2 Future Challenges	228
5.3 References	231
 Bibliography.....	 233
Appendix	242

List of Tables

The page numbers are given in parenthesis.

Table 2.1 Spin Hamiltonian parameters from field- and frequency-domain magnetic resonance spectroscopy (44)

Table 2.2 Crystal data and structure refinement for complex **2** and **3** (52)

Table 2.3 Distance of perchlorates and ferryl unit from water molecule (54)

Table 2.4 Distances of hydrogen atoms from the ferryl unit before and after normalization. Standard uncertainties are not given for average bond lengths because all atoms have different environments. See Figure 2.16. (54)

Table 2.5 Average Fe–N bond lengths in Å from DFT-calculated structures of the most reactive complexes $[\text{Fe}^{\text{IV}}(\text{O})(\text{Me}_3\text{NTB})(\text{L})]^{2+}$ and $[\text{Fe}^{\text{IV}}(\text{O})(\text{TQA})(\text{L})]^{2+}$ (56)

Table 2.6 Structural and spectroscopic properties of the oxoiron(IV) complexes (56)

Table 2.7 Summary of 2nd-order rate constants (k_2) for complex **3**, as derived from plots in Figure 2.20. HAT rates were measured under N₂. (63)

Table 2.8 Comparison of second order rate constants (k_2) of reactions of other complexes with different substrates at 298 K, unless stated in parenthesis (63)

Table 2.9 k_{obs} of reaction of 1 mM **1** with 0.8 M cyclohexane in 1 mL acetonitrile solution at different temperatures, which were obtained to account for the slowness of the reaction and self-decay. $k_2 = k_{\text{obs}}/[0.8]$. (67)

Table 2.10 Eyring Parameters for reaction of substrates with complexes **1**, **2** and **3** discussed in this paper (see Figures 2.21-2.22 and 2.24-2.25, and Table 11), and rates at –40 °C. (69)

Table 2.11 Table of plot used in Figure 2.26. On the x-axis, the Fe–N_{average} lengths are obtained from Tables 2.5 and 2.6. The log k_2 (not log k_2') were plotted on the y-axis. The rates of reaction with cyclohexane at –40 °C were obtained from Eyring parameters (see Tables 2.11 and Figures 2.21-2.22). (73)

Table 2.12 Bond metrics of DFT-optimized structures used for calculations of spin-state splitting energies calculated using M06-L/def2TZVP (81)

Table 2.13 Half-lives of oxoiron(IV) complexes based on N4Py framework with generated from iron(II) precursors with different oxidants, measured at 298 K with 1-mM acetonitrile solutions (82)

Table 3.1 Spectroscopic properties of ferryl complexes based on BnTPEN (96)

Table 3.2 Spectroscopic properties of Fe^{IV}(O) complexes based on N4Py (97)

Table 3.3 Bond metrics (in Å) of BnTPEN-derived ferryl complexes (101)

Table 3.4 Computed spin state splitting energies at the PW6B95/def2-TZVP level of theory, obtained by Dr Johannes Klein. (107)

Table 3.5 HAT and OAT reactivity of BnTPEN-substituted ferryl complexes at 298 K unless otherwise specified. (109)

Table 3.6 Crystal data and structure refinement for complex **0** and **1-B**. (146)

Table 3.7 Eyring parameters for the reaction of different oxoiron(IV) complexes with cyclohexane and thioanisole. (159)

Table 3.8 Bond metrics (in Å) and angles (in °) of [Fe^{II}(BnTPEN)(X)]⁺ structures. (171)

Table 4.1 Properties of oxoiron(IV) complexes evaluated in this work. (181)

Table 4.2 ¹H NMR spectroscopic properties for complex [Fe^{IV}(O)(N2Py2Q)]²⁺ obtained in acetonitrile-*d*₃ at 298 K. (187)

Table 4.3 Theoretical chemical shifts predicted for [Fe^{IV}(O)(N2Py2Q)]²⁺ (in ppm) at 233 K. (199)

Table 4.4 Theoretical chemical shifts predicted for complexes **2** and **3** (in ppm) at 233 K. (200)

Table 4.5 ¹H NMR spectroscopic properties for complexes containing benzimidazoles or quinolines in the N4Py framework, obtained at 298 K. (213)

Table 4.6 Computed spin state splitting energies at the PW6B95/def2-TZVP level of theory. (217)

Table 4.7 Comparison of the relative energies of the **C₁** and **C_s** isomers of complexes **1** and **2** at the PW6B95/def2-TZVP level of theory. All energetics are in kcal mol⁻¹. (218)

List of Figures and Schemes

The numbers in parenthesis at the end indicate the page numbers for the figures.

Figure 1.1 Mechanism of dioxygen activation at the active site of the non-heme iron enzyme called alpha-ketoglurate dependent taurine-dioxygenase. (4)

Figure 1.2 The parent oxoiron(IV) complexes supported by different frameworks variants of which span over half of the oxoiron(IV) complexes reported thus far. (5)

Figure 1.3 Tetragonal (left) and trigonal (right) ligand field splitting diagrams of $S = 1$ and $S = 2$ oxoiron(IV) complexes, and a pie chart showing the span of complexes in different spin states and ligand fields. (6)

Figure 1.4 Introduction of alpha-methyl groups on pyridines in parent $S = 1$ complex $[\text{Fe}^{\text{IV}}(\text{O})(\text{TPA})(\text{L})]^{2+}$ (left) results in $S = 2$ complex $[\text{Fe}^{\text{IV}}(\text{O})(6\text{Me}_3\text{TPA})(\text{L})]^{2+}$ (middle) and replacement of its pyridines with quinolines results in $[\text{Fe}^{\text{IV}}(\text{O})(\text{TQA})(\text{L})]^{2+}$ (right). (7)

Figure 1.5 Binding modes of N4Py to transition metals in +2 oxidation state. (9)

Figure 1.6 Differences in the ligands supporting oxoiron(IV) complexes (with different half-lives). (10)

Figure 1.7 DFT predicted NMR spectra for different isomeric forms of the complex $[\text{Fe}^{\text{IV}}(\text{O})(\text{TPA}(\text{L}))]^{2+}$ in the $S = 1$ spin state. Figure adapted from reference ⁴⁰. (14)

Figure 1.8 DFT predicted NMR spectra of the complex $[\text{Fe}^{\text{IV}}(\text{O})(\text{tpa}^{\text{Ph}})]^-$ in the $S = 1$ and $S = 2$ spin state. Figure adapted from reference ⁴⁰. (15)

Scheme 2.1 d-orbital splitting diagrams of the oxoiron(IV) complexes in different spin states and ligand fields. (21)

Figure 2.1 Reactive and thermally unstable $S = 1$ and $S = 2$ $\text{Fe}^{\text{IV}}(\text{O})$ complexes supported by tetradentate ligands. (23)

Figure 2.2 Previously reported modifications on the N4Py framework. (27)

Figure 2.3 The $\text{Fe}^{\text{IV}}(\text{O})$ complexes supported by ligands based on N4Py framework, examined in this chapter. (28)

Figure 2.4 ESI-MS of complexes **2** (left) and **3** (right). (36)

Figure 2.5 Near-IR features of **1** (dashes), **2** (gray), and **3** (black) in 1 mm CH_3CN solutions. Inset shows the region from 400 to 1100 nm. (38)

Figure 2.6 FTIR spectra of ferrous precursors of **2** (a) and **3** (b). Insets show expanded fingerprint region from 1700 to 650 cm^{-1} . (39)

Figure 2.7 FTIR spectra of ferryl complexes **2** (a) and **3** (b). Insets show expanded fingerprint region from 1700 to 650 cm^{-1} . (40)

Figure 2.8 The full FTIR spectra (top) of **2** (black) and **3** (red) overlaid, and zoomed in spectra (bottom) from 800 to 870 cm^{-1} . (41)

Figure 2.9 Mössbauer spectra of a sample containing complex **2** (black lines) measured under variable field and variable temperature conditions, as indicated in the figure. The corresponding spectral simulations (red lines) used the following parameters: $D = 25 \text{ cm}^{-1}$, $E/D = 0$, $g_x = g_y = g_z = 2.0$, $A_x/g_n\beta_n = A_y/g_n\beta_n = -22.2 \text{ T}$, $\delta = -0.02 \text{ mm/s}$, $\Delta E_Q = 1.36 \text{ mm/s}$, $\eta = 0.6$. The black vertical arrows indicate spectral features belonging to high-spin ferric impurities that represent < 5% of the total iron in the sample. (43)

Figure 2.10 Mössbauer spectra of a sample containing complex **3** (black lines) measured under variable field and variable temperature conditions, as indicated in the figure. The corresponding spectral simulations (red lines) used the following parameters: $D = 26 \text{ cm}^{-1}$, $E/D = 0$, $g_x = g_y = g_z = 2.0$, $A_x/g_n\beta_n = A_y/g_n\beta_n = -22.5 \text{ T}$, $\delta = 0.03 \text{ mm/s}$, $\Delta E_Q = 0.56 \text{ mm/s}$, $\eta = 0.3$. (43)

Figure 2.11 HFEPR spectra of **3** (top, black trace), **2** (bottom, black trace) and **1** at 4.5 K and 609.6 GHz. The red lines are simulations using spin Hamiltonian parameters as in Table 2.1 except for $D = 24.35 \text{ cm}^{-1}$ for **3**. (46)

Figure 2.12 Field vs. energy (frequency) maps of magnetic resonance transitions of **2** (top) and **3** (bottom) at 4.5 K. The squares are experimental points while the curves are simulations using spin Hamiltonian parameters best-fitted through the least-squares method as listed in Table 2.1. Black curves: parallel turning points; red curves: perpendicular turning points (not observed by HFEPR); green curve: off-axis turning point in **3** (observed by FIRMS, see Figure 2.14). The region above $\sim 22 \text{ cm}^{-1}$ ($\sim 660 \text{ GHz}$) was not probed by HFEPR given that it requires a non-routine setup, and the FIRMS technique was available. (47)

Figure 2.13 A contour (false-color) map of magnetic transitions obtained by FIRMS for **3**. A darker color indicates a stronger absorption. A zero-field magnetic transition is clearly visible at 24.3 cm^{-1} . This transition develops into turning points of a powder spectrum, two of which move to higher energies with increasing field, reaching $\sim 1.25 \text{ THz}$ at 17 T, which positively allows the transition to be identified as magnetic (the many phonon transitions active in the FIR region do not respond to increasing magnetic field). The abscissa value of 15 cm^{-1} represents the approximate cutoff of the FIRMS instrument; therefore the part of the map below this value is left blank, but is probed in the field domain by HFEPR as seen in Figure 2.12. (47)

Figure 2.14 Simulations of two most prominent turning points in the powder spectrum of **3** (dashed lines) superimposed on the FIRMS map of resonances. Adjusting g_{\perp} in the simulations provided the value of 2.08(5) as in Table 2.1. (48)

Figure 2.15 Space filling models (top) for **2** and **3**, and ORTEP showing water molecules (bottom) proximal to the ferryl unit as well as perchlorate ions. (55)

Figure 2.16 Front and side views of the ORTEP plots of **2** (left) and **3** (right), shown with thermal ellipsoids set at 50% probability. Water molecules, counterions, and select H atoms have been removed for clarity. The dotted line shows the tilt from the Fe–N_{am} axis. (58)

Figure 2.17A The crystal structures of cations [Zn^{II}(N2Py2Q)(MeCN)]²⁺ and ferrous precursors to **3**, **3b**, and **3a** (left to right), without any H atoms for clarity. (61)

Figure 2.17B Overlaid ball-and-stick diagrams of the iron(II) precursors to **3b** and **3a** (green). Hydrogen atoms are omitted for clarity. The rightmost structure shows increased torsion angle between Fe–N_{MeCN} with the left set of pyridines compared with the other, which prevents the former from causing steric hindrance. (61)

Figure 2.18 Evans–Polanyi plot for **3** at 25 °C, and previously published data for **1** and **2**. (62)

Figure 2.19. Spectral changes (a) observed over time in the reaction of **3** (1.0 mM) with a C–H substrate in CH₃CN at 25 °C. Absorption-time decay profile (b) upon reaction of **3** with different concentrations of cumene obtained by following 770 nm. It is fitted with an exponential function shown with red curves. Inset shows table with all the parameters for this function with various concentrations. The decay profiles from other substrates were fit similarly. (64)

Figure 2.20 k_2 plots for the reactions of different substrates with **3**. The slopes of the fitted red lines represent the second-order rate constants (k_2) at 298 K. (65)

Figure 2.21 k_2 plots at different temperatures for reaction of **2** (top) and **3** (bottom) with cyclohexane. The second order rate constants (k_2) were measured in the temperature range of 288 K to 318 K (plots are color coded with temperature) using 1 mM solutions of oxoiron(IV) complexes in acetonitrile. These rate constants were measured to obtain Eyring plots shown in Figure 2.24. (66)

Figure 2.22 k_2 plots for the reactions of thioanisole with **1** at different temperatures. The second order rate constants (k_2) were measured in the temperature range of 263 K to 293 K (plots are color coded with temperature) using 1 mM solutions of complex **1** in acetonitrile. (67)

Figure 2.23 k_2 plots for the reactions of thioanisole with **2** (red) and **3** (black) at 233 K. The slopes of the fitted lines represent the second-order rate constants (k_2). (68)

Figure 2.24 Eyring Plot for the reaction of cyclohexane (a) with **2** (black squares) and **3** (red squares), and with complex **1** (b). (68)

Figure 2.25 Eyring plot for the reaction of thioanisole with **1**. (69)

Figure 2.26 Correlation of $\log k_2$ values for thioanisole at $-40\text{ }^\circ\text{C}$ (squares) and $\log k_2'$ for cyclohexane at $25\text{ }^\circ\text{C}$ (triangles) and at $-40\text{ }^\circ\text{C}$ (circles) vs the average Fe–N bond lengths for **1** – **3** based on crystallographic data. The bottom plot is extended to $r_{av} = 2.20\text{ \AA}$ to determine whether this correlation also holds true for the $S = 2$ complex $[\text{Fe}^{\text{IV}}(\text{O})(\text{TQA})(\text{L})]^{2+}$ (**5**, open circle) and complex $[\text{Fe}^{\text{IV}}(\text{O})(\text{Me}_3\text{NTB})(\text{L})]^{2+}$ (**6**, crosses). The average Fe–N bond length for **5** and **6** were based on their DFT-optimized 6-coordinate structures, in $S = 1$ and 2 spin states. **5** and **6** are the first two complexes from left depicted in Figure 2.1. (71)

Figure 2.27 Correlation of HAT reactivity with D values (see Table 2.1). (72)

Figure 2.28 ^1H NMR spectrum of $6\text{Me}_2\text{N}4\text{Py}$ (top, CD_3CN), $\text{N}2\text{Py}2\text{Q}$ (middle, CD_2Cl_2) and $\text{N}2\text{Py}2\text{B}$ (bottom, CD_3CN). (78)

Figure 2.29. ^1H NMR spectrum of $[\text{Fe}^{\text{II}}(\text{N}2\text{Py}2\text{B})(\text{CH}_3\text{CN})]\text{OTf}$ in CD_3CN with an inset: zoomed from -2 to 5 ppm. (78)

Figure 2.30. ^1H NMR (a) and COSY (b) spectra of $[\text{Fe}^{\text{II}}(\text{N}2\text{Py}2\text{Q})\text{OTf}]\text{OTf}$ in CD_3CN . (79)

Figure 2.31 Front view of complex **1** (left) and **4** (right), along with non-bonded contact distances from oxygen atom of the ferryl unit to the alpha-H or alpha-carbon of the pyridines. The aryl rings are shown as stick figures. (80)

Figure 2.32 Resonance Raman spectrum of 5 mM isolated complex **2** dissolved in MeCN, measured at 233 K using two different lasers (shown above). (80)

Figure 2.33 Resonance Raman spectrum of isolated complex **1*** dissolved in CH_3CN , measured as frozen solution at 77 K, using 515 nm laser. (81)

Figure 3.1 The oxoiron(IV) complexes examined for their structure-reactivity relationship (90)

Figure 3.2 Correlation of $\log k_2'$ values of cyclohexane with the average length of Fe–N bonds in $\text{N}4\text{Py}$ -based ferryl complexes (solid circles). The plot is extended to 2.20 \AA to determine if this correlation holds true for the $S = 2$ complex $[\text{Fe}^{\text{IV}}(\text{O})(\text{TQA})(\text{MeCN})]^{2+}$, for which $r_{\text{average}}(\text{Fe}-\text{N})$ bonds is DFT-based. (92)

Figure 3.3 Oxoiron(IV) complexes based on BnTPEN framework investigated. (94)

Figure 3.4 Strategy used to avoid isomeric forms in doubly and singly substituted oxoiron(IV) complexes, exemplified using **1-6Me** and **2-6Me**. (94)

Figure 3.5 Absorption-time plots for self-decay of deuterated and non-deuterated complexes of **2-6Me** and **1-6Me** at different temperatures. Inset in the bottom picture zooms into the first two minutes of decay. (98)

Figure 3.6 ORTEP plots of **0** and **1-B** with thermal ellipsoids at 50% probability. Counterions and hydrogen atoms have been removed for clarity. (99)

Figure 3.7 Absorption spectra of mono-substituted (a), and disubstituted and trisubstituted (b) oxoiron(IV) complexes examined in this chapter. (102)

Figure 3.8 FTIR spectra of **0** and **1-B** complexes. (104)

Figure 3.9 Mössbauer spectra and corresponding simulation of samples at 4.2 K with various external magnetic fields. (A) **1-6Me** (14% HS-ferric subtracted); (B) **1-Q** (18% HS-ferric subtracted) The black traces represent the experimental spectra (0kG: raw spectra; 10-70 kG, raw spectra after removing high-spin ferric), and the red traces represent the simulation contributed by $S = 1$ species only. Ruixi Fan performed these experiments. (105)

Figure 3.10. Structures calculated for oxoiron(IV) complexes in the $S = 1$ spin state. Geometries were obtained at the PW6B95/def2-TZVP level of theory in the gas phase. Depictions were made using IboView.²⁹⁻³⁰ (107)

Figure 3.11 Plot of the computed spin state splitting energies at the PW6B95/def2-TZVP level of theory versus the number of substitutions made to the BnTPEN ligand framework. The black square shows the reference value for the unsubstituted ligand; red dots refer to 6Me substitutions and blue triangles correspond to quinoline substitutions. (108)

Figure 3.12 Evans-Polanyi plots showing HAT reactivity of compounds with benzimidazole (green) and quinoline (red) modifications in different orientations around the ferryl center using N4Py (top) and BnTPEN (down) frameworks. (111)

Figure 3.13 Evans-Polanyi plots showing the reactivity increase observed for oxoiron(IV) complexes when quinolines replace the pyridines (left), or α -methyl substituents (right) are introduced on each pyridine in the BnTPEN ligand. The **3-6Me** rates are increased by 3 log units to adjust for the 65 K difference in temperature at which they were obtained. Similar trends in HAT reactivity are observed for ferryl complexes with quinoline substitutions in this series. (114)

Figure 3.14 Steric interactions of proximal hydrogen atoms in different ferryl complexes. Top: top-view of 50% ORTEPS of **1-B**, **1-Q** (DFT structure) and **0** shown from left to right, with a mean plane drawn on the pyridine with which distance of the proximal H atom is measured. Middle: front-view of N4Py based complexes, with distance of the proximal atoms with the oxygen atom. Bottom: side-view of N4Py-based complexes, showing tilts induced by the ligands on the ferryl unit. (117)

Figure 3.15 Correlation of reactivity (obtained from second-order rate constants at 233 K with cyclohexane and thioanisole) with average Fe-L bond lengths of

different complexes. From left to right, ligands supporting Fe^{IV}(O) complexes are N4Py, N2Py2B, BnTPEN, B-BnDPEN, Q-BnDPEN, N2Py2Q, DQBnPEN, Me₃NTB (represented by a ✕), TMC-O, and TQA. Hollow shapes represent DFT-obtained structural data, whereas solid ones represent experimental data. *All rate constants determined using stopped-flow instrument were obtained by our collaborator at Tufts University, Marc C. Piquette.* (125)

Figure 3.16 Correlation of oxoiron(IV) complexes' λ_{\max} (plotted only for S = 1 complexes) and isomer shifts with their reactivity, supported by ligand frameworks from left to right: N4Py, N2Py2B, BnTPEN, B-BnDPEN, N2Py2Q, Q-BnDPEN, DQBnPEN, TMC-O, TQA. Crosses belong to [Fe^{IV}(O)(Me₃NTB)(L)]²⁺, blue shapes to thioanisole and red shapes to cyclohexane. (126)

Scheme 3.1 The synthetic route for the precursor to the monosubstituted ligands. (130)

Scheme 3.2 The synthetic route for the precursor to the disubstituted ligands. (131)

Scheme 3.3 Synthesis of QBnDPEN (131)

Scheme 3.4 Synthesis of 6MeBnTPEN (132)

Scheme 3.5 Synthesis of BBnDPEN (133)

Scheme 3.6 Synthesis of 6Me₂BnTPEN (135)

Scheme 3.7 Synthesis of DQBnPEN (137)

Scheme 3.8 Synthesis of 6Me₃BnTPEN (138)

Scheme 3.9 Synthesis of BnTQEN. (138)

Figure 3.17 Second-order rate constants for the reaction of thioanisole with **0**, measured at different temperatures (left) and Eyring plot (right) for the reaction of **0** with thioanisole, from which the Eyring parameters listed in Table 3.7 were obtained. (147)

Figure 3.18 Second-order rate constants for reactions of HAT substrates at 298 K, and for thioanisole (OAT) at 233 K with complex **1-B**. Eyring plot of **1-B** with cyclohexane is also shown on the bottom right. The k_2 were obtained by reacting 0.8 M cyclohexane with acetonitrile solution of **1-B** at different temperatures. (149)

Figure 3.19 Second-order rate constants for reactions of HAT substrates at 298 K (except cyclohexane for which these rates were determined at more than one temperature), and for thioanisole (OAT) at 233 K with complex **1-Q**. (151)

Figure 3.20 Second-order rate constants for reactions of HAT substrates at 298 K and for thioanisole (OAT) at 233 K with complex **1-6Me**. (153)

Figure 3.21 Second-order rate constants for reactions of HAT substrates at 298 K (except cyclohexane for which these rates were determined at more than one temperature), and for thioanisole (OAT) at 233 K with complex **2-Q**. (155)

Figure 3.22 Second-order rate constants for reactions of HAT substrates at 298 K and for thioanisole (OAT) at 233 K with deuterated complex **2-6Me-d**. (156)

Figure 3.23 Second-order rate constants for reactions of HAT substrates and thioanisole (OAT) at 233 K with deuterated complex **3-6Me-d**. (157)

Figure 3.24 Eyring plots for the reactions of cyclohexane with different oxoiron(IV) complexes. Owing to the thermal instability or reactivity of different complexes, a temperature range of 263 K. to 318 K was used to get the rate constants. (158)

Figure 3.25 ^1H NMR spectra of Q-BnDPEN (top) in acetone- d_6 , and 6MeBnTPEN (bottom) in DCM- d_2 (* indicates either solvent or artifacts.) (160)

Figure 3.26 ^1H NMR spectra of 6Me₂BnTPEN (top) in acetone- d_6 , and DQBnPEN (bottom) in DCM- d_2 (* indicates either solvent or artifacts.) (161)

Figure 3.27 ^1H NMR spectra of 6Me₃BnTPEN (top) in DCM- d_2 , and BnTQEN (bottom) in chloroform- d (* indicates either solvent or artifacts.) (162)

Figure 3.28 ^1H NMR spectra of iron(II) precursors with quinolines in CD_2Cl_2 , $[\text{Fe}^{\text{II}}(\text{QBnDPEN})\text{OTf}]\text{OTf}$ (top), $[\text{Fe}^{\text{II}}(\text{DQBnPEN})\text{OTf}]\text{OTf}$ (middle) and $[\text{Fe}^{\text{II}}(\text{BnTQEN})\text{OTf}]\text{OTf}$ (bottom). (163)

Figure 3.29 ^1H NMR spectra of $[\text{Fe}^{\text{II}}(6\text{MeBnTPEN})\text{OTf}]\text{OTf}$ (top) and $[\text{Fe}^{\text{II}}(\text{BnTPEN})\text{OTf}]\text{OTf}$ (bottom) in CD_2Cl_2 . (164)

Figure 3.30 ^1H NMR spectra of $[\text{Fe}^{\text{II}}(6\text{Me}_2\text{BnTPEN})\text{OTf}]\text{OTf}$ in CD_2Cl_2 . The top spectrum has deuterated benzylic methylene and methyl protons. (164)

Figure 3.31 ^1H NMR spectra of $[\text{Fe}^{\text{II}}(6\text{Me}_3\text{BnTPEN})\text{OTf}]\text{OTf}$ in CD_2Cl_2 . The top spectrum has deuterated benzylic methylene and methyl protons. (165)

Figure 3.32 Fe K-edge X-ray absorption near-edge structures (XANES, fluorescence excitation) of iron(IV) complexes **1-6Me-d** (top) and **1-Q** (bottom) (167)

Figure 3.33 Fourier-transformed k-space EXAFS data of **1-Q** at 10 K. Inset shows the k-space spectrum. (168)

Figure 3.34 Crystal structures of iron(II) complexes supported by alpha-substituted BnTPEN framework. 50% probability ORTEPS were shown for the heterocycles that were modified, and the remaining part was shown as sticks for clarity, as was the removal of all H-atoms, solvent molecules and counterions. (169)

Figure 4.1 Oxoiron(IV) complexes examined in this work that contain increasing number of quinolines or pyridine donors with alpha-substituents. (178)

Figure 4.2 UV-visible spectra of 1-mM acetonitrile solutions of oxoiron(IV) complexes **0** (light gray), **1** (gray) and **2** (black) on the left; and **3** (light gray), **3a** (gray) and **3b** () on the right at 233 K. (181)

Figure 4.3 Mössbauer spectra of **1**, **2** and **3a**. (182)

Figure 4.4 Stacked ^1H NMR spectra of **0** (top) at 233 K, $[\text{Fe}^{\text{IV}}(\text{O})(\text{N4Py})]^{2+}$ (middle) at 298 K and $[\text{Fe}^{\text{IV}}(\text{O})(\text{BnTPEN})]^{2+}$ (bottom) at 298 K, with pyridines and corresponding shifts highlighted in red. (183)

Figure 4.5 Stacked ^1H NMR spectra of $[\text{Fe}^{\text{IV}}(\text{O})(\text{N4Py})]^{2+}$ (top) and $[\text{Fe}^{\text{IV}}(\text{O})(\text{N2Py2Q})]^{2+}$ (bottom) at 298 K, with quinolines shifts in red. Inset shows the expanded region from 0 to 21 ppm. # = solvent. Corresponding structures of the complexes are shown along with the spectra. (186)

Figure 4.6 ^1H COSY NMR spectrum of complex $[\text{Fe}^{\text{IV}}(\text{O})(\text{N2Py2Q})]^{2+}$ in acetonitrile- d_3 at 233 K from 0 to 35 ppm. Only the peaks at 19 and 20.8 ppm are found to have relaxation properties at this temperature that allow them to talk with each other. The lower temperature was chosen to minimize the self-decay of $[\text{Fe}^{\text{IV}}(\text{O})(\text{N2Py2Q})]^{2+}$ over the course of data collection time (over 12 h) on a 10 mM sample. (188)

Figure 4.7 Stacked ^1H NMR spectra of $[\text{Fe}^{\text{IV}}(\text{O})(\text{QBPA})(\text{L})]^{2+}$ (**1**, top) and $[\text{Fe}^{\text{IV}}(\text{O})(\text{N2Py2Q})]^{2+}$ (bottom) at 233 K, with quinolines shifts in red. Inset shows the expanded region from 0 to 24 ppm. (189)

Figure 4.8 ^1H NMR spectra of **1a** (top, 233 K), $[\text{Fe}^{\text{IV}}(\text{O})(6\text{Me}_2\text{N4Py})]^{2+}$ (middle, 233 K; inset zooms into diamagnetic region of spectrum to reveal the signals of β proton), and $[\text{Fe}^{\text{IV}}(\text{O})(\text{N4Py})]^{2+}$ (bottom, 298 K). (190)

Figure 4.9a ^1H COSY NMR spectrum of complex $[\text{Fe}^{\text{IV}}(\text{O})(6\text{Me}_2\text{N4Py})]^{2+}$ in acetonitrile- d_3 at 233 K from -2 to 35 ppm. T cross peaks, between the β and γ protons of two different pyridines are shown. (191)

Figure 4.9b Zoomed ^1H COSY NMR spectrum of 10 mM $[\text{Fe}^{\text{IV}}(\text{O})(6\text{Me}_2\text{N4Py})]^{2+}$ complex in acetonitrile- d_3 from -2 to 15 ppm at 233 K (lower temperature was chosen to minimize the self-decay over 12 h). (192)

Figure 4.10 Stacked ^1H NMR spectra from top to bottom: **3**, **3a**, **2** and **3b** obtained at 233 K in CD_3CN . Quinoline signals are colored red. (194)

Figure 4.11 Stacked ^1H NMR spectra of oxoiron(IV) complex (top) and after its decay (bottom) at 233 K for complexes **2** (a), **3** (b) and **3a** (c). (197)

Figure 4.12 Evans-Polanyi plots for complexes **0** and **1** (rate constants obtained at 273 K), and **2** and **3** (rate constants obtained at 233 K). (200)

Figure 4.13 k_2 plots for the reactions of different HAT substrates with $[\text{Fe}^{\text{IV}}(\text{O})(\text{TPA})(\text{L})]^{2+}$. The slopes of the fitted red lines represent the second-order rate constants (k_2) at 273 K. The oxoiron(IV) complex was generated using 1.2 eq of ArIO in TFE, followed by addition of substrate. (208)

Figure 4.14 k_2 plots for the reactions of different HAT substrates with $[\text{Fe}^{\text{IV}}(\text{O})(\text{QBPA})(\text{L})]^{2+}$. The slopes of the fitted red lines represent the second-order rate constants (k_2) at 273 K. The oxoiron(IV) complex was generated using 1.2 eq of ArIO followed by addition of substrate. (209)

Figure 4.15 k_2 plots for the reactions of different HAT substrates with $[\text{Fe}^{\text{IV}}(\text{O})(\text{BQPA})(\text{L})]^{2+}$. The slopes of the fitted red lines represent the second-order rate constants (k_2) at 233 K. The oxoiron(IV) complex was generated using 2 eq of ArIO followed by addition of substrate. (209)

Figure 4.16 Stacked ^1H NMR spectrum of complexes (top) $[\text{Fe}^{\text{IV}}(\text{O})(\text{N2Py2Q})]^{2+}$ and (down) $[\text{Fe}^{\text{IV}}(\text{O})(\text{N2Py2B})]^{2+}$ in CD_3CN at 298 K from -70 to 70 ppm, along with assignments. Peaks for pyridines are in **black** and quinolines and benzimidazoles are in **red**. (211)

Figure 4.17 Similarities between NMR peaks of different heterocycles aligned parallel to the ferryl unit in oxoiron(IV) complexes. (213)

Figure 4.18 Possible orientations of the pyridine heterocycle around the $\text{Fe}^{\text{IV}}=\text{O}$ unit. (214)

Figure 4.19 ^1H NMR resonances for an equatorial pyridine oriented parallel to the $S = 1$ $\text{Fe}^{\text{IV}}=\text{O}$ unit in $[\text{Fe}^{\text{IV}}(\text{O})(\text{N4Py})]^{2+}$ (top, left); an equatorial pyridine oriented perpendicular to the oxoiron(IV) unit in $[\text{Fe}^{\text{IV}}(\text{O})(\text{BnTPEN})]^{2+}$ (top, right); and an

axial pyridine trans to the oxo atom in $[\text{Fe}^{\text{IV}}(\text{O})(\text{TMC-Py})]^{2+}$ (bottom, left) and $[\text{Fe}^{\text{IV}}(\text{O})(\text{Py5Me}_2)]^{2+}$ (bottom, middle). All resonances are highlighted, along with respective pyridines of these complexes. (215)

Figure 4.20 ^1H NMR spectra of complex **3** in acetonitrile- d_3 at 233 K (top), and in acetone- d_6 at 193 K (bottom). (216)

Figure 4.21 Structural depictions of the oxoiron(IV) complexes studied. Structures corresponding to the $S = 1$ spin state are shown. Geometries were obtained at the PW6B95/def2-TZVP level of theory in the gas phase. Depictions were made using IboView.³⁷⁻³⁸ (217)

Figure 4.22 Plot of the computed spin state splitting energies at the PW6B95/def2-TZVP level of theory and the number of quinoline substitutions made. Red dots show data for the TPA ligand framework (C_1 and C_s symmetric structures were considered for QBPA and BQPA ligands, respectively). Data computed for an analogous series of quinoline substitutions to the BnTPEN ligand framework (black squares) are shown for comparison. (218)

Abbreviations

(ArF ₂) ₂ N4Py	1,1-bis(6-(2,6-difluorophenyl)pyridin-2-yl)- <i>N,N</i> -bis(pyridin-2-ylmethyl)methanamine
2,3-DMB	2,3-dimethylbutane
6Me ₂ BnTPEN	<i>N</i> -benzyl- <i>N',N'</i> -bis((6-methylpyridin-2-yl)methyl)- <i>N</i> -(pyridin-2-ylmethyl)ethane-1,2-diamine
6Me ₂ N4Py	1,1-di(di6-methylpyridine-2-yl)- <i>N,N</i> -bis(pyridine-2-ylmethyl)methanamine
6Me ₃ BnTPEN	<i>N</i> -benzyl- <i>N,N',N'</i> -tris((6-methylpyridin-2-yl)methyl)ethane-1,2-diamine
6Me ₃ TPA	tris(6-methyl-2-pyridylmethyl)amine
6MeBnTPEN	<i>N'</i> -benzyl- <i>N''</i> -((6-methylpyridin-2-yl)methyl)- <i>N''</i> -bis(pyridin-2-ylmethyl)ethane-1,2-diamine)
6MeBQPA	6-methylpyridyl-2-methyl)bis(2-quinolylmethyl)amine
6MeTPA	6-methyl-2-pyridylmethyl)bis(2-pyridylmethyl)amine
BBnDPEN	<i>N</i> -benzyl- <i>N</i> -((1-methyl-1 <i>H</i> -benzoimidazol-2-yl)methyl)- <i>N,N</i> -bis(pyridin-2-ylmethyl-)ethane-1,2-diamine
BDE	Bond dissociation energy
BnTPEN	<i>N</i> -benzyl- <i>N,N',N'</i> -tris(yridine-2-ylmethyl)ethane-1,2-diamine
BnTQEN	<i>N</i> -benzyl- <i>N,N',N'</i> -tris(quinolin-2-ylmethyl)ethane-1,2-diamine
BQPA	2-pyridylmethyl)bis(2-quinolylmethyl)amine)
<i>c</i> -hex	cyclohexane
COSY	homonuclear correlation spectroscopy
<i>D</i>	Zero-field splitting parameter
DFT	Density functional theory
DQBnPEN	<i>N</i> -benzyl- <i>N</i> -(pyridin-2-ylmethyl)- <i>N',N'</i> -bis(quinolin-2-ylmethyl)ethane-1,2-diamine
ESI-MS	Electrospray-Ionisation-mass spectrometry
EXAFS	Extended X-Ray Absorption Fine Structure
FIRMS	Far infrared magnetic resonance spectroscopy
FTIR	Fourier-Transform Infra-Red
HAA	Hydrogen atom abstraction
HAT	Hydrogen-atom-transfer
HFEP	High-field and frequency electron paramagnetic resonance
<i>k</i> ₂	Second-order rate constant
MB	Mössbauer
<i>m</i> CPBA	<i>meta</i> -chloroperbenzoic acid
Me ₃ NTB	tris((1-methyl-1 <i>H</i> -benzo[d]imidazol-2-yl)methyl)amine
MeCN	Acetonitrile
N ₂ Py ₂ B	<i>N,N</i> -bis((1-methyl-1 <i>H</i> -benzoimidazol-2-yl)methyl)-1,1-di(pyridine-2-yl)methanamine
N ₂ Py ₂ Q	1,1-di(pyridin-2-yl)- <i>N,N</i> -bis(quinolin-2-ylmethyl)methanamine
N ₄ Py	1,1-di(dipyridine-2-yl)- <i>N,N</i> -bis(pyridine-2-ylmethyl)methanamine
N ₄ Py**	<i>N,N</i> -bis(4-methoxy-3,5-dimethyl-2-pyridylmethyl)- <i>N</i> bis(2-pyridyl)methylamine)
N ₄ Py ₆ Me ₂	1,1-di(dipyridine-2-yl)- <i>N,N</i> -bis(6-methyl-pyridine-2-ylmethyl)methanamine
ⁿ Bu-P2DA	<i>N</i> -(1',1'-bis(2-pyridyl)pentyl)iminodiacetate

NMR	Nuclear magnetic resonance
OAT	Oxygen-atom-transfer
ORTEP	Oak Ridge Thermal Ellipsoid Plot Program
OTf	triflate
PFIB	pentafluoriodosylbenzene
PhSMe	thioanisole
QBnDPEN	<i>N</i> '-benzyl- <i>N</i> '', <i>N</i> ''-bis(pyridin-2-ylmethyl)- <i>N</i> '-(quinolin-2-ylmethyl)ethane-1,2-diamine
QBPA	(2-quinolylmethyl)bis(2-pyridylmethyl)amine
rR	resonance Raman
RTPEN	<i>N</i> -alkyl- <i>N</i> ', <i>N</i> '-tris(2-pyridylmethyl)ethane-1,2-diamine
TauD- J	Taurine-dioxygenase intermediate J
TMC	1,4,8,11-tetramethyl-1,4,8,11-tetraazacyclotetradecane
TMCO	4,8,12-trimethyl-1-oxa-4,8,12-triazacyclotetradecane
TMS	tetramethylsilane
TPA	tris(2-pyridylmethyl)amine
tpa ^{Ph}	tris(5-phenylpyrrol-2-ylmethyl)amine
TPEN	<i>N</i> , <i>N</i> , <i>N</i> ', <i>N</i> '-tetrakis(pyridine-2-ylmethyl)ethane-1,2-diamine
TPENA	<i>N</i> , <i>N</i> , <i>N</i> '-tris(2-pyridylmethyl)ethylenediamine- <i>N</i> '-acetate
TQA	tris(2-quinolylmethyl)amine
TSR	Two-state reactivity
UV-Vis	Ultra-Violet-Visible
XANES	X-ray Absorption Near Edge Structure
XAS	X-ray absorption spectroscopy
zfs	Zero-field splitting

Chapter 1:
**Oxoiron(IV) Complexes Supported by Various Ligand Frameworks and
Their NMR Signatures**

1.1 Scope and Aim of this Thesis

Chapter 1 briefly highlights the prevalence of oxoiron(IV) intermediates in enzymes, and their role in the activation of strong C–H bonds. It also further details synthetic efforts made by bioinorganic chemists to mimic the properties and reactivity of these intermediates, and points to the use of different ligand frameworks to help in obtaining the crystal structures of reactive oxoiron(IV) complexes. It also details the use of these manifolds to define a broad range of reactivity properties for these synthetic complexes and correlate them with spectroscopic and structural features to bridge the gap between the complexes in the $S = 1$ and $S = 2$ spin state. Finally, the chapter highlights the use of NMR spectroscopy as a complementary tool to elucidate solution-state structures and spin states of oxoiron(IV) complexes.

Chapter 2 surveys the recent developments in reports of oxoiron(IV) complexes supported by the variants of the ligand N4Py, and uses a novel approach to obtain crystal structures of at least two reactive oxoiron(IV) complexes with up to a 1000-fold higher reactivity.

Chapter 3 describes synthetic efforts to expand the number of oxoiron(IV) complexes, so that an even wider range of reactivity can be obtained. This effort allows us to determine the trends observed in reactivity of oxoiron(IV) complexes and correlate them (over a wider scope of ligand frameworks) with the spectroscopy and the structure of oxoiron(IV) complexes, to formulate generalizable themes of properties that determine the reactivity of oxoiron(IV) complexes.

Chapter 4 demonstrates the use of NMR spectroscopy as an innovative tool to determine solution-state structures of oxoiron(IV) complexes in different spin states, and lays out the foundation for its complementary use along with Mössbauer spectroscopy to determine spin states of oxoiron(IV) complexes in solution state.

1.2 Oxoiron(IV) Intermediates in Non-Heme Iron Enzymes

Aerobic life ranging from bacteria to complex eukaryotic organisms such as human beings has evolved to utilize dioxygen (O_2) from air to carry out diverse oxidative chemistry. The oxidative power of this molecule is used in many vital metabolic processes critical to existence of life, including the generation of “molecular energy unit of currency” ATP (adenosine triphosphate), the degradation of xenobiotics, syntheses of important biomolecules, and many others. Non-heme and heme-based iron enzymes are important tools employed by these organisms to use dioxygen and couple its oxidative capabilities with the activation of very inert chemical bonds.

Many of the non-heme iron enzymes harness the power of atmospheric oxygen to generate oxoiron(IV) intermediates as the key substrate-activating species during their catalytic cycles. For example, oxoiron(IV) motifs are involved in oxidation of one of the strongest aliphatic C–H bonds (bond dissociation energy = 105 kcal/mol) of methane to methanol, a transformation carried out by a diiron enzyme called soluble methane monooxygenase, using a diiron(IV) intermediate called **Q**.¹ Similar tetragonal oxoiron(IV) motifs have also been used recently generated in zeolites recently to achieve the same chemical transformation.²

The first mononuclear oxoiron(IV) enzymatic intermediate TauD-**J** was characterized in 2003 by Krebs and Bollinger in the enzyme taurine/alpha-ketoglutarate-dependent dioxygenase, which is responsible for catalyzing the hydroxylation of the C_1 position of taurine.³ This function is used as a means of recycling sulfur in the cell.⁴ In the reduced form of the enzyme, the iron(II) active metal center is bound to two histidines and one aspartate residue in a facial arrangement. This arrangement is common to many mononuclear iron-containing enzymes and is referred to as the two-histidine-one-carboxylate facial triad.⁵⁻⁷ The other sites of the iron(II) center are bound to water molecules.

The generally accepted mechanism of dioxygen activation in the active site of the non-heme iron enzyme called alpha-ketoglutarate dependent taurine-dioxygenase

is proposed in Figure 1.1. Introduction of alpha-ketoglutarate into the active site results in displacement of two of the water molecules to allow it to act as a bidentate ligand. Subsequent addition of substrate expels the remaining water molecule, to give rise to a 5-coordinate iron center, which then activates dioxygen from the air. This activation results in the coordinative saturation of iron, and its oxidation to form an Fe^{III}-superoxo intermediate. This intermediate is then proposed to attack the electrophilic 2-oxo carbon atom of the bidentate alpha-ketoglutarate ligand, to now form an Fe^{IV}-alkylperoxo intermediate. Further O–O and C–C bond breaking steps finally result in the removal of carbon dioxide, succinate, and a terminal Fe^{IV}-oxo species that can cleave C–H bonds.⁸ This attack on the Fe=O bond results in formation of an iron(III) hydroxide species and a substrate radical, that in turn rebounds to the iron center to yield oxidized product and the iron(II) starting point of the catalytic cycle.

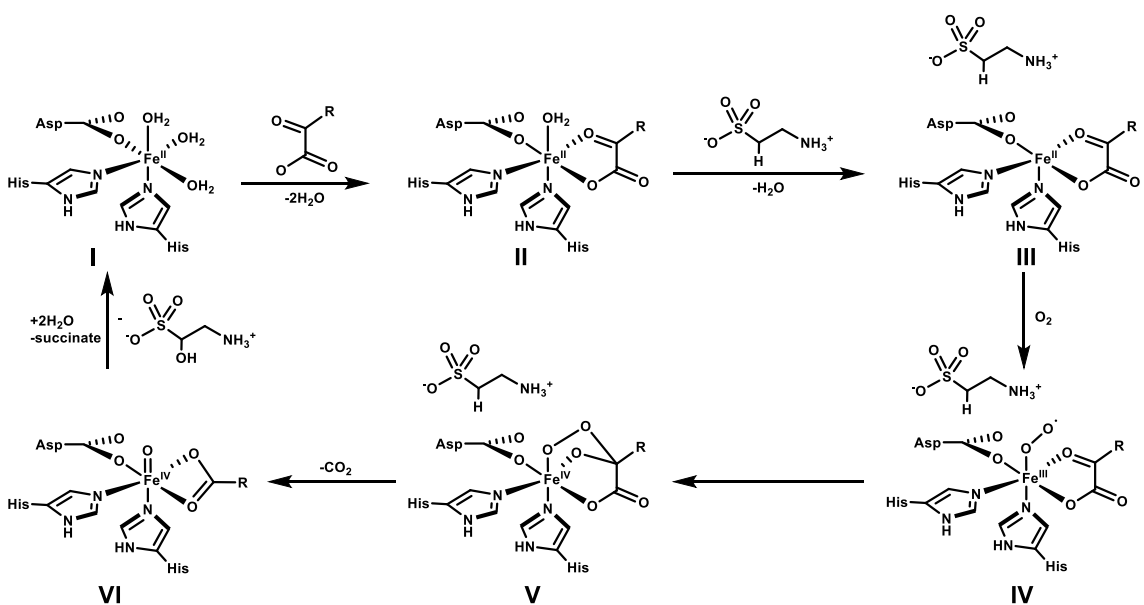


Figure 1.1 Mechanism of dioxygen activation at the active site of the non-heme iron enzyme called alpha-ketoglutarate dependent taurine-dioxygenase.

The trapping and identification of the oxoiron(IV) intermediates in this enzyme were enabled by the use of perdeuterated taurine, so that its rate of reaction with the intermediate was significantly slowed (as demonstrated by a KIE of 50), enabling

it to be thoroughly characterized.³ Since then, oxoiron(IV) intermediates of several enzymes have been characterized using similar strategies.⁹⁻¹⁵ Incidentally, all the intermediates in the enzymes have a ground spin state of $S = 2$, and isomer shifts in the range of 0.22 – 0.30 mm/s, as determined by their Mössbauer spectra. The $S = 2$ ground spin state of these ferryl intermediates is often attributed to the weak field ligand donors found in the active center of the enzyme and is a characteristic feature for these intermediates so far. Although the crystal structures of the enzymatic oxoiron(IV) intermediates would conclusively establish their geometry and structure, their thermal instability makes them harder to crystallize relative to the synthetic nonheme oxoiron(IV) compounds.

1.3 Synthetic Nonheme Oxoiron(IV) Complexes

Efforts to characterize oxoiron(IV) complexes in synthetic bioinorganic chemistry were jumpstarted in 2003 with the structural characterization of the first oxoiron(IV) intermediate supported by a macrocyclic ligand (Figure 1.2), namely $[\text{Fe}^{\text{IV}}(\text{O})(\text{TMC})(\text{MeCN})]^{2+}$ (where MeCN is the solvent acetonitrile and TMC is 1,4,8,11-tetramethyl-1,4,8,11-tetraazacyclotetradecane).¹⁶ However, this complex was found to be in the $S = 1$ spin state using Mössbauer spectroscopy and had a lower isomer shift ($\delta = 0.17$ mm/s) than that of the only enzymatic intermediate characterized at the time (TauD- \mathcal{J}) which had a larger isomer shift of 0.30 mm/s. This synthetic complex was also found to have reactivity properties far inferior than those of the enzymes. Bioinorganic chemists have mounted significant efforts after the structural and spectroscopic characterization of this complex to model oxoiron(IV) motifs in enzymes, and a short summary of these synthetic endeavors in the context of complexes examined in this thesis is detailed below.

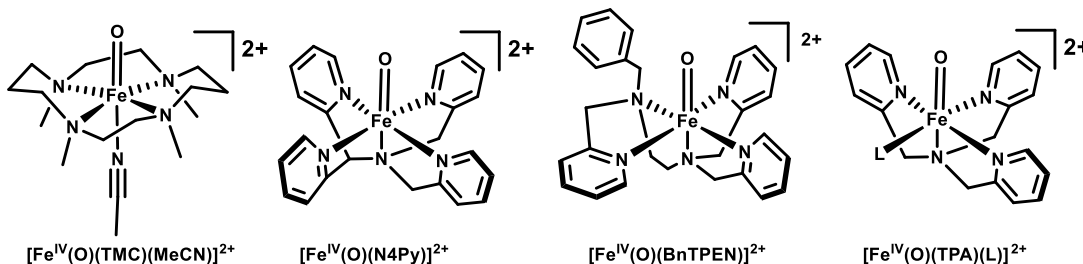


Figure 1.2 The parent oxoiron(IV) complexes supported by different ligand frameworks, variants of which span over half of the oxoiron(IV) complexes reported thus far.

Over 90 synthetic nonheme oxoiron(IV) complexes have been reported so far in attempts that aimed to spectroscopically, functionally or structurally model the enzymatic intermediates.¹⁷⁻¹⁸ Almost all of these oxoiron(IV) species are supported by polydentate frameworks, and only 7 have been characterized in the $S = 2$ ground spin state found in the enzymes, with the remaining found in the $S = 1$ ground spin state. Of the complexes in the $S = 2$ spin state, five are supported by ligands with a trigonal bipyramidal fold around the iron center, and two are proposed to have a tetragonal geometry. The $S = 1$ oxoiron(IV) intermediates on the other hand, are all supported by ligands with tetragonal ligand field around the iron(IV) center (Figure 1.3).

While one of the goals of bioinorganic chemists has been to make more $S = 2$ oxoiron(IV) complexes, only one of those efforts has succeeded in achieving similarities to the enzymatic complexes in both reactivity and spectroscopy. This failure is partly rooted in the lack of stability of most of the complexes that are $S = 2$ in nature, which has prevented structural insight into the factors that contribute to these $S = 2$ complexes' reactive nature.

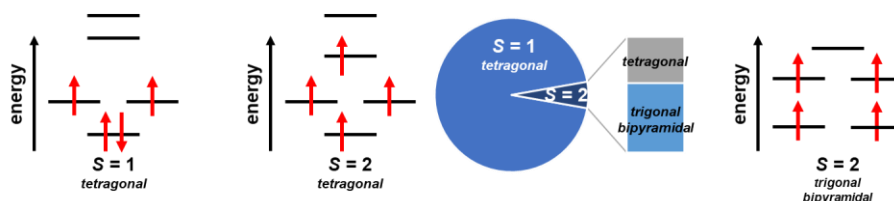


Figure 1.3 Tetragonal (left) and trigonal (right) ligand field splitting diagrams of $S = 1$ and $S = 2$ oxoiron(IV) complexes, and a pie chart showing the span of complexes in different spin states and ligand fields.

Therefore a number of approaches have been taken by synthetic chemists to synthesize oxoiron(IV) intermediates that have similarities to the signatures of enzymatic intermediates.¹⁹ Despite the lack of structural information available on

enzymatic oxoiron(IV) intermediates, over a dozen of the 90 oxoiron(IV) complexes have been crystallographically characterized. Many of them share a common ligand framework based on either the macrocyclic ligand TMC or the pyridine-rich N4Py and BnTPEN ligands (see next two sections and Figure 1.2). Upon perusal of the structurally characterized oxoiron(IV) landscape and the successful strategies employed to develop spectroscopic and structural analogs of enzymatic oxoiron(IV) intermediates, one can begin to develop correlations of their structural and spectroscopic signatures with their reactivity. Specifically, this effort has the potential to provide indirect insight into the aspects that govern the reactivity of enzymatic and synthetic oxoiron(IV) intermediates, as well as the role of the primary coordination sphere in determining the reactivity of oxoiron(IV) motifs. This thesis aims to explore these structural and spectroscopic correlations with reactivity, as will be explained in the next two sections of this chapter.

The most successful effort in the Que lab to make a synthetic oxoiron(IV) complex with electronic and functional properties similar to those of the enzymatic intermediates is represented by $[\text{Fe}^{\text{IV}}(\text{O})(\text{TQA})(\text{L})]^{2+}$, where TQA = tris(2-quinolylmethyl)amine (Figure 1.4). TQA is a tetradentate tripodal ligand containing three quinoline donors that supports an $S = 2$ oxoiron(IV) center. However, it has a half-life of only 15 minutes at 233 K, which has prevented its crystallographic characterization. Its 'parent' complex on the other hand, $[\text{Fe}^{\text{IV}}(\text{O})(\text{TPA})(\text{L})]^{2+}$, where TPA is (tris(2-pyridylmethyl)amine), contains three pyridine donors, has an $S = 1$ spin state and is stable for over a day at 233 K.²⁰

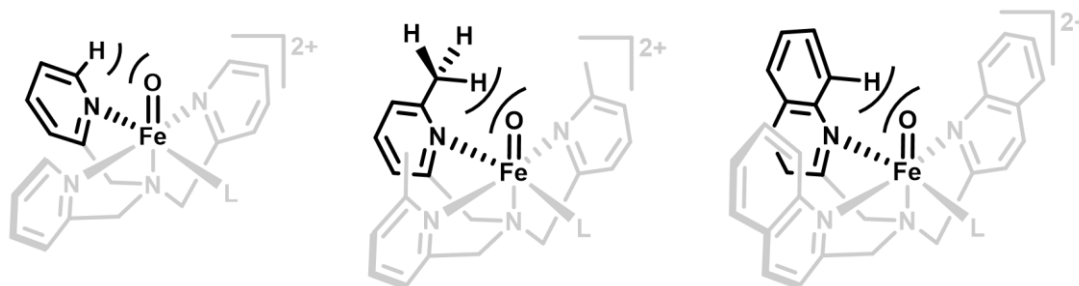


Figure 1.4 Introduction of alpha-methyl groups on pyridines in parent $S = 1$ complex $[\text{Fe}^{\text{IV}}(\text{O})(\text{TPA})(\text{L})]^{2+}$ (left) results in $S = 2$ complex $[\text{Fe}^{\text{IV}}(\text{O})(6\text{Me}_3\text{TPA})(\text{L})]^{2+}$

(middle) and replacement of its pyridines with quinolines results in $[\text{Fe}^{\text{IV}}(\text{O})(\text{TQA})(\text{L})]^{2+}$ (right).

The reasons for the different spin states in the two tetragonal oxoiron(IV) complexes supported by the same general framework can be understood upon examination of iron(II) complexes supported by the parent TPA and 6Me₃TPA (tris(6-methyl-2-pyridylmethyl)amine) ligands.²¹ The iron(II) complex supported by TPA is diamagnetic (as evidenced by its ¹H NMR spectrum), and that supported by 6Me₃TPA ligand is paramagnetic (evidenced by its paramagnetically shifted peaks), indicating its *S* = 2 nature. Furthermore, the iron(II) complex supported by 6Me₃TPA has its pyridyl donors 0.2 angstroms farther away from the iron center. This difference can be attributed to the steric interactions of the 6-methyl protons, which likely cause the Fe–N_{py} bond lengths to increase and weaken the binding of the pyridine donors into the metal center, resulting in a weakened ligand field that allows its four d-orbital electrons to adopt the unpaired *S* = 2 configuration.

The quinoline H8 protons in $[\text{Fe}^{\text{IV}}(\text{O})(\text{TQA})(\text{L})]^{2+}$ likely have similar interactions with the oxoiron(IV) unit, although such effects have not been observed crystallographically until recently in oxoiron(IV) complexes.²² These steric interactions increase the Fe–N bond length, and hence the sigma-donation of quinoline nitrogen into the metal center, thus weakening the equatorial ligand field, which in a tetragonal complex would lower the energy of the $d_{x^2-y^2}$ orbitals, and tune the ligand field of the oxoiron(IV) complex enough for the iron center to adapt the *S* = 2 spin state configuration.

In this thesis, proof for such steric interactions is provided using structural characterization of an oxoiron(IV) complex containing quinoline rings, which increase the average Fe–N bond lengths of the oxoiron(IV) complex by 0.08 Å, and shows a ferryl unit that directly gets affected by such interactions, as detailed in the next section.

1.4 Oxoiron(IV) Complexes Supported by Modified N4Py-Based Ligands

N4Py (1,1-di(dipyridine-2-yl)-N,N-bis(pyridine-2-ylmethyl)methanamine) is a pentadentate C_s -symmetric ligand that was first synthesized in the Que lab in 1995.²³ It has been recently shown to support an unexpected binding mode in a dinuclear platinum(II) species.²⁴ But when it binds iron(II) metal, it supports a low-spin, 6-coordinate and mononuclear complex with the sixth coordination site bound by a solvent (Figure 1.5), which can be replaced with different oxygen-related motifs to model intermediates related to oxygen activation.

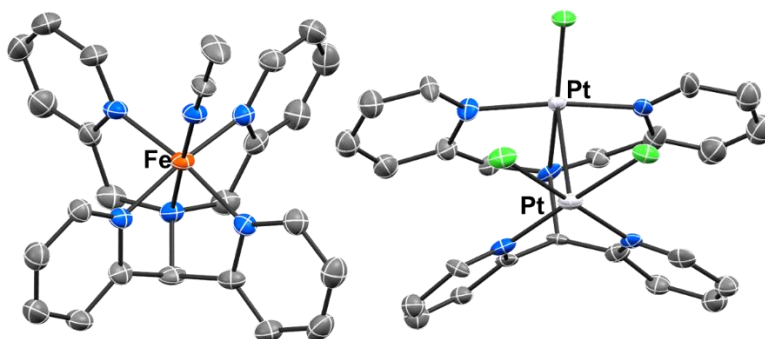


Figure 1.5 Binding modes of N4Py to transition metals in +2 oxidation state.

Its C_s -symmetric iron(II) precursor has two pairs of equatorial pyridines, and an axial tertiary amine. The two pyridines attached to the bis(pyridyl)methylamine half of the ligand have larger torsional angles ($26\text{--}28^\circ$) with the axially bound ligand than the pair of pyridines on the bis(pyridyl-2-methyl)amine half of the ligand (where these angles are $7\text{--}13^\circ$). Nevertheless, all four pyridines are approximately aligned parallel to the axis formed by the Fe–N_{amine} and the axial ligand, and in the way these pyridines are connected, the framework is somewhat rigid and does not allow the pyridines to move. The ligand framework has proven its versatility in its ability to support reactive intermediates in both iron(III) and iron(IV) oxidation states, and these intermediates can oxidize strong C–H bonds of cyclohexane in the +4 oxidation state.^{23, 25} Furthermore, N4Py also has only five benzylic protons (which are the weakest bonds in the ligand, with a bond dissociation energy of \approx

90 kcal/mol), which further increases its robustness as a ligand that can support transition metal-based species that could activate strong C-H bonds.

TPA is a related but similar ligand, which has also been used by the Que group extensively to support both mononuclear and dinuclear nonheme high-valent intermediates.^{20-21, 26-27} Interestingly, the difference between the N4Py and TPA ligands is only the additional pyridine donor in N4Py, which replaces one of the methylene protons in TPA (Figure 1.6)

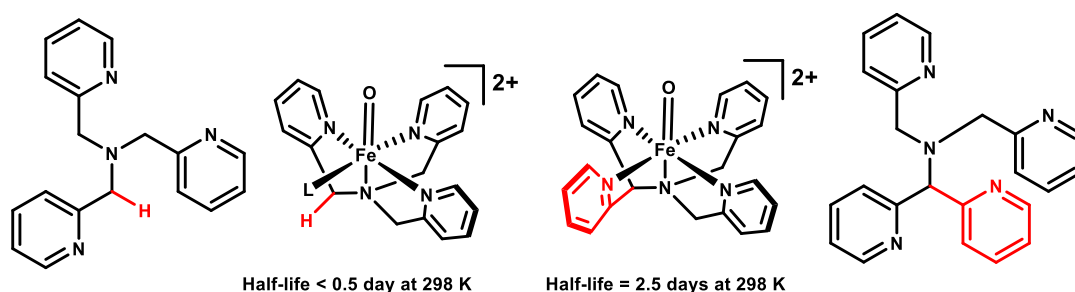


Figure 1.6 Differences in the ligands supporting oxoiron(IV) complexes (with different half-lives).

N4Py supported the first structurally characterized oxoiron(IV) intermediate that could activate the strong bonds of cyclohexane.²⁸ Its thermal stability ($t_{1/2} = 60$ h at 298 K) makes this ligand a very attractive candidate in pursuits of structural information on unstable complexes based on similar framework. The variants of this ligand containing a quinoline heterocycle have been recently reported, and utilized to make reactive oxomanganese(IV) complexes, for example.²⁹ We have used this framework to stabilize and crystallographically characterize the first examples of unstable oxoiron(IV) complexes that contain heterocycles other than pyridines, namely quinolines and benzimidazoles.²² These two heterocycles have also been found in the ligand frameworks of very reactive oxoiron(IV) complexes, and hence N4Py serves as a useful tool to obtain structural information on complexes that contain these heterocycles. This work is presented in Chapter 2.

1.5 Oxoiron(IV) Complexes Supported by Modified BnTPEN-Based Ligands

The hexadentate TPEN ligand (*N,N,N',N'*-tetrakis(pyridine-2-ylmethyl)ethane-1,2-diamine), which has an ethylenediamine linker bound to four 2-picolyl groups, can be made into a pentadentate ligand if one of its pyridyl arms are replaced with a non-coordinating benzyl group.³⁰ Such a pentadentate ligand framework, namely BnTPEN (*N*-benzyl-*N,N',N'*-tris(2-pyridylmethyl)ethane-1,2-diamine) wraps around iron center so that the resulting complex has no element of symmetry (Figure 1.2), and has been used by McKenzie and coworkers extensively in their work on isolating intermediates related to this framework.³⁰ A number of iron(II) complexes supported by this ligand have been structurally characterized, wherein the axial ligand is tuned to affect the properties of the iron(II) center.³¹

The oxoiron(IV) complex supported by BnTPEN at the time was one of the most reactive oxoiron(IV) complexes which could also react with cyclohexane at room temperature, but owing to its 10-fold lower stability (half-life of 6 h at 298 K), it could not be structurally characterized. Nevertheless RTPEN (or *N*-alkyl-*N,N',N'*-tris(2-pyridylmethyl)ethane-1,2-diamine) ligands have been used to support various iron(III) peroxo intermediates, and recently, substitutions that enable hydrogen bonding on RTPEN's dangling R groups have even enabled selective formation of an Fe^{IV}(O) or an Fe^{III}(OOH) intermediate from the reaction of iron(II) precursor with H₂O₂, which has allowed controlled heterolytic versus homolytic O-O bond cleavage through a secondary coordination sphere.³² This functionality also speaks to the versatility of this ligand framework in providing an ability to tune ligand fields around the iron center and generate different intermediates. Other modifications on this ligand framework have involved use of acetate groups to replace the pyridyl arms on the TPEN framework to generate a negatively charged TPENA ligand (*N,N,N'*-tris(2-pyridylmethyl)ethylenediamine-*N'*-acetate). The iron(II) complex supported by this ligand reacts with iodosylbenzene to form a seven-coordinate iron(III) complex, which is considered to be a masked Fe^V(O) compound that can catalyze oxygenation of sulfides.³³ Its ability to carry out

oxygen atom transfer catalytically has been studied extensively by Wang and coworkers using extensive theoretical work on the complex.³⁴

The complex $[\text{Fe}^{\text{IV}}(\text{O})(\text{BnTPEN})]^{2+}$ is an order of magnitude more reactive than $[\text{Fe}^{\text{IV}}(\text{O})(\text{N4Py})]^{2+}$ in its hydrogen atom transfer and oxygen atom transfer abilities.²⁵ While it is just another oxoiron(IV) complex supported by a tetragonal ligand field, alpha-substituents on this ligand's pyridines have not been introduced. Its equatorial ligand field can therefore be tuned by doing so, which would change the energy level of the $d_{x^2-y^2}$ orbital. If the equatorial ligand field is weakened, the splitting of the d orbitals decreases, and the metal center also becomes more electrophilic. This electrophilicity can potentially explain the higher observed reactivity of resulting oxoiron(IV) complexes in this framework, and it is possible that one can change the spin state of the molecules in this framework and go from $S = 1$ to $S = 2$, like the enzymatic intermediates.

The BnTPEN parent ligand wraps around the iron(IV) unit such that it has an equatorial amine and three equatorial pyridines (in contrast to four in N4Py). One of the three equatorial pyridines is bound 'perpendicular' to the axis formed by the sixth ligand and the iron center, and the remaining two pyridines are parallel to this axis. The ethylene diamine linker allows this framework to be relatively less rigid than that of N4Py. But overall, presence of pyridine in a different orientation enables examination of orientation of heterocycles and their effects on spectroscopy, structure and reactivity of the oxoiron(IV) complexes. This is the reason why oxoiron(IV) complexes supported by BnTPEN framework are of great interest, and will be examined in this thesis. We have sequentially replaced the pyridines in the complex with sterically encumbering quinolines or introduced alpha-substituents like methyl groups to make more reactive oxoiron(IV) complexes. However, this has resulted in oxoiron(IV) complexes that are comparably reactive to $[\text{Fe}^{\text{IV}}(\text{O})(\text{TQA})(\text{L})]^{2+}$ and for some of them the determination of rate constants required the use of stopped flow instrument. This data is presented in Chapter 3.

1.6 Solution-State NMR Spectroscopic Studies of Oxoiron(IV) Complexes

NMR spectroscopy is a great structural tool that can probe the solution state structure and the electronic properties of oxoiron(IV) complexes. There are only a few examples of cases where it has been explored for pyridine-rich oxoiron(IV) complexes,^{28, 35} and in many of those cases, the NMR spectra are not fully assigned.³⁶⁻³⁹ Some studies on TMC-based oxoiron(IV) complexes have proven useful in the identification of different isomeric forms of an oxoiron(IV) intermediates, but other than that NMR spectroscopy is not generally used as a regular tool for characterization of oxoiron(IV) complexes, and there are no studies on the the NMR spectra of $S = 2$ oxoiron(IV) complexes. Given the number of unpaired electrons (Figure 1.3) and subsequently different magnetic properties of resulting complexes, it is worth noting that the complexes in the $S = 1$ and $S = 2$ spin states are likely going to have very different paramagnetic shifts in their ^1H NMR spectra. This difference in electronic properties highlights two uses for NMR spectroscopy: 1) in addition to Mössbauer spectroscopy, it can also serve as a tool to determine the spin state of the oxoiron(IV) complexes; 2) it can be used to determine the solution-state structure of oxoiron(IV) complexes.

Two examples can be used to highlight both the use cases. Borgogno *et al.* have used DFT methods to predict NMR spectra of the $S = 1$ $[\text{Fe}^{\text{IV}}(\text{O})(\text{TPA})(\text{L})]^{2+}$ complex in two different isomeric forms (shown in Figure 1.7),⁴⁰ and also used the same methods to predict NMR spectra of an $S = 2$ $[\text{Fe}^{\text{IV}}(\text{O})(\text{tpa}^{\text{Ph}})]^-$ complex (where $\text{tpa}^{\text{Ph}} = \text{tris}(5\text{-phenylpyrrol-2-ylmethyl})\text{amine}$) in quintet and triplet ground spin states (Figure 1.8), to highlight how these paramagnetic shifts are different.⁴¹

Determination of solution-state geometry:

There are two C_s -symmetric isomers of $[\text{Fe}^{\text{IV}}(\text{O})(\text{TPA})(\text{L})]^{2+}$, and one of them has all of its pyridines arranged equatorially around the iron center and aligned parallel to the oxoiron(IV) unit. In the other isomer, the pyridines have different configurations, such that two of them are arranged equatorially around the iron center but are perpendicular to the oxoiron(IV) unit, and one pyridine is trans to the

oxoiron(IV) unit (Figure 1.7). NMR spectroscopy can be useful in determining the solution state spectra for all the complexes. This set of different configurations is also helped by access to NMR spectra of complexes in which pyridines are in all three different alignments (trans, perpendicular or parallel to the ferryl unit) and can help further assignment of solution-state structures of these complexes.

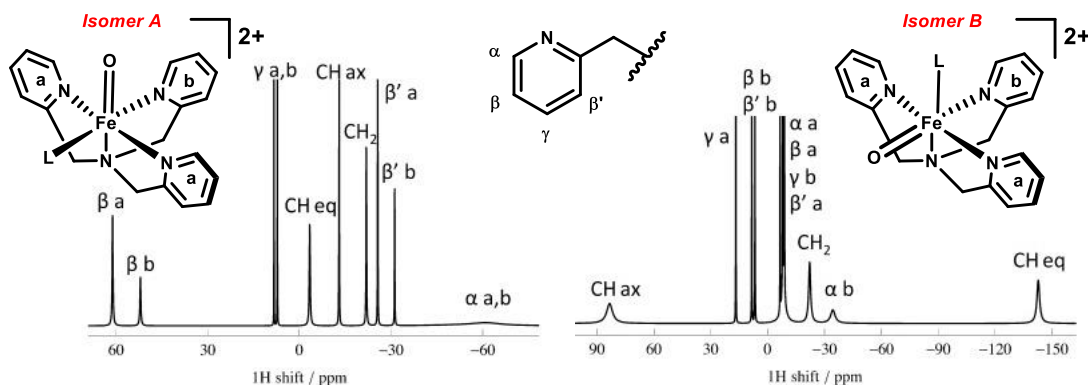


Figure 1.7 DFT predicted NMR spectra for different isomeric forms of the complex $[\text{Fe}^{\text{IV}}(\text{O})(\text{TPA}(\text{L}))_2]^{2+}$ in the $S = 1$ spin state. Figure adapted from reference ⁴⁰.

The predicted NMR spectra of the two isomers are reproduced in Figure 1.7 and indicate that the pyridine proton signals in both the isomers of the complex are quite distinct from each other. In the isomer A, the β' and β proton signals of all three equatorial pyridines are paramagnetically shifted upfield and downfield respectively. But in isomer B, there are two distinct pyridines. β' and β proton signals for pyridines perpendicular to the oxoiron(IV) unit are both shifted upfield below 0 ppm, and the pyridine trans to the oxo has its pyridine β' and β proton signals shifted downfield and upfield. These variations in signals of the isomers are distinct enough from each other that ^1H -NMR spectrum of the complex can shed light into the solution-state structure.

The ^1H -NMR spectrum of $[\text{Fe}^{\text{IV}}(\text{O})(\text{tpa}^{\text{Ph}})]^-$ looks different in quintet and triplet spin states, as seen from different paramagnetic shifts of H_a and H_b protons in the

spectrum of this complex shown in Figure 1.8. Unfortunately, the NMR spectra of the $S = 2$ complexes are not reported, so this DFT method remains to be verified experimentally, although it has been found to be fairly accurately predict the NMR spectra of $S = 1$ oxoiron(IV) complexes. The differences in paramagnetic shifts are very obvious indicators that NMR spectroscopy can be a useful tool to distinguish the spin state of the oxoiron(IV) complexes.

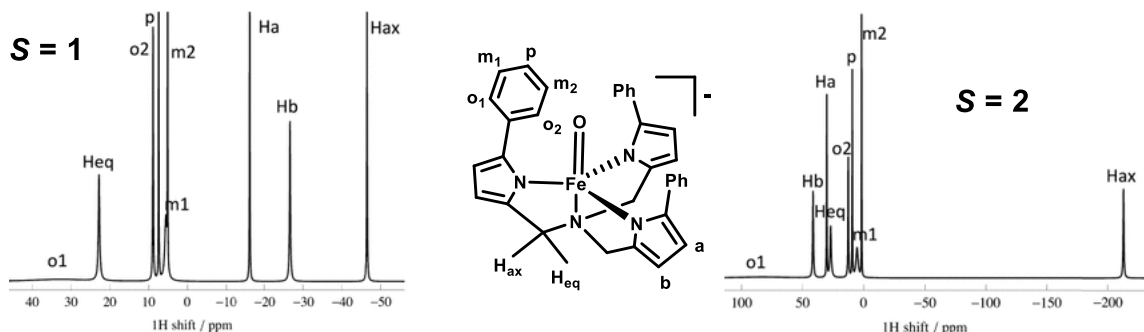


Figure 1.8 DFT predicted NMR spectra of the complex $[\text{Fe}^{\text{IV}}(\text{O})(\text{tpa}^{\text{Ph}})]^-$ in the $S = 1$ and $S = 2$ spin state. Figure adapted from reference ⁴⁰.

In this thesis, we use some of the complexes in the $S = 2$ ground spin state to test this method experimentally and provide yet NMR spectroscopy as yet another informative tool another tool for the bioinorganic community to obtain this information.

Furthermore, because we know that transition to the spin state $S = 2$ occurs when all the pyridines in complex $[\text{Fe}^{\text{IV}}(\text{O})(\text{TPA})(\text{L})]^{2+}$ are replaced by quinolines or alpha-methyl substitutions are made on the pyridines, we wanted to explore at what point this change occurs. Just like the case of N4Py and BnTPEN series of oxoiron(IV) complexes, we have made sequential changes in the parent complex $[\text{Fe}^{\text{IV}}(\text{O})(\text{TPA})(\text{L})]^{2+}$ and introduced quinoline heterocycles. The resulting complexes have been examined by NMR spectroscopy and in doing so, we have identified a complex in the process that exhibits spin-crossover behavior. Detailed reactivity studies of these new complexes accompany these results. This data is presented in Chapter 4.

1.7 References

1. Banerjee, R.; Proshlyakov, Y.; Lipscomb, J. D.; Proshlyakov, D. A., *Nature* **2015**, *518*, 431.
2. Bols, M. L.; Hallaert, S. D.; Snyder, B. E. R.; Devos, J.; Plessers, D.; Rhoda, H. M.; Dusselier, M.; Schoonheydt, R. A.; Pierloot, K.; Solomon, E. I.; Sels, B. F., *J. Am. Chem. Soc.* **2018**, *140* (38), 12021-12032.
3. Price, J. C.; Barr, E. W.; Tirupati, B.; Bollinger, J. M.; Krebs, C., *Biochemistry* **2003**, *42* (24), 7497-7508.
4. van der Ploeg, J. R.; Weiss, M. A.; Saller, E.; Nashimoto, H.; Saito, N.; Kertesz, M. A.; Leisinger, T., *J. Bacteriol.* **1996**, *178* (18), 5438.
5. Hegg, E. L.; Jr, L. Q., *Eur. J. Biochem.* **1997**, *250* (3), 625-629.
6. Koehntop, K. D.; Emerson, J. P.; Que, L., *J. Biol. Inorg. Chem.* **2005**, *10* (2), 87-93.
7. Kal, S.; Que, L., *J. Biol. Inorg. Chem.* **2017**, *22* (2), 339-365.
8. Bollinger Jr, J. M.; Price, J. C.; Hoffart, L. M.; Barr, E. W.; Krebs, C., *Eur. J. Inorg. Chem.* **2005**, *2005* (21), 4245-4254.
9. Tamanaha, E.; Zhang, B.; Guo, Y.; Chang, W.-c.; Barr, E. W.; Xing, G.; St. Clair, J.; Ye, S.; Neese, F.; Bollinger, J. M.; Krebs, C., *J. Am. Chem. Soc.* **2016**, *138* (28), 8862-8874.
10. Wong, S. D.; Srnec, M.; Matthews, M. L.; Liu, L. V.; Kwak, Y.; Park, K.; Bell III, C. B.; Alp, E. E.; Zhao, J.; Yoda, Y.; Kitao, S.; Seto, M.; Krebs, C.; Bollinger, J. M.; Solomon, E. I., *Nature* **2013**, *499*, 320.
11. Sinnecker, S.; Svensen, N.; Barr, E. W.; Ye, S.; Bollinger, J. M.; Neese, F.; Krebs, C., *J. Am. Chem. Soc.* **2007**, *129* (19), 6168-6179.
12. Galonić Fujimori, D.; Barr, E. W.; Matthews, M. L.; Koch, G. M.; Yonce, J. R.; Walsh, C. T.; Bollinger, J. M.; Krebs, C.; Riggs-Gelasco, P. J., *J. Am. Chem. Soc.* **2007**, *129* (44), 13408-13409.
13. Eser, B. E.; Barr, E. W.; Frantom, P. A.; Saleh, L.; Bollinger, J. M.; Krebs, C.; Fitzpatrick, P. F., *J. Am. Chem. Soc.* **2007**, *129* (37), 11334-11335.

14. Panay, A. J.; Lee, M.; Krebs, C.; Bollinger, J. M.; Fitzpatrick, P. F., *Biochemistry* **2011**, *50* (11), 1928-1933.
15. Yu, C.-P.; Tang, Y.; Cha, L.; Milikisiyants, S.; Smirnova, T. I.; Smirnov, A. I.; Guo, Y.; Chang, W.-c., *J. Am. Chem. Soc.* **2018**, *140* (45), 15190-15193.
16. Rohde, J.-U.; In, J.-H.; Lim, M. H.; Brennessel, W. W.; Bukowski, M. R.; Stubna, A.; Münck, E.; Nam, W.; Que, L., *Science* **2003**, *299* (5609), 1037.
17. McDonald, A. R.; Que, L., Jr., *Coord. Chem. Rev.* **2013**, *257* (2), 414-428.
18. Klein, J. E. M. N.; Que, L., Biomimetic High-Valent Mononuclear Nonheme Iron-Oxo Chemistry. In *Encyclopedia of Inorganic and Bioinorganic Chemistry*, John Wiley & Sons, Ltd: 2016; p; DOI: 10.1002/9781119951438.eibc2344
19. Puri, M.; Que, L., *Acc. Chem. Res.* **2015**, *48* (8), 2443-2452.
20. Lim, M. H.; Rohde, J.-U.; Stubna, A.; Bukowski, M. R.; Costas, M.; Ho, R. Y. N.; Münck, E.; Nam, W.; Que, L., *Proc. Nat. Acad. Sci.* **2003**, *100* (7), 3665.
21. Zang, Y.; Kim, J.; Dong, Y.; Wilkinson, E. C.; Appelman, E. H.; Que, L., Jr., *J. Am. Chem. Soc.* **1997**, *119*, 4197-4205.
22. Rasheed, W.; Draksharapu, A.; Banerjee, S.; Young, V. G.; Fan, R.; Guo, Y.; Ozerov, M.; Nehr Korn, J.; Krzystek, J.; Telsler, J.; Que, L., *Angew. Chem. Int. Ed.* **2018**, *57* (30), 9387-9391.
23. Lubben, M.; Meetsma, A.; Wilkinson, E. C.; Feringa, B.; Que Jr, L., *Angew. Chem. Int. Ed.* **1995**, *34* (13-14), 1512-1514.
24. Lo, W. K. C.; Huff, G. S.; Preston, D.; McMorran, D. A.; Giles, G. I.; Gordon, K. C.; Crowley, J. D., *Inorganic Chemistry* **2015**, *54* (14), 6671-6673.
25. Kaizer, J.; Klinker, E. J.; Oh, N. Y.; Rohde, J.-U.; Song, W. J.; Stubna, A.; Kim, J.; Münck, E.; Nam, W.; Que, L., Jr., *J. Am. Chem. Soc.* **2004**, *126* (2), 472-473.
26. Xue, G.; De Hont, R.; Münck, E.; Que Jr, L., *Nat. Chem.* **2010**, *2*, 400.
27. Paine, T. K.; Costas, M.; Kaizer, J.; Que Jr, L., *J. Biol. Inorg. Chem.* **2006**, *11* (3), 272-276.
28. Klinker, E. J.; Kaizer, J.; Brennessel, W. W.; Woodrum, N. L.; Cramer, C. J.; Que, L., Jr., *Angew. Chem. Int. Ed.* **2005**, *44* (24), 3690-3694.

29. Massie, A. A.; Denler, M. C.; Cardoso, L. T.; Walker, A. N.; Hossain, M. K.; Day, V. W.; Nordlander, E.; Jackson, T. A., *Angew. Chem. Int. Ed.* **2017**, *56* (15), 4178-4182.
30. Duelund, L.; Hazell, R.; McKenzie, C. J.; Preuss Nielsen, L.; Toftlund, H., *J. Chem. Soc., Dalton Trans.* **2001**, (2), 152-156.
31. Ortega-Villar, N.; Ugalde-Saldívar, V. M.; Muñoz, M. C.; Ortiz-Frade, L. A.; Alvarado-Rodríguez, J. G.; Real, J. A.; Moreno-Esparza, R., *Inorg. Chem.* **2007**, *46* (18), 7285-7293.
32. Cheaib, K.; Mubarak, M. Q. E.; Sénéchal-David, K.; Herrero, C.; Guillot, R.; Clémancey, M.; Latour, J.-M.; de Visser, S. P.; Mahy, J.-P.; Banse, F.; Avenier, F., *Angew. Chem. Int. Ed.* **2019**, *58* (3), 854-858.
33. Lennartson, A.; McKenzie, C. J., *Angew. Chem. Int. Ed.* **2012**, *51* (27), 6767-6770.
34. Kang, Y.; Li, X.-X.; Cho, K.-B.; Sun, W.; Xia, C.; Nam, W.; Wang, Y., *J. Am. Chem. Soc.* **2017**, *139* (22), 7444-7447.
35. Duban, E. A.; Bryliakov, K. P.; Talsi, E. P., *Eur. J. Inorg. Chem.* **2007**, *2007* (6), 852-857.
36. Mukherjee, G.; Lee, C. W. Z.; Nag, S. S.; Alili, A.; Cantú Reinhard, F. G.; Kumar, D.; Sastri, C. V.; de Visser, S. P., *Dalton Trans.* **2018**, *47* (42), 14945-14957.
37. Singh, R.; Ganguly, G.; Malinkin, S. O.; Demeshko, S.; Meyer, F.; Nordlander, E.; Paine, T. K., *Inorg. Chem.* **2019**.
38. Sahu, S.; Zhang, B.; Pollock, C. J.; Dürr, M.; Davies, C. G.; Confer, A. M.; Ivanović-Burmazović, I.; Sieglar, M. A.; Jameson, G. N. L.; Krebs, C.; Goldberg, D. P., *J. Am. Chem. Soc.* **2016**, *138* (39), 12791-12802.
39. Rana, S.; Biswas, J. P.; Sen, A.; Clémancey, M.; Blondin, G.; Latour, J.-M.; Rajaraman, G.; Maiti, D., *Chem. Sci.* **2018**, *9* (40), 7843-7858.
40. Borgogno, A.; Rastrelli, F.; Bagno, A., *Chem. Eur. J.* **2015**, *21* (37), 12960-12970.

41. Bigi, J. P.; Harman, W. H.; Lassalle-Kaiser, B.; Robles, D. M.; Stich, T. A.; Yano, J.; Britt, R. D.; Chang, C. J., *J. Am. Chem. Soc.* **2012**, *134* (3), 1536-1542.

Chapter 2

Oxoiron(IV) Complexes Supported by N4Py-Based Ligands

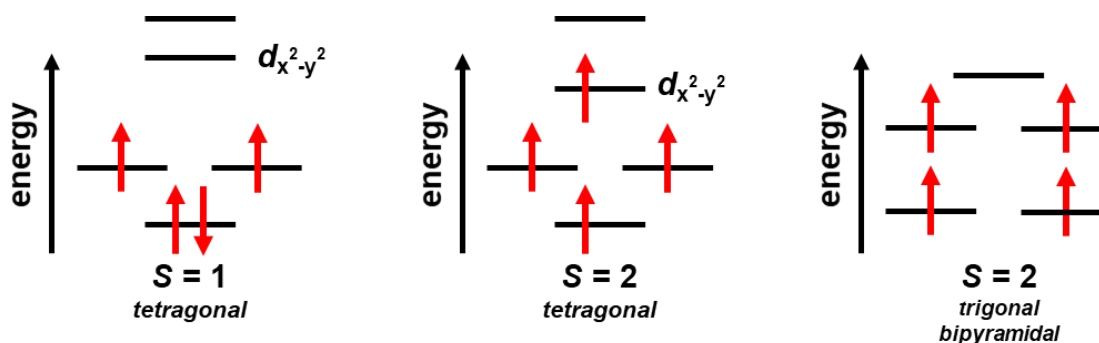
Parts of this chapter were published in:

Rasheed, W.; Draksharapu, A.; Banerjee, S.; Young, V. G.; Fan, R.; Guo, Y.; Ozerov, M.; Nehrkorn, J.; Krzystek, J.; Telser, J.; Que, L., Jr. "Crystallographic Evidence for a Sterically Induced Ferryl Tilt in a Nonheme Oxoiron(IV) Complex that makes it a Better Oxidant" *Angew. Chem. Int. Ed.* **2018**, *57*, 9387

2.1 Introduction

In the catalytic cycles of many oxygen activating nonheme iron oxygenases and oxidases, $S = 2$ oxoiron(IV) intermediates are often found to be directly implicated in a diverse range of chemical transformations.¹ These transformations include hydroxylation of un-activated aliphatic C–H bonds, epoxidation of C=C bonds, as well as desaturation of C–C bonds among others.² Bioinorganic chemists have mounted a significant effort to mimic the oxoiron(IV) intermediates involved in the catalytic cycles of these non-heme iron oxygenases, and there are now about 90 synthetic variants, although most are found in the $S = 1$ ground spin state, unlike the $S = 2$ ground spin state described for the enzymes.³⁻⁶

The few mononuclear $S = 2$ oxoiron(IV) complexes characterized thus far have been reported using two strategies.⁷ One strategy employed the use of sterically bulky tripodal ligands to support the ferryl unit. These ligand frameworks enforced a trigonal bipyramidal geometry around the iron(IV) center, which led the Fe d-orbitals to arrange in two pairs of energetically degenerate singly-occupied orbitals, thus favoring a high-spin ($S = 2$) configuration (Scheme 2.1, right).⁸⁻⁹ The ligand frameworks used to enable this configuration also blocked access to the ferryl unit, which is responsible for activating strong C–H bonds. So, the resulting $S = 2$ oxoiron(IV) complexes were found to be relatively sluggish oxidants.



Scheme 2.1 d-orbital splitting diagrams of the oxoiron(IV) complexes in different spin states and ligand fields.

The second strategy used to populate $S = 2$ ground spin state in ferryl complexes employed weaker-field ligands compared with those based on tertiary amines and *N*-heterocycles like pyridines and benzimidazoles. This strategy enabled formation of more reactive oxoiron(IV) complexes in $S = 2$ ground spin state. To start, Bakac and coworkers¹⁰ reported the $S = 2$ $[\text{Fe}^{\text{IV}}(\text{O})(\text{H}_2\text{O})_5]^{2+}$ ion in acidic aqueous solution, in which the ferryl unit was coordinated by five weak-field aqua ligands. While it was also found to be very reactive towards oxidation of organic substrates, its extremely short-lived nature ($t_{1/2} \approx$ only 20 seconds at room temperature) prevented further characterization by crystallography.

A relatively more stable compound is the $S = 2$ iron(IV) complex $[\text{Fe}^{\text{IV}}(\text{O})(\text{TQA})(\text{L})]^{2+}$ (where TQA = tris(2-quinolylmethyl)amine, Figure 2.1), which exhibits the fastest rate of oxidation of cyclohexane found thus far for any mononuclear synthetic oxoiron(IV) complex, and is also a functional and spectroscopic model for the TauD-**J** intermediate.¹¹ This complex has an axial amine bound to three quinoline heterocycles arranged equatorially around the iron(IV) center. It is proposed that the steric effects of the quinoline donors increase the Fe–N bond lengths, thereby weakening the iron(IV) ligand field to afford the observed $S = 2$ ground state. The change in spin state from $S = 1$ to $S = 2$ is achieved because sterically encumbering quinoline donors replace the strong-field donors of pyridines and lower the energy of the $d_{x^2-y^2}$ orbital of the iron(IV) center, thus bringing it closer to the d_{xy} orbital. This likely enables a new configuration whereby an unpaired electron resides in both d_{xy} and the $d_{x^2-y^2}$ orbital (in addition to the unpaired electrons in d_{xz} and d_{yz}), thus resulting in a ground spin state change from $S = 1$ to $S = 2$. A similar effect is also enforced by the introduction of an alpha-methyl substituent on the pyridine, whereby steric effects of the methyl protons are proposed to increase the Fe–N bond lengths of the resulting complex $[\text{Fe}^{\text{IV}}(\text{O})(6\text{Me}_3\text{TPA})(\text{L})]^{2+}$, where $6\text{Me}_3\text{TPA} =$ tris((6-methylpyridin-2-yl)methyl)amine and result in the change from $S = 1$ to $S = 2$ ground spin state. This is an especially interesting change, because most of the synthetic oxoiron(IV)

complexes have been characterized only in the $S = 1$ ground spin state, and the direct evidence for such a steric change can help design more synthetic oxoiron(IV) complexes with $S = 2$ ground spin state.

One way to quantitatively examine the steric effects of quinolines around the ferryl unit is to obtain crystal structure of the oxoiron(IV) compounds containing these modifications. Due to their thermal instability ($t_{1/2} \approx 15$ min in MeCN at -40 °C), it has not been possible to obtain the crystal structure or reliable XAS spectroscopic analyses of the highly reactive $S = 2$ complexes $[\text{Fe}^{\text{IV}}(\text{O})(\text{TQA})(\text{L})]^{2+}$ or $[\text{Fe}^{\text{IV}}(\text{O})(6\text{Me}_3\text{TPA})(\text{L})]^{2+}$ (Figure 2.1).

Interestingly, Nam and co-workers have also reported another very similarly reactive oxoiron(IV) complex, albeit in the $S = 1$ spin state, which is supported by *N*-methylbenzimidazoles, $[\text{Fe}^{\text{IV}}(\text{O})(\text{Me}_3\text{NTB})(\text{L})]^{2+}$, ($\text{Me}_3\text{NTB} = \text{tris}((1\text{-methyl-1H-benzo}[d]\text{imidazol-2-yl)methyl)amine)$) (Figure 2.1).¹² Its hydrogen-atom abstraction ability is comparable to that of $[\text{Fe}^{\text{IV}}(\text{O})(\text{TQA})(\text{L})]^{2+}$, but it is even more unstable than the latter, with a half-life of only about 1-2 minutes in MeCN at -40 °C. Thus, the most reactive synthetic analogues of these intermediates are supported by tetradentate tripodal ligands with *N*-methylbenzimidazole or quinoline or 6-methylpyridine donors, but their instability precludes structural characterization.

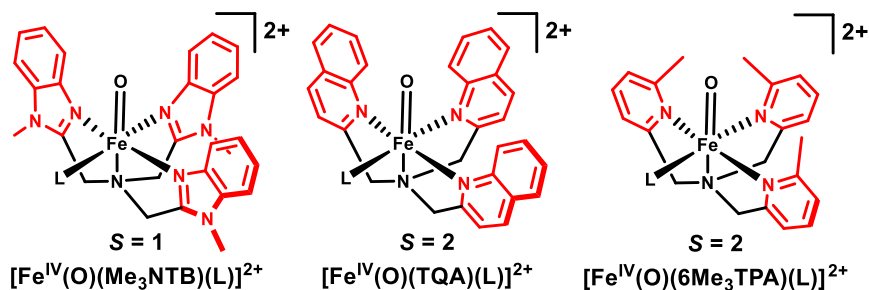


Figure 2.1 Reactive and thermally unstable $S = 1$ and $S = 2$ $\text{Fe}^{\text{IV}}(\text{O})$ complexes supported by tetradentate ligands.

We have thus embarked on a systematic effort to compare the structures and reactivity of a series of $\text{Fe}^{\text{IV}}(\text{O})$ complexes supported by pentadentate ligands, that contain *N*-methylbenzimidazoles, quinolines, or alpha-methyl substituted

pyridines, to determine whether such complexes can be stabilized, and possibly crystallized. This would enable us to establish a possible correlation of structure with its reactivity, in addition to lending structural insight into how these modified pyridines, quinolines and benzimidazoles arrange around the ferryl center. This chapter lays out the results of those efforts.

As a starting point, we have chosen $[\text{Fe}^{\text{IV}}(\text{O})(\text{N4Py})]^{2+}$ (**1**, N4Py = 1,1-di(pyridin-2-yl)-*N,N*-bis(pyridin-2-ylmethyl)methanamine), the second oxoiron(IV) complex to be crystallographically characterized, which is relatively stable ($t_{1/2} = 60$ h at 25 °C). The N4Py ligand has an axial amine and four equatorial pyridines that can be subdivided into two distinct pairs of pyridine donors.¹³⁻¹⁴ At least four different groups have taken on an effort to modify one of the two pairs of pyridines to determine how the properties of the resulting ferryl complexes are affected.¹⁵⁻¹⁸

Note: After the experimental results from this chapter were published, more groups have conducted reactivity studies on complexes described in this chapter, including measurement of kinetic isotope effects for the reactions of these complexes with C–H substrates,¹⁹ as well as halogenations carried out using iron(II) halide complexes supported by same frameworks, which occur after the initial hydrogen-atom-abstraction by ferryl complexes discussed in this chapter.²⁰ Other groups have even reported complexes similar to the ones in this chapter, both in the context of iron and manganese metal centers,²¹⁻²² as well as in the context of the ligand modifications introduced.²³ Fortunately, the higher stability as well as purity of the complexes we reported has enabled active discussion and exploration of the rich chemistry provided by N4Py framework, and enhanced the studies conducted by other groups. In this chapter, all the experimental developments up to March 2019 are included to provide an insight into this versatile framework.

Six different types of modifications have been reported for this ligand framework, and the types of the modifications and properties of the metal complexes resulting from them are categorized below:

Introduction of carboxylate donors: The first modification on N4Py framework was reported by the Que group in 2012, and used weak-field oxygen donors similar to those in $[\text{Fe}^{\text{IV}}(\text{O})(\text{H}_2\text{O})_5]^{2+}$. The modified ligand introduced carboxylate ligands on the N4Py framework to form the ligand dubbed *n*Bu-P2DA (*n*Bu-P2DA = *N*-(1',1'-bis(2-pyridyl)pentyl)iminodiacetate). $[\text{Fe}^{\text{IV}}(\text{O})(\textit{n}\text{Bu-P2DA})]^{2+}$ was originally designed to mimic the carboxylate-rich active sites of taurine dioxygenase's ferryl intermediate, using a 2-carboxylate-2-pyridine set of equatorial ligands (Figure 2.2).²⁴ However, its thermal instability at temperatures even below $-60\text{ }^\circ\text{C}$ prevented its crystallographic characterization, and while it was a structural model of TauD-**J**, its $S = 1$ spin state and low reactivity prevented it from being a spectroscopic and functional analog of this enzymatic intermediate.

Introduction of aryl rings on pyridines: Sahu *et al.* made the second modification on N4Py, wherein aryl groups replaced the 6-H's of the pyridines on the bis(pyridyl)methylamine half of the N4Py ligand.^{18, 25} Out of the two aryl modifications, they reported the crystal structure of $[\text{Fe}^{\text{IV}}(\text{O})(\text{ArF}_2)_2\text{N4Py}]^{2+}$ (complex **4**, Figure 2.2), where the aryl groups were 2,6-difluorophenyl rings. The fluorine or the hydrogen atoms on the aryl rings are situated such that these ferryl complexes end up undergoing *intramolecular* hydroxylation of the aryl rings when warmed to higher temperatures, and likely impede their *intermolecular* reactivity studies with substrates at room temperature.

Introduction of 6Me-groups on the pyridines: On the bis(pyridyl)methylamine half of the N4Py ligand, replacement of the pyridine 6-H's with methyl groups has also been recently reported, but the resulting complex has reduced thermal stability and attempts to get its crystal structures were not successful.²³ Interestingly, the effect of the introduction of an alpha-methyl substituent on the pyridine on the bis(pyridin-2-ylmethyl) half has been also examined for the parent complex recently, and interplay of sterics and electronics was just recently reported between the two substitutions.²⁶ However, the steric effects upon the introduction of an alpha-methyl substituent on the pyridines have only been investigated using

computational methods, and crystallographic insight to experimentally quantify these effects is not available.

Introduction of N-methylbenzimidazole heterocycles: N2Py2B is an N4Py variant where two of the pyridines are replaced with *N*-methylbenzimidazoles.¹⁵ Detailed structural or spectroscopic characterization on oxoiron(IV) supported by this ligand, that is $[\text{Fe}^{\text{IV}}(\text{O})(\text{N2Py2B})]^{2+}$ (**2**) (Figure 2.3) was not provided in the original report because of its thermal instability, but its reactivity profile was examined extensively. An oxomanganese(IV) complex supported by this ligand was recently reported and compared, but unlike its oxoiron(IV) counterpart, this complex has muted reactivity with hydrocarbons and with oxygen-atom transfer substrates.²² In this chapter, crystallographic characterization of this complex along with other spectroscopic details is reported.

Introduction of electronically rich pyridines: In N4Py**, two pyridines have electron-donating methyl groups on 3- and 5-position, and a methoxy group on the 4-position. Although $[\text{Fe}^{\text{IV}}(\text{O})(\text{N4Py}^{**})]^{2+}$ (**1***) has been reported before (Figure 2.2), detailed information on its spectroscopic characterization and reactivity profile is not available.¹⁶ Despite its thermal stability, structural data on this complex has not been obtained. The corresponding $[\text{Mn}^{\text{IV}}(\text{O})(\text{N4Py}^{**})]^{2+}$ is found to be much less reactive than its parent $[\text{Mn}^{\text{IV}}(\text{O})(\text{N4Py})]^{2+}$ complex, but in the case of $\text{Fe}^{\text{IV}}(\text{O})$ complexes, both complexes have comparable HAT reactivity profiles with cumene and ethylbenzene. This complex was crystallographically characterized and information about its bond metrics are also discussed.

Introduction of quinolines: N2Py2Q is an N4Py variant where two of the pyridines are replaced with quinolines (Figure 2.3). The complex $[\text{Mn}^{\text{IV}}(\text{O})(\text{N2Py2Q})]^{2+}$ and some of its reactivity has been described by Massie *et al.*, but the corresponding $\text{Fe}^{\text{IV}}(\text{O})$ was not reported.^{17, 21} We report the crystallographic characterization of the complex $[\text{Fe}^{\text{IV}}(\text{O})(\text{N2Py2Q})]^{2+}$ (**3**) in this chapter, and correlate its reactivity with structure.²⁷

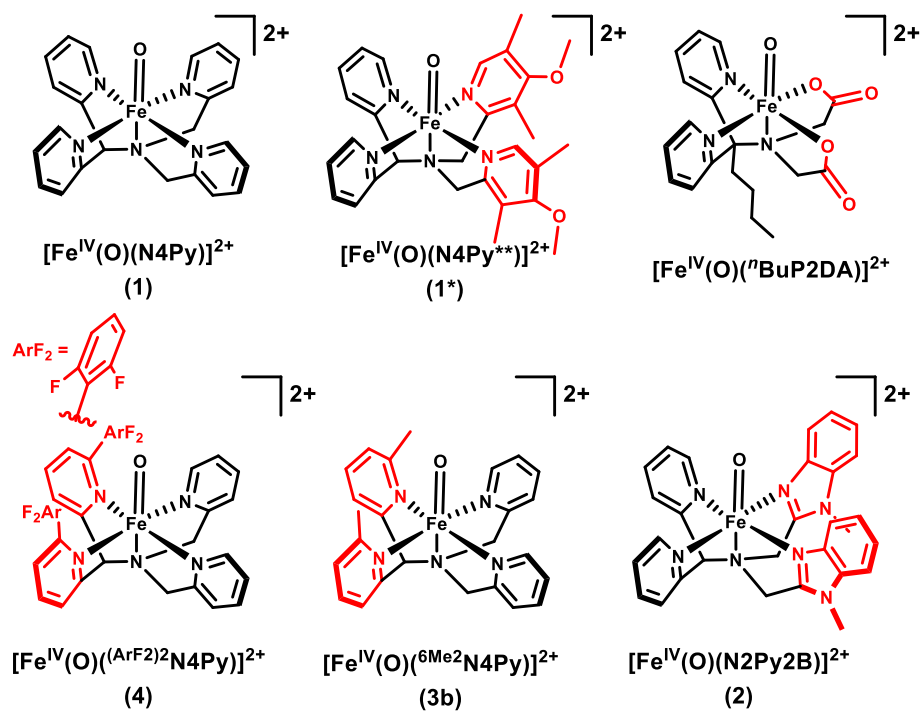


Figure 2.2 Previously reported modifications on the N4Py framework.

This chapter examines the effects of making heterocyclic modifications on the N4Py framework, and in this regard, some of the previously reported variants of the N4Py ligand have been synthesized, wherein the two pyridine donors on the bis(pyridyl-2-methyl)amine half are replaced either by *N*-methylbenzimidazoles (N2Py2B), quinolines (N2Py2Q), 6-methylpyridines or 4-methoxy-3,5-dimethylpyridines (N4Py**). The complexes examined in this chapter for their reactivity and spectroscopic effects are shown in Figure 2.3.

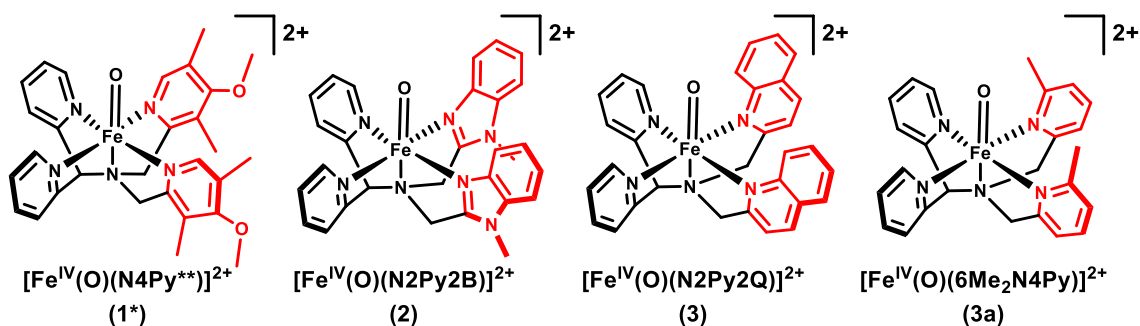


Figure 2.3 The Fe^{IV}(O) complexes supported by ligands based on N4Py framework, examined in this chapter.

2.2 Experimental Section

All materials were bought from Sigma Aldrich or Fischer Scientific, unless otherwise noted. The substrates cyclohexane, cyclooctane, 2,3-dimethylbutane, toluene, ethylbenzene, and cumene used in kinetic experiments were passed through a plug of silica before use, and triphenylmethane was recrystallized from ethanol, and its stock solutions were made in dichloromethane in a nitrogen-filled glovebox. Thioanisole solution was made outside the glovebox in acetonitrile. Fe^{II}(OTf)₂·2CH₃CN was prepared according to the published procedure.²⁸ All oxygen and moisture sensitive compounds were synthesized in a nitrogen-filled glovebox. All kinetic experiments were carried out under nitrogen.

The ligand and iron(II) precursor, [Fe^{II}(N4Py)(MeCN)](OTf)₂ of ferryl complexes **1**, and **1*** was synthesized as reported, as was the ligand and iron(II) precursor to **2**, [Fe^{II}(N2Py2B)(MeCN)](OTf)₂. N2Py2B = *N,N*-bis((1-methyl-1*H*-benzimidazol-2-yl)methyl)-1,1-di(pyridin-2-yl)methanamine. The ligand N2Py2Q (1,1-di(pyridin-2-yl)-*N,N*-bis(quinolin-2-ylmethyl)methanamine) was synthesized based on a modified procedure, and the synthesis of ligand 6Me₂N4Py is detailed below.

¹H NMR spectra were recorded on a Bruker 400 or 500 MHz spectrometer at 298 K. Elemental analyses were carried out by Atlantic Microlab (Norcross, GA). UV-vis spectra were recorded on a HP8453A diode array spectrometer equipped with a cryostat from Unisoku Scientific Instruments (Osaka, Japan). Electrospray

ionization mass spectrometry (ESI-MS) experiments were performed on a Bruker BioTOF II mass spectrometer using a spray chamber voltage of 4000 V and a carrier gas temperature of 200 °C. IR spectra of synthetic samples were recorded on a Nicolet iS5 FT-IR spectrometer with an ATR source.

Mössbauer spectra were recorded with two spectrometers, using Janis Research (Wilmington, MA) SuperVaritemp dewars that allow studies in applied magnetic fields of up to 7.5 T in the temperature range from 1.5 to 200 K. A LakeShore Model 331A temperature controller was used to control the temperature in experiments. Mössbauer spectral simulations were performed using the WMOSS software package (SEE Co, Edina, Minnesota). Isomer shifts are quoted relative to α -Fe metal at 298 K. The spectra were plotted by SpinCount developed by Prof. Michael Hendrich at Carnegie Mellon University.²⁹

The experimental setup for HFEPR and FIRMS was used as reported earlier.³⁰⁻³¹

2.2.1 Synthesis of the ligands and complexes

Synthesis of the parent ligand N4Py and the iron(II) complex

Ligand and iron(II) precursor to **1**, $[\text{Fe}^{\text{II}}(\text{N4Py})(\text{MeCN})](\text{OTf})_2$ was synthesized as reported before.³² Iron(II) perchlorate was replaced with the iron(II) triflate to avoid the former's explosive risks.

Synthesis of the ligand N4Py and the iron(II) complex**

The ligand and the iron(II) precursor $[\text{Fe}^{\text{II}}(\text{N4Py}^{**})(\text{MeCN})](\text{OTf})_2$ was synthesized using previously reported procedure.¹⁶

Synthesis of the ligand N2Py2B

The ligand was synthesized using previously reported procedure.¹⁵

Synthesis of the ligand N2Py2Q

The ligand was synthesized using a slightly modified previously published procedure.¹⁷ Two equivalents of 2-(chloromethyl)quinoline hydrochloride (1.20 g,

5.64 mmol) were dissolved in 4 mL of 5M NaOH solution. To this solution, bis(2-pyridyl)methylamine (0.52 g, 2.82 mmol, 1 equivalent) in 2 mL of acetonitrile was added dropwise. An additional 6 mL of acetonitrile was used to completely transfer the amine. After a day of stirring in open air, oily brown droplets were found to be floating in a light brown aqueous solution (and all acetonitrile had evaporated). To this solution, 2 mL of acetonitrile was added. 4 days after stirring the reaction, a light beige colored solid had crashed out, which was filtered, and washed with 10 mL of water, and dried under high vacuum. The original procedure used HPF_6 to crash out the solid from the oil as a salt, but it was not added in this case because the solid crashed out of the reaction mixture itself to give 1 g of product (76%). The ligand was characterized using ^1H NMR spectroscopy and found to be pure enough for metalation.

Note: *Hexafluorophosphoric acid (HPF_6) was used exclusively to precipitate out the ligands where necessary, to avoid explosive risks associated with perchloric acid (HClO_4). Perchlorate salts used in the following procedures are shock and heat-sensitive explosives, and should be handled with care. Wherever possible, perchlorate salts were replaced with triflate or hexafluorophosphate salts. Note however, that while replacement of HClO_4 with HPF_6 avoids explosion risks of the former, the latter is highly toxic and appropriate safety gear must be worn and the compounds handled carefully.*

Synthesis of the ligand 6Me₂N4Py (precursor to 3a)

2-(chloromethyl)-6-methylpyridyl hydrochloride (1 g, 5.61 mmol) was weighed in a 6-dram vial, followed by 4 mL of 5M NaOH. To this solution, di(pyridin-2-yl)methanamine (0.52 g, 2.8 mmol) was added directly, followed by 2 mL of 5 M NaOH. This solution was stirred for 48 h. Brown globular droplets were found to be floating in the solution, along with a small amount of yellow powder. DCM (3 x 10 mL) was added to this suspension to extract all the organics into the solvent from water. The combined fractions of DCM solutions were dried with MgSO_4 , and concentrated to obtain a brown solid. The brown solid was brought in an ice bath,

and cold hexafluorophosphoric acid solution (2 mL) was carefully pipetted into it to allow precipitation of a yellow solid. To use this ligand, the hexafluorophosphate salt had to be worked up with basic solution of sodium hydroxide, and extracted into the DCM layer, dried with MgSO₄, and concentrated to yield a brown solid. ¹H NMR (400 MHz, CD₃CN) δ 8.48 (d, 2H, α-*H*), 7.73-7.69 (m, 4H, γ-*H*), 7.53 (t, 2H, β'-*H*), 7.37 (d, 2H, β'-*H*), 7.20 (td, 2H, β-*H*), 7.02 (m, 2H, β-*H*), 5.29 (s, 1H, β-*H*), 3.84 (s, 4H, CH₂), 2.44 (s, 6H, Me-*H*).

Synthesis of Fe^{II}(N2Py2B)(CH₃CN)](OTf)₂

The [Fe^{II}(N2Py2B)(CH₃CN)](ClO₄)₂ complex was synthesized following the reported procedure.¹⁵ An alternative synthesis used Fe^{II}(OTf)₂•2CH₃CN as a metal source and followed the procedure reported for the perchlorate salt to give a red solid, but the procedure was done anaerobically. [⁵⁷Fe^{II}(N2Py2B)(CH₃CN)](OTf)₂ was prepared in a similar manner using ⁵⁷Fe^{II}(OTf)₂•2CH₃CN as the metal source. The ¹H NMR spectrum of the complex in CD₃CN showed a set of paramagnetically shifted peaks identical to those found for the perchlorate salt. ¹H NMR (400 MHz, CD₃CN) δ 37.99, 34.50, 29.82, 26.02, 18.19, 16.37, 12.21, 8.29, 5.64, 5.06, 2.20. The crystal structure ORTEP and its bond metrics were reported with bound acetonitrile on the 6th coordination site.

Synthesis of [Fe^{II}(N2Py2Q)(OTf)]OTf

In a nitrogen-filled glove box, Fe^{II}(OTf)₂•2CH₃CN (377 mg, 0.86 mmol) was dissolved in 1 mL CH₂Cl₂, and then transferred dropwise into a solution of N2Py2Q (402 mg, 0.86 mmol) in 1 mL CH₂Cl₂ to yield a reddish-brown solution. This solution was stirred overnight, and then concentrated *in vacuo* to remove all the CH₂Cl₂. At this point, 10 mL diethyl ether was added, and the solution was stirred for an hour. A dirty yellow solid was isolated as a powder in approximately 70% yield from this solution after filtration and could be recrystallized from slow diffusion of diethyl ether into a concentrated acetonitrile or dichloromethane solution. Anal. calculated for C₃₃H₂₅F₆FeN₅O₆S₂•3H₂O [Fe^{II}(N2Py2Q)(OTf)]OTf•3H₂O: C, 45.27;

H, 3.57; N, 8.00. Found: C, 45.78; H, 3.25; N, 7.49. $[\text{}^{57}\text{Fe}^{\text{II}}(\text{N}2\text{Py}2\text{Q})(\text{OTf})]\text{OTf}$ was prepared in a similar manner using $^{57}\text{Fe}^{\text{II}}(\text{OTf})_2 \cdot 2\text{CH}_3\text{CN}$ as the metal source. The ^1H NMR spectrum of iron(II) complex in CH_3CN showed a set of paramagnetically shifted peaks spanning 200 ppm, some of which were assigned using COSY NMR spectroscopy. ^1H NMR (400 MHz, CD_3CN) δ 136 (1H, br py- α -H), 110 (2H, Q- CH_2), 94.68 (2H, Q- CH_2), 58 (2H, py- β -H), 44.69 (2H, Q-3-H), 33.44 (py- β -H), 27.40 (2H, Q-7-H), 22.65 (2H, Q-4-H), 18 (2H, py- γ -H), 9 (2H, Q-5-H).

The crystal structure of this complex was reported recently²⁰, showing a bound triflate counterion for this complex's 6th coordination site.

Synthesis of $[\text{Fe}^{\text{II}}(\text{6Me}_2\text{N4Py})(\text{OTf})]\text{OTf}$

In a nitrogen-filled glove box, $\text{Fe}^{\text{II}}(\text{OTf})_2 \cdot 2\text{CH}_3\text{CN}$ (377 mg, 0.86 mmol) was dissolved in 1 mL CH_2Cl_2 , and then transferred dropwise into a solution of $\text{6Me}_2\text{N4Py}$ (402 mg, 0.86 mmol) in 1 mL CH_2Cl_2 to yield a brown solution. This solution was left to stir overnight, and then concentrated *in vacuo* to remove all the CH_2Cl_2 . At this point, 10 mL diethyl ether was added, and the solution was stirred for an hour. A dirty brown solid was isolated as a powder in approximately 70% yield from this solution after filtration and could be recrystallized from slow diffusion of diethyl ether into a concentrated acetonitrile or dichloromethane solution. ^1H NMR (400 MHz, 298 K in CD_2Cl_2) δ 148.41 (1H, br py- α), 130.15 (2H, py- CH_2), 122.84 (1H, py- CH_2), 59.14 (2H, py- β/β'), 54.42 (2H, py- β/β'), 47.08 (2H, 6Me-py- β/β'), 28.40 (2H, 6Me-py- β/β'), 18.42 (2H, py- γ), 14.69 (2H, py- γ), -23.66 (6H, 6Me- CH_3).

While elemental analysis or crystallographic information on this complex could not be obtained, triflate is the likely counterion bound to the 6th coordination site, as is often found for the $S = 2$ iron(II) complexes supported by pentadentate ligands and synthesized using iron(II) triflate as the metal source. Using other iron(II) salts with a different counterion, a crystal structure for this complex where acetonitrile is bound on the 6th coordination was reported in 2004.³³

Because the crystal structure of the iron(IV) complex could not be obtained, efforts to examine its reactivity in detail were not carried out.

Synthesis of [Fe^{IV}(O)(N4Py^{})](ClO₄)₂ (1^{*}) and [Fe^{IV}(O)(N4Py)](ClO₄)₂ (1)**

NaClO₄ (314 mg, 2.57 mmol) and ceric ammonium nitrate (CAN) (133 mg, 0.243 mmol) were dissolved in 1 mL water to give a yellow solution. This mixture was then transferred to a solution of iron(II) precursor (0.065 mmoles) in 0.5 mL acetonitrile to yield a blue solution in a minute. This solution was left overnight at 2-8 °C, and the next day blue solid crystals could be seen in light bluish green solution of water and acetonitrile. This solid was carefully filtered, and washed with 1 mL water, and the resulting solid was dried overnight in high vacuum to yield a blue solid. Both solids are highly soluble in water, so only sparing amount of water was used.

Alternative methods to make both the solids involve addition of excess amount of oxidants like ArIO in iron(II) acetonitrile solutions at room temperature, and stirring in for half-an hour, which then forms the complexes in full yield. The complexes are then kept in refrigerator to crash out any ArIO.

Synthesis of [Fe^{IV}(O)(N2Py2B)](ClO₄)₂ (2)

NaClO₄ (314 mg, 2.57 mmol) and ceric ammonium nitrate (CAN) (133 mg, 0.243 mmol) were dissolved in 3 mL water to give a yellow solution. This mixture was then transferred to a solution of [Fe^{II}(N2Py2B)(MeCN)](ClO₄)₂ (50 mg, 0.065 mmoles) in 1 mL acetonitrile to yield a blue solution, which precipitated in a minute to give a blue solid. This solid was filtered, and washed with 2 mL water, and the resulting solid was dried overnight in high vacuum to yield a greenish-blue powder (30 mg, 62% yield). Crystals suitable for X-ray crystallography were grown by dissolving 10 mg of the solid in 0.2 mL acetonitrile and adding a water solution of NaClO₄ (50 mg in 1.8 mL). Slow evaporation of acetonitrile at 2-5 °C over the course of 8 h formed bluish green crystals suitable for X-ray diffraction. Anal. calcd.

for $C_{29}H_{27}Cl_2FeN_7O_9 \cdot H_2O$ [$Fe^{IV}(O)(N_2Py_2B)(ClO_4)_2 \cdot H_2O$]: C, 45.69; H, 3.83; N, 12.86, Cl, 9.30. Found: C, 45.25; H, 3.88; N, 12.78, Cl, 9.39.

About 50 mg of solid **2** for HFEPF/FIRMS experiments was prepared in a similar manner.

Synthesis of [$^{57}Fe^{IV}(O)(N_2Py_2B)(PF_6)_2$]

The oxoiron(IV) complex was generated from the labeled iron(II) precursor. The iron(II) precursor was dissolved in approximately 200 μ L CH_3CN . Adding 4 eq ceric ammonium nitrate (CAN, $(NH_4)_2[Ce(NO_3)_6]$) in 0.5 mL H_2O to the iron(II) solution changed the color of the solution to bluish green within a minute. Upon addition of 20 eq NH_4PF_6 in 100 μ L H_2O to the vial, a precipitate formed from the solution immediately, and the solution was kept at 2-5 $^{\circ}C$ for 10 minutes to allow more precipitate to form. This solid was filtered on a sintered fine frit as a blue solid, washed with 5 mL H_2O , and dried overnight under high vacuum to give a bluish green solid. A 2-mM solution was made in CH_3CN and passed through a syringe filter, transferred into a Mössbauer cup, and then frozen in liquid nitrogen.

Synthesis of [$Fe^{IV}(O)(N_2Py_2Q)(ClO_4)_2$] (3**)**

$NaClO_4$ (314 mg, 2.57 mmol) and ceric ammonium nitrate (CAN) (133 mg, 0.243 mmol) were dissolved in 3 mL water to give a yellow solution. This mixture was then transferred to a solution of [$Fe^{II}(N_2Py_2Q)OTf$]OTf (50 mg, 0.061 mmoles) in 1 mL CH_3CN to yield a dirty-green solution, which precipitated in a minute to give a dark green solid. The solution was kept for two hours at 2-5 $^{\circ}C$ to allow for further precipitation. This solid was filtered, and washed with 2 mL water, and the resulting solid was dried overnight in high vacuum to yield a green powder (25 mg, 55% yield). Crystals suitable for X-ray crystallography were grown by dissolving 10 mg of the solid in 0.2 mL CH_3CN , and adding an aqueous solution of $NaClO_4$ (50 mg in 1.8 mL). Slow evaporation of CH_3CN at 2-5 $^{\circ}C$ over the course of a few hours formed green crystals suitable for X-ray diffraction. Anal. calcd. for

C₃₁H₂₅Cl₂FeN₅O₉•3H₂O [Fe^{IV}(O)(N₂Py₂Q)](ClO₄)₂•3H₂O: C, 46.99; H, 3.94; N, 8.84. Found: C, 46.87; H, 3.48; N, 9.04.

About 50 mg of solid **3** for HFEPR/FIRMS experiments was prepared in a similar manner.

Synthesis of [⁵⁷Fe^{IV}(O)(N₂Py₂Q)](PF₆)₂

The oxoiron(IV) complex was generated from corresponding labeled iron(II) complex. The starting ferrous precursor was dissolved in approximately 200 μL CH₃CN, and then reacted with 4 eq ceric ammonium nitrate (CAN, (NH₄)₂[Ce(NO₃)₆]) in 0.5 mL water, changing the color of the solution to dark green in a minute. Upon addition of 20 eq NH₄PF₆ in 100 μL H₂O to the vial, a precipitate formed immediately from the solution, and the solution was kept at 2-5 °C for 10 minutes to allow more precipitate to crash out. This solid was filtered on a sintered fine frit, washed with 5 mL water, and then dried overnight under high vacuum to give a dark green solid. A 2-mM solution in CH₃CN was made, transferred into a Mössbauer cup, and then frozen in liquid nitrogen.

Synthesis of [Fe^{IV}(O)(6Me₂N₄Py)](OTf)₂ (**3a**)

1 mM CH₃CN solutions of **3a** were generated at room temperature in acetonitrile solution using 1-1.5 equivalents of 2-(^tBuSO₂)-C₆H₄IO (1-(*tert*-butylsulfonyl)-2-iodosylbenzene in 2,2,2-trifluoroethanol or DCM-*d*₂. Solid C₆F₅IO or pentafluoriodosylbenzene can also be used to generate the ferryl complex. While its ceric ammonium nitrate solution in water could be used to generate the complex, it could not be used to isolate the complex. It is possible that benzimidazole and quinoline rings in **2** and **3** help in stacking and packing of the complexes **2** and **3** so that the solids crash out right away, but attempts to crash out **3a** were not successful using cerium(IV) ammonium nitrate. Furthermore, the proximity of benzylic methyl groups to the ferryl unit also likely makes the ferryl complex unstable, thus preventing it from crashing out. The complex where the 6-

methyl groups were introduced on the other pair of pyridines of N4Py framework was reported recently, and could also not be crystallized.²³

2.2.2 ESI-MS of complexes **2** and **3**

Dilute acetonitrile solutions at room temperature of each of the oxoiron(IV) complexes were injected into the spectrometer at 200 °C to obtain the data. ESI-MS analysis of these solutions reveals major peaks at m/z 272.58 and 269.50 for **2** and **3**, values expected for the dicationic $[\text{Fe}^{\text{IV}}(\text{O})(\text{L})]^{2+}$ complexes. Cationic peaks for complexes **1***, **3a** and **3b** were reported in their original reports.^{16, 23, 26}

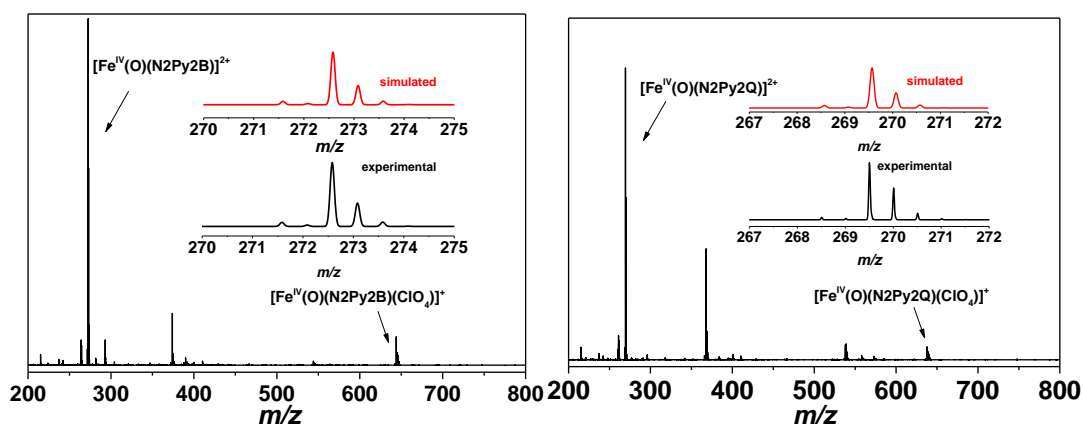


Figure 2.4 ESI-MS of complexes **2** (left) and **3** (right).

2.2.3 UV-Visible spectroscopy and thermal stability of the complexes

At 25 °C, 1 mM MeCN solutions of **2** and **3** have half-lives of 150 minutes, which is about 20-fold shorter than for the parent complex **1** (3600 minutes). Complex **1*** is even more stable, so its half-life of 3000 minutes was measured at a slightly elevated temperature of 30 °C.¹⁶ The choice of oxidant used can also impact the half-life, so that only solids for **2** and **3** are isolated and redissolved to measure half-lives, and **1** and **1*** were generated using solid iodosylbenzene.

The half-life of a 1-mM CH₃CN solution of **3a** at room temperature is 40 minutes when generated with excess solid C₆F₅IO, and 30 minutes when formed using 1.5 equivalents of PhI(OAc)₂ in acetonitrile solution.²⁶ Interestingly, its isomer **3b** has

a half-life of only 14 minutes at room temperature when generated using *m*CPBA,²³ but the half-life is 130 minutes when formed using 1.5 equivalents of PhI(OAc)₂ in acetonitrile solution (Table 2.13).²⁶ Therefore the choice of oxidant may impact the stability of the complexes. The half-lives of **3a** and **3b** are much lower than that of the unsubstituted parent complex **1**, and can also be attributed to the greater number of benzylic positions (11 benzylic protons, 6 of them close to the ferryl unit), compared with **3** (5 benzylic protons, none close to the ferryl unit). Furthermore, the oxidant can also play an important role as is seen in the case of **3b**.

Complexes **1–3** exhibit near-IR absorption bands, assigned previously in the case of **1** ($\lambda_{\text{max}} = 695 \text{ nm}$) to ligand field transitions.³⁴ For **2** and **3**, the absorbance maxima red-shift to 725 and 770 nm, respectively, suggesting a progressive weakening of the ligand field strength as two pyridine donors are replaced by *N*-methylbenzimidazoles (in **2**) and quinolines (in **3**). For **3**, this notion is further manifested by the appearance of higher-wavelength shoulders at 890 and 930 nm, similar to features observed for [Fe^{IV}(O)(TMC)(X)]⁺ complexes (TMC = 1,4,8,11-tetramethyl-1,4,8,11-tetraazacyclotetradecane) when the axial MeCN ligand is replaced by anions.³⁵ The absorption spectra of **1** and **1***, as well as those of **3** and **3a** exhibit similar λ_{max} that do not differ by much. **3b** however, has a λ_{max} of 740 nm, which is less red-shifted than **3** and **3a**. Because the red-shifts indicate a weakening of the ligand field, this shows that ligand field in **3** and **3a** is more weakened than in **3b**, and also gives hints on the two pairs of heterocycles on pyridines being inequivalent. When two pyridines are attached on the methine-half of the N4Py framework, the 6-pyridine protons are farther from the oxygen atom, and hence making substitutions there causes the pyridines to be different, and have different effects (Figure 2.31).

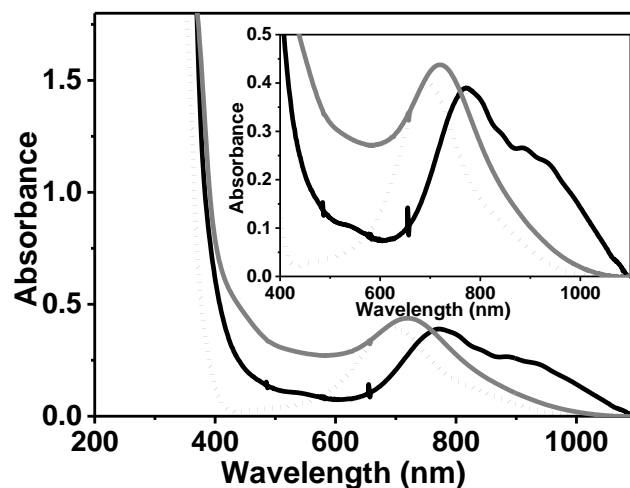


Figure 2.5 Near-IR features of **1** (dashes), **2** (gray), and **3** (black) in 1 mm CH₃CN solutions. Inset shows the region from 400 to 1100 nm.

2.2.4 Vibrational spectroscopy

The solid samples were directly used *without* grinding and placed on the diamond tip of the FTIR spectrometer. Complexes **2** and **3** display $\nu(\text{Fe}=\text{O})$ features at 842 and 834 cm^{-1} , respectively, compared to 843 cm^{-1} for **1**, showing that only the introduction of quinolines in **3** influences $\nu(\text{Fe}=\text{O})$.³⁶⁻³⁸ *Note: Perchlorate salts are explosive and should be handled with care.* The resonance Raman spectra for **1*** shows 839 cm^{-1} (Figure 2.33) and complex 2 can also be seen through this spectroscopy (Figure 2.32).

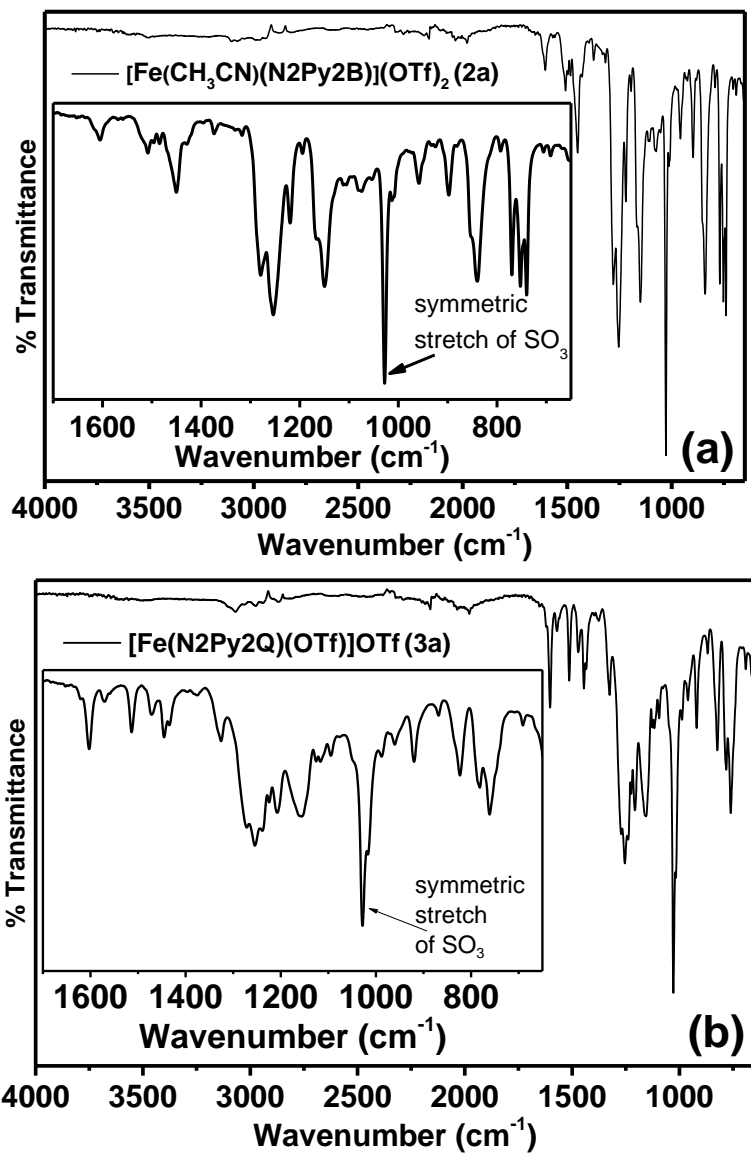


Figure 2.6 FTIR spectra of ferrous precursors of **2** (a) and **3** (b). Insets show expanded fingerprint region from 1700 to 650 cm^{-1} .

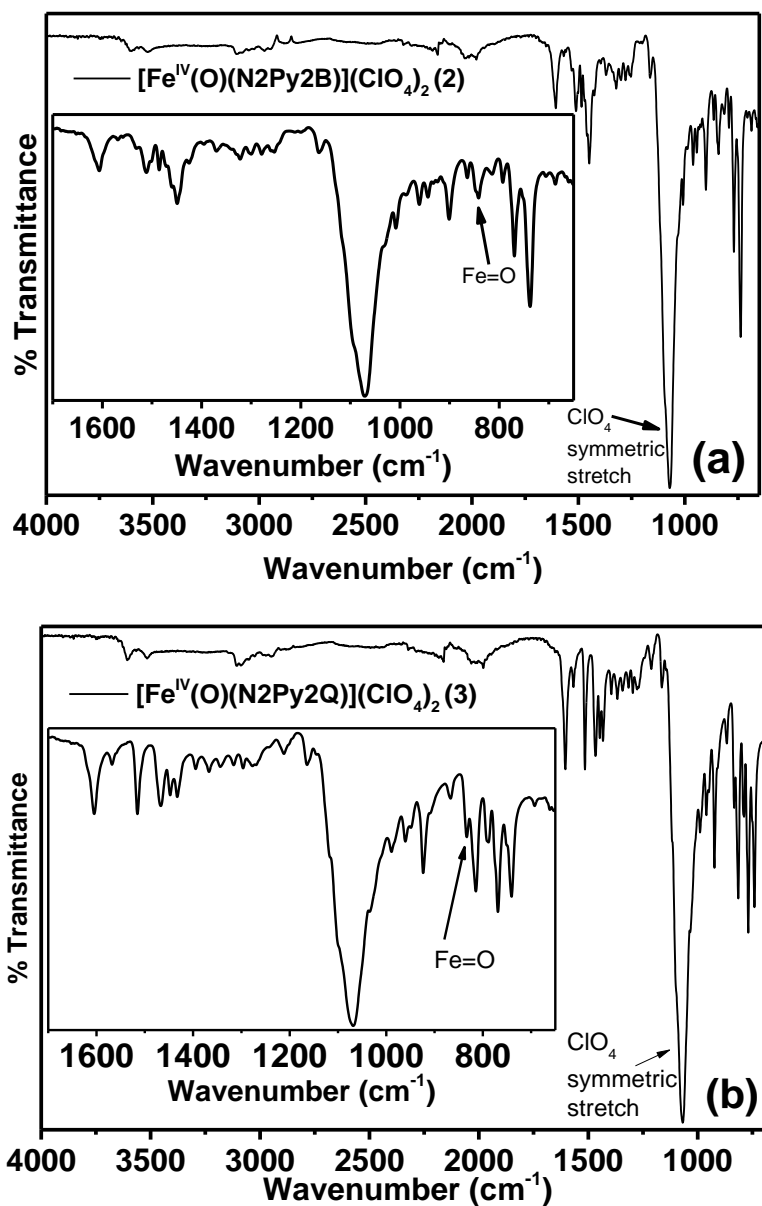


Figure 2.7 FTIR spectra of ferryl complexes **2** (a) and **3** (b). Insets show expanded fingerprint region from 1700 to 650 cm^{-1} .

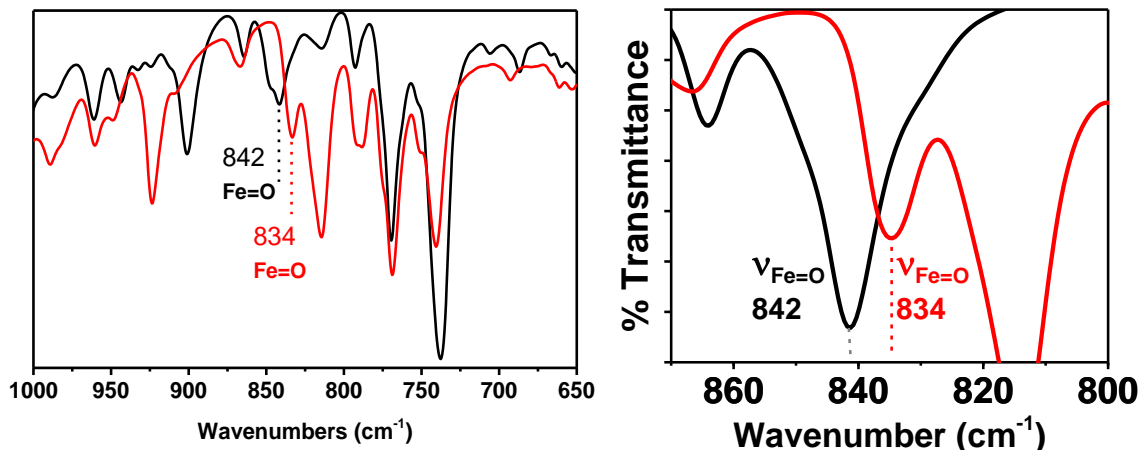


Figure 2.8 The full FTIR spectra (left) of **2** (black) and **3** (red) overlaid, and zoomed in spectra (right) from 800 to 870 cm^{-1} .

2.2.5 Mössbauer Spectroscopy

Complexes **2** and **3** exhibit Mössbauer spectra with parameters quite similar to those for **1**, and those of **2** match those reported by Mitra et al.¹⁵ Their behavior in applied magnetic fields as detailed below indicates that they are typical of the $S = 1$ non-heme oxoiron(IV) complexes described in the past fifteen years.^{5, 39}

Mössbauer samples containing complexes **2** or **3** were first studied at 4.2 K with a small external magnetic field applied along the direction of the gamma radiation (Figures 2.9 and 2.10). The observation of quadrupole doublets under these measurement conditions confirmed that **2** and **3** have integer spin ground states. The simulations on these low field data provided information on isomer shifts (δ) and quadrupole splittings (ΔE_Q). The samples were then subjected to variable field and variable temperature measurements in order to determine the spin state and ^{57}Fe nuclear hyperfine interaction parameters. The spectral simulations using an $S = 1$ spin Hamiltonian with a large positive D value ($D = 25 \text{ cm}^{-1}$ for **2** and 26 cm^{-1} for **3**) satisfactorily reproduced all the variable field and variable temperature spectra for both complex **2** and **3** (Figures 2.9 and 2.10).

The $S = 1$ spin Hamiltonian is expressed as:

$$\hat{H} = D \left[\left(\hat{S}_z^2 - \frac{2}{3} \right) + \frac{E}{D} (\hat{S}_x^2 - \hat{S}_y^2) \right] + \beta \hat{\mathbf{S}} \cdot \mathbf{g} \cdot \vec{\mathbf{B}} + \hat{\mathbf{S}} \cdot \mathbf{A} \cdot \hat{\mathbf{I}} - g_n \beta_n \vec{\mathbf{B}} \cdot \hat{\mathbf{I}} + \hat{H}_Q$$

$$\hat{H}_Q = \frac{eQV_{zz}}{12} \left[\hat{I}_z^2 - \frac{15}{4} + \eta(\hat{I}_x^2 - \hat{I}_y^2) \right]$$

where D and E are the axial and rhombic zero-field splitting (ZFS) parameters, \vec{B} represents the applied magnetic field, \hat{I} is the nuclear spin of ^{57}Fe , \mathbf{A} is the magnetic hyperfine tensor, V_{zz} is the largest principal component of the electric field gradient (EFG) tensor, Q is the ^{57}Fe nuclear excited state quadrupole moment, and η ($= (V_{xx} - V_{yy})/V_{zz}$) is the asymmetric parameter. The spectral simulation assumes that \mathbf{A} , EFG, and ZFS tensors are collinear. In addition, the simulation assumes that $E = 0$, which is supported by HFEP data (see the next section). For the simulations on 4.2 K spectra, slow electronic relaxation limit was assumed, and for the simulations on spectra measured at elevated temperatures, the fast electronic relaxation limit was assumed.

To determine D values, high-field Mössbauer spectra were measured at 4.2 K and at elevated temperatures (in the temperature range between 15 K and 50 K). At 4.2 K, the variable field spectra are determined by the magnetic hyperfine interactions in the xy plane, namely $\vec{B}(i) = -\langle S_i \rangle A_i / g_n \beta_n$ ($i = x, y$), and $\langle S_{x,y} \rangle$ is inversely proportional to D with electronic systems having large D values. Therefore, D and A_x, A_y cannot be independently determined by using the 4.2 K spectra alone. However, at elevated temperatures (20 – 50 K), $\langle S_{x,y} \rangle$ is independent of D , allowing one to determine A_x and A_y . Thus by group fitting both 4.2 K spectra and spectra measured at elevated temperatures, one can determine D values relatively accurately. At high temperatures, such as 80 K used in this study, the electronic system is under the fast relaxation limit, so the ^{57}Fe hyperfine field is proportional to the thermally averaged expectation value of \mathbf{S} , namely $\vec{B}(i) = -\langle S_i \rangle_{th} A_i / g_n \beta_n$ ($i = x, y, z$) and is sufficiently small due to the $1/T$ dependence on $\langle S_i \rangle_{th}$ (Curie's law behavior). As a consequence, the spectra at 80 K are largely determined by the externally applied field and the EFG tensor. Therefore, the sign of ΔE_Q and η can be determined by using 80 K spectra. The determined spin Hamiltonian parameters obtained from variable-field variable-

temperature Mössbauer spectra of **2** and **3** are listed in the captions of Figures 2.9 and 2.10.

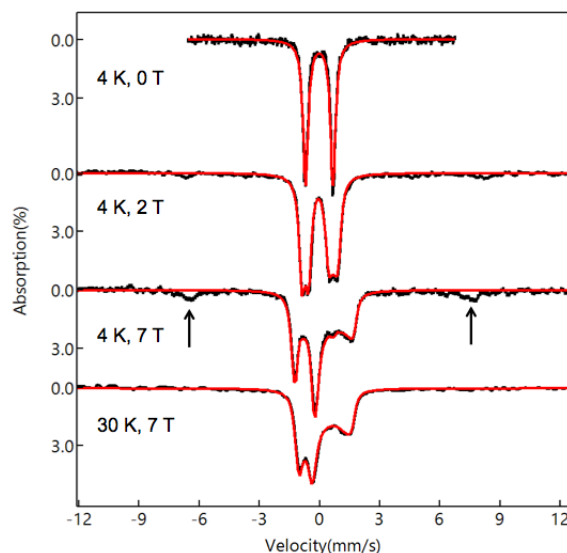


Figure 2.9 Mössbauer spectra of a sample containing complex **2** (black lines) measured under variable field and variable temperature conditions, as indicated in the figure. The corresponding spectral simulations (red lines) used the following parameters: $D = 25 \text{ cm}^{-1}$, $E/D = 0$, $g_x = g_y = g_z = 2.0$, $A_x/g_n\beta_n = A_y/g_n\beta_n = -22.2 \text{ T}$, $\delta = -0.02 \text{ mm/s}$, $\Delta E_Q = 1.36 \text{ mm/s}$, $\eta = 0.6$. The black vertical arrows indicate spectral features belonging to high-spin ferric impurities that represent < 5% of the total iron in the sample.

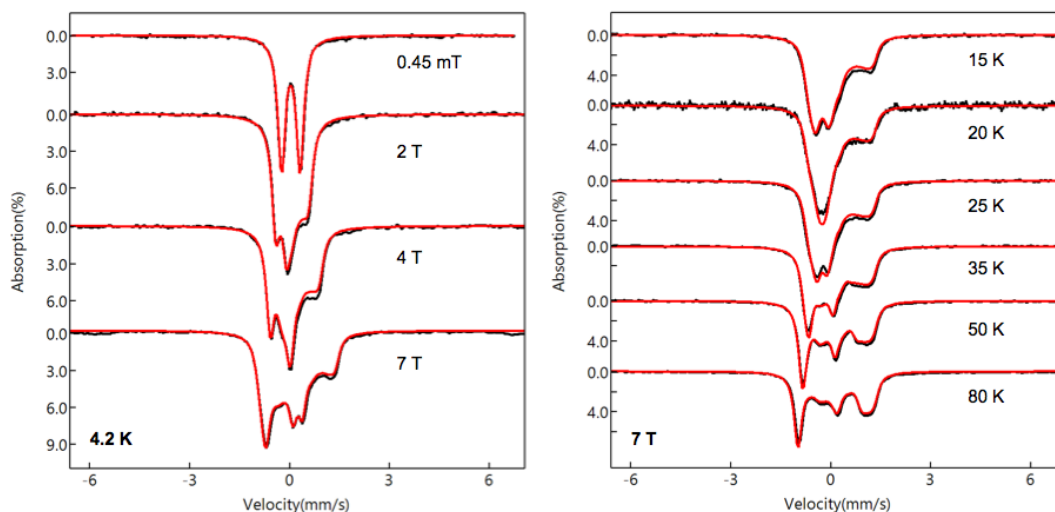


Figure 2.10 Mössbauer spectra of a sample containing complex **3** (black lines) measured under variable field and variable temperature conditions, as indicated in the figure. The corresponding spectral simulations (red lines) used the

following parameters: $D = 26 \text{ cm}^{-1}$, $E/D = 0$, $g_x = g_y = g_z = 2.0$, $A_x/g_n\beta_n = A_y/g_n\beta_n = -22.5 \text{ T}$, $\delta = 0.03 \text{ mm/s}$, $\Delta E_Q = 0.56 \text{ mm/s}$, $\eta = 0.3$.

2.2.6 High-Frequency and -Field EPR (HFEP) and FIRMS spectroscopy

High-frequency and -field EPR (HFEP) and frequency-domain spectroscopy with applied fixed magnetic fields (FIR magnetic spectroscopy or FIRMS) have also been found to be useful for characterizing the electronic structures of iron(IV) complexes. These techniques are optimally performed on 25–50 mg powder samples,⁴⁰⁻⁴² although frozen solution studies are feasible in certain cases.⁴³ Fortunately, **2** and **3** are relatively stable solids that allow the determination of their zero-field splitting (zfs) parameters (axial, D ; rhombic, E) with high precision by concerted use of these two complementary techniques. FIRMS provides a direct measure of the zfs in these complexes by observation of the $|S, M_S\rangle = |1, 0\rangle \leftrightarrow |1, \pm 1\rangle$ transition, while HFEP provides complementary information without the complication of non-magnetic vibrations (phonons) that are also found in this very low frequency region of interest. We have found D to increase from 22.05 cm^{-1} for **1**⁴⁰ to 23.3 and 24.3 cm^{-1} for **2** and **3**, respectively, with $E \cong 0$ in each case. This trend of increasing D suggests a progressive decrease in the energy gap between the ground $S = 1$ and the excited spin states, as these excited states contribute to the zfs in inverse proportion to their relative energies above the ground state.

Table 2.1 Spin Hamiltonian parameters from field- and frequency-domain magnetic resonance spectroscopy

Complex	$D \text{ (cm}^{-1}\text{)}$	$E \text{ (cm}^{-1}\text{)}$	g_{\perp}	g_{\parallel}
1 ⁴⁰	22.05(5)	0.000(25)	2.03(1)	1.95(5)
2	23.3(1)	0.00(5)	2.08	2.006(3)
3	24.3(1)	0.00(5)	2.08(5)	2.000(5)

^a Value assumed identical to that experimentally determined by FIRMS for **3**.

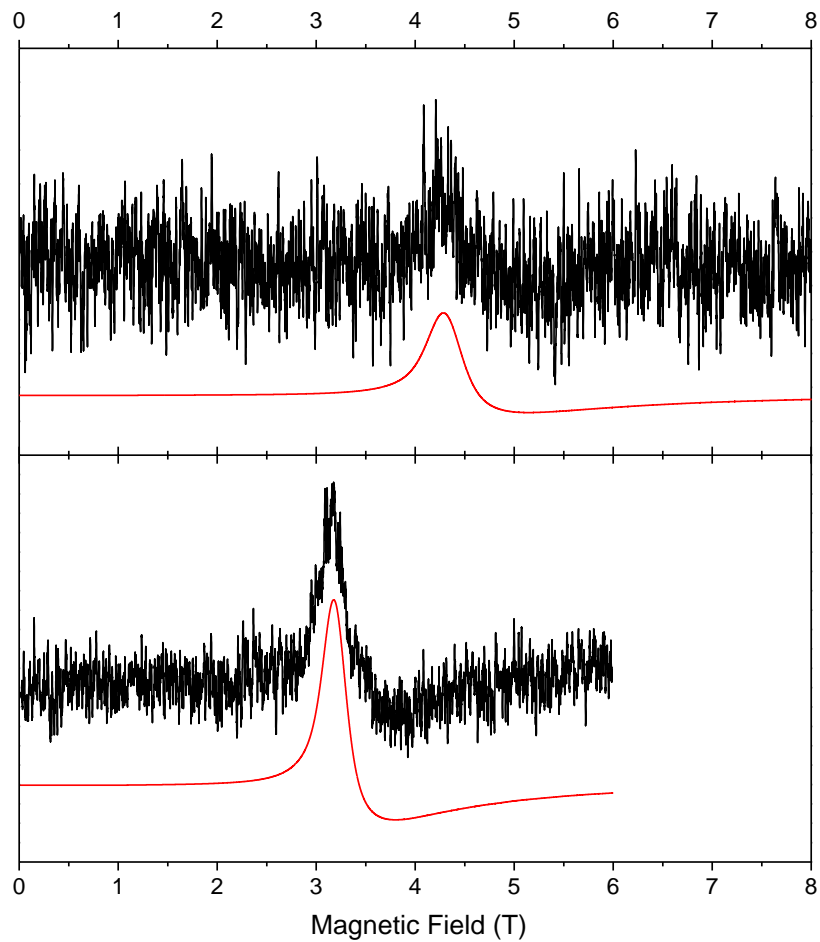


Figure 2.11 HFEPR spectra of **3** (top, black trace), **2** (bottom, black trace) and **1** at 4.5 K and 609.6 GHz. The red lines are simulations using spin Hamiltonian parameters as in Table 2.1 except for $D = 24.35 \text{ cm}^{-1}$ for **3**.

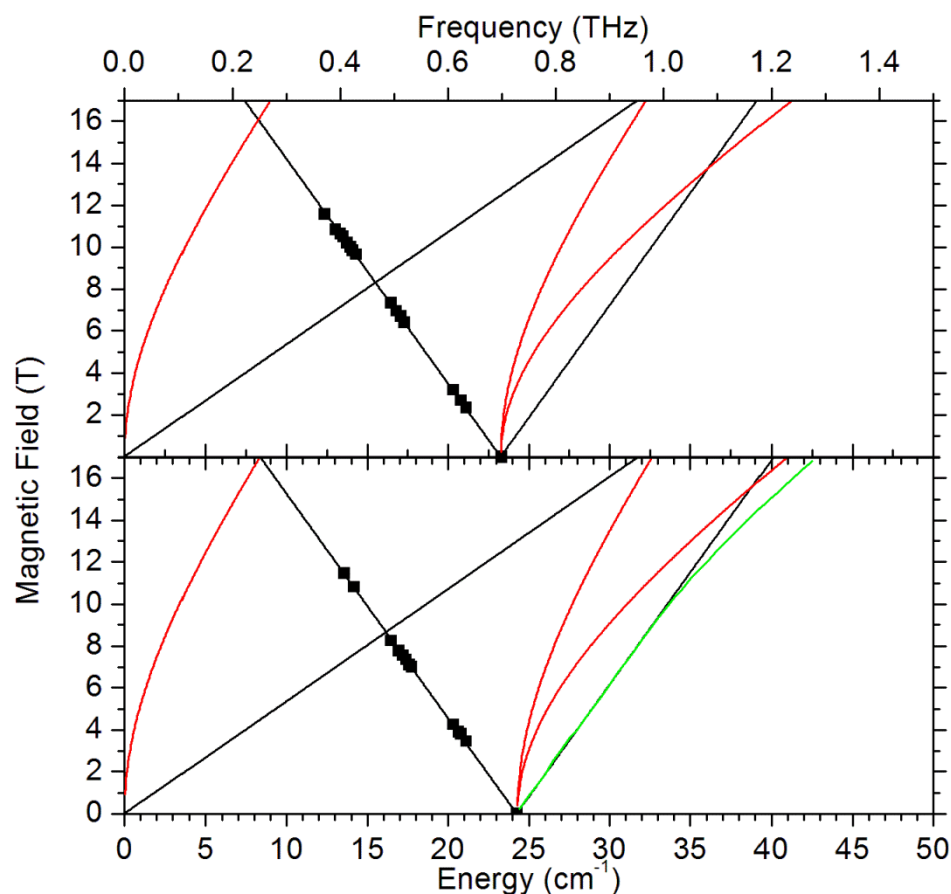


Figure 2.12 Field vs. energy (frequency) maps of magnetic resonance transitions of **2** (top) and **3** (bottom) at 4.5 K. The squares are experimental points while the curves are simulations using spin Hamiltonian parameters best-fitted through the least-squares method as listed in Table 2.1. Black curves: parallel turning points; red curves: perpendicular turning points (not observed by HFEPR); green curve: off-axis turning point in **3** (observed by FIRMS, see Figure 2.14). The region above $\sim 22 \text{ cm}^{-1}$ ($\sim 660 \text{ GHz}$) was not probed by HFEPR given that it requires a non-routine setup, and the FIRMS technique was available.

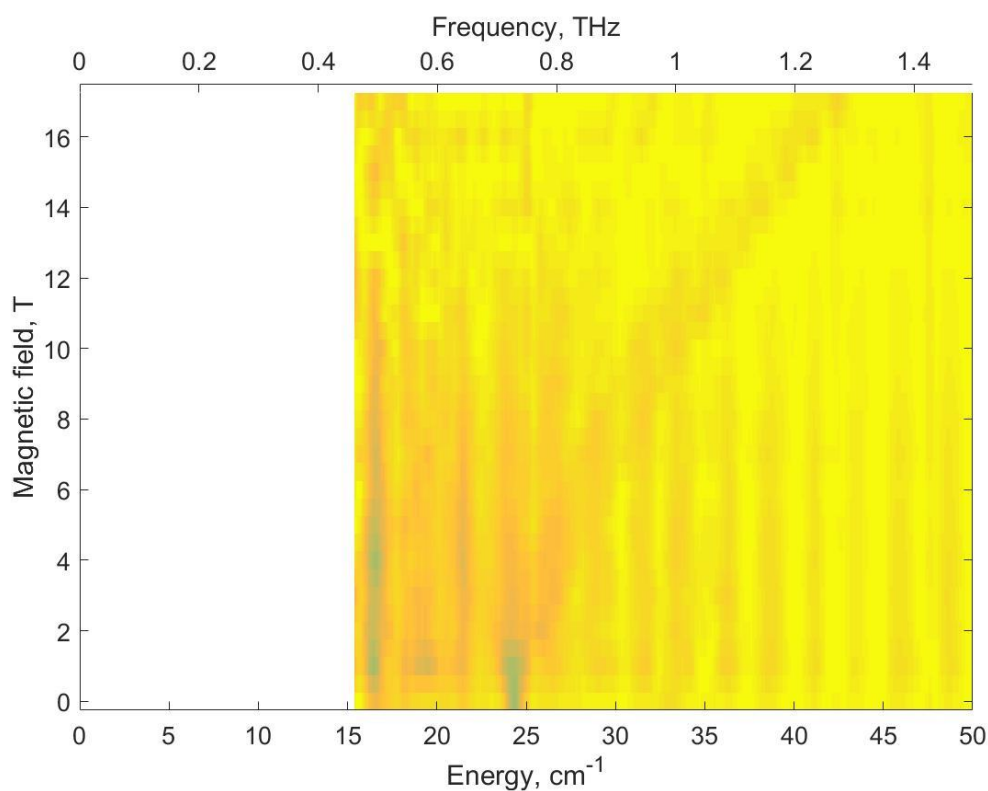


Figure 2.13 A contour (false-color) map of magnetic transitions obtained by FIRMS for **3**. A darker color indicates a stronger absorption. A zero-field magnetic transition is clearly visible at 24.3 cm^{-1} . This transition develops into turning points of a powder spectrum, two of which move to higher energies with increasing field, reaching $\sim 1.25 \text{ THz}$ at 17 T , which positively allows the transition to be identified as magnetic (the many phonon transitions active in the FIR region do not respond to increasing magnetic field). The abscissa value of 15 cm^{-1} represents the approximate cutoff of the FIRMS instrument; therefore, the part of the map below this value is left blank, but is probed in the field domain by HFEPR as seen in Figure 2.12.

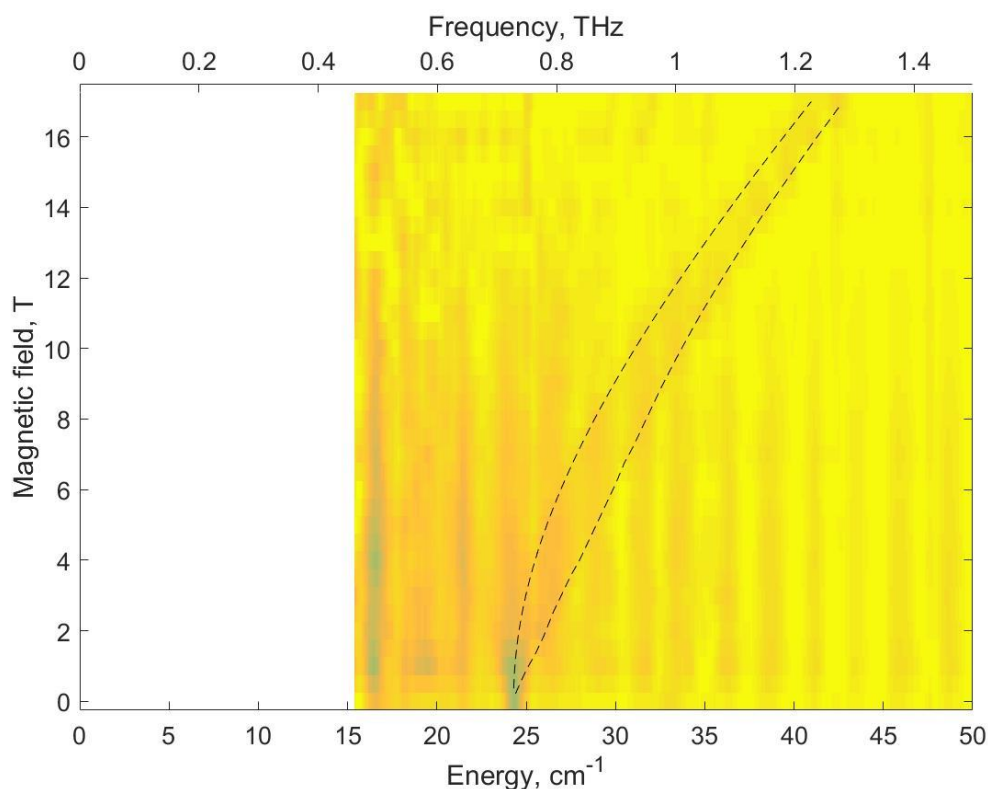


Figure 2.14 Simulations of two most prominent turning points in the powder spectrum of **3** (dashed lines) superimposed on the FIRMS map of resonances. Adjusting g_{\perp} in the simulations provided the value of 2.08(5) as in Table 2.1.

Contribution of the $S = 2$ Excited State to the Zero-Field-Splitting (D) Parameter:

Ligand field theory (LFT) calculations were performed to explore the effect of the spin quintet energy. When the quintet state contribution is ignored for both complexes **2** and **3**, the zero-field splitting (ZFS) parameter turns out to be small ($D \approx +7 \text{ cm}^{-1}$) and is barely dependent on the choice of Racah parameters (interelectronic repulsion), since the complexes are all $S = 1$, and their energy levels change only in a second-order fashion.

This indicates that the quintet ($S = 2$) excited state is a key contributor to the ZFS parameter (D) of these tetragonal oxidoiron(IV) complexes. Specifically, it is the

relative energy of a 5A_1 (in C_{4v}) excited state, which corresponds to the hole in the d_{z^2} orbital, so the spin orbit coupling (SOC) effect is an electron going from the filled d_{xy} orbital (lowest in energy) to the empty $d_{x^2-y^2}$ orbital (with a spin flip). The equatorial ligand-field is crucial in determining the energy of the $d_{x^2-y^2}$ orbital, and thus D . The perturbation theory for this effect is given by the following equation:

$$D = \Delta E'(\pm 1) - \Delta E'(0) = \frac{\zeta^2}{(E({}^5A_1) - E({}^3A_2))} \left(-1 - \left(-\frac{4}{3} \right) \right)$$

$$= \frac{1}{3} \frac{\zeta^2}{(E({}^5A_1) - E({}^3A_2))}$$

The exact calculation using Racah at 70% of free-ion (where the quintet state is low in energy) gives $D = +31 \text{ cm}^{-1}$, while using triplets only gives $D = +7 \text{ cm}^{-1}$ (as above), so the total quintet contribution to D is $+24 \text{ cm}^{-1}$. This agrees well with the above equation since the energy splitting is $\approx 2000 \text{ cm}^{-1}$, and $\zeta = 400$ (for this calculation), so $\frac{1}{3} \times \frac{400^2}{2000} \approx 27 \text{ cm}^{-1}$, which is close given that only one quintet excited state is used in the above equation.

Because the spin quintet excited state has significant contributions into the zfs parameter D , the above complexes support the notion that such excited states could be involved in the hydrogen-atom abstraction abilities of the complexes **2** and **3**. However, the D values do not change by a large amount in going from complex **1** to **2** to **3** and the differences in HAT rates span at least two orders of magnitude. It is thus important to note that other effects could be playing a role in explaining the reactivity, and they are discussed in the reactivity section of this chapter.

2.2.7 X-Ray Crystallography

Data collection and structure refinement details for complexes **2** and **3** are detailed below, along with strategies to model water molecule as well as comparison of bond metrics with the literature data.

Complex 2:

A crystal (approximate dimensions: 0.15 x 0.12 x 0.1 mm) was placed onto the tip of a 0.5 mm MiTeGen loop and mounted on a Bruker, Photon-II CPAD diffractometer for a data collection at 100(2) K.⁴⁴ A preliminary set of cell constants was calculated from reflections harvested from three sets of 12 frames. These initial sets of frames were oriented such that orthogonal wedges of reciprocal space were surveyed. This produced initial orientation matrices determined from 691 reflections. The data collection was carried out using MoK α radiation (graphite monochromator) with a frame time of 30 seconds and a detector distance of 6.0 cm. A randomly oriented region of reciprocal space was surveyed to the extent of one sphere and to a resolution of 0.70 Å. Four major sections of frames were collected with 1° steps in ω at four different ϕ settings and a detector position of -28° in 2θ . The intensity data were corrected for absorption and decay.⁴⁵ Final cell constants were calculated from the xyz centroids of 2725 strong reflections from the actual data collection after integration.⁴⁶ Please refer to Table 2.2 for additional crystal and refinement information. The structure was solved using SHELXS-97 (Sheldrick 2008)⁴⁷⁻⁴⁸ and refined using SHELXL-2018/3 (Sheldrick, 2018).⁴⁹ The space group Pna2₁ was determined based on systematic absences and intensity statistics. A direct-methods solution was calculated which provided most non-hydrogen atoms from the E-map. Full-matrix least squares/difference Fourier cycles were performed which located the remaining non-hydrogen atoms. All non-hydrogen atoms were refined with anisotropic displacement parameters. All C–H hydrogen atoms were placed in ideal positions and refined as riding atoms with

relative isotropic displacement parameters. The H atoms of water molecules were modeled as detailed below. The final full matrix least squares refinement converged to $R1 = 0.0475$ and $wR2 = 0.1114$ (F2, all data).

Complex 3:

A crystal (approximate dimensions: 0.150 x 0.120 x 0.100 mm) was placed onto the tip of a 0.5 mm MiTeGen loop and mounted on a Bruker photon-II CPAD diffractometer for a data collection at 100(2) K.⁴⁴ A preliminary set of cell constants was calculated from reflections harvested from three sets of 12 frames. These initial sets of frames were oriented such that orthogonal wedges of reciprocal space were surveyed. This produced initial orientation matrices determined from 258 reflections. The data collection was carried out using MoK α radiation (graphite monochromator) with a frame time of 30 seconds and a detector distance of 6.0 cm. A randomly oriented region of reciprocal space was surveyed to the extent of one sphere and to a resolution of 0.70 Å. Six major sections of frames were collected with 1° steps in ω at four different ϕ settings and a detector position of -28° in 2θ . The intensity data were corrected for absorption and decay.⁴⁵ Final cell constants were calculated from the xyz centroids of 9988 strong reflections from the actual data collection after integration.⁴⁶ Please refer to Table 2.2 for additional crystal and refinement information. The structure was solved using SHELXS-97 (Sheldrick 2008)⁴⁷⁻⁴⁸ and refined using SHELXL-2018/3 (Sheldrick, 2018).⁴⁹ The space group Pna2₁ was determined based on systematic absences and intensity statistics. A direct-methods solution was calculated which provided most non-hydrogen atoms from the E-map. Full-matrix least squares/difference Fourier cycles were performed which located the remaining non-hydrogen atoms. All non-hydrogen atoms were refined with anisotropic displacement parameters. No possible restraints on the perchlorate ions were applied for the residual electron density of 1.32 around the perchlorate ion, because the perchlorate ion was not completely disordered. All C–H hydrogen atoms were placed in ideal positions and refined as riding atoms with relative isotropic displacement parameters. The H

atoms of water molecules were modeled as detailed below. The final full matrix least squares refinement converged to $R1 = 0.0581$ and $wR2 = 0.1568$ (F2, all data).

Table 2.2 Crystal data and structure refinement for complex **2** and **3**.

Crystallographic details	Complex 2	Complex 3
CCDC Identification Code	1835339	1835337
Empirical formula	$C_{29}H_{29}Cl_2FeN_7O_{10}$	$C_{31}H_{27}Cl_2FeN_5O_{10}$
Formula weight	762.34	756.32
Temperature	100(2) K	100(2) K
Wavelength	0.71073 Å	0.71073 Å
Crystal system	Orthorhombic	Orthorhombic
Space group	Pna2 ₁	Pna2 ₁
Unit cell dimensions	$a = 18.684(7)$ Å	$a = 18.8809(6)$ Å
	$b = 12.816(4)$ Å	$b = 12.7142(4)$ Å
	$c = 12.870(5)$ Å	$c = 12.7866(4)$ Å
Volume	3081.9(19) Å ³	3069.49(17) Å ³
Z	4	4
Density (calculated)	1.643 Mg/m ³	1.637 Mg/m ³
Absorption coefficient	0.735 mm ⁻¹	0.735 mm ⁻¹
F(000)	1568	1552
Crystal color, morphology	blue-green, block	green, block
Crystal size	0.15 x 0.12 x 0.1 mm ³	0.150 x 0.120 x 0.100 mm ³
Theta range for data collection	2.243 to 26.346°	2.259 to 30.524°
Index ranges	$-23 \leq h \leq 20$, $-15 \leq k \leq 15$, $-16 \leq l \leq 15$	$-26 \leq h \leq 26$, $-18 \leq k \leq 18$, $-18 \leq l \leq 18$
Reflections collected	22366	73781
Independent reflections	6253 [$R(\text{int}) = 0.0515$]	9374 [$R(\text{int}) = 0.0482$]
Observed reflections	5096	8108
Completeness to theta = 25.242°	99.9%	99.9%
Absorption correction	Multi-scan	Multi-scan
Refinement method	Full-matrix least-squares on F^2	Full-matrix least-squares on F2

Crystallographic details	Complex 2	Complex 3
Data / restraints / parameters	6253 / 6 / 460	9374 / 3 / 448
Goodness-of-fit on F2	1.035	1.037
Final <i>R</i> indices [$I > 2\sigma(I)$]	<i>R</i> 1 = 0.0475, <i>wR</i> 2 = 0.1031	<i>R</i> 1 = 0.0581, <i>wR</i> 2 = 0.1486
<i>R</i> indices (all data)	<i>R</i> 1 = 0.0663, <i>wR</i> 2 = 0.1114	<i>R</i> 1 = 0.0699, <i>wR</i> 2 = 0.1568
Absolute structure parameter	-0.014(10)	-0.002(5)
Largest diff. peak and hole	0.556 and -0.483 e.Å ⁻³	1.320 and -0.737 e.Å ⁻³

Modeling the H atoms of water molecules in 2 and 3

In both the crystal structures of **2** and **3**, a water molecule is within hydrogen bonding distances of a ferryl unit (Table 2.3), and is also proximal to the two perchlorate counterions (2.77 to 2.88 Å away), as shown in Figure 2.15. These counterions therefore likely have a significant portion of the H-bonding with the water molecule in their respective crystal structures. Note that the perchlorate ions have significantly strong H bonding with the water molecule, which then helps bring the negative (perchlorate) and the positive (cation) charges closer to each other in the lattice.

In the absence of neutron diffraction data, X-ray crystallography cannot assign the hydrogen atoms, so water molecule's hydrogen atoms were reasonably modelled using its distance with the oxoiron(IV) center as well as the perchlorate ions.

In **2**, one of the perchlorate ions is rotationally disordered around axis the O–Cl axis close to the water molecule (about 2.77 Å away). The water molecule in the crystal structure of **2** is just about 2.8 Å away from the other perchlorate and the ferryl unit and is modelled by placing the H atom between both the ferryl unit and the perchlorate ion. With this modelling, the refinement yields an H–O–H angle of about 116.5° in the water molecule.

In **3**, the water molecule is only within moderate H-bonding distance of the ferryl unit (about 3.13 Å away from the water's oxygen atom) but is even closer to the perchlorate counterions. Therefore, perchlorate oxygen atoms are the only ones involved in H-bonding with water. With this modelling, the refinement yields an H–O–H angle of about 130.84° in the water molecule.

Table 2.3 Distance of perchlorates and ferryl unit from water molecule

Distance from water (Å)	Perchlorate 1	Perchlorate 2	Oxoiron(IV) Unit
2	2.864	2.821	2.834
3	2.824	2.768	3.138

Normalized positions of C–H bonds proximal to the ferryl unit:

For comparisons of distances of C–H atoms of pyridyl (α), quinolyl (H8) and *N*-methylbenzimidazolyl (H7) groups from the oxo of the ferryl unit in the crystal structures of **1**, **2**, and **3**, all C–H atoms were normalized post-refinement to reflect the more realistic positions of the hydrogen atoms for C–H atoms (Table 2.4). Normalization of aromatic C–H bonds increases their bond length from 0.95 Å to about 1.09 Å along the bond vector, which is the average C–H bond length one would expect to find through neutron diffraction.⁵⁰ Note however, that the crystal structures were not of neutron diffraction quality, and so all C–H hydrogen atoms were placed in ideal positions and refined as riding atoms with relative isotropic displacement parameters.

Table 2.4 Distances of hydrogen atoms from the ferryl unit before and after normalization. Standard uncertainties are not given for average bond lengths because all atoms have different environments. See Figure 2.16.

Complex	Fe=O...H distance (Å)	Before normalization	After normalization
1	H _{py(α)}} ...O	2.556	2.517
	H _{py(α)}} ...O	2.743	2.717
2	H _{py(α)}} ...O	2.811, 2.767	2.739, 2.784
	aver. H _{py(α)}} ...O	2.789	2.762
	H _{Bn(H7)}} ...O	2.730, 2.680	2.657, 2.606

	aver. $H_{Bn(H7)} \cdots O$	2.70	2.632
3	$H_{py(\alpha)} \cdots O$	2.702, 2.731	2.705, 2.676
	aver. $H_{py(\alpha)} \cdots O$	2.72	2.691
	$H_{Q(H8)} \cdots O$	2.152, 2.158	2.040, 2.047
	aver. $H_{Q(H8)} \cdots O$	2.16	2.044

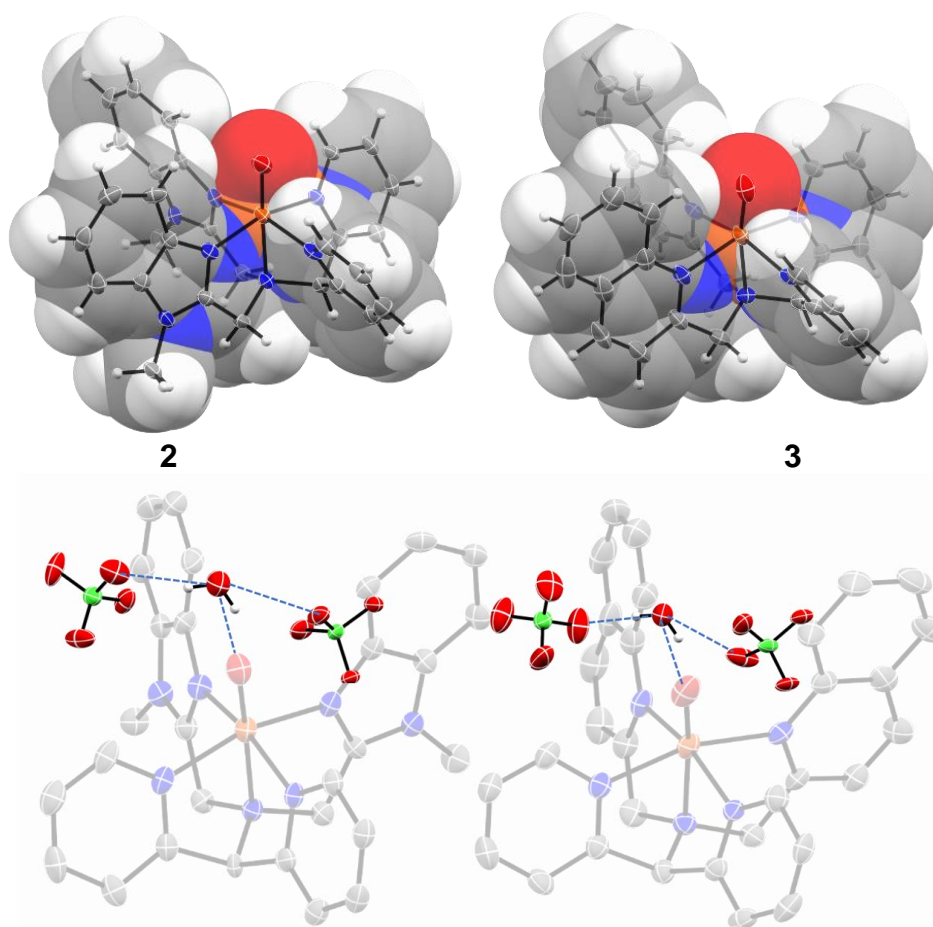


Figure 2.15 Space filling models (top) for **2** and **3**, and ORTEP showing water molecules (bottom) proximal to the ferriyl unit as well as perchlorate ions.

2.3 Comparisons of Crystallographic and Spectroscopic Data

Complexes **2** and **3** can be generated by treating 1:3 CH_3CN/H_2O solutions of the corresponding iron(II) precursors with 4 equivalents of ceric ammonium nitrate (CAN) as the oxidant. Subsequent addition of excess sodium perchlorate to the

reaction mixtures results in the precipitation of solids, which can be recrystallized for crystallographic analysis. The crystal structures of **2** and **3** have been depicted in the previous section, and their bond metrics and spectroscopic properties with can be compared with those of **1** and **4** in Table 2.6.

Complexes **1** and **1*** have very similar bond metrics, and introduction of electron-donating methyl and methoxy groups only slightly increases the overall average Fe-N bond lengths by about 0.01 Å. The Fe=O bond lengths are comparable at 1.653(1) and 1.639(5) Å for **1*** and **1** respectively, as are their vibrational stretches at 839-842 cm⁻¹. The increased donation expected from introduction of methoxy and methyl groups on pyridines is not born out by significant changes of Fe-N_{py} bond lengths, which is also spectroscopically seen from a very slight change only in the UV-visible λ_{max}. The N_{ax}-Fe=O angle remains linear as expected, because alpha-H of pyridines are not substituted. This also leads to an orthogonality of the angle between the ferryl unit and the mean plane defined by the equatorial ligands. Unlike the case of complex **3**, which has steric interactions with quinolyl groups, the ferryl units of **1*** and **1** are found to be fairly linear.

Table 2.5 Average Fe–N bond lengths in Å from DFT-calculated structures of the most reactive complexes [Fe^{IV}(O)(Me₃NTB)(L)]²⁺ and [Fe^{IV}(O)(TQA)(L)]²⁺

Complex	[Fe ^{IV} (O)(TQA)(L)] ²⁺		[Fe ^{IV} (O)(Me ₃ NTB)(L)] ²⁺		
	O _h	C _{3v}	O _h	O _h	C _{3v}
Geometry	O _h	C _{3v}	O _h	O _h	C _{3v}
Spin State (S)	2	2	1	2	2
Average Fe—N	2.152	2.057	2.026	2.135	2.042
Reference	11		12, 51		

Table 2.6 Structural and spectroscopic properties of the oxoiron(IV) complexes

Complexes	1 a	1*	2 b	3	4 c
r(Fe=O), Å	1.639(5)	1.653(1)	1.656(4)	1.677(5)	1.6600(16)
r(Fe–N _{pyridine}), Å	1.964(5)	1.972(2)	1.995(5)	2.023(4)	2.0269(17)
		1.970(2)	1.983(5)	2.022(4)	2.0408(17)
r(Fe–N _{heterocycle}), Å	1.949(5)	1.967(2)	1.950(5)	2.073(4)	1.9730(18)
		1.946(2)	1.954(5)	2.067(4)	1.9771(18)
r(Fe–N _{amine}), Å	2.033(8)	2.048(2)	2.115(6)	2.084(4)	2.0511(17)
av. r(Fe–N), Å	1.972	1.981	1.999	2.053	2.014
∠N _{amine} –Fe–O, °	179.4(3)	178.1(3)	177.0(2)	170.5(2)	177.40(8)
∠N _{eq. plane} –Fe–O, °	89.4	89.6	88.3	82.4	86.9
v(Fe=O), cm ⁻¹ d	843	839	842	834	n. d.
δ, mm s ⁻¹ a	-0.04	n. d.	-0.02	0.03	0.0318, 25
ΔE _Q , mm s ⁻¹ a	0.93	n. d.	1.36	0.56	0.54
D, cm ⁻¹ (MB)	24(2)52	n. d.	25(1)	26(2)	2318, 25
D, cm ⁻¹ (HFEPFR & FIRMS)	22.05(5)	n. d.	23.3(1)	24.3(1)	n. d.
	40				
λ ^{max} , nm	695	692 (430)	725	770	75018, 25
(ε, M ⁻¹ cm ⁻¹)	(400)		(450)	(380)	

[a] Data from refs 13-14, 36, 38, 40, 52 as noted in each case. [b] Data for **2** from ref 15, except for its crystal structure, D value and Fe=O stretch reported herein. [c] Data for **4** from ref 18, 25. The modified pyridyl rings in **4** are on the bis(pyridyl-2-methyl)amine half of the ligand (Figure 2.2). [d] Vibrational data for **2** and **3** from FTIR and for **1** from resonance Raman spectroscopy. Abbreviations: MB: Mössbauer. n.d.: not determined.

2.3.1 Discussion of crystal structures:

Key data for **2** and **3** from their crystal structures (Figure 2.16) are listed in Table 2.6 and compared to those of the ‘parent’ complex **1** and the related complex **4**.

Complexes **1** – **3** have Fe=O bonds that lengthen systematically from 1.639(5) Å in **1** to 1.656(4) and 1.677(5) Å in **2** and **3**, respectively, as two of the pyridines in **1** are replaced by larger heterocycles, *N*-methylbenzimidazoles in **2** and quinolines in **3**. The average Fe–N bond length concomitantly increases from 1.972 Å in **1** to 1.999 Å in **2** and 2.053 Å in **3**. These trends are also observed for **4**, which differs from **2** and **3** in that a different pair of pyridines is modified (Figure 2.2 and Figure 2.3). For the substitution in **4**, the phenyl rings are found to rotate about the C–C bonds connecting the phenyl ring to the pyridine such that they become approximately perpendicular to the bound pyridines, thereby minimizing unfavorable steric interactions. When the bond metrics for **4** are considered relative to those for **1** – **3**, **4** falls between **2** and **3** (Table 2.6).

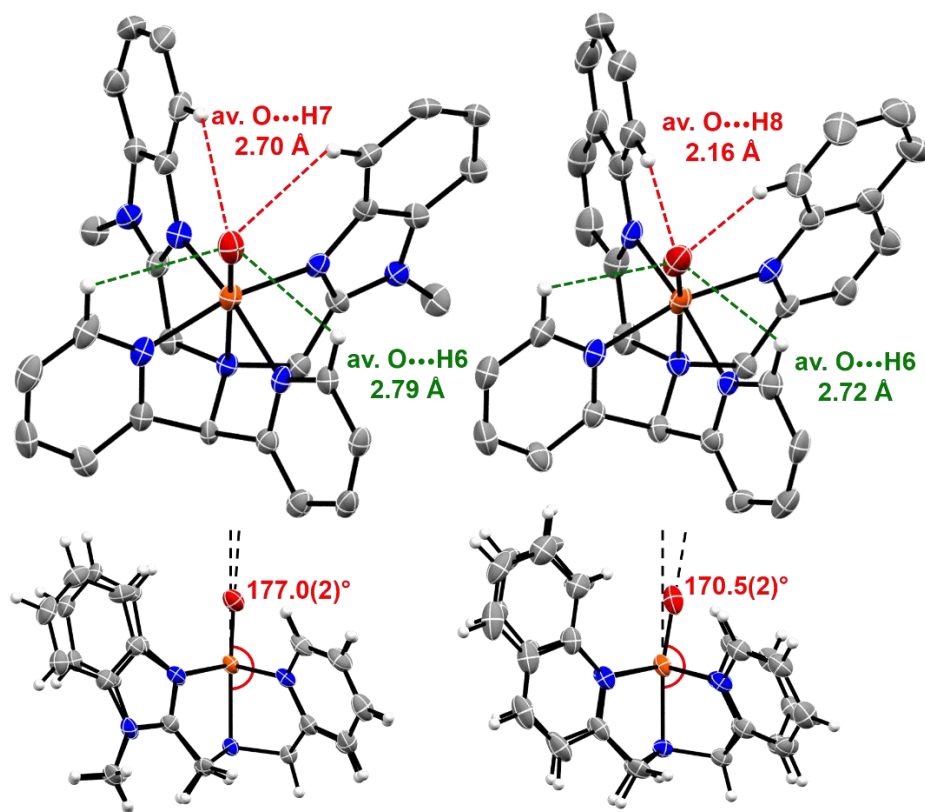


Figure 2.16 Front and side views of the ORTEP plots of **2** (left) and **3** (right), shown with thermal ellipsoids set at 50% probability. Water molecules, counterions, and select H atoms have been removed for clarity. The dotted line shows the tilt from the Fe–N_{am} axis.

The trends among complexes **1–4** discussed above very likely arise from the steric and electronic effects of the heterocycles that replace two of the pyridine donors on the N4Py framework. The steric effect is best demonstrated in the crystal structure of **3**, which shows that the H8 atoms of the two quinolines are on average only about 2.16 Å away from the oxo atom (Figure 2.16). For comparison, the corresponding H7 atoms of the benzimidazole donors are much farther away, at 2.70 Å from the oxo atom in **2**, a distance similar to those found for the 6-H protons of the unsubstituted pyridine rings in **1 – 4** (which range from \approx 2.5–2.8 Å). As a consequence, the quinoline 8-H protons would appear to exert a steric effect that results in a tilt of the Fe=O unit in **3** away from the quinoline rings, leading to the observed N_{am}–Fe–O angle of 170.5° (Figure 2.16). For comparison, the N_{am}–Fe–O angles observed for **1**, **2** and **4** are much closer to that for a linear arrangement, namely 179.4(3)°, 177.0(2)° and 177.40(8)°, respectively. Consistent with this proposed steric effect, the slight tilts found for **2** and **4** relative to **1** are oriented away from the bulkier heterocycles.

The basicity of the heterocycles increases from quinoline to pyridine to benzimidazole⁵³, and its effects on the bond lengths of the equatorial ligands can be seen in the short benzimidazole Fe–N bond lengths of 1.950(5) Å in **2**. The stronger binding of benzimidazole induces a *trans* effect which increases the equatorial pyridine Fe–N bond lengths. This, along with the longer axial Fe–N 2.115(5) Å, increases the average Fe–N bond length for complex **2**. Steric effects in complex **3** are responsible for its longer Fe–N bond lengths, and outweigh the electronic effects of quinolines.

2.3.2 Inequivalence of pyridine heterocycles on N4Py

Complexes **3a** and **3b** are oxoiron(IV) complexes supported by the N4Py framework with alpha-methyl group substitutions on two different pairs of pyridines, but could not be crystallographically characterized owing to their thermal instability. This may be attributed to the proximal benzylic methyl protons that are weak C-H bonds prone to intramolecular hydrogen-atom-abstraction. While these alpha-

methyl substituents on the pyridines are employed to impart steric bulk on the oxoiron(IV) complex, they are also some of the weakest C-H bonds on the framework. However the crystal structures of iron(II) precursors for both the complexes are available from the literature, and upon comparison, the inequivalency of the pyridines can be inferred. In both the crystal structures, the 6th coordination site is an acetonitrile ligand, and it is affected by the sterics of the alpha-methyl groups, only in the case where the methyl groups are introduced on the bis(pyridin-2-methyl) part of the ligand. The N_{am}-Fe-N_{N_{CM}e} angle is 167.6(1)° in one case, but 178.6(4)° in the other (Figure 2.17A). Even in the iron(II) precursor of complex **3**, the iron(II) crystal structure has been found to have an N_{am}-Fe-O_{OTf} angle of 168.3(2)°. ^{20, 23, 33} The 12.5° degree tilt observed on the 6th site of ferrous precursors of **3** and **3a** contrasts with the iron(II) precursor of the parent ferrous precursor of **1** and **3b**. Singh *et al.* found that introducing alpha-methyl substitutions increases the reactivity of the complexes by an order of magnitude for some of the substrates. When quinoline substitutions are introduced, the overall rates of reaction increase by over two orders of magnitude. Introduction of 6-methyl groups instead of the quinolines which result in the complex **3a** also result in similar increase in the rates of reaction. ²⁶

Furthermore, the acetonitrile-bound zinc(II) complex supported by N2py2Q ligand has also been obtained, and shows a larger tilt as shown in Figure 2.17A below, indicating the steric effects of quinolines. The presence of tilt of acetonitrile in the precursor of **3a** and its absence in precursor of **3b** likely has to do with the way the pyridines are oriented around the metal center. In Figure 2.17B the ball-and-stick diagram obtained from the crystal structures of the complexes are overlaid such that the iron, nitrogen of the amine, and the methine carbon of the ligand framework are aligned. It clearly shows that 6-methyl groups are closer to the sixth coordination site when they are introduced on the precursor of **3a**.

This can further be deduced from the crystal structures of parent oxoiron(IV) complex **1** as well as its iron(II) precursor. In **1**, the alpha protons of the pyridines

at the bis(pyridin-2-methyl) part of the ligand framework are closer to the metal center (Figure 2.31) than the corresponding protons on the other half of this ligand framework, thus preventing pyridines farther from the metal center from inducing a steric tilt on the 6th ligand that coordinates on the metal centers supported by these pentadentate ligands. Lastly in all the iron(II) and iron(IV) complexes discussed in this chapter, the torsion (or dihedral) angle across the Fe-N bond between the Fe-L₆th and the pyridine is much smaller on the bis(pyridin-2-methyl) half of the ligand than the same angle between the Fe-L₆th with the pyridines on the other side of the framework. The reduced torsion therefore forces modifications on these pyridine to introduce steric interactions between the alpha-substituents and the 6th-coordinated ligand, and can explain why steric hindrance from one side of the ligand is more than the other.

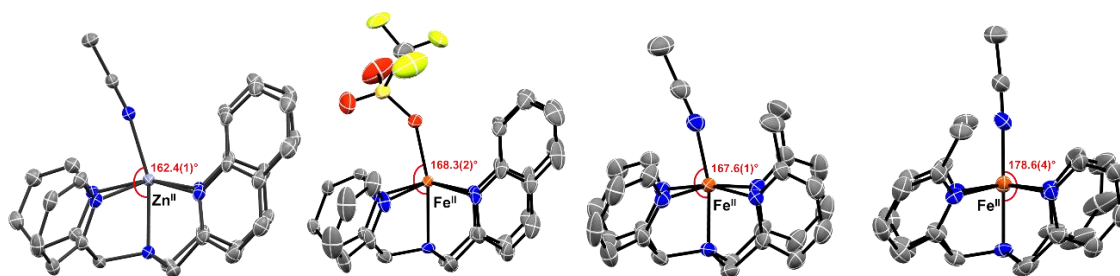


Figure 2.17A The crystal structures of cations $[\text{Zn}^{\text{II}}(\text{N}_2\text{Py}_2\text{Q})(\text{MeCN})]^{2+}$ and ferrous precursors to **3**, **3b**, and **3a** (left to right), without any H atoms for clarity.

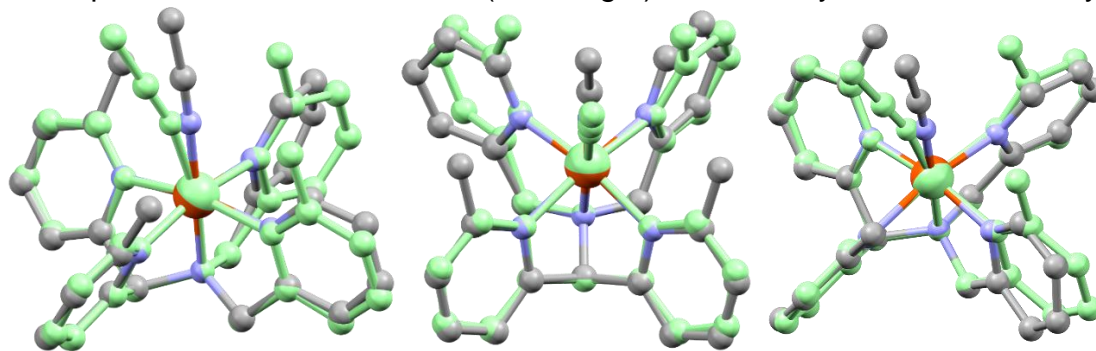


Figure 2.17B Overlaid ball-and-stick diagrams of the iron(II) precursors to **3b** and **3a** (green). Hydrogen atoms are omitted for clarity. The rightmost structure shows increased torsion angle between Fe-N_{MeCN} with the left set of pyridines compared with the other, which prevents the former from causing steric hindrance.

2.4 Reactivity and kinetic studies for 2 and 3

The structural differences in the 1–3 series are also reflected in their HAT and OAT rates. Figure 2.18 shows plots of $\log k_2'$ values for 1–3 (where k_2' is k_2 divided by the number of equivalent substrate C–H bonds that can be attacked, Table 2.7) versus the C–H bond dissociation energy, which reveal reasonably linear correlations for the three sets of data, as observed previously for a number of oxoiron(IV) complexes. The rate differences among the three complexes (Table 2.8) become larger for substrates with stronger C–H bonds, resulting in a decrease in the slopes from 1 to 2 and then to 3. The oxygen atom transfer rates to thioanisole at $-40\text{ }^\circ\text{C}$ also increase from 1 to 3, by over four orders of magnitude after extrapolating the value for 1 to $-40\text{ }^\circ\text{C}$ from its Eyring parameters (Table 2.11).

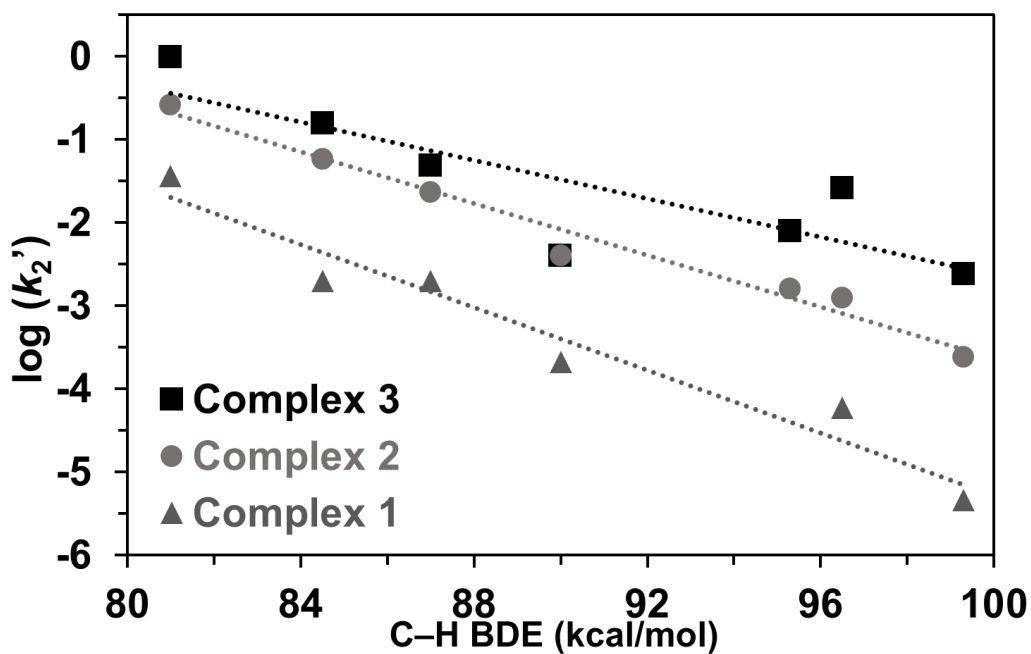


Figure 2.18 Evans–Polanyi plot for 3 at $25\text{ }^\circ\text{C}$, and previously published data for 1 and 2.

Table 2.7 Summary of 2nd-order rate constants (k_2) for complex **3**, as derived from plots in Figure 2.20. HAT rates were measured under N₂.

Substrate	D _{C-H} (kcal/mol)	Temperature (°C)	k_2 (M ⁻¹ s ⁻¹)	k_2' (M ⁻¹ s ⁻¹)
TPM	81	25	1	1
Cumene	84.5	25	0.16	0.16
Ethylbenzene	87	25	0.1	0.05
Toluene	90	25	0.012	0.004
Cyclooctane	95.3	25	0.13	0.0081
2,3-DMB*	96.5	25	0.054	0.027
Cyclohexane	99.3	25	0.029	0.0024
Thioanisole		-40	7.4	
*2,3-DMB = 2,3-dimethylbutane				

Table 2.8 Comparison of second order rate constants (k_2) of reactions of other complexes with different substrates at 298 K, unless stated in parenthesis

Substrates	1 ^{13, 54}	2 ¹⁵	3
TPM	0.037	0.27	1
Cumene	0.002	0.06	0.16
Ethylbenzene	0.004	0.048	0.1
Toluene	0.00063	0.012	0.012
Cyclooctane		0.026	0.13
2,3-DMB	0.00012	0.0025	0.054
Cyclohexane	0.000055	0.0029	0.029
Thioanisole	0.0002 (-40 °C)	0.78 (-40 °C)	7.4 (-40 °C)

2.4.1 Second-order rate constants of complex **3**

All experiments were conducted with 1 mL solutions of 1 mM ferryl complexes in acetonitrile at 298 K for HAT (hydrogen-atom-transfer) substrates and 233 K for thioanisole (OAT, or oxygen-atom-transfer substrate), unless otherwise stated. The pseudo-first order decay curves from absorption vs time profiles (e.g. Figure 2.19) were obtained by monitoring the decrease in absorbance at 770 nm (e.g. Figure 2.19) with time. These profiles at various concentrations were fit with an

exponential decay function using Origin Pro 2016. The rates (k_{obs}) were plotted against different concentrations of substrates, and their slopes represent 2nd order rate constants (k_2), as shown in Figure 2.20.

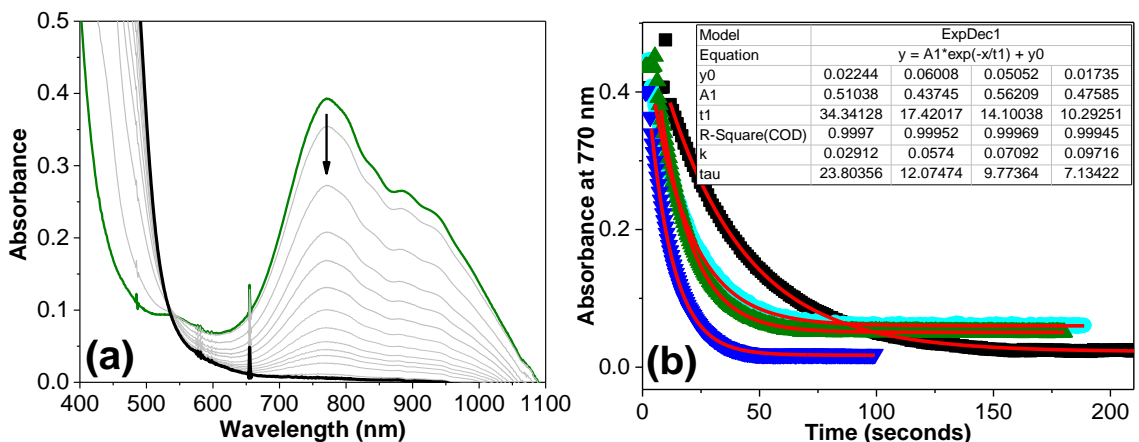
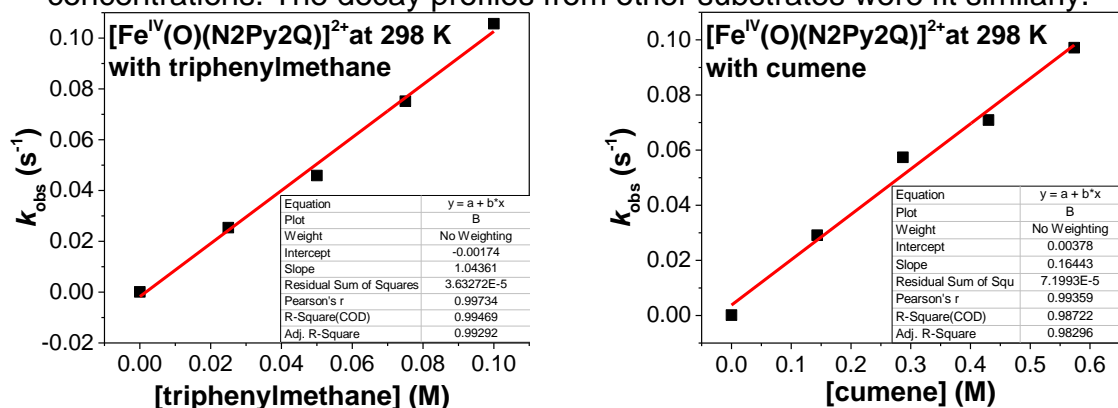


Figure 2.19 Spectral changes (a) observed over time in the reaction of **3** (1.0 mM) with a C–H substrate in CH₃CN at 25 °C. Absorption vs time decay profiles (b) upon reaction of **3** with different concentrations of cumene obtained by following 770 nm. It is fitted with an exponential function shown with red curves. Inset shows a table with all the parameters for this function with various concentrations. The decay profiles from other substrates were fit similarly.



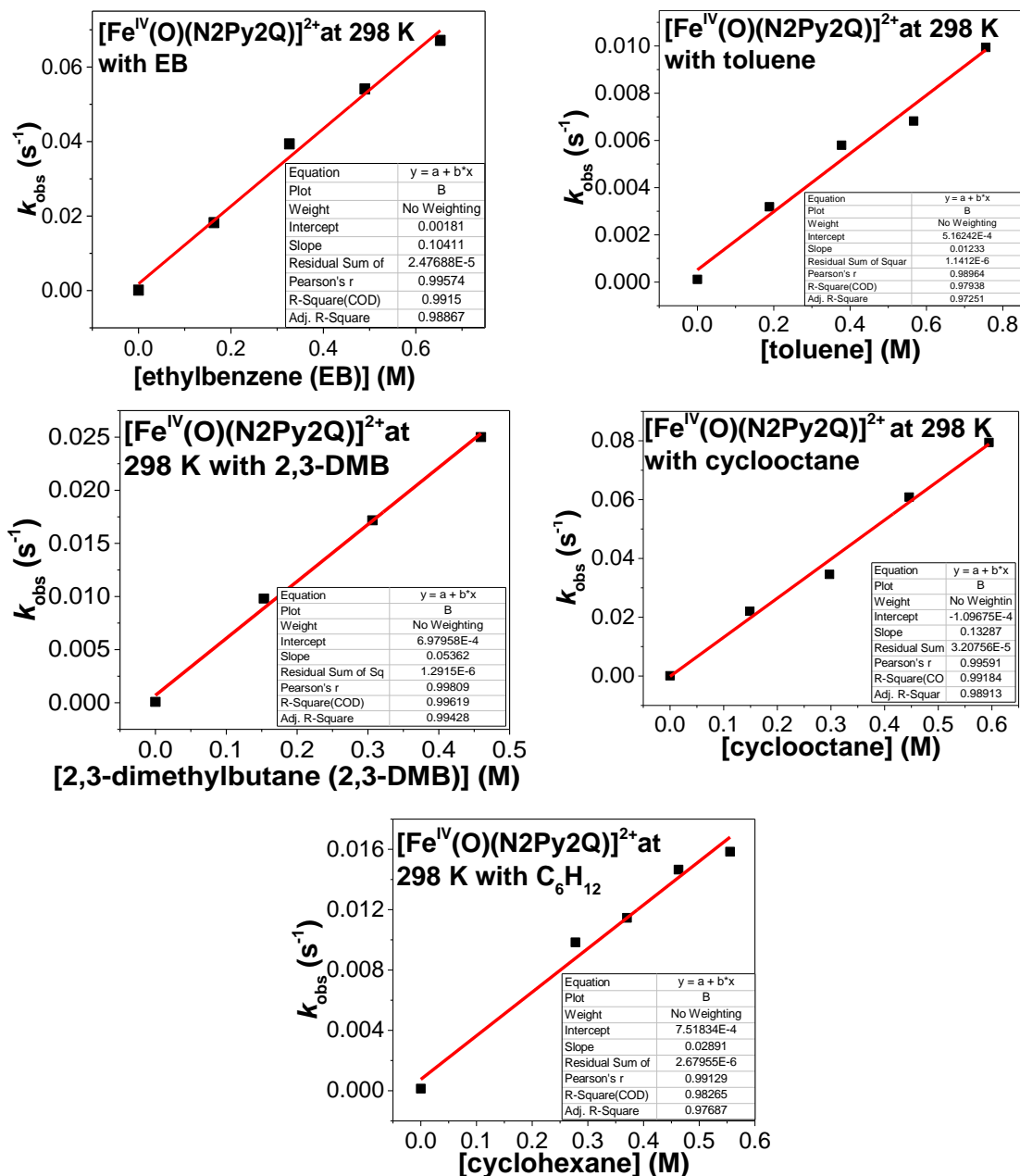


Figure 2.20 k_2 plots for the reactions of different substrates with **3**. The slopes of the fitted red lines represent the second-order rate constants (k_2) at 298 K.

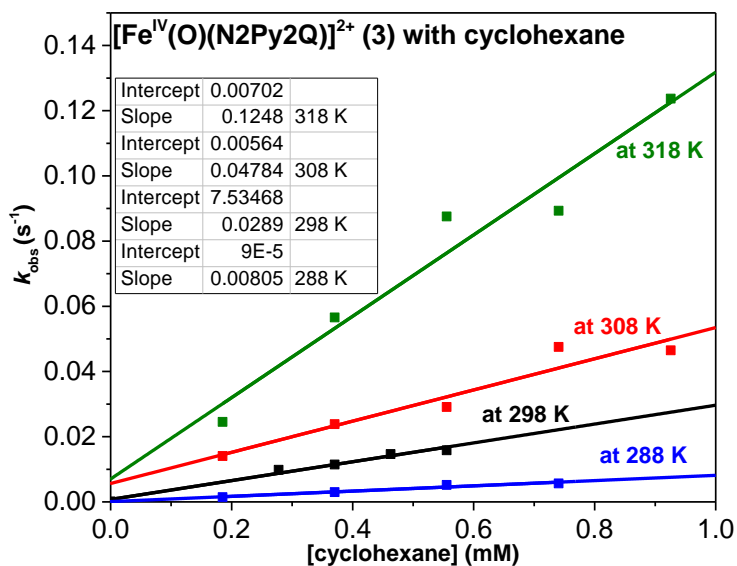
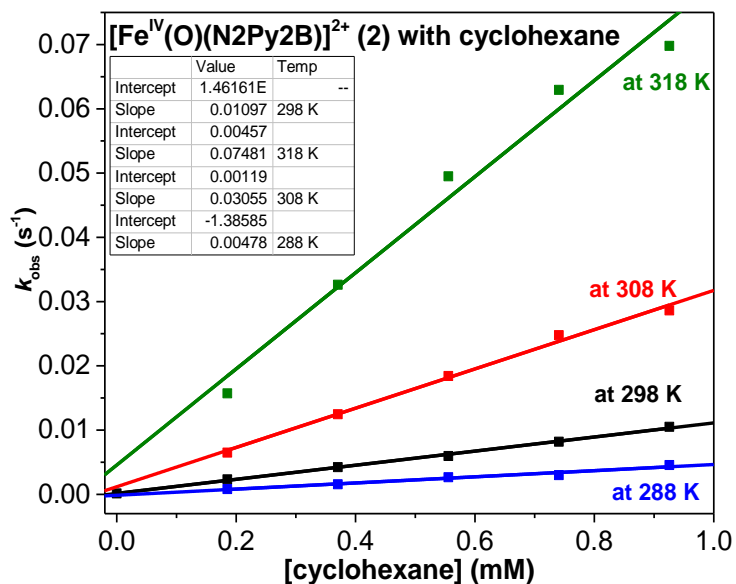


Figure 2.21 k_2 plots at different temperatures for the reactions of **2** (top) and **3** (bottom) with cyclohexane. The second order rate constants (k_2) were measured in the temperature range of 288 K to 318 K (plots are color coded with temperature) using 1 mM solutions of oxoiron(IV) complexes in acetonitrile. These rate constants were measured to obtain Eyring plots shown in Figure 2.24.

Table 2.9 k_{obs} of the reaction of 1 mM **1** with 0.8 M cyclohexane in 1 mL acetonitrile solution at different temperatures, which were obtained to account for the slowness of the reaction and self-decay. $k_2 = k_{\text{obs}}/[0.8]$.

Temperature (°C)	k_{obs} (s ⁻¹)
25	4.4×10^{-5}
30	5.94×10^{-5}
35	1.08×10^{-4}
40	1.65×10^{-4}

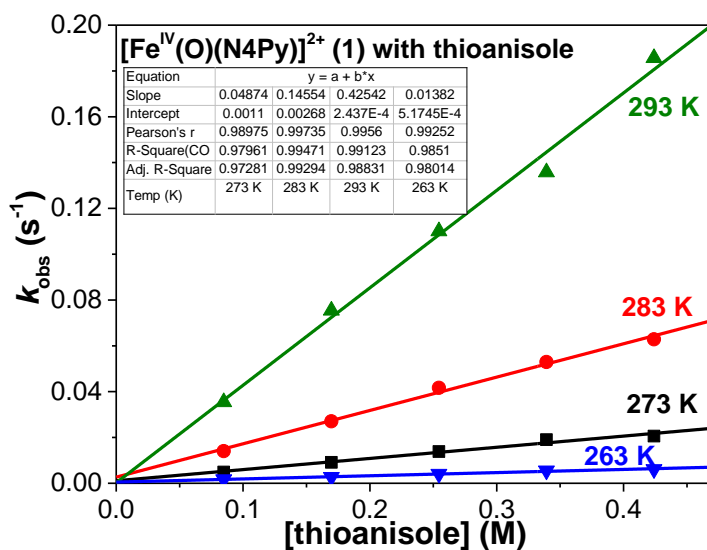


Figure 2.22 k_2 plots for the reactions of thioanisole with **1** at different temperatures. The second order rate constants (k_2) were measured in the temperature range of 263 K to 293 K (plots are color coded with temperature) using 1 mM solutions of complex **1** in acetonitrile.

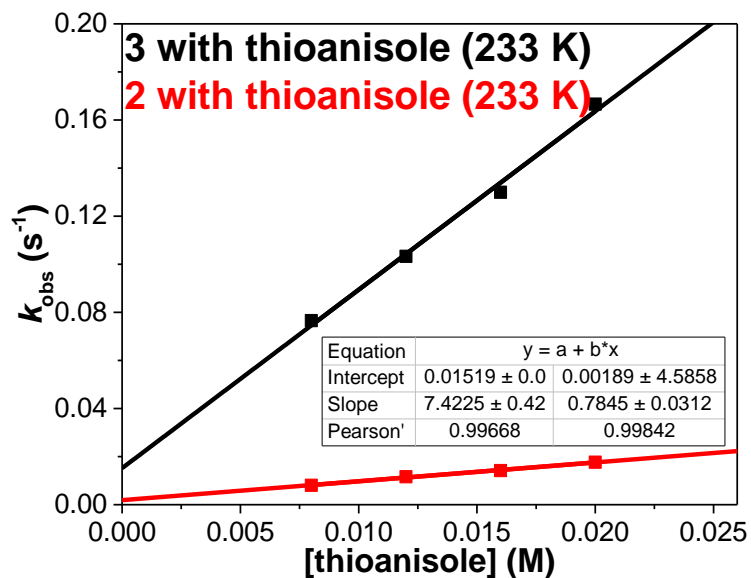


Figure 2.23 k_2 plots for the reactions of thioanisole with **2** (red) and **3** (black) at 233 K. The slopes of the fitted lines represent the second-order rate constants (k_2).

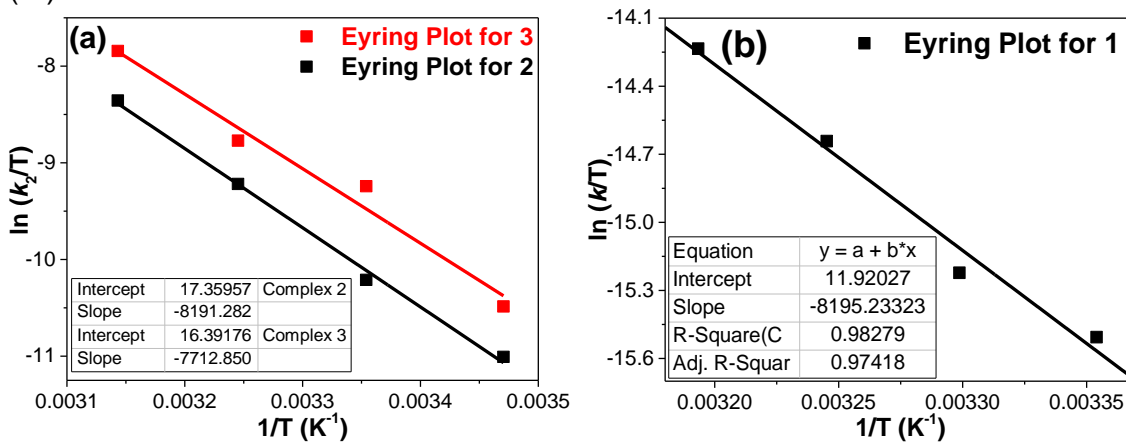


Figure 2.24 Eyring plots for the oxidation of cyclohexane by **2** (black squares) and **3** (red squares) (a), and by **1** (b).

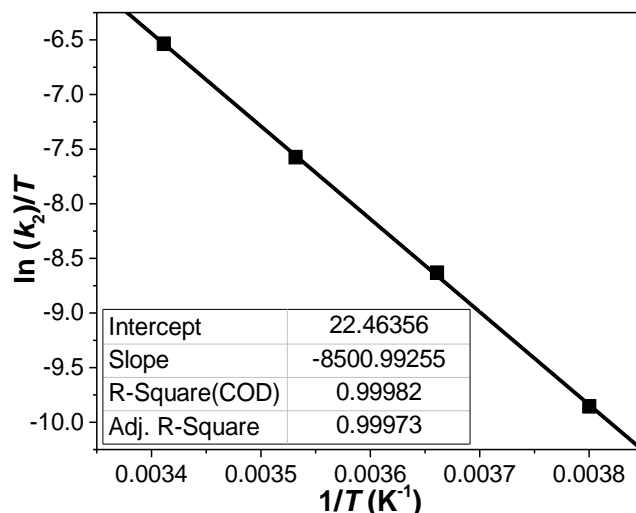


Figure 2.25 Eyring plot for the reaction of thioanisole with **1**.

Table 2.10 Eyring Parameters for reaction of substrates with complexes **1**, **2** and **3** discussed in this paper (see Figures 2.21-2.22 and 2.24-2.25, and Table 2.9), and rates at $-40\text{ }^{\circ}\text{C}$. The ΔS^{\ddagger} values are low in all the reactions, indicating an associative mechanism for these reactions.

CYCLOHEXANE			
Complex	ΔH^{\ddagger} (kcal/mol)	ΔS^{\ddagger} (cal/mol K)	Rate at $-40\text{ }^{\circ}\text{C}$ (k_2 in $\text{M}^{-1}\text{s}^{-1}$)
1 ($[\text{Fe}^{\text{IV}}(\text{O})(\text{N4Py})]^{2+}$)	16.3	-23.5	1.9×10^{-8}
2 ($[\text{Fe}^{\text{IV}}(\text{O})(\text{N2Py2B})]^{2+}$)	16.3	-12.7	4.5×10^{-6}
3 ($[\text{Fe}^{\text{IV}}(\text{O})(\text{N2Py2Q})]^{2+}$)	15.3	-14.6	1.3×10^{-5}
THIOANISOLE			
1 ($[\text{Fe}^{\text{IV}}(\text{O})(\text{N4Py})]^{2+}$)	16.9	-2.6	0.0002

2.4.2 DFT-optimized structures & spin-state splitting energies of **1**, **2** and **3**

Even though crystal structures for complexes **1-3** were available, DFT-optimizations were still done using M06-L functional with basis set def2TZVP, and then spin state splitting energies were obtained. Interestingly, the energy difference between the triplet and the quintet state in the case of complex **1** was

larger than 5.7 kcal/mol, but the differences in spin state energies in complexes **2** and **3** was just 2.8 and 2.1 kcal/mol. Interestingly in the DFT optimized structures of all the complexes that contain benzimidazole donors, no bending of the ferryl unit is observed, as expected from the lack of steric interactions proffered by the 5-membered imidazole ring in the heterocycle. Consistent with the higher basicity of this heterocycle, the $S = 1$ and $S = 2$ structures both possess the shortest Fe- $N_{\text{benzimidazole}}$ bond lengths. Furthermore the ferryl tilt is observed in both $S = 1$ and $S = 2$ optimized structures of complexes **3**, despite the longer Fe-N bond lengths of $S = 2$ complex **3**, although this bending is slightly larger in the $S = 1$ structure. In general the $S = 2$ structures have Fe-N bond lengths 0.07 to 0.1 Å longer than those in the the $S = 1$ complexes. The spin state splitting energies between complexes **2** and **3** are essentially the same. This can be attributed to the fact that the bend of the ferryl unit in $S = 2$ complex **3** remains preserved even with longer Fe-N lengths, thus mitigating a potential expected difference. The bond metrics of these DFT-optimized structures are listed in Table 2.12.

2.5 Correlation of reactivity with structural data

Figure 2.26 shows a remarkable correlation between $\log k_2'$ values and the average Fe-N bond lengths found for **1** – **3**. Such a correlation has not previously been possible due to the paucity of crystal structures of related non-heme oxoiron(IV) complexes. With the structures of **2** and **3** reported herein, in combination with the previously reported structure of **1**, we now have three complexes with the *same* polydentate ligand framework with which to relate structure and function. Indeed we find that the substrate oxidation rates of **1** – **3** increase proportionately with the average Fe-N bond length found for the oxoiron(IV) oxidant (Figure 2.26, Table 2.8), so the oxoiron(IV) complex with the longer average Fe-N bond length gives rise to the more reactive complex.

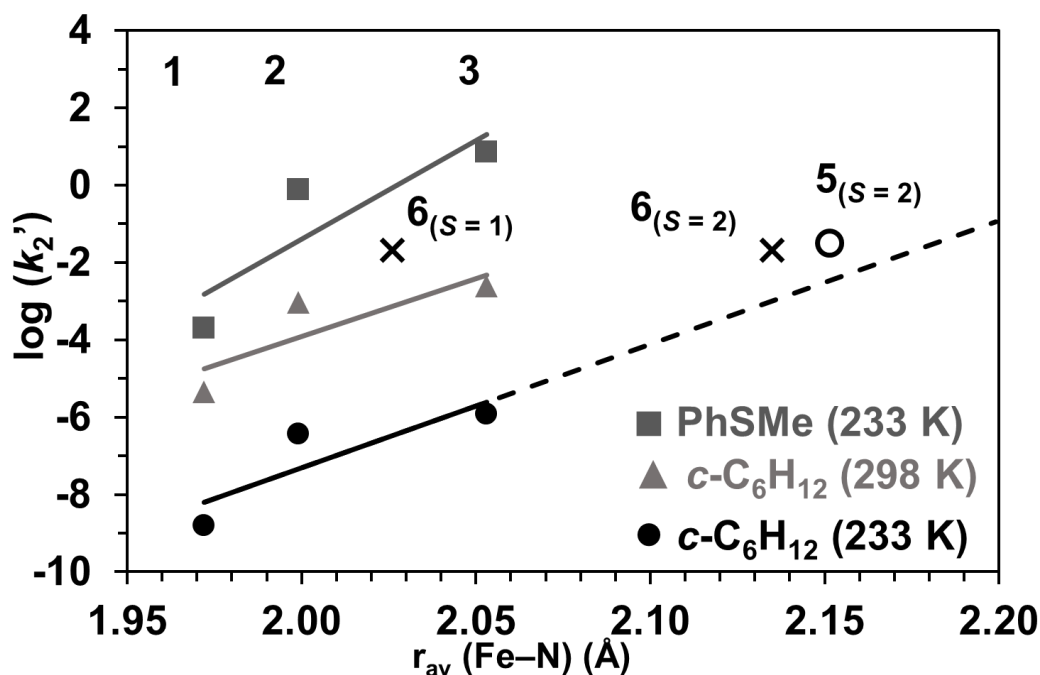


Figure 2.26 Correlation of $\log k_2$ values for thioanisole at -40 °C (squares) and $\log k_2'$ values for cyclohexane at 25 °C (triangles) and at -40 °C (circles) vs the average Fe–N bond lengths for **1** – **3** based on crystallographic data. The bottom plot is extended to $r_{av} = 2.20$ Å to determine whether this correlation also holds true for the $S = 2$ complex $[\text{Fe}^{\text{IV}}(\text{O})(\text{TQA})(\text{L})]^{2+}$ (**5**, open circle) and complex $[\text{Fe}^{\text{IV}}(\text{O})(\text{Me}_3\text{NTB})(\text{L})]^{2+}$ (**6**, crosses). The average Fe–N bond length for **5** and **6** were based on their DFT-optimized 6-coordinate structures, in $S = 1$ and 2 spin states. **5** and **6** are the first two complexes from left depicted in Figure 2.1.

As a simple interpretation, the observed correlation could reflect an increase in the electrophilicity of the $S = 1$ $\text{Fe}^{\text{IV}}=\text{O}$ unit with the increase in the average Fe–N bond length. A more complex argument to rationalize the HAT trends would involve the Two-State-Reactivity (TSR) model proposed by Shaik,⁵⁵⁻⁵⁶ where the lengthening of the average Fe–N bond should weaken the ligand field and thus decrease the energy gap between the $S = 1$ ground state and the $S = 2$ excited state that governs the reactivity of the $\text{Fe}^{\text{IV}}=\text{O}$ unit. This notion is supported by our HFEPFR measurements, which show an increase in the zero-field splitting (ZFS) parameter D in 1-cm^{-1} increments from **1** to **3** (Table 2.6). The increase in the zfs is purely an increase in D as the rigorously axial nature ($E \approx 0$) of the electronic structure of the

oxoiron(IV) unit is maintained upon going from **1** to **2** to **3**, despite the tilting of the Fe=O unit. Thus the reactivity trend observed for **1** – **3** can be fit into the TSR model (Figure 2.26).

Figure 2.27 shows a series correlations where $\log k_2'$ values are plotted versus D parameters. Such correlations have not been shown previously before due to the paucity of accurate D values for Fe^{IV}(O) complexes in the same polydentate framework.

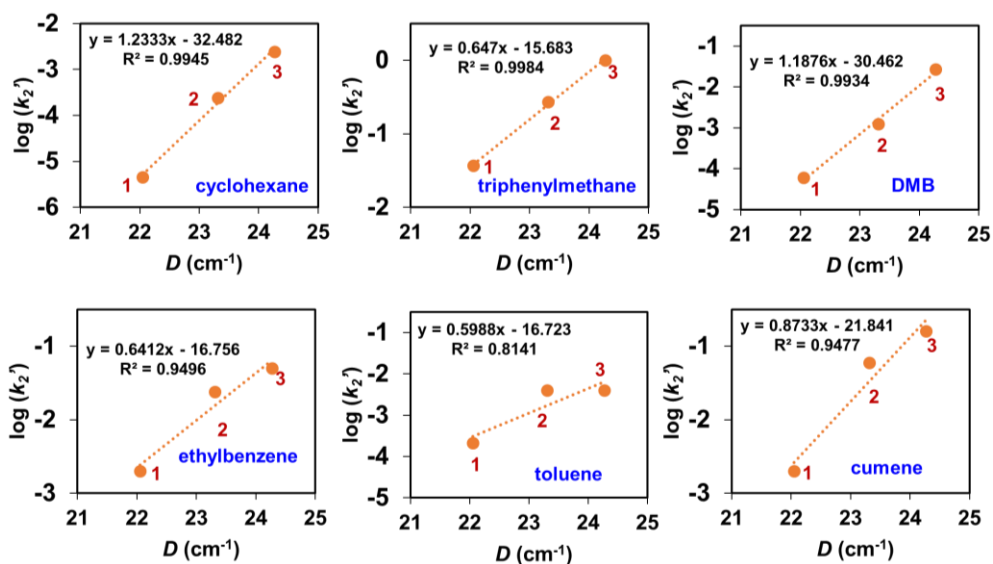


Figure 2.27 Correlation of HAT reactivity with D values (see Table 2.1).

However, accurate measurements of the D values require access to pure solids, which limits the number of complexes available for such an analysis to the less reactive subset of such complexes. While the LFT measurements discussed in the HFEPFR section do support the notion that excited quintet spin state has significant contributions into the $S = 1$ ground spin state, more complexes with accurate D values are needed to support the TSR model experimentally, and lay a solid foundation. While variable field and temperature Mössbauer spectroscopy can be used to obtain such values, the values obtained by this approach have larger uncertainties for too small a range of D values to be useful. Even if accurate D values are obtained and LFT calculations are done to show a significant

contribution of the $S = 2$ quintet excited state into the ground spin state, a direct experimental verification of this excited state's role in the HAT reactivity may still be difficult to verify because transition states are typically unobservable.

Table 2.11 Table for the plots shown in Figure 2.26. On the x-axis, the Fe– N_{average} lengths are obtained from Tables 2.5 and 2.6. The $\log k_2$ (not $\log k_2'$) were plotted on the y-axis. The rates of reaction with cyclohexane at -40 °C were obtained from Eyring parameters (see Tables 2.9-10 and Figures 2.21-2.22).

Substrates	1	2	3
HAT k_2 at 25 °C (used in Figure 2.18)			
TPM	0.037	0.27	1
Cumene	0.002	0.06	0.16
Ethylbenzene	0.004	0.048	0.1
Toluene	0.00063	0.012	0.012
Cyclooctane	–	0.026	0.13
2,3-DMB	0.00012	0.0025	0.054
Cyclohexane	0.000055	0.0029	0.029
k_2 at -40 °C and logarithms (used in Figure 2.26)			
Thioanisole (k_2)	0.0002	0.78	7.4
Thioanisole ($\log k_2$)	-3.71158	-0.10791	0.869232
Cyclohexane (k_2)	1.9×10^{-8}	4.5×10^{-6}	1.3×10^{-5}
Cyclohexane ($\log k_2'$)	-8.80043	-6.4305	-5.91
$\log k_2'$ at 25 °C (used in Figure 2.18)			
TPM	-1.4318	-0.5686	0
Cumene	-2.70	-1.2218	-0.7959
Ethylbenzene	-2.70	-1.6198	-1.3010
Toluene	-3.6778	-2.3979	-2.3979
Cyclooctane		-2.7891	-2.090
2,3-DMB	-4.2218	-2.9031	-1.5686
Cyclohexane	-5.3388	-3.6168	-2.6168
$\log k_2'$ at 25 °C (used in Figure 2.18)			
Cyclohexane	-5.33882	-3.03779	-3.61678

To put this structure/reactivity correlation into a broader context, we have checked where the HAT values reported for the $S = 2$ $[\text{Fe}^{\text{IV}}(\text{O})(\text{TQA})(\text{NCMe})]^{2+}$ (**5**) and $S =$

1 $[\text{Fe}^{\text{IV}}(\text{O})(\text{Me}_3\text{NTB})(\text{NCMe})]^{2+}$ (**6**) might fall on this plot (Figure 2.1). These two complexes are the most reactive oxoiron(IV) complexes found to date, and also contain benzimidazole and quinoline donors, but their high reactivity has precluded their crystallographic characterization. Thus DFT calculations have been employed to obtain structural information (Table 2.5).

Due to their thermal instability, reaction rates for **5** and **6** have been measured at -40 °C. For proper comparison, $\log k_2$ values for **1** – **3** at -40 °C were obtained from Eyring plots for cyclohexane oxidation (Figures 2.20-22, Table 2.9) and then plotted in Figure 2.25 versus the average Fe–N distance derived from previously reported DFT calculations. To our surprise, the point for **5** actually falls close to the line defined by the HAT values for **1** – **3**, despite the fact that **5** is a bona fide $S = 2$ complex and unlike the $S = 1$ complexes **1** – **3** used to define the correlation line. This apparent correlation raises the prospect that the average Fe–N bond length in $\text{Fe}^{\text{IV}}=\text{O}$ complexes may serve as a useful measure for relative HAT reactivity.

Complex **6** presents an interesting test case, as it has been characterized by Nam using Mössbauer spectroscopy to have an $S = 1$ ground spin state at 80 K and below but exhibits HAT rates comparable to those of $S = 2$ complex **5**.^{12, 51, 57} When its cyclohexane HAT rate is added into Figure 2.26 using the average Fe–N distance of 2.026 Å calculated for the MeCN-bound $S = 1$ complex, the point falls far from the line (Figure 2.26). However, a better agreement with the line is obtained by using the longer average Fe–N distance of 2.135 Å calculated for the 6-coordinate $S = 2$ complex, supporting the speculation by Nam that **6** becomes $S = 2$ at -40 °C to account for its observed higher HAT reactivity. However Nam has suggested that **6** becomes an $S = 2$ trigonal bipyramidal complex at this temperature. With this geometry, the calculated average Fe–N distance shortens to 2.042 Å, and the plotted point would fall far off the line. A significant shortening of the average Fe–N distance is also predicted for trigonal bipyramidal **5**, and the plotted point would be similarly incongruent with the correlation. Recent XAS studies on **6** however, report that this complex has an Fe–N bond length of 2.04

angstroms, and NMR studies report that it remains 6-coordinate at higher temperature. Thus if we were to use the bond lengths reported from XAS studies on the correlation in Figure 2.25, this complex would not fall on the line. Further studies are thus required to rationalize the unexpectedly high reactivity of **6**.

Correlation of spin density with the reactivity of the complexes

Saouma *et al.* have suggested that the spin density on the abstracting atom in ferryl complexes does not correlate with its HAT reactivity.⁵⁸ On the other hand, Ye *et al.* propose that nonheme oxoiron(IV) intermediates gain oxyl radical character approaching the C–H bond activation transition state. In mononuclear iron enzymes, Neidig *et al.* postulate the existence of a similar radical character on the oxo atom of the oxoiron(IV) intermediates.⁵⁹

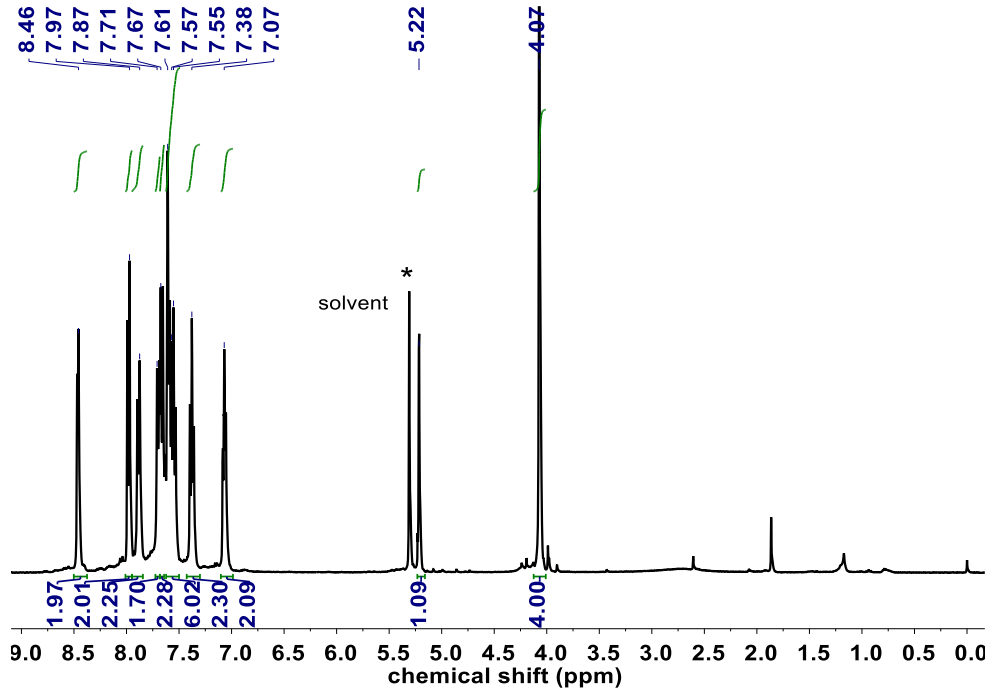
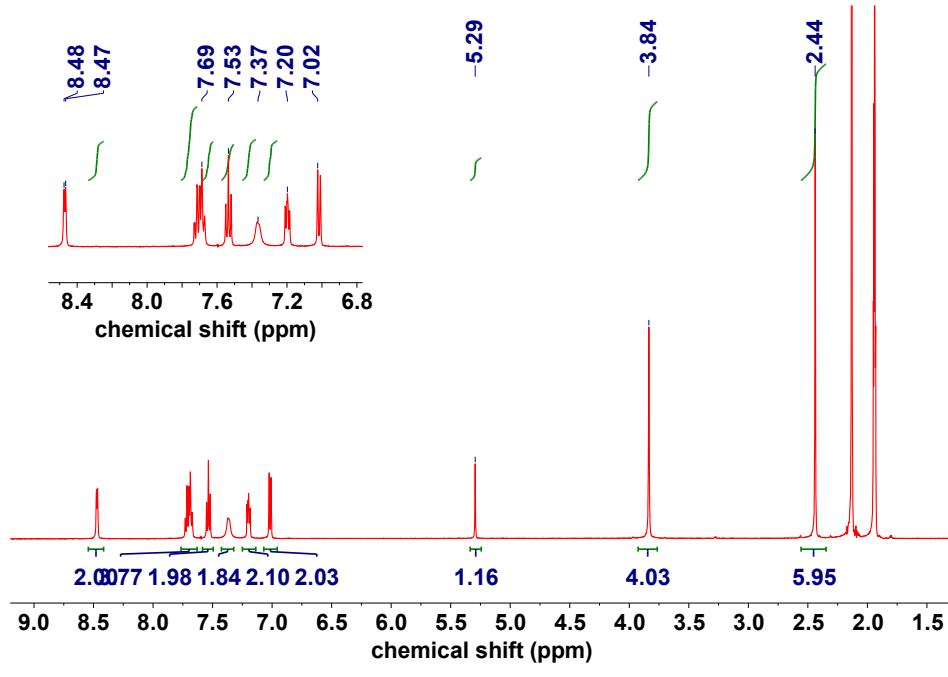
Whether there is a correlation between spin density on the oxo atom of the ferryl unit and the HAT reactivity is not fully settled in the literature due to differences in the results of the calculations.⁶⁰ If the actual oxidant during the HAT process were to become an Fe^{III}-O• radical when the reaction approaches to the transition state, then the higher unpaired spin density on the oxo atom at the ground state of the oxidant (Fe^{IV}=O) would translate to higher reactivity, due to the effective lowering of the activation barrier. Elongation of the Fe=O bond *en route* to the transition state in an HAT reaction would lower its activation barrier, hinting at a higher radical character and spin density on the oxo atom at this point. Complex **3** has the longest Fe=O bond length of the complexes crystallized in the N4Py framework. This geometric feature therefore may increase spin density on this complex, and be responsible for its higher reactivity. However, the Fe=O bond lengths found for oxoiron(IV) complexes **1-4** span a much smaller range of distances (0.04 Å) and have 3 × esd's of 0.01-0.02 Å, so these values make these complexes less distinct from each other. Indeed, calculations on complexes **2**, **3** and **4** (done using a B3LYP functional with the basis set 6-311G) reveal very similar spin density values (from 0.88 to 0.89 to 0.92 respectively), despite significant differences in reactivity between the complexes discussed in this chapter. Further studies are thus

required to address the issue of spin density and reactivity. On a similar note, the vibrational Fe=O stretching vibrations found for **1**, **2**, and **3** also only differ by less than 10 cm^{-1} . Assuming that the Fe=O stretch reflects its bond strength, the expectations that the reactivity of the Fe=O unit should be reflected in its Fe=O bond distance or its stretching frequency are not borne out.

2.6 Conclusion

In summary, **2** and **3** represent the first oxoiron(IV) complexes with *N*-methylbenzimidazole or quinoline donors to be crystallographically characterized, shedding light on how these modifications can affect the Fe=O environment. Based on this work, it is evident that the quinolyl donors of **3** exert steric effects that increase the average Fe–N bond length and tilt the Fe=O unit away from these donors, resulting in higher HAT and OAT rates relative to **1** and **2**. While complex **3a** was not further explored because of its thermal instability, deuteration of the benzylic positions on this ligand should be considered as a potential strategy to increase stability and perhaps allow structural data to be obtained. Nevertheless, the crystal structure of the starting precursor of this complex does indicate that steric hindrance enforced by 6-methyl groups likely exists on **3a**.

Lastly, increasing the number of quinolines to three in complex **5** further lengthens the average Fe–N distance and makes the Fe=O unit change its spin state to $S = 2$, further enhancing its reactivity and lending credence to the correlation between reactivity and average Fe–N distance shown in Figure 2.26.



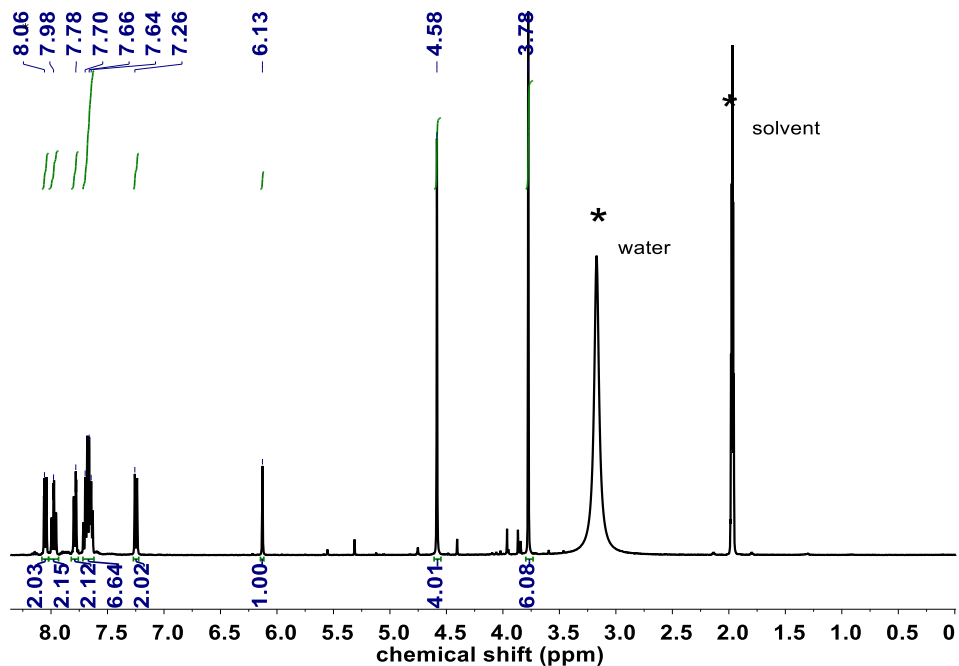


Figure 2.28 ^1H NMR spectrum of 6Me₂N₄Py (top, CD₃CN), N₂Py₂Q (middle, CD₂Cl₂) and N₂Py₂B (bottom, CD₃CN).

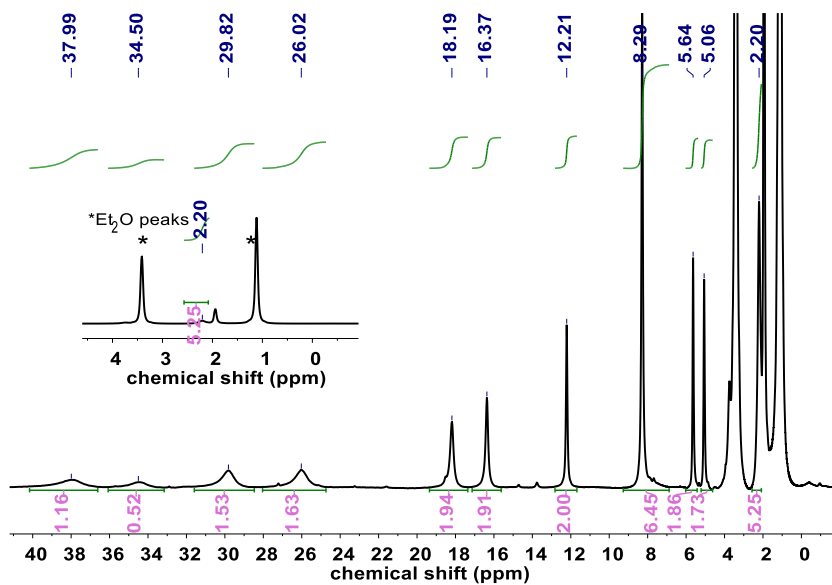


Figure 2.29 ^1H NMR spectrum of $[\text{Fe}^{\text{II}}(\text{N}_2\text{Py}_2\text{B})(\text{CH}_3\text{CN})]\text{OTf}$ in CD₃CN with an inset: zoomed from -2 to 5 ppm

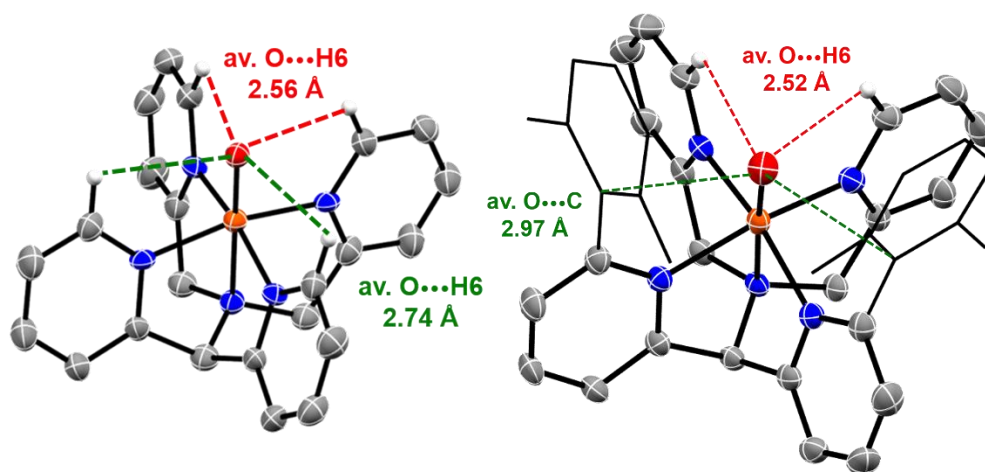


Figure 2.31 Front view of complex **1** (left) and **4** (right), along with non-bonded contact distances from oxygen atom of the ferryl unit to the alpha-H or alpha-carbon of the pyridines. The aryl rings are shown as stick figures.

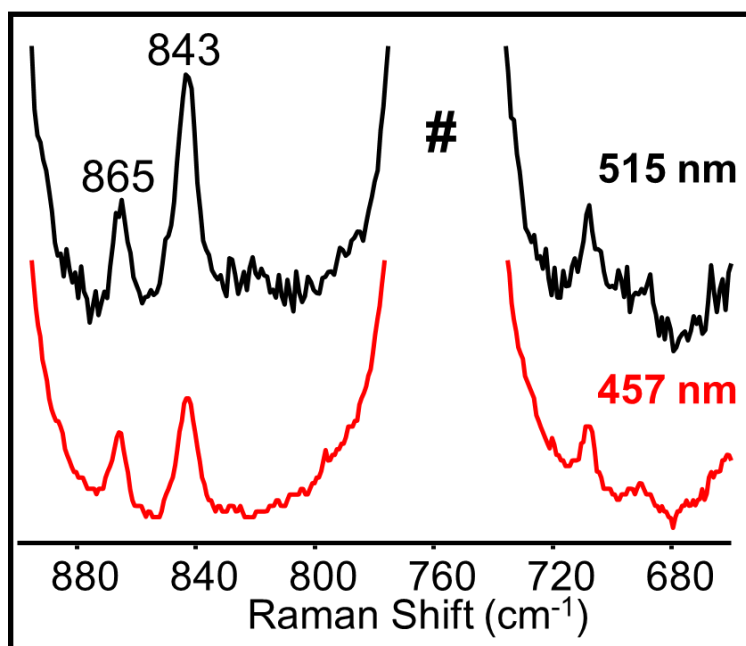


Figure 2.32 Resonance Raman spectrum of 5 mM isolated complex **2** dissolved in MeCN, measured at 233 K using two different lasers (shown above).

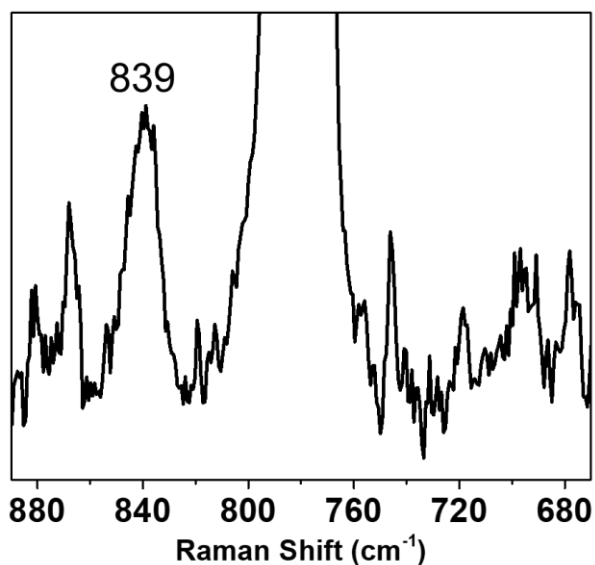


Figure 2.33 Resonance Raman spectrum of isolated complex **1*** dissolved in CH₃CN, measured as frozen solution at 77 K, using 515 nm laser. # = solvent

Table 2.12 Bond metrics of DFT-optimized structures used for calculations of spin-state splitting energies calculated using M06-L/def2TZVP

Complexes (all values in Å, unless stated)	1, S = 1	1, S = 2	2, S = 1	2, S = 2	3, S = 1	3, S = 2
N-Fe=O, °	179.96	179.52	177.83	177.28	170.33	171.29
N _{mean-plane} -Fe=O, °	88.8	87.4	88.8	89.6	82.6	84.3
Fe-N _{average}	2.013	2.124	2.018	2.128	2.039	2.141
aver. Fe-N _{equatorial}	1.993	2.122	1.983	2.11	2.029	2.149
Fe-N _{amine}	2.093	2.132	2.158	2.201	2.083	2.113
Fe-N _{pyridine}	1.998, 1.998	2.098, 2.097	2.003, 2.003	2.168, 2.180	2.004, 2.002	2.153, 2.151
Fe-N _{heterocycle}	1.987, 1.987	2.146, 2.146	1.964, 1.963	2.048, 2.043	2.053, 2.055	2.147, 2.143

Table 2.13 Half-lives of oxoiron(IV) complexes based on N4Py framework with generated from iron(II) precursors with different oxidants, measured at 298 K with 1-mM acetonitrile solutions

Complexes	1	1*	2	3	3a	3b
oxidant used	PhIO	PhIO	isolated		<i>m</i> CPBA, PhI(OAc) ₂	PhI(OAc) ₂ , PFIB
half-life (min)	3600	‡3000	150	150	14, 130	30, 40
reference	13	16	15	27	23, 26	26
PFIB: pentafluoroiodosylbenzene; <i>m</i> CPBA: <i>meta</i> -chloroperbenzoic acid; PhIO: iodosylbenzene; PhI(OAc) ₂ : (diacetoxyiodo)benzene. ‡t _{1/2} at 303 K.						

2.6 Acknowledgments

The work described in this chapter could not have been accomplished without the help and collaboration of a number of extremely talented scientists. First and foremost, Dr Apparao Draksharapu helped me develop and refine a method to crystallize and crash out the ferryl complexes. This enabled me to crystallize out a number of ferryl complexes that I would otherwise not have been able to obtain. Saikat Banerjee helped in the synthesis of the precursor of the ligand N2py2B, for which I was able to obtain the ferryl complex and characterize it structurally and spectroscopically. Mössbauer experiments described in this paper were carried out by Ruixi Fan and analyzed by both Professor Yisong Guo and Ruixi Fan. Ruixi Fan also did spin density calculations for the complexes described in this chapter. Dr Victor Young helped modeling water molecules around the ferryl center and the perchlorate ions, and also helped me improve my analysis of crystal structure of these complexes. Professor Joshua Telser and Dr Jurek Krzystek worked with Dr Mike Ozerov to obtain high-field and frequency-EPR and FIRMS data on complexes **2** and **3**, which was used to obtain zero-field splitting parameters, along with help from Dr Mike Ozerov, and Dr Joscha Nehrkorn. Dr Johannes E. M. N. Klein was involved in numerous discussions regarding these complexes, particularly with regards to how to discuss the tilted ferryl complex and highlighting its unique structure, and obtaining spin-state splitting energies of the $S = 1$ and $S = 2$ complexes.

2.8 References

1. Kal, S.; Que, L., *J. Biol. Inorg. Chem.* **2017**, *22* (2), 339-365.
2. Krebs, C.; Galonić Fujimori, D.; Walsh, C. T.; Bollinger, J. M., *Acc. Chem. Res.* **2007**, *40* (7), 484-492.
3. Klein, J. E. M. N.; Que, L., Biomimetic High-Valent Mononuclear Nonheme Iron-Oxo Chemistry. In *Encyclopedia of Inorganic and Bioinorganic Chemistry*, John Wiley & Sons, Ltd: 2016; p; DOI: 10.1002/9781119951438.eibc2344
4. Engelmann, X.; Monte-Pérez, I.; Ray, K., *Angew. Chem. Int. Ed.* **2016**, *55* (27), 7632-7649.
5. McDonald, A. R.; Que, L., Jr., *Coord. Chem. Rev.* **2013**, *257* (2), 414-428.
6. Nam, W.; Lee, Y.-M.; Fukuzumi, S., *Acc. Chem. Res.* **2014**, *47* (4), 1146-1154.
7. Puri, M.; Que, L., *Acc. Chem. Res.* **2015**, *48* (8), 2443-2452.
8. England, J.; Guo, Y.; Farquhar, E. R.; Young Jr, V. G.; Münck, E.; Que Jr, L., *J. Am. Chem. Soc.* **2010**, *132* (25), 8635-8644.
9. Lacy, D. C.; Gupta, R.; Stone, K. L.; Greaves, J.; Ziller, J. W.; Hendrich, M. P.; Borovik, A. S., *J. Am. Chem. Soc.* **2010**, *132* (35), 12188-12190.
10. Pestovsky, O.; Stoian, S.; Bominaar, E. L.; Shan, X.; Münck, E.; Que Jr, L.; Bakac, A., *Angew. Chem. Int. Ed.* **2005**, *44* (42), 6871-6874.
11. Biswas, A. N.; Puri, M.; Meier, K. K.; Oloo, W. N.; Rohde, G. T.; Bominaar, E. L.; Münck, E.; Que, L., *J. Am. Chem. Soc.* **2015**, *137* (7), 2428-2431.
12. Seo, M. S.; Kim, N. H.; Cho, K.-B.; So, J. E.; Park, S. K.; Clémancey, M.; Garcia-Serres, R.; Latour, J.-M.; Shaik, S.; Nam, W., *Chem. Sci.* **2011**, *2* (6), 1039-1045.
13. Kaizer, J.; Klinker, E. J.; Oh, N. Y.; Rohde, J.-U.; Song, W. J.; Stubna, A.; Kim, J.; Münck, E.; Nam, W.; Que, L., Jr., *J. Am. Chem. Soc.* **2004**, *126* (2), 472-473.
14. Klinker, E. J.; Kaizer, J.; Brennessel, W. W.; Woodrum, N. L.; Cramer, C. J.; Que, L., Jr., *Angew. Chem. Int. Ed.* **2005**, *44* (24), 3690-3694.

15. Mitra, M.; Nimir, H.; Demeshko, S.; Bhat, S. S.; Malinkin, S. O.; Haukka, M.; Lloret-Fillol, J.; Lisensky, G. C.; Meyer, F.; Shteinman, A. A.; Browne, W. R.; Hrovat, D. A.; Richmond, M. G.; Costas, M.; Nordlander, E., *Inorg. Chem.* **2015**, *54* (15), 7152-7164.
16. Rana, S.; Dey, A.; Maiti, D., *Chem. Commun.* **2015**, *51* (77), 14469-14472.
17. Massie, A. A.; Denler, M. C.; Cardoso, L. T.; Walker, A. N.; Hossain, M. K.; Day, V. W.; Nordlander, E.; Jackson, T. A., *Angew. Chem. Int. Ed.* **2017**, *56* (15), 4178-4182.
18. Sahu, S.; Quesne, M. G.; Davies, C. G.; Dürr, M.; Ivanović-Burmazović, I.; Siegler, M. A.; Jameson, G. N. L.; de Visser, S. P.; Goldberg, D. P., *J. Am. Chem. Soc.* **2014**, *136* (39), 13542-13545.
19. Mukherjee, G.; Lee, C. W. Z.; Nag, S. S.; Alili, A.; Cantú Reinhard, F. G.; Kumar, D.; Sastri, C. V.; de Visser, S. P., *Dalton Trans.* **2018**, *47* (42), 14945-14957.
20. Rana, S.; Biswas, J. P.; Sen, A.; Clémancey, M.; Blondin, G.; Latour, J.-M.; Rajaraman, G.; Maiti, D., *Chem. Sci.* **2018**, *9* (40), 7843-7858.
21. Massie, A. A.; Sinha, A.; Parham, J. D.; Nordlander, E.; Jackson, T. A., *Inorg. Chem.* **2018**, *57* (14), 8253-8263.
22. Denler, M. C.; Massie, A. A.; Singh, R.; Stewart-Jones, E.; Sinha, A.; Day, V. W.; Nordlander, E.; Jackson, T. A., *Dalton Trans.* **2019**.
23. Singh, R.; Ganguly, G.; Malinkin, S. O.; Demeshko, S.; Meyer, F.; Nordlander, E.; Paine, T. K., *Inorg. Chem.* **2019**.
24. McDonald, A. R.; Guo, Y.; Vu, V. V.; Bominaar, E. L.; Münck, E.; Que, L., *Chem. Sci.* **2012**, *3* (5), 1680-1693.
25. Sahu, S.; Zhang, B.; Pollock, C. J.; Dürr, M.; Davies, C. G.; Confer, A. M.; Ivanović-Burmazović, I.; Siegler, M. A.; Jameson, G. N. L.; Krebs, C.; Goldberg, D. P., *J. Am. Chem. Soc.* **2016**, *138* (39), 12791-12802.
26. de Visser, S.; Mukherjee, G.; Kumar, D.; Sastri, C.; Alili, A.; Barman, P., *Chem. Eur. J.* **2019**, *0* (Just Accepted).

27. Rasheed, W.; Draksharapu, A.; Banerjee, S.; Young, V. G.; Fan, R.; Guo, Y.; Ozerov, M.; Nehrkorn, J.; Krzystek, J.; Telser, J.; Que, L., *Angew. Chem. Int. Ed.* **2018**, *57* (30), 9387-9391.
28. Hagen, K. S., *Inorg. Chem.* **2000**, *39*, 5867-5869.
29. Petasis, D. T.; Hendrich, M. P., Chapter Eight - Quantitative Interpretation of Multifrequency Multimode EPR Spectra of Metal Containing Proteins, Enzymes, and Biomimetic Complexes. In *Methods in Enzymology*, Qin, P. Z.; Warncke, K., Eds. Academic Press: 2015; Vol. 563, pp 171-208.
30. Hassan, A. K.; Pardi, L. A.; Krzystek, J.; Sienkiewicz, A.; Goy, P.; Rohrer, M.; Brunel, L. C., *J. Magn. Reson.* **2000**, *142* (2), 300-312.
31. Ludwig, J.; Vasilyev, Y. B.; Mikhailov, N. N.; Poumirol, J. M.; Jiang, Z.; Vafek, O.; Smirnov, D., *Phys. Rev. B* **2014**, *89* (24), 241406.
32. Lubben, M.; Meetsma, A.; Wilkinson, E. C.; Feringa, B.; Que Jr, L., *Angew. Chem. Int. Ed.* **1995**, *34* (13-14), 1512-1514.
33. Spek, A. L.; Schoondergang, M. F. J.; Feringa, B. L., *CSD Communication* **2004**, CCDC 232796.
34. Decker, A.; Rohde, J.-U.; Que, L., Jr.; Solomon, E. I., *J. Am. Chem. Soc.* **2004**, *126* (17), 5378-5379.
35. Jackson, T. A.; Rohde, J.-U.; Seo, M. S.; Sastri, C. V.; DeHont, R.; Stubna, A.; Ohta, T.; Kitagawa, T.; Münck, E.; Nam, W.; Que, L., Jr., *J. Am. Chem. Soc.* **2008**, *130* (37), 12394-12407.
36. Draksharapu, A.; Angelone, D.; Quesne, M. G.; Padamati, S. K.; Gómez, L.; Hage, R.; Costas, M.; Browne, W. R.; de Visser, S. P., *Angew. Chem. Int. Ed.* **2015**, *54* (14), 4357-4361.
37. Draksharapu, A.; Rasheed, W.; Klein, J. E. M. N.; Que, L., *Angew. Chem. Int. Ed.* **2017**, *56* (31), 9091-9095.
38. Lee, Y.-M.; Dhuri, S. N.; Sawant, S. C.; Cho, J.; Kubo, M.; Ogura, T.; Fukuzumi, S.; Nam, W., *Angew. Chem. Int. Ed.* **2009**, *48* (10), 1803-1806.

39. Chanda, A.; Shan, X.; Chakrabarti, M.; Ellis, W. C.; Popescu, D. L.; Tiago de Oliveira, F.; Wang, D.; Que, L., Jr.; Collins, T. J.; Münck, E.; Bominaar, E. L., *Inorg. Chem.* **2008**, *47* (9), 3669-3678.
40. Krzystek, J.; England, J.; Ray, K.; Ozarowski, A.; Smirnov, D.; Que, L., Jr.; Telser, J., *Inorg. Chem.* **2008**, *47* (9), 3483-3485.
41. Telser, J.; Krzystek, J.; Ozarowski, A., *J. Biol. Inorg. Chem.* **2014**, *19* (3), 297-318.
42. Bucinsky, L.; Breza, M.; Lee, W.-T.; Hickey, A. K.; Dickie, D. A.; Nieto, I.; DeGayner, J. A.; Harris, T. D.; Meyer, K.; Krzystek, J.; Ozarowski, A.; Nehrkorn, J.; Schnegg, A.; Holldack, K.; Herber, R. H.; Telser, J.; Smith, J. M., *Inorg. Chem.* **2017**, *56* (8), 4751-4768.
43. Bucinsky, L.; Rohde, G. T.; Que, L.; Ozarowski, A.; Krzystek, J.; Breza, M.; Telser, J., *Inorg. Chem.* **2016**, *55* (8), 3933-3945.
44. APEX3, Bruker Analytical X-ray Systems, Madison, WI (2016).
45. SADABS, Bruker Analytical X-ray Systems, Madison, WI (2016).
46. SAINT, Bruker Analytical X-ray Systems, Madison, WI (2016).
47. SHELXTL, Bruker Analytical X-Ray Systems, Madison, WI (2008).
48. Sheldrick, G. M., *Acta Cryst.* **A64**, 112-122 (2008).
49. Sheldrick, G. M., *Acta Cryst.* **C71**, 3-8 (2015).
50. Rowland, R. S.; Taylor, R., *J. of Phys. Chem.* **1996**, *100* (18), 7384-7391.
51. Lee, N. Y.; Mandal, D.; Bae, S. H.; Seo, M. S.; Lee, Y.-M.; Shaik, S.; Cho, K.-B.; Nam, W., *Chem. Sci.* **2017**, *8* (8), 5460-5467.
52. Jensen, M. P.; Costas, M.; Ho, R. Y. N.; Kaizer, J.; Mairata i Payeras, A.; Münck, E.; Que, L., Jr.; Rohde, J.-U.; Stubna, A., *J. Am. Chem. Soc.* **2005**, *127* (30), 10512-10525.
53. Lõkov, M.; Tshepelevitsh, S.; Heering, A.; Plieger, P. G.; Vianello, R.; Leito, I., *Eur. J. Org. Chem.* **2017**, *2017* (30), 4475-4489.
54. Wang, D.; Ray, K.; Collins, M. J.; Farquhar, E. R.; Frisch, J. R.; Gómez, L.; Jackson, T. A.; Kerscher, M.; Waleska, A.; Comba, P.; Costas, M.; Que, L., *Chem. Sci.* **2013**, *4* (1), 282-291.

55. Klinker, E. J.; Shaik, S.; Hirao, H.; Que, L., Jr, *Angew. Chem. Int. Ed.* **2009**, *48* (7), 1291-1295.
56. Mandal, D.; Mallick, D.; Shaik, S., *Acc. Chem. Res.* **2018**, *51* (1), 107-117.
57. Bae Seong, H.; Seo Mi, S.; Lee, Y. M.; Cho, K. B.; Kim, W. S.; Nam, W., *Angew. Chem. Int. Ed.* **2016**, *55* (28), 8027-8031.
58. Saouma, C. T.; Mayer, J. M., *Chem. Sci.* **2014**, *5* (1), 21-31.
59. Neidig, M. L.; Decker, A.; Choroba, O. W.; Huang, F.; Kavana, M.; Moran, G. R.; Spencer, J. B.; Solomon, E. I., *PNAS* **2006**, *103* (35), 12966-12973.
60. Srnec, M.; Wong, S. D.; Matthews, M. L.; Krebs, C.; Bollinger, J. M.; Solomon, E. I., *J. Am. Chem. Soc.* **2016**, *138* (15), 5110-5122.

Chapter 3:
Oxoiron(IV) Complexes Supported by BnTPEN-Based Ligands

3.1 Introduction

In the fifteen years that have followed the discovery of oxoiron(IV) intermediates in nonheme oxygenases and oxidases¹⁻⁵, bioinorganic chemists have flocked to make their spectroscopic, functional and structural analogs.⁶ This has been driven in large part by the diverse reactivity enabled by these ferryl intermediates, which form in enzymes as a result of activation of O₂ by nonheme iron(II) centers, and then coupling it to the oxidation of different substrates.⁷ Many of these oxidations involve inert aromatic and aliphatic C–H bonds hydroxylation, C–H halogenation, C–H desaturation to form C=C bonds, C=C bond epoxidation, heterocyclic ring formation, and decarboxylation.⁸ The diversity of the oxidations carried out by these species speak to the importance of these intermediates.⁷

While bioinorganic chemists have synthesized structural, functional, and/or spectroscopic mimics of these intermediates, *none* of the analogs have modeled enzymatic intermediates in all three aspects.⁹ Furthermore, over 80% of these complexes have not been structurally characterized, thus encumbering formulation of experimentally derived structural-functional and -spectroscopic relationships for these compounds.

Unlike the enzymatic ferryl intermediates, which have $S = 2$ ground spin states, a clear majority of the 90 or so synthetic models have an $S = 1$ ground spin state. Typically, all model complexes in either ground spin state are found to be less reactive than the $S = 2$ enzymatic intermediates. There is one striking exception of a reactive and thermally unstable $S = 2$ oxoiron(IV) complex, namely $[\text{Fe}^{\text{IV}}(\text{O})(\text{TQA})(\text{L})]^{2+}$, which is supported by a tripodal ligand TQA (tris(2-quinolylmethyl)amine), containing three equatorial quinolines and an axial amine (Figure 3.1).¹⁰ While this intermediate spectroscopically and functionally models the enzymatic intermediates, its thermal instability contributes to the dearth of structural information on this complex. Despite its inherent instability, this compound remains the only model that resembles enzymatic intermediates in its electronic properties.

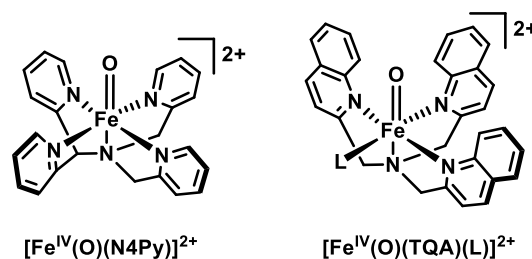


Figure 3.1 The oxoiron(IV) complexes examined for their structure-reactivity relationship

In our efforts to gain insight into enzymatic analogs, we have crystallographically characterized an oxoiron(IV) complex that contains quinoline heterocycles (Chapter 2) similar to $[\text{Fe}^{\text{IV}}(\text{O})(\text{TQA})(\text{L})]^{2+}$, namely $[\text{Fe}^{\text{IV}}(\text{O})(\text{N2Py2Q})]^{2+}$, where $\text{N2Py2Q} = 1,1\text{-di(pyridin-2-yl)-}N,N\text{-bis(quinolin-2-ylmethyl)methanamine}$. In this complex, the quinolines are oriented parallel to the ferryl unit and their protons exert steric hindrance on the oxoiron(IV) unit. This steric hindrance has two consequences: it increases the average Fe–N bond lengths of this complex by over 0.08 Å compared to the parent complex which only contained pyridines, and tilts the oxoiron(IV) unit away from the z-axis.¹¹ Both the effects lead to an increase in the electrophilicity of the iron(IV) center, thus increasing its reactivity. The quinoline heterocycles in the complex $[\text{Fe}^{\text{IV}}(\text{O})(\text{TQA})(\text{L})]^{2+}$ likely have similar steric effects on the oxoiron(IV) unit, making it the most reactive oxoiron(IV) complex reported thus far. The steric hindrance of quinolines in the case of $[\text{Fe}^{\text{IV}}(\text{O})(\text{TQA})(\text{L})]^{2+}$ also leads to a change in the spin state from $S = 1$ to $S = 2$, making the complex a closer analog of enzymatic intermediate.

Introduction of 6-methyl groups on pyridines or the replacement of pyridines with quinolines has similar steric effects. The introduction of alpha-methyl substituents on pyridines in the tripodal ligand framework of TPA (tris(2-pyridylmethyl)amine) results in 6Me₃TPA ((tris(6-methyl-2-pyridylmethyl)amine)). The iron(II) centers supported by these two ligands have different spin states, as evidenced by NMR spectroscopy.¹² The $S = 0$ complex $[\text{Fe}^{\text{II}}(\text{TPA})(\text{MeCN})_2]^{2+}$ has Fe–N_{py} bond lengths that are 0.2 angstroms shorter on average than those in the $S = 2$ complex

$[\text{Fe}^{\text{II}}(\text{6Me}_3\text{TPA})(\text{MeCN})_2]^{2+}$. Similarly, in $[\text{Fe}^{\text{IV}}(\text{O})(\text{6MeTPA})(\text{L})]^{2+}$, where 6MeTPA contains only one 6-methylpyridine on the TPA framework, has a much more red-shifted near-IR absorption band compared with that of the unsubstituted complex $[\text{Fe}^{\text{IV}}(\text{O})(\text{TPA})(\text{L})]^{2+}$, indicating a weakened ligand field. This weakened ligand field likely arises from increased Fe–N bond lengths as a result of steric effects imposed by the 6-methyl groups.¹³

The structural data obtained for tetragonal oxoiron(IV) complexes so far shows that average Fe–L bond lengths extend from 1.95 Å to 2.10 Å (a span of 0.15 Å), but in this range, the iron center does not change its spin state from $S = 1$ to $S = 2$. To allow for a wider range of average Fe–L bond lengths, we can extend it from 1.95 Å to 2.20 Å (a span of 0.25 Å). The average Fe–L bond lengths can be experimentally or computationally obtained for ferryl complexes and correlated with their hydrogen-atom transfer (HAT) and oxygen-atom transfer (OAT) reactivity to develop a structure-reactivity relationship and used to model enzymatic intermediates.

It is likely that the oxoiron(IV) complex $[\text{Fe}^{\text{IV}}(\text{O})(\text{TQA})(\text{L})]^{2+}$ has longer average Fe–N bond lengths, as predicted by its computational model (2.15 Å). When a few oxoiron(IV) complexes' reactivity (represented by log of their second-order rate constants) is plotted against their available structural information (Figure 3.2), the computational model falls close to the line defined by those points, thus highlighting the validity of this a model, and also indicating the need to obtain more structural and reactivity information to establish this correlation further. This correlation has also been discussed in depth in Chapter 2.

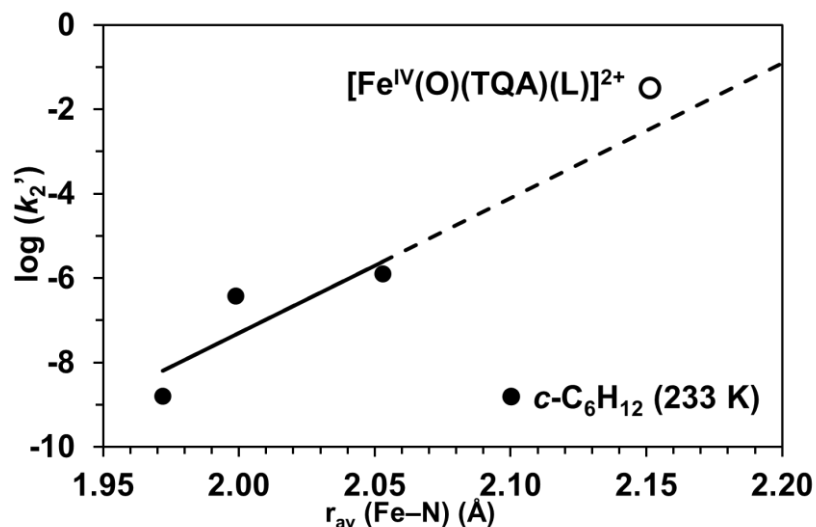


Figure 3.2 Correlation of $\log k_2'$ values of cyclohexane with the average length of Fe–N bonds in N4Py-based ferryl complexes (solid circles). The plot is extended to 2.20 Å to determine if this correlation holds true for the $S = 2$ complex [Fe^{IV}(O)(TQA)(MeCN)]²⁺, for which $r_{\text{average}}(\text{Fe–N})$ bonds is DFT-based.

We have sought to solidify this correlation by inclusion of additional Fe^{IV}(O) complexes supported by a different framework, namely BnTPEN (*N*-benzyl-*N,N',N'*-tris(pyridin-2-ylmethyl)ethane-1,2-diamine) to populate the correlation shown in Figure 3.2. The parent complex [Fe^{IV}(O)(BnTPEN)]²⁺ (**0**) is found to be an order of magnitude more reactive than [Fe^{IV}(O)(N4Py)]²⁺ in both hydrogen-atom and oxygen-atom transfer reactivity, and thus represents a reasonable starting point for making modified complexes based on this framework.¹⁴⁻¹⁵ This chapter examines seven new oxoiron(IV) complexes synthesized for this purpose and details the crystallographic description of two of these complexes, along with an examination of structure- and spectroscopy-reactivity relationships.

The complex **0** has been shown by NMR spectroscopy to have two of its three equatorial pyridine rings aligned parallel to the oxoiron(IV) unit and the third equatorial pyridine aligned perpendicular to the Fe^{IV}=O unit.¹⁶ This arrangement of perpendicular pyridine ring on the BnTPEN framework is responsible for its C_1 symmetry. It also enables investigation of role of the heterocycle orientation in the

reactivity of these oxoiron(IV) complexes. The lack of symmetry in **0** however, requires systematic introduction of substitutions, to avoid formation of mixtures. Herein, we replace complex **0**'s pyridines with different heterocycles, and introduce alpha-substituents on its pyridines (similar to the ones used by Snider *et al.*¹⁷) to obtain seven new complexes that tune ligand field strength of **0**, and try to obtain structural information wherever possible (Figure 3.3). The lack of symmetry also requires systematic introduction of these substituents to minimize possibility of forming isomeric mixtures (Figure 3.4). Therefore, *only* the perpendicular heterocycle, *both* the parallel heterocycles, or *all* three heterocycles are substituted to obtain the newer oxoiron(IV) complexes. This attempt at systematic modifications is not required for $[\text{Fe}^{\text{IV}}(\text{O})(\text{N4Py})]^{2+}$ and $[\text{Fe}^{\text{IV}}(\text{O})(\text{TMC})(\text{MeCN})]^{2+}$ (where TMC is a macrocyclic ligand), which both possess an $\approx C_{4v}$ symmetry.

Nomenclature used to define the complexes:

In this study, the complexes are numbered from **0** to **3**, to indicate the number of modifications made to the parent complex **0**, and the letters after the numbers indicate the type of modification (Figure 3.3). For example, **3-6Me** represents introduction of a 6-methyl substituent on all three pyridines; **2-Q** indicates substitution of the two pyridines parallel to the $\text{Fe}^{\text{IV}}(\text{O})$ unit with quinolines; and **1-B** indicates substitution of the pyridine perpendicular to the $\text{Fe}^{\text{IV}}(\text{O})$ unit with *N*-methylbenzimidazole on the BnTPEN framework. The structural and/or spectroscopic characterization of these complexes is accompanied by investigation into how their reactivity is affected by the arrangement of the heterocycles around the oxoiron(IV) center as well as how it enhances the scope of structure-reactivity and spectroscopic-reactivity relationships.

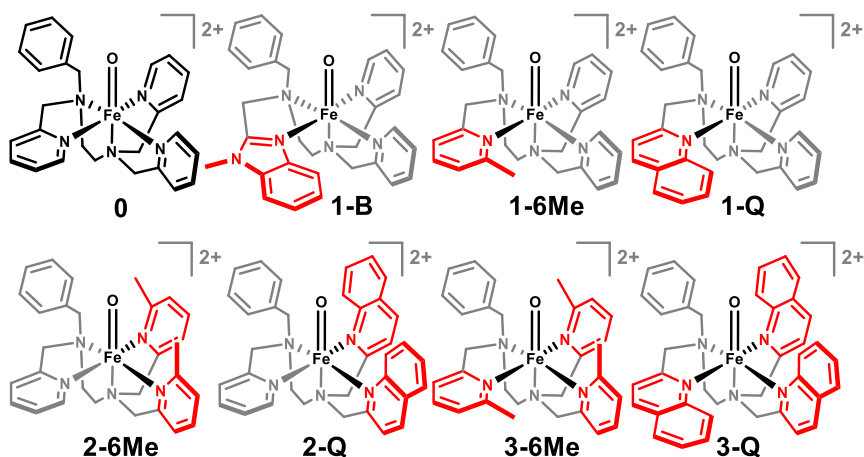


Figure 3.3 Oxoiron(IV) complexes based on BnTPEN framework investigated.

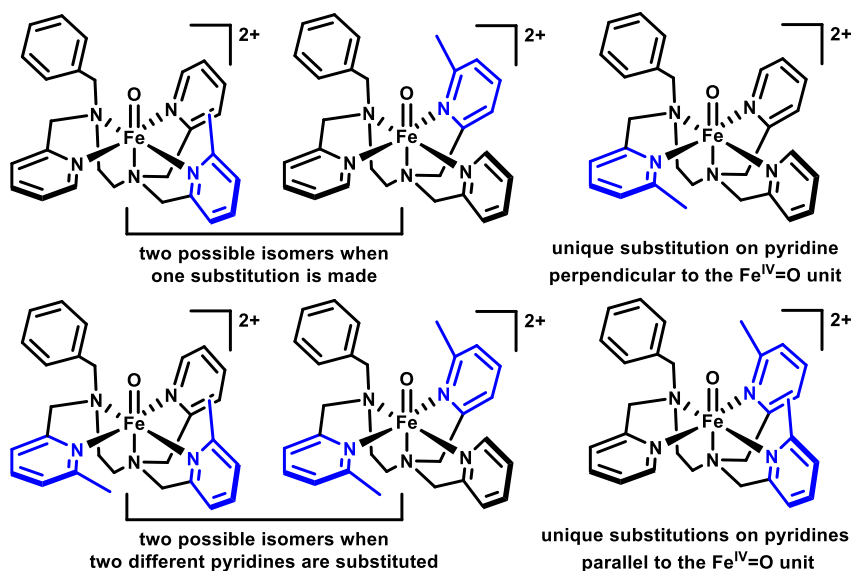


Figure 3.4 Strategy used to avoid isomeric forms in doubly and singly substituted oxoiron(IV) complexes, exemplified using **1-6Me** and **2-6Me**.

3.2 Results

The syntheses of the mono- and di-substituted ligands involve separate functionalization of the amines in ethylenediamine linkers of the BnTPEN framework. To selectively carry out the substitutions, a singly protected ethylenediamine (specifically *N*-acetyethylenediamine) is employed. To functionalize its unprotected amine, it is subjected to either reductive amination

with 2-substituted aldehydes of heterocycles (or benzaldehyde) or nucleophilic substitution with the 2-substituted methylchlorides of heterocycles. Once the two requisite arms are installed on the unprotected amine, the other amine is deprotected (with acid hydrolysis to remove the acetyl group) to reveal the other amine. This amine is then subjected to either nucleophilic substitutions or reductive amination again with the respective precursors (2-substituted aldehydes or 2-substituted methylchlorides of heterocycles). To synthesize the parent and the tri-substituted ligands, *N*-benzylethylenediamine is subjected to nucleophilic substitution with 2-substituted methylchlorides of heterocycles. The detailed syntheses, indicating the choice of base used for nucleophilic substitution, or the reducing agents used for reductive amination, are laid out in the experimental section.

The iron(II) precursors to oxoiron(IV) complexes are generated from the anaerobic mixing of the equimolar amount of ligands with iron(II) triflate in dichloromethane, and the solution is then concentrated and stirred in diethyl ether. After filtering and washing the solids formed with more diethyl ether, the salts are either further crystallized using slow diffusion of ether into concentrated dichloromethane solutions, or directly taken for further experimentation.

All the nonheme oxoiron(IV) complexes can be generated from solutions of iron(II) precursors in acetonitrile, using 1-2 equivalents of the oxidant 1-(*tert*-butylsulfonyl)-2-iodosylbenzene ((*t*BuSO₂)C₆H₄IO, or ArIO) dissolved in 2,2,2-trifluoroethanol, at appropriate temperatures. Some oxoiron(IV) complexes can also be generated by the oxidation of CH₃CN/H₂O iron(II) solutions using cerium(IV) ammonium nitrate, which can then precipitated out by treatment with sodium perchlorate. In some cases, crystals can also be obtained at 2-8 °C. See experimental section for more details.

3.2.1 Thermal Stability of the Ferryl Complexes

Table 3.1 lists the half-lives of 1-mM acetonitrile solutions of the ferryl complexes measured at room temperature, unless otherwise specified. Complexes **0** and **1-B** have comparable half-lives of 360¹⁴ and 270 minutes, respectively, while **1-6Me** and **1-Q** have $t_{1/2} \approx 25$ -30 minutes, which is a 10-fold decrease in thermal stability compared with **0**, which likely precludes their crystallographic characterization. Deuteration of all 11 benzylic protons in **1-6Me** increases its half-life to about 1 hour at room temperature, but still prevents its crystallization. When the rate of self-decay of deuterated complex **1-6Me-d₁₁** and non-deuterated **1-6Me-h₁₁** is followed, a KIE of 2.2 at 298 K can be obtained (Figure 3.5).

Table 3.1 Spectroscopic properties of ferryl complexes based on BnTPEN

Complex	0	1-B	1-6Me	1-Q	2-Q	2-6Me	3-6Me	3-Q
S	1	1	1	1	1	1	-	-
$\nu(\text{Fe=O}), \text{cm}^{-1}$	833	835	-	-	-	-	-	-
$\Delta E_Q, \text{mm s}^{-1}$	0.87	0.74	+1.00	+1.00	0.40	0.40	-0.40	-0.40
$\delta, \text{mm s}^{-1}$	0.01	0.03	0.04	0.04	0.09	0.09	0.17	0.17
D, cm^{-1}	23 (MB) 23.41(2) (FIRMS)	24.35(2) (FIRMS)	26(5)	30(5)	29(5)	29(5)	-	-
$\lambda_{\text{max}}, \text{nm}$	739	753	777	777	814, 1000	810, 1000	830, 1050	830, 1050
$\epsilon, \text{M}^{-1} \text{cm}^{-1}$	400	250	220	220	300, 350	250, 350		
$r(\text{Fe=O}), \text{\AA}$	1.653(1)	1.651(3)	1.611	1.65*				
av. $r(\text{Fe-N}), \text{\AA}$	2.0126	2.019	2.060	2.02* 2.059	2.06	2.059	S = 2 2.196 S = 1 2.088	S = 2 2.197 S = 1 2.087
$t_{1/2} (298 \text{ K}), \text{min}$	360	270	25	30	3	0.133 (<i>h₁₄</i>) 3 (<i>d₁₄</i>)	**1 (<i>h₁₇</i>) > 6 (<i>d₁₇</i>)	< **1
<i>All values in italics are DFT-derived. *Values obtained from XAS analysis. **Measured at 233 K. MB = Mössbauer, FIRMS = Frequency-domain magnetic resonance spectroscopy</i>								

Table 3.2 Spectroscopic properties of Fe^{IV}(O) complexes based on N4Py

Ligand L =	N4Py	N2py2B	sr ₂ N4Py	N2py2Q	6Me ₂ -N4Py	N4Py-6Me ₂	Ar ₂ N4Py
reference	14	11, 18	19	11	20	21	22
$\nu(\text{Fe}=\text{O}), \text{cm}^{-1}$	843	842	839	833	-	-	-
$ \Delta E_Q , \text{mm s}^{-1}$	0.93	1.36	-	0.56	0.62	-	0.54
$\delta, \text{mm s}^{-1}$	-0.04	-0.02	-	0.03	0.05	-	0.03
$\lambda_{\text{max}}, \text{nm}$	695	725	692	770	740	775	750
$\epsilon, \text{M}^{-1} \text{cm}^{-1}$	400	450	430	380	220 ²⁰ 340 ²¹	200	250
$r(\text{Fe}=\text{O}), \text{\AA}$	1.639(5)	1.656(4)	1.653(1)	1.677(5)	<i>1.619</i>	<i>1.654</i>	1.660(2)
av. $r(\text{Fe}-\text{N}), \text{\AA}$	1.972	1.999	1.981	2.053	<i>2.040</i>	<i>2.032</i>	2.014
$t_{1/2}, \text{min}$	3600	150	3000 (303 K)	150	14 ²⁰ 130 ²¹	30	-

DFT-derived values in italics.

In the singly substituted complexes, the sole pyridine perpendicular to the ferryl unit in **0** is replaced with a different heterocycle, namely an *N*-methylbenzimidazole, a quinoline or a 6-methylpyridine, and the 10-fold difference in thermal stability between **1-B** and **1-Q/1-6Me** contrasts with the case of [Fe^{IV}(O)(N4Py)]²⁺ family (Table 3.2), where the heterocycles are aligned parallel to the ferryl unit and quinoline or *N*-methylbenzimidazole substitutions result in complexes with similar half-lives (150 minutes).

The introduction of α -substituents on two pyridines parallel to Fe=O unit in **0** results in considerably unstable complexes, so that **2-6Me** and **2-Q** have respective half-lives of 8 seconds and 3 minutes at 298 K (Table 3.1). These disubstituted complexes are much more unstable than when two quinolines are introduced in [Fe^{IV}(O)(N4Py)]²⁺, which result in a 20-fold increase in thermal instability. Compared with **0**, **2-6Me** and **2-Q** experience a more than 100-fold increase in thermal instability. Deuteration of the 14 benzylic protons in **2-6Me** increases its half-life to 3 minutes, making it comparable to that of **2-Q**. When the rate of self-decay of deuterated complex **2-6Me-d₁₄** and non-deuterated complex **2-6Me-h₁₄** is followed, a KIE of 22 at 298 K can be obtained (Figure 3.5).

The different increase in half-lives (or thermal stability) upon deuteration of weakest C-H bonds in the ligands in the cases of **1-6Me** and **2-6Me** is remarkable, and the 10-fold difference in the KIE for the self-decay rates between two

complexes (**1-6Me** and **2-6Me**) can be explained by different proximity of the benzylic bonds in **1-6Me** and **2-6Me** to the oxoiron(IV) unit. (Figure 3.5).

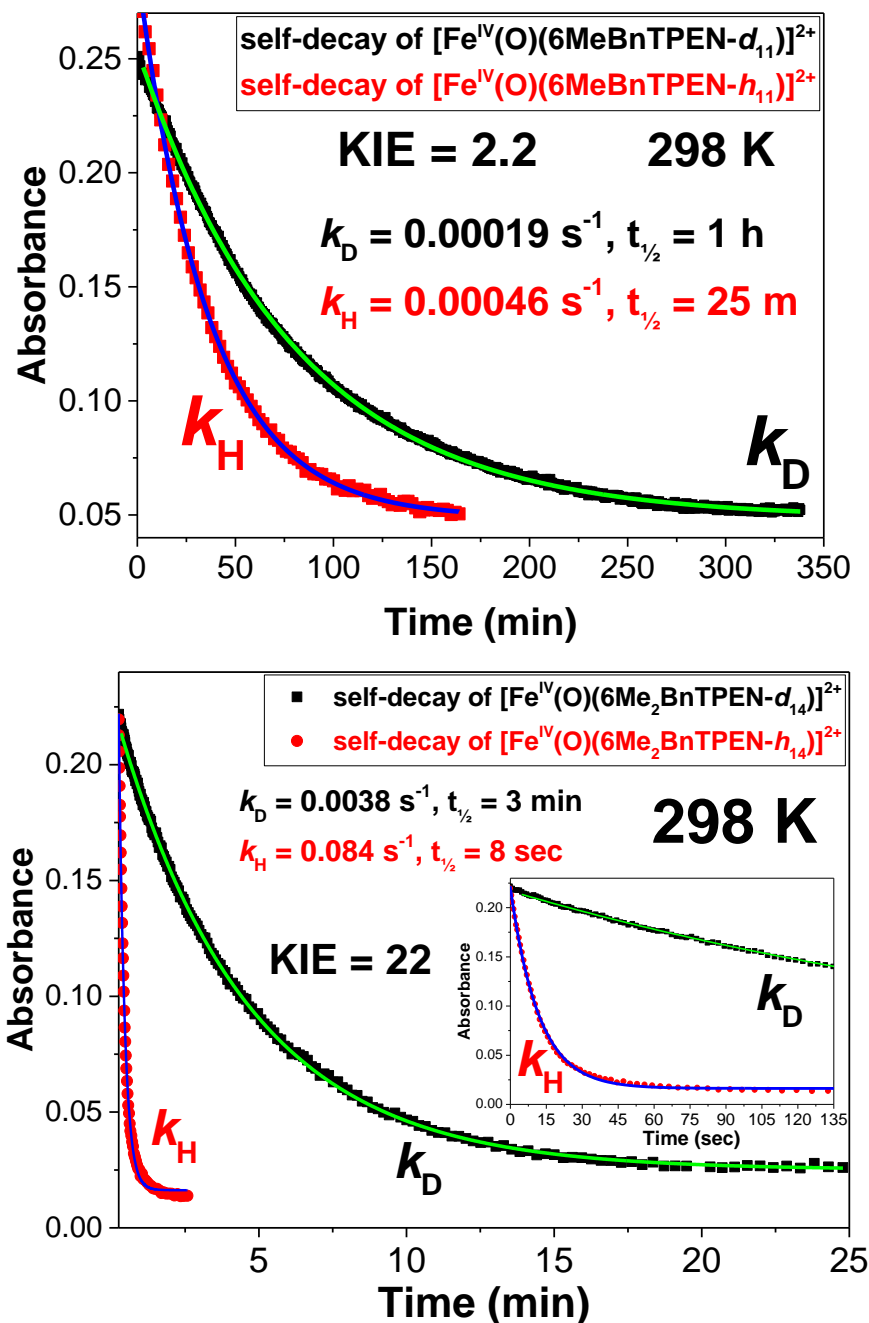


Figure 3.5 Absorption-time plots for self-decay of deuterated and non-deuterated complexes of **2-6Me** and **1-6Me** at different temperatures. Inset in the bottom picture zooms into the first two minutes of decay.

The introduction of the third alpha-substituent decreases thermal stability even further, so that the complexes **3-6Me** and **3-Q** are extremely short-lived at 298 K and cannot be observed. Deuteration of the 17 benzylic protons in **3-6Me-h₁₇** results in complex **3-6Me-d₁₇**. This enables this fleeting intermediate to be generated at 298 K, but its half-life is only about 10 seconds, and not long enough for us to be able to measure its reactivity at ambient temperatures. Therefore, we chose to lower the temperature to 233 K, to measure its reactivity. Both **3-6Me-h₁₇** and **3-Q** have longer half-lives of ≈ 1 minute at 233 K but are still very unstable. The deuterated **3-6Me-d₁₇** however lives long enough at this temperature ($t_{1/2} > 5$ min) so that its HAT reactivity can be obtained at 233 K.

3.2.2 Structural Characterization of Ferryl Complexes

The complexes **0** and **1-B** are the first set of completely C_1 -symmetric ferryl complexes to be crystallographically characterized. Both the complexes have two pyridines aligned parallel to the oxoiron(IV) unit, and an equatorial heterocycle aligned perpendicular to the oxoiron(IV) unit (Figure 3.6). All atoms of the perpendicular heterocycle in **0** and **1-B** are found to be in the mean plane defined by the four equatorial donor atoms.

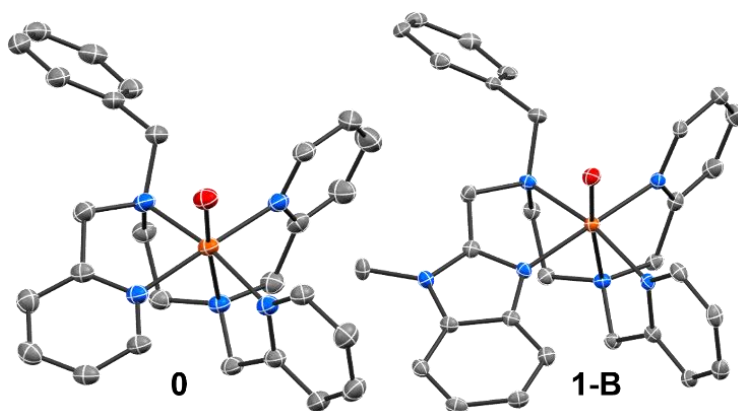


Figure 3.6 ORTEP plots of **0** and **1-B** with thermal ellipsoids at 50% probability. Counterions and hydrogen atoms have been removed for clarity.

The Fe=O bond lengths found for both **0** and **1-B** are comparable at 1.653(2) and 1.651(3) Å, and the longest bonds belong to the Fe—N_{am} bonds in both complexes

(2.045(2) to 2.096(3) Å), consistent with what is observed for all ferryl complexes.⁹ Interestingly, the benzimidazole donor in **1-B** has a very short Fe—N bond at 1.964(3) Å and exerts a trans effect on the equatorial pyridine, so that its Fe—N_{py} bond length is lengthened to 1.993(3) Å, as also seen in the case of the ferryl complex [Fe^{IV}(O)(N2Py2B)]²⁺, where two benzimidazole donors (Fe—N_{bnzlm} = 1.950-1.954 Å) exert a trans effect on the pyridines and increase their bond lengths very slightly (Fe—N_{trans-py} = 1.995-1.983 Å).¹¹ This is consistent with the higher basicity of benzimidazoles compared with pyridines.²³ In both **0** and **1-B**, the Fe—N_{py} bond lengths range from 1.962(3) to 1.993(3) Å, and the orientation of the equatorial pyridine around the ferryl center does not impact the Fe—N_{py} bond length. The average lengths of all five Fe—N bonds in **0** and **1-B** are also comparable at 2.013 and 2.019 Å, respectively. While the N_{am}-Fe-O angles are about 173.3° and 175.2° in **0** and **1-B**, respectively (which give rise to an apparent bending of the ferryl unit), no tilt is induced by the presence of ligands on the ferryl units, as evidenced from their almost ideal orthogonality with the mean plane formed by equatorial ligands.

The average Fe—N bond lengths of the parent complex **0** (at 2.013 Å) rises slightly when one pyridine is replaced with *N*-methylbenzimidazole in **1-B** (2.019 Å). When a single pyridine is replaced with quinoline in **1-Q**, it is expected that the average Fe—N bond lengths will rise even further, due to the steric hindrance introduced between the H8 protons of quinoline perpendicular to the ferryl unit, and the mean plane of the pyridine, which would increase the quinoline's Fe—N bond. However, a crystal structure to demonstrate this effect could not be obtained. When the quinoline is parallel to the ferryl unit, as observed in the case of [Fe^{IV}(O)(N2Py2Q)]²⁺, the average Fe—N bond lengths rise by about 0.08 Å compared with those in [Fe^{IV}(O)(N4Py)]²⁺. However, [Fe^{IV}(O)(N2Py2Q)]²⁺ has two quinolines, and **1-Q** has one. In the absence of crystal structure, we must rely on a DFT-optimized *S* = 1 structure, which predicts an average Fe—N bond length = 2.065 Å, about 0.04 Å higher than those in **1-B** and **0**.

Table 3.3 Bond metrics (in Å) of BnTPEN-derived ferryl complexes

Complexes	0	1-B	1-Q DFT S = 1	1-6Me DFT S = 1	2-Q DFT S = 1	2-6Me DFT S = 1
$r(\text{Fe}=\text{O})$	1.653(2)	1.651(3)	1.611	1.611	1.618	1.615
aver. $r(\text{Fe}-\text{N})$	2.0126	2.019	2.065	2.0602	2.06	2.0594
$r(\text{Fe}-N_{\text{am}}(\text{ax}))$	2.083(2)	2.096(3)	2.131	2.128	2.082	2.087
$r(\text{Fe}-N_{\text{am}}(\text{eq}))$	2.045(2)	2.080(3)	2.023	2.025	2.046	2.050
$r(\text{Fe}-N_{\perp})$	1.987(2)	1.964(3)	2.181	2.164	2.059	2.056
$r(\text{Fe}-N_{\parallel})$	1.983(2) 1.965(2)	1.993(3) 1.962(3)	2.002 1.988	2.000 1.984	2.082 2.031	2.065 2.039

3.2.3 Spectroscopic Characterization of Ferryl Complexes

3.2.3.1 UV-visible Spectroscopy

Complexes **1-B**, **1-Q** and **1-6Me** exhibit near-IR absorption bands characteristic of d-d transitions that have been identified previously for other tetragonal oxoiron(IV) complexes, such as $[\text{Fe}^{\text{IV}}(\text{O})(\text{N4Py})]^{2+}$ by Decker *et al.*²⁴ These bands are red-shifted from those of the parent complex **0** at $\lambda_{\text{max}} = 739$ nm to $\lambda_{\text{max}} = 753$ nm for **1-B**, and to 777 nm for both **1-Q** and **1-6Me**. The parent complex **0** also has a shoulder at 860 nm, which red-shifts to 890 nm for **1-B** and 930 nm for both **1-Q** and **1-6Me** (Figure 3.7). The red-shifted bands indicate a weakened ligand field. The extinction coefficients of the major bands found for these complexes at 298 K in acetonitrile are about 200-250 $\text{M}^{-1} \text{cm}^{-1}$, almost half of the value associated with the parent complex **0** ($\epsilon = 400 \text{ M}^{-1} \text{cm}^{-1}$), as shown in Table 3.1.

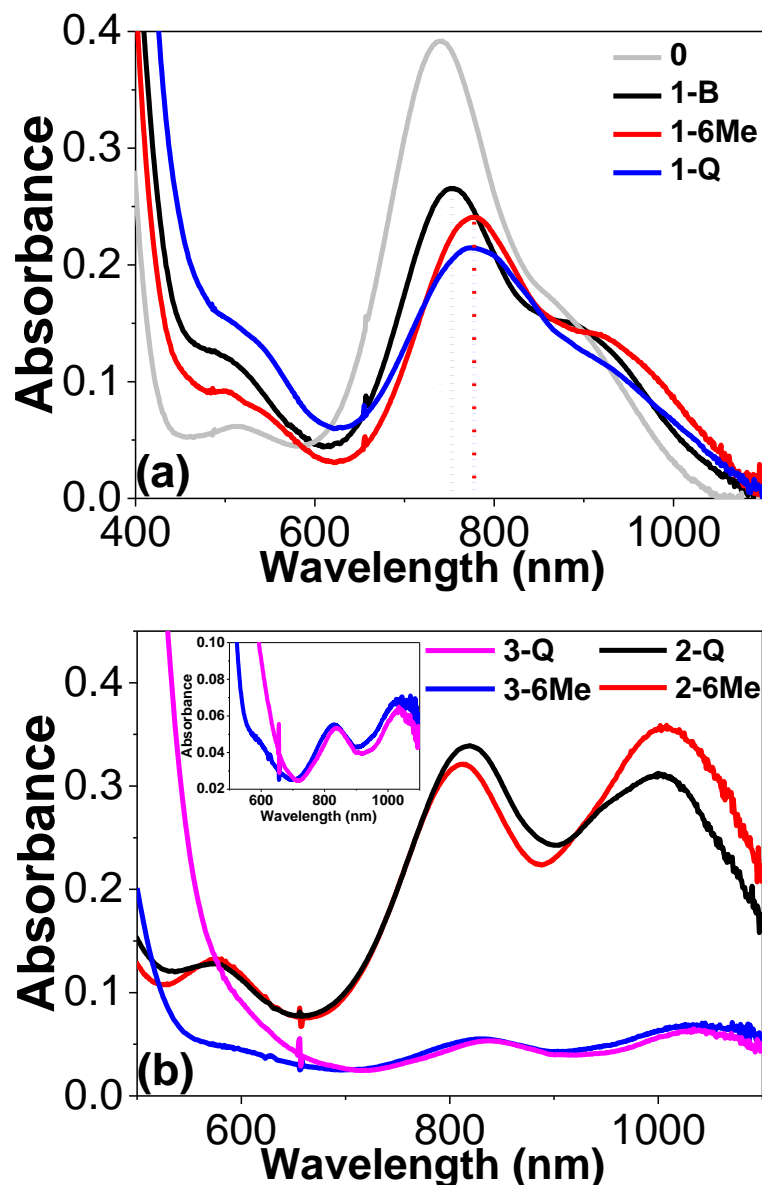


Figure 3.7 Absorption spectra of mono-substituted (a), and disubstituted and trisubstituted (b) oxoiron(IV) complexes examined in this chapter.

2-6Me and **2-Q** have d-d absorption bands even more resolved into distinct features around ≈ 580 , 810-820 and 1000 nm (Figure 3.7), similar to those in $[\text{Fe}^{\text{IV}}(\text{O})(\text{TMC})(\text{X})]^+$.²⁵⁻²⁶ The near-IR bands around 800 nm and 1000 nm have extinction coefficients around $300\text{-}350 \text{ M}^{-1} \text{ cm}^{-1}$ at room temperature in acetonitrile. Compared with the singly substituted complexes, the bands at 810 nm of **2-6Me** and **2-Q** are red-shifted by 30 nm, and over 70 nm when compared with

the parent complex. This red-shift in the bands clearly represents even further weakening of the ligand field, which also makes these complexes drastically unstable at room temperature. Both the bands in complexes **2-6Me** and **2-Q** are even more red-shifted when new alpha-substitution is introduced, so that the resulting complexes **3-6Me** and **3-Q** have $\lambda_{\max} = 835$ nm and 1035 nm. The extinction coefficients cannot be obtained for these complexes, because parallel Mössbauer experiments which would indicate the concentration of actual oxoiron(IV) complex, were not successful.

In the N4Py framework, when the pyridines are replaced with quinolines or *N*-methylbenzimidazoles, there is no significant change in extinction coefficients measured in acetonitrile at room temperature. However, upon introduction of these modifications on BnTPEN framework, extinction coefficients of mono-substituted complexes under the same conditions are almost halved (see Table 3.1), and in disubstituted and trisubstituted complexes, the extinction coefficients are lower than the parent complex.

3.2.3.2 Vibrational Spectroscopy

The oxoiron(IV) complexes examined in this series exhibit a vibrational stretch characteristic for such complexes. These data are typically measured through FTIR, resonance Raman or NRVS spectroscopy. Because solid samples of both complexes **0** and **1-B** can be accessed, the solid-state FTIR spectra (Figure 3.8) of both **0** and **1-B** show comparable $\nu(\text{Fe}=\text{O})$ stretches at 833 cm^{-1} and 835 cm^{-1} . Replacement of equatorial pyridines with benzimidazoles on ferryl complexes with multidentate ligand frameworks such as N4Py and BnTPEN does not alter the vibrational stretch observed, regardless of whether the benzimidazole is oriented perpendicular or parallel to the ferryl unit (see Table 3.1 and 3.2). This observed insensitivity may be due to the lack of steric interactions with the oxo unit imposed by these heterocycles. Other compounds in this series can only be prepared as solutions, but exhibit intense fluorescence in their resonance Raman spectra, thus preventing detection of the vibrational stretch associated with the ferryl complexes.

1-Q (like **1-B**) is not expected to have any interaction with the ferryl unit and would not show significant deviation in the ferryl vibration. However, when quinoline heterocycles are aligned parallel to the ferryl unit, a steric interaction likely exists with the ferryl unit (as also seen in the case of crystallographically characterized $[\text{Fe}^{\text{IV}}(\text{O})(\text{N}2\text{Py}2\text{Q})]^{2+}$), and we can expect a change in vibrational stretch, although experimental verification is needed.

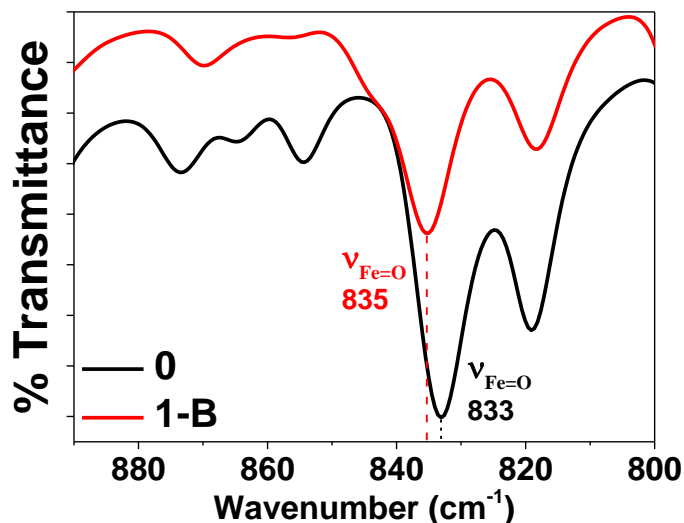


Figure 3.8 FTIR spectra of **0** and **1-B** complexes.

3.2.3.3 Mössbauer Spectroscopy

The 4.2 K Mössbauer spectra of unlabeled **1-B** solid, and Fe-57-enriched, 1-mM frozen solution samples of **1-Q**, **1-6Me**, **2-6Me** and **2-Q** in acetonitrile show that the samples consist of over 80% oxoiron(IV) species. These complexes reveal an $S = 1$ spin manifold when magnetic fields up to 70 kG are applied, similar to that reported for the parent complex **0**.¹⁴ High-spin ferric ($S = 5/2$) components were first subtracted based on the magnetized six-line feature. The inner magnetized features were then simulated using an $S = 1$ Hamiltonian (for the major ferryl species) and an $S = 0$ Hamiltonian (a minor di-ferric contaminant). The experimental spectra and simulations of $S = 1$ species are plotted in Figure 3.9. All the simulation parameters of these species are shown in Tables 3.1 and 3.2.

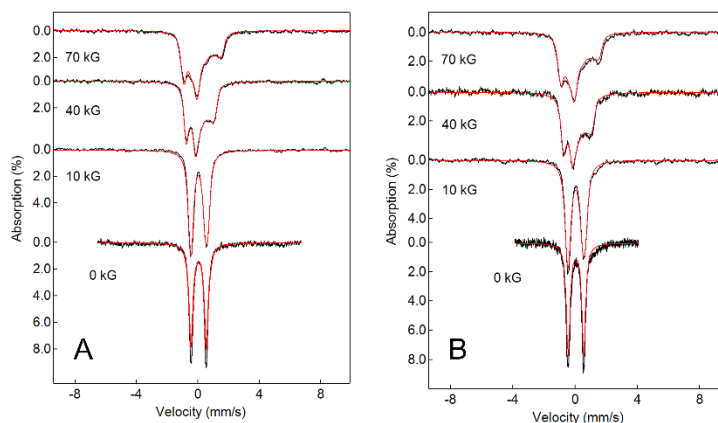


Figure 3.9 Mössbauer spectra and corresponding simulation of samples at 4.2 K with various external magnetic fields. (A) **1-6Me** (14% HS-ferric subtracted); (B) **1-Q** (18% HS-ferric subtracted) The black traces represent the experimental spectra (0kG: raw spectra; 10-70 kG, raw spectra after removing high-spin ferric), and the red traces represent the simulation contributed by $S = 1$ species only. Ruixi Fan performed these experiments.

Variable-field and variable temperature studies are not carried out on **0** and **1-B** to determine its zero-field-splitting parameter (zfs) D or confirm its spin state. The zfs parameter D indicates contribution of excited spin states into the ground spin state, which is usually correlated with higher reactivity of complexes. Because of a dearth of accurate D values and the fact that correlation doesn't necessarily imply causation. D values are instead determined using a combination of HFEPR and FIRMS spectroscopy. The D value for complex **0** and **1-B** is 23.41 cm^{-1} and 24.35 respectively and are less than 1 cm^{-1} apart.

Complexes **1-B**, **1-6Me** and **1-Q** have higher isomer shifts than 0.01 mm/s in **0**. These values are consistent with those observed for typical $S = 1$ oxoiron(IV) complexes.⁶ While the magnitude of the quadrupole splitting decreases in going from **0** to **1-B**, it rises in going from **0** to **1-Q** and **1-6Me** (see Table 3.1), indicating that **0** and **1-B** have greater electronic symmetry compared to those of **1-Q** and **1-6Me**.

The isomer shifts further rise to 0.09 mm/s in **2-6Me** and **2-Q**, and the quadrupole splitting decreases from $+1.00 \text{ mm/s}$ in **1-Q/1-6Me** to 0.40 mm/s . The zfs

parameters obtained from Mössbauer spectroscopy for all complexes are within error of each other. Between di-substituted and mono-substituted complexes, the modifications are made on different parts of the ligand, and thus effects on the zfs parameters may not show a systematic trend of increasing D value upon introduction of each of the subsequent modifications. Furthermore, because the variable field experiments were done only at 4.2 K, there is a relatively larger uncertainty in the D value parameters. Given that D values do not change drastically, Mössbauer spectroscopy may not be able to distinguish between D values of these complexes.

3.2.4 Computed Spin State Splitting Energies of Ferryl Complexes

For the series of oxoiron(IV) complexes bearing differently substituted BnTPEN ligands, spin-state splitting energies were computed for the $S = 1$ and $S = 2$ spin states. The introduction of steric bulk in the α -position leads to a systematic decrease in the calculated spin-state splitting energies and ultimately leads to the prediction of high-spin ground states for the complexes having multiple substitutions. As can be seen from Table 3.4, the inclusion of zero-point vibrational energies (ZPE) leads to a decrease in the spin-state splitting energies, an effect described previously in the literature.²⁷⁻²⁸ A plot of the computed spin state splitting energies reveals a direct correlation with the number of substitutions made and the spin state splitting energies (Figure 3.10). It should be noted that the introduction of α -Me-groups in the 6-position of the pyridine substituents or replacement with quinoline (Q) groups results in comparable changes to the spin state splitting energies. Based on the computational studies herein, **3-Q** and **3-6Me** are predicted to be high-spin complexes, although in the absence of any experimental data, we refrain from making absolute spin state assignments.

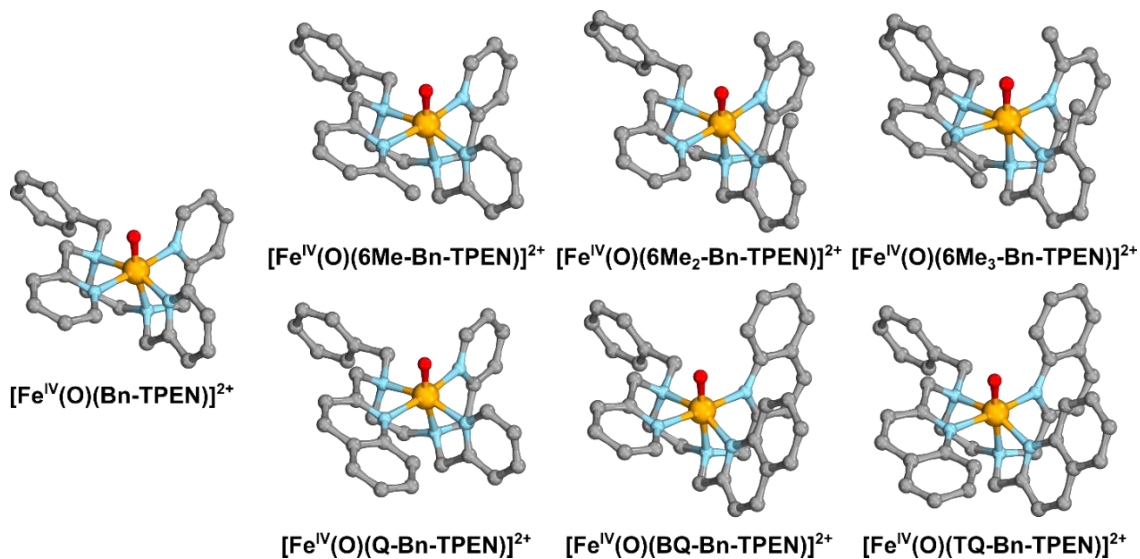


Figure 3.10. Structures calculated for oxoiron(IV) complexes in the $S = 1$ spin state. Geometries were obtained at the PW6B95/def2-TZVP level of theory in the gas phase. Depictions were made using IboView.²⁹⁻³⁰

Table 3.4 Computed spin state splitting energies at the PW6B95/def2-TZVP level of theory, obtained by Dr Johannes Klein.

Complex	$\Delta E(\text{Q-T})$ [kcal mol ⁻¹]	$\Delta E_{\text{ZPE}}(\text{Q-T})$ [kcal mol ⁻¹]
0	3.5	2.3
1-6Me	1.4	0.2
2-6Me	-0.3	-1.5
3-6Me	-3.4	-4.7
1-Q	0.9	-0.2
2-Q	-0.8	-1.9
3-Q	-3.7	-4.8

All calculations were performed using Turbomole v7.0.1,³¹⁻³³ with the PW6B95 functional³⁴ and the def2-TZVP basis set.³⁵ All calculations were carried out in the gas phase and numerical second derivatives were computed to confirm that a minimum was reached, showing no imaginary frequencies. For ZPE corrections small frequencies ($< 100 \text{ cm}^{-1}$) were raised to 100 cm^{-1} .³⁶⁻³⁷ Calculations were accelerated by the MARI-J approach³⁸ using Weigend's fitting basis sets.³⁹ Grid m5 was used throughout.

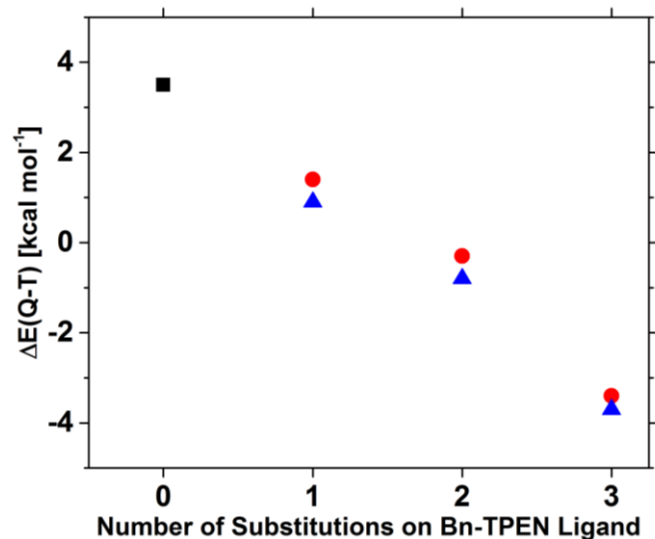


Figure 3.11 Plot of the computed spin state splitting energies at the PW6B95/def2-TZVP level of theory versus the number of substitutions made to the BnTPEN ligand framework. The black square shows the reference value for the unsubstituted ligand; red dots refer to 6Me substitutions and blue triangles correspond to quinoline substitutions.

3.2.5 Reactivity of Ferryl Complexes

Table 3.5 lists the second order rate constants obtained for the reactions of oxoiron(IV) complexes with different substrates at given temperatures.

Table 3.5 HAT and OAT reactivity of BnTPEN-substituted ferryl complexes at 298 K unless otherwise specified.

Second order rate constants (k_2), measured at 298 K, given in $M^{-1} s^{-1}$							
Substrates	0	1-B	1-6Me	1-Q	2-6Me	2-Q	*3-6Me
TPM	0.083	0.23	0.99	3.2	6.2	9.2	1.9
Cumene	0.042	0.042	0.034	0.069	6.2	3.6	3.1
Ethylbenzene	0.069	0.035	0.13	0.1	2.9	1.8	2.1
Toluene	0.0089	0.0057	0.0252	0.031	0.45	0.18	0.23
2,3-DMB	8.1×10^{-4}	0.0035	0.023	0.031	1.1	0.97	0.24
<i>c</i> -C ₆ H ₁₂	3.9×10^{-4}	0.0012	0.011	0.025	0.41	0.29	-
<i>c</i> -C ₆ H ₁₂ (233 K)	1.6×10^{-7}	2.3×10^{-7}	-	3.0×10^{-5}	-	1.2×10^{-4}	0.066
PhSMe (233 K)	0.0025	0.068	1.7	3.6	270	390	-

*All rates for **3-6Me** measured at 233 K owing to its instability at 298 K. All OAT rates measured at 233 K. Other 233 K HAT rates obtained from Eyring analyses.

Reactivity of mono-substituted oxoiron(IV) complexes

Complexes **1-Q** and **1-6Me** introduce a quinoline or 6-methylpyridine in **0** to replace the pyridine that lies perpendicular to the Fe=O unit, resulting in more reactive oxoiron(IV) complexes. This increase in reactivity resembles that seen for $[Fe^{IV}(O)(N4Py)]^{2+}$ with similar substitutions (Figure 3.12). Interestingly, **1-B** is mostly comparable to **0** in its HAT reactivity but is about 30 times faster at OAT to thioanisole than **0**. However, compared to **0**, **1-6Me** and **1-Q** are at least 2-3 orders of magnitude higher in their OAT reactivity, and an order of magnitude faster in their HAT reactivity.

Figure 3.12 illustrates these interesting reactivity results for **1-B**, **1-Q** (or **1-6Me**), showing correlations of $\log k_2'$ values (where k_2' is k_2 divided by the number of equivalent substrate C-H bonds that can be attacked) versus the C-H bond dissociation energy for the complexes with the N4Py and the BnTPEN frameworks. These plots reveal reasonably linear correlations for the three sets of data in each

framework, as observed previously for a number of oxoiron(IV) complexes. The rate differences among the three complexes in each series become larger for substrates with stronger C–H bonds, resulting in a progressive decrease in the slopes in going from the parent complex **0** to the complexes with benzimidazole and quinoline substituents. In the N4Py series, the heterocycles are roughly aligned parallel to the oxoiron(IV) unit, whereas in the BnTPEN series, mono-substituted complexes have the modified heterocycle aligned perpendicular to the ferryl unit. When the oxoiron(IV) complexes in the two frameworks are compared together, it appears that oxoiron(IV) complexes containing quinolines have increased HAT rates of reaction regardless of their orientation relative to the ferryl unit. However, oxoiron(IV) complexes containing benzimidazoles have higher HAT rates when they replace the pyridines are oriented parallel to the ferryl unit, but when they replace the pyridines oriented perpendicular to the ferryl unit, their HAT reactivity does not change compared with the parent complex.

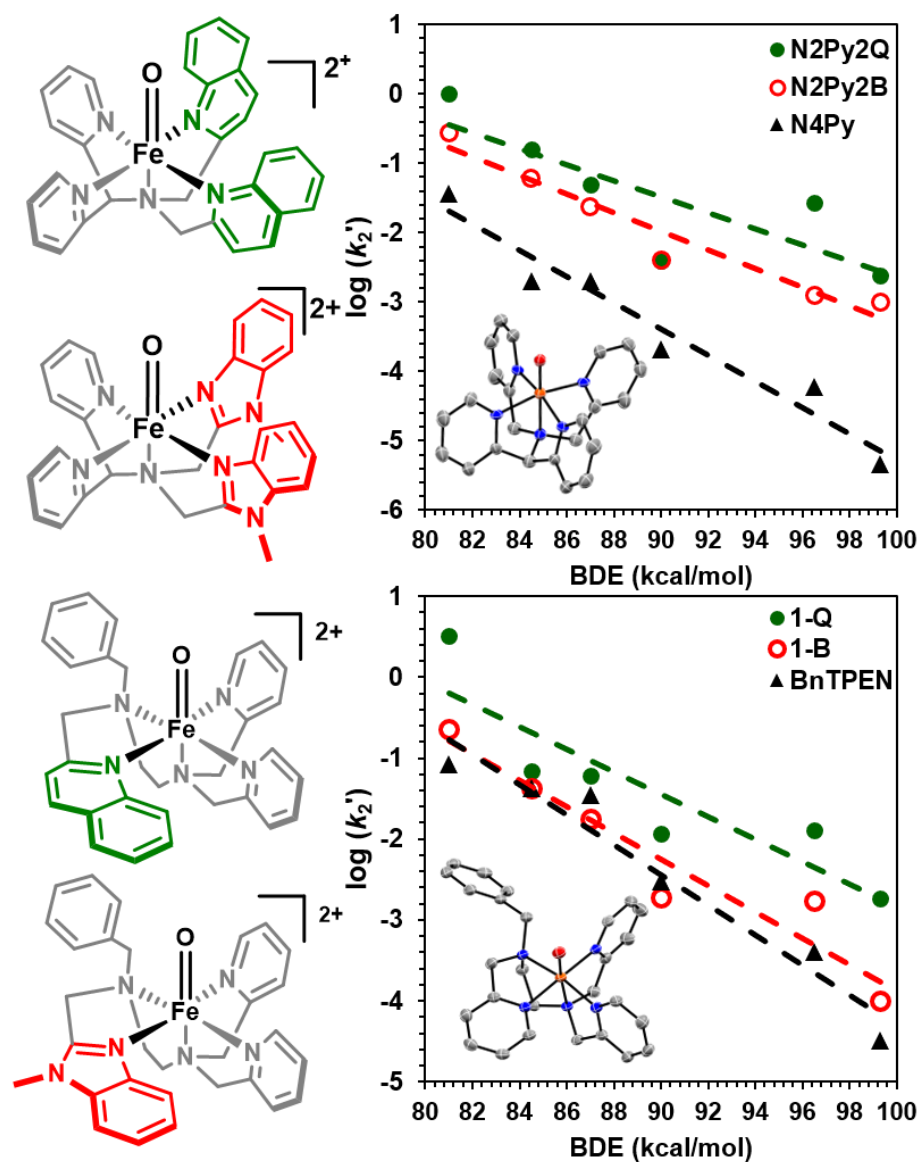


Figure 3.12 Evans-Polanyi plots showing HAT reactivity of compounds with benzimidazole (green) and quinoline (red) modifications in different orientations around the ferryl center using N4Py (top) and BnTPEN (down) frameworks.

Reactivity of di- and tri-substituted oxoiron(IV) complexes

The ferryl complex **2-Q** abstracts hydrogen atoms from C-H substrates at a rate which is at least an order of magnitude faster than **1-Q**. As an example, in going from complexes **0** to **1-Q** to **2-Q** at 298 K, the second order rate constants (k_2) with cyclohexane increase by 1:50:750. **2-Q** therefore has the highest HAT rates at 298 K reported for any ferryl complex. Similarly, **2-Q** transfers its oxygen atom to thioanisole at 233 K at least two orders of magnitude faster than **1-Q**. Therefore, in going from **0** to **1-Q** to **2-Q** the rate constants for OAT to thioanisole change even more dramatically than those for HAT, with the ratio 1:1000:100,000 at 233 K. In fact, the OAT rates are so high that **2-Q** requires the use of a stopped-flow instrument to accurately determine these second-order rate constants.

The same patterns of HAT and OAT reactivity ratios (seen for **0**, **1-Q**, and **2-Q**) are observed when 6-methylpyridine substitutions are made on the parent complex **0** to form the complexes **1-6Me** and **2-6Me**, as shown by their second-order rate constants (k_2) with cyclohexane, thioanisole and other substrates (Table 3.5). Figure 3.13 shows the correlation of the $\log k_2'$ values (where k_2' is k_2 divided by the number of equivalent substrate C-H bonds that can be attacked) versus the C-H bond dissociation energy for complexes with increasing number of 6-methylpyridines for complex **0**, **1-6Me** and **2-6Me**, which reveals reasonably linear correlations for the three sets of data in this framework, all measured at 298 K.

The thermal instability of **3-6Me** and **3-Q** ($t_{1/2}$ of a few seconds at 298 K) prevents measurement of the second-order rate constants for their reactions with substrates at room temperature. However, when benzylic positions in the ligand framework of **3-6Me** are deuterated, it is stabilized long enough at 233 K to enable determination of these k_2 values. To draw comparisons with the parent complex **0** as well as mono- and di-substituted complexes, second-order rate constants for their reactions with substrates need to be determined at 233 K. We have found that the second-order rate constants for the reactions of cyclohexane with oxoiron(IV)

complexes supported by N4Py-based ligands vary by about 3 orders of magnitude between 298 K and 233 K.¹¹ To establish this further, we extrapolated the second-order rate constant for the reaction of **0** with cyclohexane at 233 K from its Eyring plot and found that **0** reacts with cyclohexane about 2400 times faster at 298 K than at 233 K. Similarly, further Eyring analyses of the reactions of cyclohexane separately with **1-B**, **1-Q** and **2-Q** reveal that their rates of reaction with cyclohexane are over 1000 times faster at 298 K than at 233 K.

With the observation that the second-order rate constants for reactions of oxoiron(IV) complexes with cyclohexane are 3 orders of magnitude higher at 298 K than at 233 K, the log k_2' values of reaction of **3-6Me** with substrates measured at 233 K are increased by 3 units and may be plotted on Figure 3.13, although a rigorous Eyring analysis has not been performed for all the substrates. Even so, we used cyclohexane as our conservative model, because its C-H bonds have high bond dissociation energy, and it shows this pattern of increased reactivity as a result of more substitutions for a series of complexes at room temperature.

Conversely, the availability of the HAT reactivity of **0**, **1-B**, **1-Q**, and **2-Q** with cyclohexane at 233 K can also help draw comparisons of second-order rate constants with **3-6Me** for which this rate is only available at 233 K. Thus, we find that at 233 K there is a 400,000-fold increase in the reaction rate of cyclohexane between **0** and **3-6Me**. Given that di-substituted and mono-substituted oxoiron(IV) complexes with quinolines or 6-methylpyridines are comparable in their rates of reaction with substrates, the rates of reaction with cyclohexane at 233 K in going from **0** to **1-Q** (or **1-6Me**) to **2-Q** (or **2-6Me**) to **3-6Me** would be in the ratio 1:200:750:400,000. Within the same ligand framework that supports oxoiron(IV) units, such an increase in rates of HAT reactions of oxoiron(IV) complexes has not been demonstrated before. Unfortunately, complexes **3-6Me** and **3-Q** were incredibly fast in their reactions with thioanisole so their second-order rate constants could not be optimized and determined using stopped-flow instrument.

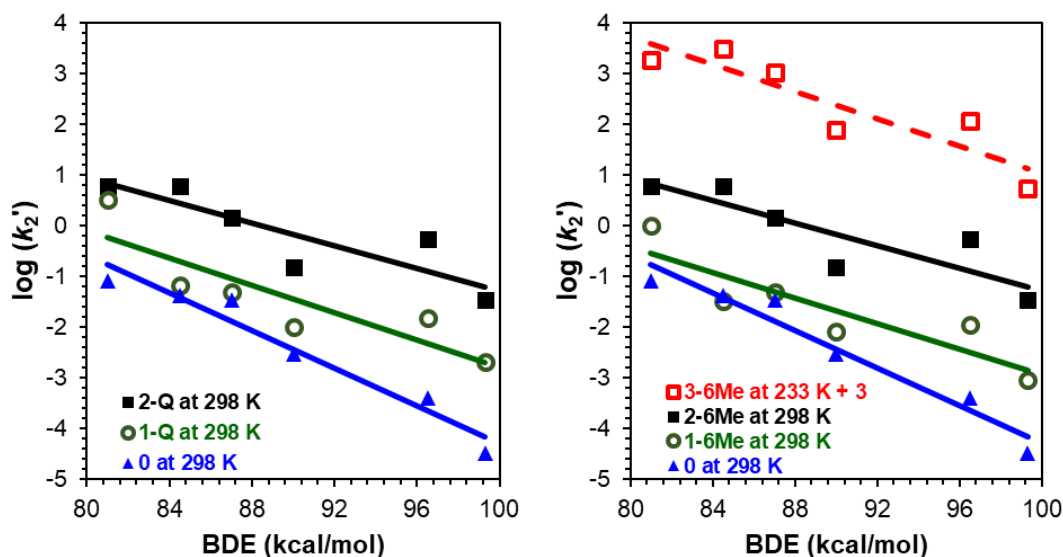


Figure 3.13 Evans-Polanyi plots showing the reactivity increase observed for oxoiron(IV) complexes when quinolines replace the pyridines (left), or α -methyl substituents (right) are introduced on each pyridine in the BnTPEN ligand. The **3-6Me** rates are increased by 3 log units to adjust for the 65 K difference in temperature at which they were obtained. Similar trends in HAT reactivity are observed for ferryl complexes with quinoline substitutions in this series.

3.3. Discussion

The BnTPEN framework uniquely enables exploration of not only the number and the types of substitutions, but also their orientations around the oxoiron(IV) unit. These differences are reflected in the spectroscopic and reactivity properties observed for the resulting newer complexes. The effects on the properties are discussed with comparisons to oxoiron(IV) complexes based on N4Py (explored in Chapter 2) where appropriate.

Effects on UV-Visible-NIR Spectral Features

All three types of modifications introduced on the parent complex **0** result in the weakening of the ligand field, as evidenced by the red-shift of their near-IR chromophores (indicated by their λ_{\max} values). The red-shift in λ_{\max} is dependent on the number of substituents introduced as well as the type of substitutions made. In general, more substitutions lead to larger red-shifts in the near-IR bands of the

oxoiron(IV) complexes, and in turn further weakening of the ligand field. Introduction of one alpha-substituent (6-methyl group on pyridine, or replacement of the pyridine with a quinoline) on **0** red-shifts its λ_{\max} value by 38 nm (as shown in Figure 3.7). Two alpha-substituents further red-shift the λ_{\max} values, but the two near-IR features in the electronic absorption spectra now become resolved so that two λ_{\max} values are observed in di-substituted complexes, similar to the TMC-based $\text{Fe}^{\text{IV}}(\text{O})$ complexes with axial anionic ligands.^{25, 40} This pattern persists with the introduction of the third alpha-substituents, but the red-shifts of the λ_{\max} values are somewhat less drastic when compared with the change observed between di-substituted and the mono-substituted complexes. This trend shows that the heterocycles oriented parallel to the Fe=O unit have a bigger effect than those that are perpendicular to the Fe=O unit. A similar effect is observed for the $[\text{Fe}^{\text{IV}}(\text{O})(\text{N4Py})]^{2+}$ series, where there is a red-shift of roughly 75 nm per two quinolines introduced.^{11, 21} Note however, in $[\text{Fe}^{\text{IV}}(\text{O})(\text{N4Py})]^{2+}$ complex the alpha-substituents were introduced as a pair rather than one at a time. The effects of introducing alpha-methyl groups on pyridines in $[\text{Fe}^{\text{IV}}(\text{O})(\text{N4Py})]^{2+}$ are the same as the effects of replacing the corresponding quinolines. All in all, the red-shift in the absorption features increases when a greater number of substitutions is introduced.

In addition to the number of substitutions, the nature of the substituent also affects the magnitude of the red-shift in the λ_{\max} values. **1-B** ($\lambda_{\max} = 753$ nm) with a single *N*-methylbenzimidazole shows a much smaller red-shift in the λ_{\max} value (about 14 nm) than **1-Q** ($\lambda_{\max} = 777$ nm) with one quinoline (about 38 nm) when compared with **0** (Table 3.1, $\lambda_{\max} = 739$ nm). While additional *N*-methylbenzimidazoles were not introduced on **0**, their systematic introduction into $[\text{Fe}^{\text{IV}}(\text{O})(\text{N4Py})]^{2+}$ has been investigated by Nordlander and coworkers, and the λ_{\max} value red-shifts by 10-15 nm per *N*-methylbenzimidazole introduced.¹⁸ A similar red-shift of 15 nm per *N*-methylbenzimidazole is observed in $[\text{Fe}^{\text{IV}}(\text{O})(\text{TPA})(\text{L})]^{2+}$ (TPA = tris(2-pyridylmethyl)amine, $\lambda_{\max} = 724$ nm) when all the pyridines are replaced by *N*-methylbenzimidazoles to form $[\text{Fe}^{\text{IV}}(\text{O})(\text{Me}_3\text{NTB})(\text{L})]^{2+}$ (Me₃NTB = tris(*N*-

methylbenzimidazol-2-yl)methyl)-amine, $\lambda_{\text{max}} = 770 \text{ nm}$).⁴¹ However in this case, the substitution was made all at once, rather than step by step. So on average, in TPA, N4Py and BnTPEN frameworks, the λ_{max} value of the oxoiron(IV) complexes red-shifts by 10-15 nm per *N*-methylbenzimidazole introduced versus about 40 nm per alpha-substituent (quinoline/6-methylpyridine) introduced, indicating that the latter weaken the ligand field more than *N*-methylbenzimidazole. Interestingly, the red-shift of the λ_{max} values is only dependent on the type or the number of modifications, but not the orientations of these heterocycles. This is exemplified by the results of these modifications on oxoiron(IV) complexes supported by TPA, N4Py and BnTPEN frameworks, in which BnTPEN contains differently oriented heterocycles but its modification results in red-shifts similar to those seen from modifying heterocycles parallel to the ferryl unit. Therefore, the orientation of the heterocycle does not appear to have a significant effect on the red-shift in the electronic absorption bands.

Structural Aspects of Modified Oxoiron(IV) Complexes

Examination of structural effects from increasing the number of substitutions in complex **0** is hampered by the thermal instability of the disubstituted and trisubstituted ferryl complexes, which has precluded their crystallographic characterization. This outcome is likely due to the many benzylic protons on the BnTPEN ligand and its substituted analogs that are prone to hydrogen atom abstraction by the reactive ferryl units they support. This is further exemplified by over 20-fold increase in lifetimes of these complexes when these protons are deuterated. So experimental attempts to study structural changes in oxoiron(IV) complexes with more than one substituents (via their solid-state structures) have not been successful. However, the parent complex **0** and one of its three monosubstituted variants (**1-B**) have been crystallographically characterized, and they enable examination of the type of substitutions made on **0** to some extent.

Among the mono-substituted complexes, the solid-state structures of **0** and **1-B** differ only slightly in the average length of all Fe-N bonds, which are 2.013 Å and

2.019 Å, respectively. For comparison, the DFT-optimized structure of **1-Q** in the $S = 1$ spin state has been obtained (see Section 3.2.4), and interesting information can be gleaned from it. For example, the average Fe-N bond length is longer (2.065 Å, see Table 3.3), and unlike the perpendicular heterocycle in the solid-state structures of **0** and **1-B**, the quinoline in the DFT-optimized structure of **1-Q** is not found to be in the plane defined by the mean equatorial donor nitrogen atoms (Figure 3.14 and Figure 3.10), likely because its H8 atom is closer to the nearest pyridine parallel to the ferryl unit, and encounters steric hindrance from it.

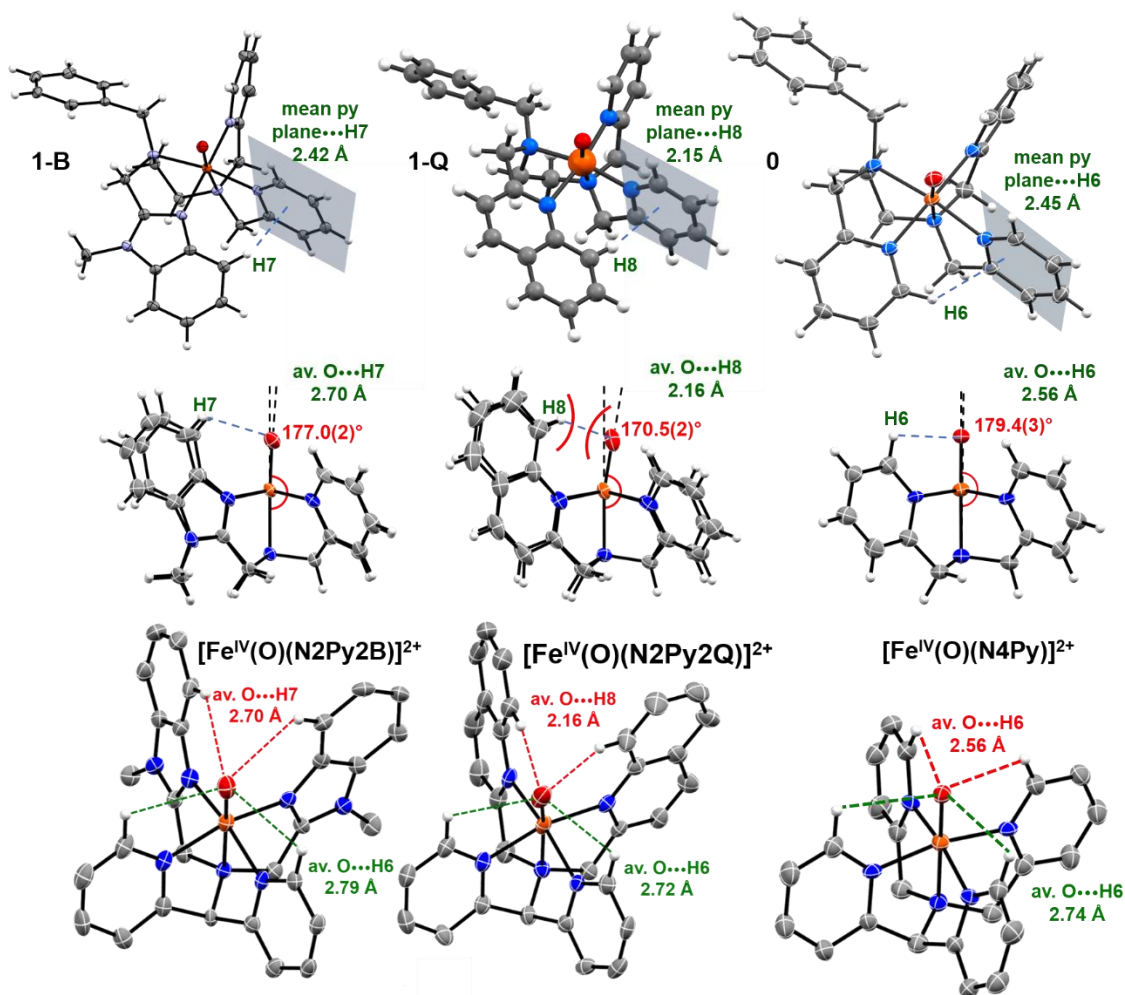


Figure 3.14 Steric interactions of proximal hydrogen atoms in different ferryl complexes. Top: top-view of 50% ORTEPS of **1-B**, **1-Q** (DFT structure) and **0** shown from left to right, with a mean plane drawn on the pyridine with which distance of the proximal H atom is measured. Middle: front-view of N4Py based complexes, with distance of the proximal atoms with the oxygen atom. Bottom: side-view of N4Py-based complexes, showing tilts induced by the ligands on the ferryl unit.

The normalized H8 proton of the quinoline heterocycle in the $S = 1$ DFT-optimized structure of **1-Q** is found to be 2.15 Å away from the plane of the closest pyridine parallel to the ferryl unit (Figure 3.14, top center), which increases the Fe-N_{quinoline} bond length to 2.18 Å, an almost 0.2 Å increase in length compared with that seen in **0** from the perpendicular pyridine. In the crystal structure of $[\text{Fe}^{\text{IV}}(\text{O})(\text{N}2\text{Py}2\text{Q})]^{2+}$, the quinoline H8 protons are found to be about 2.16 Å (when C–H bond lengths are normalized, this distance is 2.05 Å) away from the oxygen atom, which results in a tilted ferryl unit (as detailed in Chapter 2). In the DFT-optimized structure of **1-Q**, the H8 atom of quinoline is 3.9 Å away from the oxygen atom because of its perpendicular orientation, and therefore there are no steric interactions between this proton and the ferryl unit, unlike what was found in the structure of $[\text{Fe}^{\text{IV}}(\text{O})(\text{N}2\text{Py}2\text{Q})]^{2+}$. Similarly in **0**, the H6 atom of the perpendicular pyridine is 3.6 Å away from the oxygen atom, and in **1-B** the H7 atom of the perpendicular *N*-methylbenzimidazole is 4.1 Å away, so there are steric interactions that would affect the oxoiron(IV) unit. In fact, the mean plane defined by the equatorial ligands and the ferryl unit in **1-B** and **0** are almost orthogonal to each other.

The BnTPEN framework is not as rigid as N4Py, and therefore it is possible that the flexibility provided by the ethylene diamine linkers in this framework may allow the heterocycles more leeway to reduce the steric interactions that 6-methylpyridines or quinolines would have with the oxygen in the ferryl unit. Indeed, in the DFT-optimized structures of $S = 1$ complexes **2-6Me** and **2-Q** the quinolines and the 6-methylpyridines are found to be torsionally rotated around the N-Fe axis and this rotation likely compensates for the steric interactions with the ferryl unit.

Similar torsional rotations are seen in the tri-substituted complexes, which are even less stable than **2-Q** and **2-6Me**.

In general, the structural features (observed from the bond metrics of the crystallographic and *in silico* DFT-optimized structures of modified Fe^{IV}(O) complexes in both N4Py and BnTPEN frameworks) indicate a weakening of the ligand field. These features show an increased average Fe–N bond length that correlates with the red-shifts observed in their λ_{max} values (Table 3.1 and Table 3.3).

Effects of Alpha-Substituents on Ferryl Vibrations

The effects of the number of substitutions and the type of substitutions on the Fe=O stretch could not be probed for all the oxoiron(IV) complexes in the BnTPEN series. This is because of the intense fluorescence observed in frozen solution state in all the complexes. However, as both **0** and **1-B** can be isolated as solids, vibrational data could be obtained from FTIR spectroscopy. Interestingly, the $\nu(\text{Fe}=\text{O})$ vibrations shown in Figure 3.8 for **0** and **1-B** are comparable to each other at around 833-835 cm⁻¹. In this case the pyridine replaced in **0** is perpendicular to the ferryl unit. Even when the pyridines and the *N*-methylbenzimidazoles (replacing the pyridines) are parallel to the ferryl unit, as seen in the case of [Fe^{IV}(O)(N4Py)]²⁺ and [Fe^{IV}(O)(N2Py2B)]²⁺, the $\nu(\text{Fe}=\text{O})$ vibrations at 842-843 cm⁻¹ do not change significantly (Table 3.2), indicating that the introduction of an *N*-methylbenzimidazole to replace pyridines in any orientation does not affect the bond strength of the ferryl unit.

When the quinoline substituent replaces pyridines in [Fe^{IV}(O)(N4Py)]²⁺, the steric hindrance of quinolines likely weakens the Fe=O bond, as observed from the longer Fe=O bond in the crystal structure of [Fe^{IV}(O)(N2Py2Q)]²⁺ and its smaller $\nu(\text{Fe}=\text{O})$ stretch. In **1-Q** the quinoline modification is not expected to have direct steric interactions with the ferryl unit, and so it would not be expected to influence $\nu(\text{Fe}=\text{O})$ just like the case of **1-B**, but in the absence of crystallographic and

vibrational data, a possible conclusion is difficult to draw for any alpha-substituted oxoiron(IV) complexes in the BnTPEN series.

Effects of Substitutions on Reactivity of the Oxoiron(IV) Complexes

The reactivity of the resulting new oxoiron(IV) complexes generally increases with the number of pyridines in **0** that are modified or replaced. This trend is in line with the overall increased electrophilicity of the iron(IV) center, as substantiated by the increased Fe–N bond lengths and the red-shifted near-IR chromophores. In fact some of the more reactive intermediates require use of a stopped-flow instrument to reliably measure the OAT rates to thioanisole at 233 K. These complexes also exhibit HAT rates that are the highest reported to date at 298 K (Table 3.5).

In addition to the number of substitutions, reactivity is also modulated by the *type* of heterocycle introduced on the ligand frameworks (in the same way they affect absorption features of these complexes), and its *orientation* relative to the Fe=O unit.

The introduction of one or two alpha-substituents in **0** increases its HAT reactivity by roughly an order of magnitude per alpha-substituent introduced, and is independent of the type and the orientation of the modified heterocycles, because the alpha-substituents' proximal hydrogen atoms enforce steric hindrance on different parts of the BnTPEN ligand framework to result in longer Fe–N bonds, whether the modified heterocycles are aligned parallel or perpendicular to the Fe^{IV}=O unit. Unfortunately, introduction of three alpha-substituents makes the resulting complexes **3-Q** and **3-6Me** extremely unstable with half-lives of a few seconds only at room temperature, so that we are unable to measure the rate constants under these conditions with the instruments at our disposal. We can measure these rates for deuterated **3-6Me** at 233 K and, after extrapolation of the second-order rate constant for cyclohexane oxidation by **0** to 233 K using the Eyring plot, we find that there is a 5 orders of magnitude difference in these rates! So, both the quinoline and the α -methyl substitutions on pyridines (independent of

their orientation) are found to affect the OAT and HAT reactivity comparably in the BnTPEN series.

However, when one *N*-methylbenzimidazole is introduced on **0**, it does not affect the OAT and HAT reactivity as much. As an example, **1-B** is just an order of magnitude faster in OAT to thioanisole than **0**, but **1-Q** and **1-6Me** are up to 3 orders of magnitude faster than **0** in OAT to thioanisole. **1-B** and **0** are similar in their HAT reactivity, and an order of magnitude less reactive than **1-6Me** and **1-Q**. So the *type* of substitutions can play an important role in determining the reactivity of the molecules. These differences in observed reactivity are also complicated by the orientation of heterocycles, as explained below.

Although an *N*-methylbenzimidazole aligned parallel to the ferryl unit has not been introduced in **0**, it has been introduced in this orientation by Mitra *et al.* in $[\text{Fe}^{\text{IV}}(\text{O})(\text{N4Py})]^{2+}$.¹⁸ The orientation of *N*-methylbenzimidazoles when introduced in **0** and $[\text{Fe}^{\text{IV}}(\text{O})(\text{N4Py})]^{2+}$ has different effects on the HAT reactivity of resulting complexes when compared with their corresponding parent complexes. After examination of the reactivity in the BnTPEN and N4Py frameworks, we can conclude that *N*-methylbenzimidazole aligned perpendicular to the ferryl unit does not impact HAT reactivity significantly, but when it is aligned parallel to the ferryl unit, it increases OAT and HAT reactivity of the resulting oxoiron(IV) complexes. The orientation of the *N*-methylbenzimidazole therefore needs to be explored further. Possible aspects to consider could include the differences in donicity of the heterocycles, as well as access to the ferryl unit in the complexes.

A perusal of the crystal structures of both **0** and **1-B** in the BnTPEN framework reported herein reveals that pyridine H6 and *N*-methylbenzimidazole H7 protons of perpendicular heterocycles in these complexes are about 2.42-2.45 Å away from the mean plane defined by the pyridine parallel to the ferryl unit (Figure 3.14), which is where the steric interactions would be expected to occur. In $[\text{Fe}^{\text{IV}}(\text{O})(\text{N4Py})]^{2+}$ and $[\text{Fe}^{\text{IV}}(\text{O})(\text{N2Py2B})]^{2+}$ however, the steric interactions of the heterocycles could occur directly between corresponding pyridyl H6 and *N*-

methylbenzimidazolyl H7 protons, and they do have slightly different proximities to the ferryl unit. However, this difference is not enough to warrant the huge changes seen in reactivity based on orientation, and a more rigorous analysis is needed to probe the structural and electronic effects of *N*-methylbenzimidazoles in the reactivity of the complexes.

The half-lives of the complexes examined in this series changes at ambient conditions from hours to minutes to seconds for some of the most reactive complexes. This has not been demonstrated before for reactive compounds. The stability of some of the complexes can be improved upon deuteration of the benzylic protons. This increase in stability is not unprecedented, as it enabled our group to report the first crystal structure of an $S = 2$ ferryl complex.⁴² Moreover deuteration of benzylic positions on a ligand that supports one of the best water oxidation catalysts has been recently demonstrated to result in an improvement of its turnover frequency.⁴³ Some C-H bond activation catalysts based on similar frameworks also show an increased robustness in catalysis.⁴⁴ The approaches we have used to deuterate the benzylic positions of complexes in this chapter are different from the reported methods and are arguably cheaper and easier, as detailed in the experimental section. Nevertheless, the increased half-lives of oxoiron(IV) complexes upon deuteration of their ligands' benzylic positions have allowed the measurement of their rate constants with different substrates at ambient conditions.

Deuteration of the α -methyl protons and other benzylic protons in the complexes **1-6Me** and **2-6Me**, and following the self-decay rate for each of the complexes shows a 10-fold higher kinetic isotopic effect in **2-6Me** compared with **1-6Me**. This can be explained by closer proximity of the ferryl unit to the α -methyl groups in **2-6Me** compared with **1-6Me**. The self-decay of **2-6Me** likely proceeds via an intramolecular HAT mechanism, whereas the 2-fold increase in stability represented by a 2.2 KIE of self-decay in **1-6Me** can be attributed to contributions from some intermolecular attack of the ferryl unit. In **3-6Me**, the self-decay of the

normal **3-6Me** is so fast that it only fleetingly exists at room temperature, and the room temperature half-life of **3-6Me** with deuterated benzylic protons is about 10 seconds. This demonstrates that increasing the number of benzylic positions in **2-6Me** by introduction of another alpha-methyl group on the remaining pyridine makes the resulting complex **3-6Me** quite unstable, so that it is quite difficult to obtain it in high yields at higher temperatures and hence examine reactivity.

3.3.1 Correlation of Structure and Reactivity

The oxoiron(IV) complexes supported by pentadentate ligands described in this chapter cover a wide ground in terms of OAT and HAT reactivity. The structural data for some of the oxoiron(IV) complexes supported by pentadentate ligands enable their correlations with the reactivity trends observed for these complexes. We first reported a structural correlation of oxoiron(IV) complexes with reactivity in Chapter 2, using average length of Fe-N bonds and the logarithms of rate constants with cyclohexane (to represent HAT) and thioanisole (for OAT). However, this correlation was limited to three complexes, and applied to systematic changes only in the N4Py framework. The wide range of reactivity available with BnTPEN framework is ideally suited to expand this correlation of structure with reactivity. Figure 3.15 expands this correlation to generalize it to more oxoiron(IV) complexes with different types of ligand fields, and a vast range of oxidative reactivity. This correlation now includes complexes in the BnTPEN, TMC, TPA and N4Py frameworks, variants of which together comprise more than half of the 90 or so synthetic oxoiron(IV) complexes reported so far. Such a correlation is needed because there is a general dearth of structural data available for oxoiron(IV) complexes, and the inclusion of experimental points from different frameworks further grounds this correlation.

This correlation is defined by complexes for which experimental average Fe-L bond length is available, either from their solid-state structures or XAS spectroscopy. As seen from the correlation of HAT reactivity, most of the points fall close to the line. The unstable compounds without solid-state structural

information have been included by using their DFT-optimized structures in the appropriate spin states (as determined by Mössbauer spectroscopy) and shown as hollow dots or squares. All the rate constants used in this correlation were obtained at 233 K, either by directly measuring the rates at those temperatures, or by using Eyring analyses. We did not use the available rate constant of complex **3-6Me**'s reaction with cyclohexane, because its spin state could not be determined, and DFT-optimized structures of these complexes in different spin states have very different bond lengths.

The complex $[\text{Fe}^{\text{IV}}(\text{O})(\text{Me}_3\text{NTB})(\text{L})]^{2+}$ is an important exception in the HAT correlation, in that it has an average Fe-N bond length of 2.06 Å (as confirmed via EXAFS analysis recently by Banerjee *et al.*⁴⁵), but is one of the most reactive oxoiron(IV) complexes reported to date.^{41, 46-47} Its rate of reaction with cyclohexane is about the same as that of the $S = 2$ complex $[\text{Fe}^{\text{IV}}(\text{O})(\text{TQA})(\text{L})]^{2+}$. However, when we plot this rate against the average of its Fe-N bond lengths, it is found to be 3 log units higher (or 3 orders of magnitude faster) in its rates of reaction with cyclohexane than predicted by its bond metrics. Interestingly, the other benzimidazole-containing pentadentate ligands that support oxoiron(IV) complexes are closer to the line and react as expected with cyclohexane. Recently, an oxomanganese(IV) complex supported by a benzimidazole rich complex has also been shown to defy the expected trends in reactivity.⁴⁸ It is possible that additional effects are at play with these complexes. Thus, benzimidazole-rich complexes need to be further explored for their HAT reactivity, and possibly thermodynamic factors at play in addition to the structural correlations should also be examined to establish a fuller picture of the reactivity landscape painted for these oxoiron(IV) complexes in different ligand fields.

The rate of OAT to thioanisole by the complex $[\text{Fe}^{\text{IV}}(\text{O})(\text{Me}_3\text{NTB})(\text{L})]^{2+}$ is the fastest reported so far ($k_2 = 21000 \text{ M}^{-1} \text{ s}^{-1}$).⁴¹ The original report did not provide the plot of rates versus concentrations to support this amazing value. In our efforts to reproduce this work, we obtained a much lower second-order rate constant of $k_2 =$

940 M⁻¹ s⁻¹ for this complex, which is 20-fold slower than reported. We also determined an OAT rate to thioanisole of 1940 M⁻¹s⁻¹ for [Fe^{IV}(O)(TQA)(L)]²⁺ and found that it was lower than expected by this correlation.

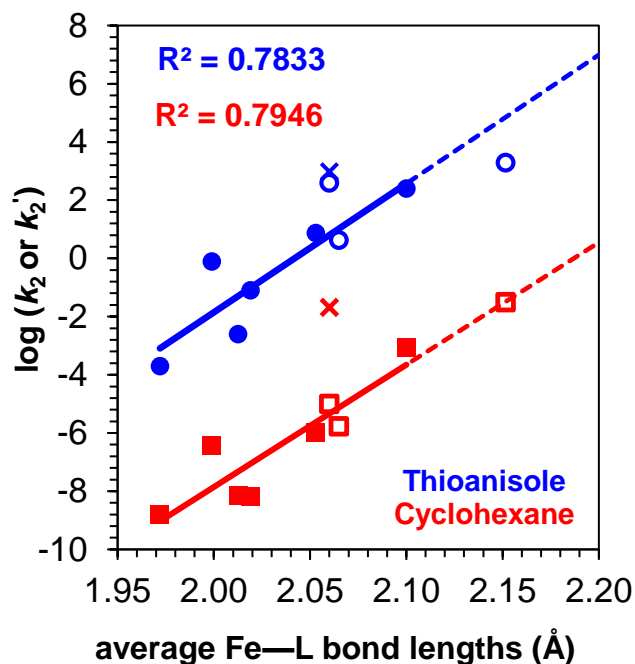


Figure 3.15 Correlation of reactivity (obtained from second-order rate constants at 233 K with cyclohexane and thioanisole) with average Fe–L bond lengths of different complexes. From left to right, ligands supporting Fe^{IV}(O) complexes are N4Py, N2Py2B, BnTPEN, B-BnDPEN, Q-BnDPEN, N2Py2Q, DQBnPEN, Me₃NTB (represented by a **x**), TMC-O, and TQA. Hollow shapes represent DFT-obtained structural data, whereas solid ones represent experimental data. *All rate constants determined using stopped-flow instrument were obtained by our collaborator at Tufts University, Marc C. Piquette.*

Except for the complexes [Fe^{IV}(O)(TQA)(L)] and [Fe^{IV}(O)(Me₃NTB)(L)], the experimental HAT rates correlate well with the DFT-predicted average Fe–N bond lengths found for most of the complexes.

3.3.2 Correlation of Spectroscopy and Reactivity

Interestingly, the series of complexes supported by BnTPEN and N4Py frameworks also provide a remarkable correlation of reactivity with spectroscopic properties. The most obvious correlation can be seen with UV-vis bands

represented by λ_{\max} for $S = 1$ oxoiron(IV) complexes (Figure 3.16). As these bands correspond to the d-d transitions of the Fe=O unit, a longer wavelength and a lower energy indicate a weakened ligand field that gives rise to a more electrophilic and therefore more reactive oxoiron(IV) complex. So a larger red-shift can represent a more reactive ferryl complex in this series of ferryl complexes supported by pentadentate ligands. Another measure of overall spectroscopic change is the Mossbauer isomer shift, which also becomes more positive with increased reactivity of these complexes, as seen in Figure 3.16.

All the rates were obtained at 233 K in the correlation and form a particularly remarkable fit of HAT reactivity with isomer shifts for complexes supported by different ligand frameworks! The point with the highest isomer shift belongs to $[\text{Fe}^{\text{IV}}(\text{O})(\text{TQA})]^{2+}$ which is a functional and spectroscopic model of enzymatic intermediate TauD-J and possesses an $S = 2$ spin state. Such a correlation with reactivity has not been shown before for Mössbauer parameters and allows us to use Mössbauer spectroscopy to possibly predict reactivity and vice versa.

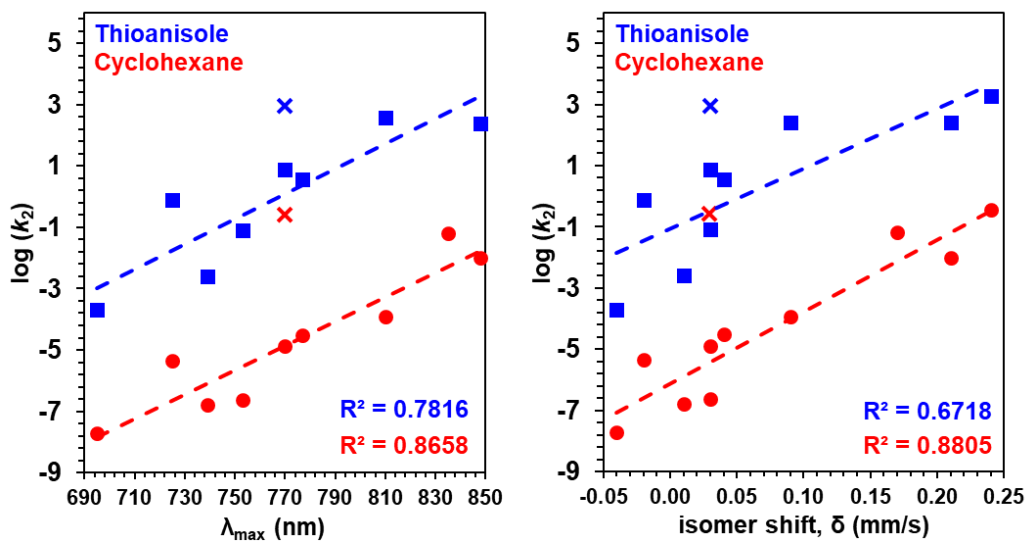


Figure 3.16 Correlation of oxoiron(IV) complexes' λ_{\max} (plotted only for $S = 1$ complexes) and isomer shifts with their reactivity, supported by ligand frameworks from left to right: N4Py, N2Py2B, BnTPEN, B-BnDPEN, N2Py2Q, Q-BnDPEN, DQBnPEN, TMCO, TQA. Crosses belong to $[\text{Fe}^{\text{IV}}(\text{O})(\text{Me}_3\text{NTB})(\text{L})]^{2+}$, blue shapes to thioanisole and red shapes to cyclohexane.

3.4 Conclusion

In conclusion, this series of oxoiron(IV) complexes supported by pentadentate ligands represent a systematic modification on donors on the polydentate ligand frameworks of N4Py and BnTPEN, encompassing reaction rates that span at least 7 orders of magnitude (with OAT). The vast range of reactivity reflects a difference in the average Fe-L bond length of just over 0.2 Å (where to find?). We demonstrate this remarkable correlation for the first time for a family of ferryl complexes. Within this spectrum of average Fe-N bond lengths, we also observe a change in spin states from $S = 1$ to $S = 2$, as we approach the reported reactivity of enzymatic nonheme $\text{Fe}^{\text{IV}}=\text{O}$ intermediates, which all have been shown to have $S = 2$ spin states.

In going from **0** to **1-6Me** to **2-6Me**, we obtain the highest rates of reaction with cyclohexane and other HAT substrates that are reported at room temperature for any ferryl complex (1:30:740). This trend also applies to the HAT rates for cyclohexane in going from **0** to **1-Q** to **2-Q**, with a 1:50:750 ratio of increasing rates.

Furthermore, correlation of reactivity with isomer shifts is unprecedented, and remains valid across N4Py and BnTPEN frameworks, which are relatively different from each other. Our crystallographic data in this report also provides the first examples of completely ferryl complexes with no symmetry whatsoever, and probes their reactivity with established complexes, to lay out foundations of a landscape on which different ferryl modifications are made. It also allows us to probe for the first time the effects of orientation of benzimidazole on reactivity and spectroscopy. We also highlight the different types of heterocycles and how they play a role in the determination of reactivity and spectroscopic properties of the oxoiron(IV) complexes.

3.5 Experimental Section

Instrumentation:

^1H NMR spectra were recorded on a Bruker 400 or 500 MHz spectrometer at 298 K, unless otherwise stated. Elemental analyses were carried out by Atlantic Microlab (Norcross, GA). UV-vis spectra were recorded on a HP8453A diode array spectrometer equipped with a cryostat from Unisoku Scientific Instruments (Osaka, Japan), which permits monitoring of the temperature of the experiments from -90 to 100 °C. All UV-vis spectra were measured in 1 cm quartz cell. Electrospray ionization mass spectrometry (ESI-MS) experiments were performed on a Bruker BioTOF II mass spectrometer using a spray chamber voltage of 4000 V and a carrier gas temperature of 200 °C. Mössbauer spectra were recorded with two spectrometers, using Janis Research (Wilmington, MA) SuperVaritemp dewars that allow studies in applied magnetic fields of up to 7.5 T in the temperature range from 1.5 to 200 K. A LakeShore Model 331A temperature controller was used to control the temperature in experiments. Mössbauer spectral simulations were performed using the WMOSS software package (SEE Co, Edina, Minnesota). Isomer shifts are quoted relative to α -Fe metal at 298 K. The spectra were plotted by SpinCount developed by Prof. Michael Hendrich at Carnegie Mellon University.

Materials:

All solvents and chemicals were purchased from Sigma-Aldrich or TCI Chemicals, and used without further purification unless otherwise stated. All liquid HAT substrates were passed through a plug of silica or alumina before use. Triphenylmethane was crystallized from ethanol, and its stock solution was made in deuterated dichloromethane. Thioanisole was either used neat, or its stock solutions prepared in acetonitrile. All iron(II) complexes were synthesized under the inert atmosphere of nitrogen or argon. $\text{Fe}^{\text{II}}(\text{OTf})_2 \cdot 2\text{CH}_3\text{CN}$ was prepared according to the published procedure.⁴⁹ All oxygen and moisture sensitive compounds were synthesized in a nitrogen-filled glovebox.

3.5.1 Syntheses and Characterization

3.5.1.1 Synthesis of ligands

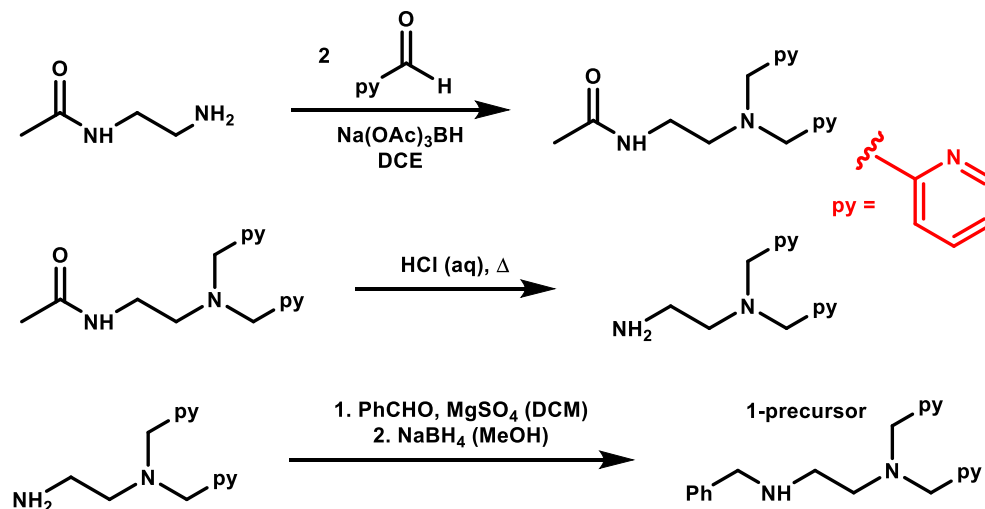
The parent ligand and triply substituted ligands:

The ligand BnTPEN was synthesized as reported.⁵⁰ Its trisubstituted variants 6Me₃BnTPEN and BnTQEN, were synthesized using a method adapted for the parent BnTPEN ligand, and required nucleophilic substitution of *N*-benzylethylenediamine with either 2-(chloromethyl)-6-methylpyridyl or 2-(chloromethyl)quinolyl hydrochloride salts in the presence of excess base, to obtain the title ligands for **3-6Me** and **3-Q** respectively. Alternatively, reductive amination of *N*-benzylethylenediamine with the corresponding aldehydes also yields the same ligands but in lower yields.

The monosubstituted ligands:

The **1-precursor** (Scheme 3.1, *N*-benzyl-*N'*,*N'*-bis(pyridin-2-ylmethyl)ethane-1,2-diamine) was synthesized as reported before.^{16, 51-52} Its synthesis involves use of reductive amination to attach two picolyl groups to *N*-acetythylenediamine, followed by removal of acetyl group from the other amine (deprotection using acid hydrolysis). The benzyl group is then attached to the deprotected amine to yield the precursor for mono-substituted ligands. The brown oil **1-precursor** is stored at -40 °C.

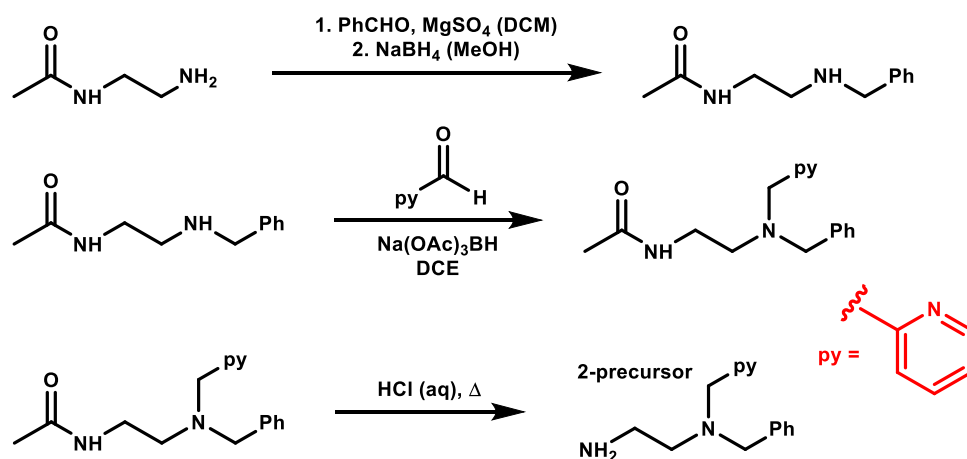
Nucleophilic substitution of **1-precursor** can be carried out separately, with 2-(chloromethyl)-6-methylpyridyl, 2-(chloromethyl)quinolyl and 2-(chloromethyl)-*N*-methylbenzimidazolyl hydrochloride salts, in order to obtain the mono-substituted ligands for **1-6Me** (6MeBnTPEN), **1-Q** (QBnDPEN) and **1-B** (BBnDPEN) respectively. Reductive amination of **1-precursor** can also be employed with 6-methyl-2-picolinaldehyde or 2-quinolinecarboxaldehyde.



Scheme 3.1 The synthetic route for the precursor to the monosubstituted ligands.

The disubstituted ligands:

The disubstituted ligands for **2-6Me** and **2-Q**, titled 6Me₂BnTPEN and DQBnPEN respectively, were synthesized from their precursor, *N*-benzyl-*N*-(pyridin-2-ylmethyl)ethane-1,2-diamine (**2-precursor**). This precursor was obtained from successive reductive aminations of the amino groups of *N*-acetylenediamine with benzaldehyde and picolinaldehyde, followed by deprotection of the other amine using acid hydrolysis to remove the acetyl group (Scheme 3.2). 6Me₂BnTPEN and DQBnPEN for **2-6Me** and **2-Q** respectively were obtained from this precursor's nucleophilic substitution with either 2-(chloromethyl)-6-methylpyridyl or 2-(chloromethyl)quinolyl hydrochloride salts in the presence of excess base.



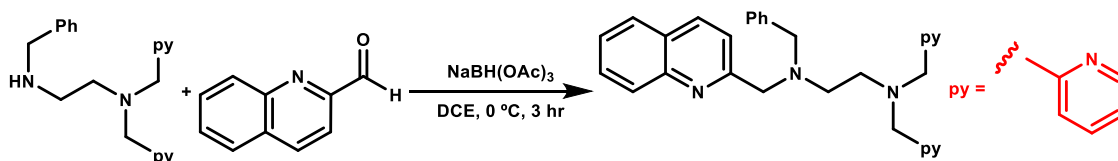
Scheme 3.2 The synthetic route for the precursor to the disubstituted ligands.

The deuteration of benzylic positions in ligands:

6MeBnTPEN-*d*₁₁, 6Me₂BnTPEN-*d*₁₄ and 6Me₃BnTPEN-*d*₁₇ are variations of the ligands with perdeuterated benzylic positions, including methyl groups as well as all the benzylic methylene groups, and were synthesized from an adapted method. Only the benzylic positions of the ligands supporting **1-6Me**, **2-6Me**, and **3-6Me** could be perdeuterated using an adapted procedure.⁵³

The detailed ligand syntheses along with their characterizations, are laid out below. ¹H NMR of ligands are shown in the end of this chapter.

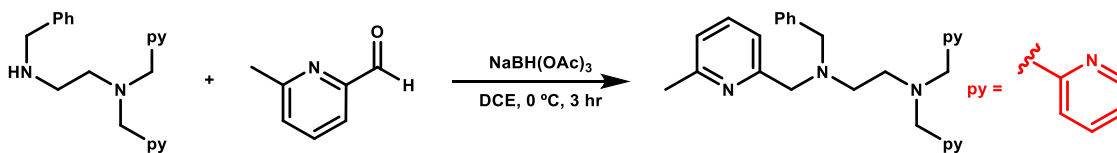
Syntheses of Monosubstituted Ligands



Scheme 3.3 Synthesis of QBnDPEN

***N'*-benzyl-*N''*,*N''*-bis(pyridin-2-ylmethyl)-*N'*-(quinolin-2-ylmethyl)ethane-1,2-diamine (QBnDPEN).** **1-precursor** (0.76 g, 2.3 mmol) and **2-quinolinecarboxaldehyde** (276 mg, 2.27 mmol) were dissolved in 15 mL of 1,2-

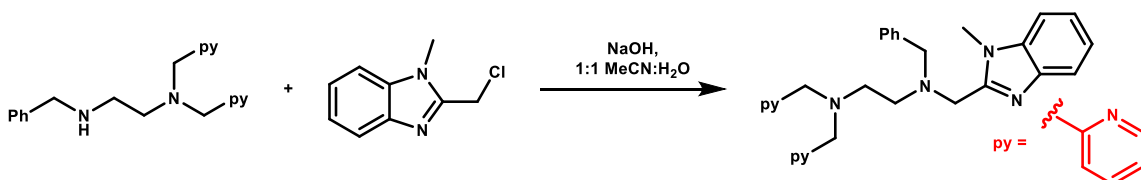
dichloroethane, in that order, followed by excess of sodium triacetoxyborohydride (675 mg, 3.2 mmol). The reaction mixture was stirred under argon for 3 hours, and then quenched with 10 mL of 2 M NaOH, followed by extraction with dichloromethane (3 × 40 mL). After drying with MgSO₄ and filtering off the solution, the solvent was removed using rotary evaporation, and then the resulting oil was recrystallized twice using hexanes to give an off-white solid. An *alternative* method to make this compound involved dissolving the **1-precursor** (0.842 g, 2.53 mmol) in 50 mL of acetonitrile, followed by (2-chloromethyl)quinoline hydrochloride salt (2.53 mmol, 0.542 g) and finally a 30 mL sodium hydroxide solution of water (7.6 mmol). The solution mixture was left under an argon purge and stirred for two days, and the solid ligand crashed out, which was washed with water and dried, to give the solid in 70% yield. The orange ligand was further recrystallized twice with hexanes to give 0.55 g of final ligand as a solid (46% yield). ¹H NMR (CD₂Cl₂, 400 MHz): δ 8.42 (d, *J* = 8 Hz, 2H, py-*H* (α)), 8.04 (d, *J* = 8 Hz, 1H, 4-Q-*H*), 7.97 (d, *J* = 8 Hz, 1H, 9-Q-*H*), 7.79 (d, *J* = 8 Hz, 1H, 6-Q-*H*), 7.68 (td, *J* = 4 Hz, 8 Hz 1H, 8-Q-*H*), 7.61 (d, *J* = 8 Hz, 1H, 3-Q-*H*), 7.51 (td, *J* = 8 Hz, 4 Hz, 3H, 2 4-py-*H* (γ), 1 7-Q-*H*), 7.38 (d, *J* = 8 Hz, 2H, 3-py-*H* (β)), 7.32-7.19 (m, 5H, Ph-*H*), 7.08 (td, *J* = 8 Hz, 4 Hz, 2H, 5-py-*H* (β)), 3.83 (s, 2H, QCH₂), 3.72 (s, 2H, pyCH₂), 3.61 (s, 2H, QCH₂), 2.72 (m, *J* = 8 Hz, 4H, en CH₂CH₂). ¹³C NMR (CD₂Cl₂) δ 161.0, 159.9, 148.8, 139.5, 136.05, 135.93, 129.1, 128.89, 128.85, 128.1, 127.5, 127.4, 126.8, 125.9, 122.6, 121.7, 121.0, 61.2, 60.7, 59.1, 52.2, 52.0.



Scheme 3.4 Synthesis of 6MeBnTPEN

***N'*-benzyl-*N'*-(6-methylpyridin-2-yl)methyl-*N''*,*N''*-bis(pyridin-2-yl)methyl)ethane-1,2-diamine (6MeBnTPEN).** The **1-precursor** (0.76 g, 2.28 mmol) and 6-methylpyridine-2-carboxaldehyde (276 mg, 2.28 mmol) were dissolved in 15 mL of 1,2-dichloroethane, in that order, followed by excess of

sodium triacetoxyborohydride (675 mg, 3.2 mmol). The reaction mixture was stirred under argon for 3 hours, and then quenched with 10 mL of 2 M NaOH, followed by extraction with dichloromethane, and washing with a saturated NaCl solution. After drying the combined organic layers with MgSO₄ and filtering off the solution, the solvent was removed using rotary evaporation, and recrystallized from hexanes to give the title compound in 79% yield. ¹H NMR (CDCl₃, 400 MHz): δ 8.48 (d, *J* = 8 Hz, 2H, py-*H* (α)), 7.56 (td, *J* = 8 Hz, 4 Hz, 2H, 2 4-py-*H* (γ)), 7.44 (td, *J* = 8 Hz, 4 Hz, 3H, py-*H* (γ)), 7.36 (d, *J* = 8 Hz, 1H, py-*H*), 7.31-7.19 (m, *J* = 8 Hz, 5H, Ph-*H*), 7.10 (d, *J* = 8 Hz, 2H, py-*H*), 6.95 (d, *J* = 8 Hz, 1H, py-*H*), 3.76 (s, 4H, pyCH₂), 3.68 (s, 2H, PhCH₂), 3.57 (s, 2H, 6Me-py-CH₂), 2.71 (m, *J* = 8 Hz, 4H, en CH₂CH₂), 2.49 (s, 3H, 6Me-*H*). ¹³C NMR (CD₂Cl₂) δ 160.6, 160.1, 157.9, 149.4, 140.2, 136.9, 136.6, 129.3, 128.6, 127.3, 123.2, 122.3, 121.5, 119.9, 61.3, 61.1, 59.5, 52.7, 52.5, 24.7.



Scheme 3.5 Synthesis of BBnDPEN

***N*-benzyl-*N*-((1-methyl-1H-benzimidazol-2-yl)methyl)-*N',N'*-bis(pyridin-2-yl)methane-1,2-diamine.** The **1-precursor** (0.508 g, 1.55 mmol) and 2-(chloromethyl)-1-methyl-1H-benzimidazole (280 mg, 1.55 mmol) were dissolved in 30 mL of acetonitrile to give a brown solution, in that order, followed by 30 mL of 1.25 M sodium hydroxide solution. The solution was stirred for 24 h at 50 °C. The next day, the reaction mixture was extracted with ethyl acetate (3 × 30 mL), and combined organic fraction was dried with magnesium sulfate and concentrated under vacuum. The left over solid was subject to high vacuum for 24 h and recrystallized from hexane to give an off-white solid. ¹H NMR ((CD₃)₂CO, 400 MHz): δ 8.34 (d, 2H, α-Py-*H*), 7.50 (t, 2H, γ-Py-*H*), 7.48 (d, 1H, Bnlm-*H*), 7.29 (d, 1H, Bnlm-*H*), 7.26 (t, 2H, β-Py-*H*), 7.26-7.04 (m, 9H, Ph-*H* and β'-Py-*H*), 3.78

(s, 2H, BnIm-CH₂), 3.63 (s, 7H, NCH₂Py and Me-BnIm), 3.54 (s, 2H, Bn-CH₂), 2.66 (m, 4H, N-CH₂CH₂).

Syntheses of Disubstituted Ligands

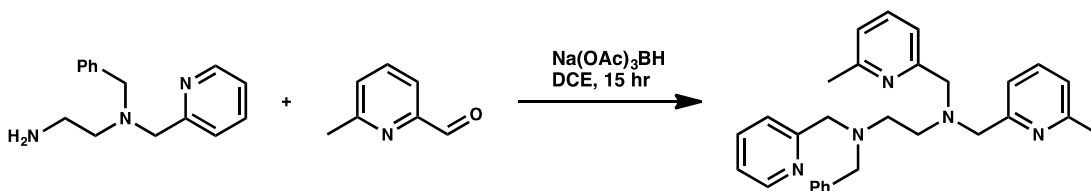
The steps to synthesize **2-precursor** are laid out below, as per Scheme 3.2. Once formed, it was separately reacted with 2 equivalents of 2-(chloromethyl)-6-methylpyridyl or 2-(chloromethyl)quinolyl hydrochloride salts in the presence of excess base to yield the title ligands 6Me₂BnTPEN and DQBnPEN respectively. Reductive amination on **2-precursor** could also be employed with 2 equivalents of 6-methyl-2-picolinaldehyde or 2-quinolinecarboxaldehyde to yield the title ligands for complexes **2-6Me** and **2-Q**.

N-(2-(benzylamino)ethyl)acetamide. N-acetylenehtylenediamine (2 g, 19.6 mmol) was dissolved in 40 mL of dichloromethane, and 2.02 g of benzaldehyde (20.7 mmol) was added to the solution, turning the solution cloudy. This was followed by excess of MgSO₄. (≈ 4 g, 33 mmol). The solution became clear after five minutes but allowed to stir for another 2 hours under argon to allow for a complete formation of imine. The solution was decanted carefully and filtered out from the magnesium sulfate, and subject to rotary evaporation, leaving behind a clear colorless oil. This oil (imine) was dissolved in 30 mL methanol and brought under argon and an ice bath, followed by slow addition of NaBH₄ (1 g, 26.4 mmol). Vigorous bubbling was observed, which died within ten minutes of addition, and after three hours of addition, 10 mL of water was added to quench the reaction. The organic layer was extracted with dichloromethane, dried with MgSO₄ and solvent was removed *in vacuo* to give a clear slightly-gray oil (3.52 g, 93% yield), which was used without further purification for the next step. ¹H NMR (CD₃CN, 400 MHz): δ 7.35-7.24 (m, 5H, Ph-H), 6.52 (br, 1H, NH-amide), 3.76 (s, 2H, Ph-CH₂), 3.24 (q, *J* = 8 Hz, 2H, BnNHCH₂), 2.65 (t, *J* = 8 Hz, 2H, CH₃CONHCH₂), 2.25 (br, 1H, NH-Bn), 1.86 (s, 3H, NHCOCH₃).

N-(2-(benzyl(pyridin-2-ylmethyl)amino)ethyl)acetamide. The product (3.52 g, 18.3 mmol) from previous reaction was dissolved in 30 mL of 1,2-dichloroethane,

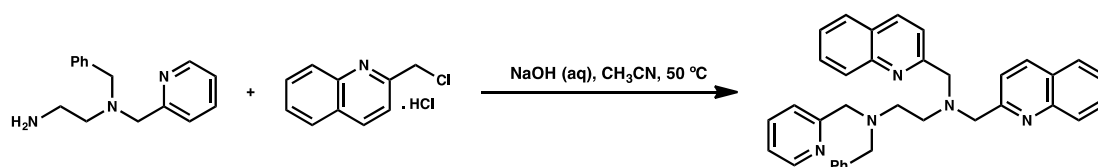
followed by addition of 2-pyridinecarboxaldehyde (1.96 g, 18.3) to form a yellow solution. The reductant sodium triacetoxyborohydride (5 g, 23.6 mmol) was then added to the mixture to give a cloudy solution which was stirred under argon for 3 hours. The solution was quenched with 5 M NaOH solution, followed by extraction into dichloromethane (3 × 40 mL). The combined organic layers were dried with magnesium sulfate and the filtered solution was subject to rotary evaporation to yield a light brown oil (96%, 5 g). ¹H NMR (CDCl₃, 400 MHz): δ 8.52 (d, *J* = 8 Hz, 1H, α-py-*H*), 7.61 (td, 1H, γ-py-*H*), 7.35-7.19 (m, 6H, Ph-*H*, 1 β-py-*H*), 7.15 (td, *J* = 8 Hz, 4 Hz, 1H, β-py-*H*), 6.79 (br, 1H, NH-amide), 3.74 (s, 2H, py-CH₂), 3.64 (s, 1H, CH₂Bn), 3.25 (q, *J* = 8 Hz, 4 Hz, 2H, PhCH₂NCH₂), 2.60 (t, *J* = 8 Hz, 2H, CH₃CONHCH₂), 1.90 (s, 3H, NHCOCH₃).

***N*-benzyl-*N*-(pyridin-2-ylmethyl)ethane-1,2-diamine (2-precursor).** The product from the previous reaction (5 g, 17.5 mmol) was dissolved in 110 mL of 5 M HCl, and refluxed for 24 hours, and then allowed to cool under ice bath. 2 M NaOH was slowly added to quench the reaction mixture in an ice bath. The basic solution was then extracted with dichloromethane (3 × 40 mL), and dried with MgSO₄. The solvent was removed using rotary evaporation, and the leftover highly viscous light brown oil was evacuated under high vacuum to yield a light brown oil (2.77 g, 69%). ¹H NMR (CDCl₃, 400 MHz): δ 8.51 (d, *J* = 8 Hz, 1H, α-py-*H*), 7.65 (dt, *J* = 8 Hz, 4 Hz, 1H, γ-py-*H*), 7.50 (d, *J* = 8 Hz, 1H, β-py-*H*), 7.35-7.19 (m, 5H, Ph-*H*), 7.15 (dt, *J* = 8 Hz, 4 Hz, 1H, β-py-*H*), 6.79 (br, 1H, NH-amide), 3.75 (s, 2H, py-CH₂), 3.65 (s, 1H, CH₂Bn), 2.75 (q, *J* = 8 Hz, 4 Hz, 2H, PhCH₂NCH₂), 2.59 (t, *J* = 8 Hz, 2H, CH₃CONHCH₂), 1.53 (br, 3H, NH₂).



Scheme 3.6 Synthesis of 6Me₂BnTPEN.

***N*-benzyl-*N'*,*N'*-bis((6-methylpyridin-2-yl)methyl)-*N*-(pyridin-2-ylmethyl)ethane-1,2-diamine. (6Me₂BnTPEN).** 0.736 g (3 mmol) of **2-precursor** was dissolved in 20 mL of 1,2-dichloroethane to give a yellow solution, to which the 6-methyl-2-pyridinecarboxaldehyde (6 mmol, 0.750 g) was added. The solution was brought under argon, and sodium triacetoxyborohydride (2 g, 9.3 mmol) was then slowly added to the mixture to form a cloudy solution, which was left stirring for 15 hours. The next day the reaction was quenched slowly with sodium hydroxide dissolved in 40 mL (1.2 g, 30 mmol) in an ice bath. The reaction mixture was then extracted into dichloromethane (3 × 50 mL) from the aqueous layer, and the mixture was dried with magnesium sulfate, which was filtered out to yield a light yellow solution. This was concentrated using rotary evaporation, and then high vacuum to give an yellowish white solid, which was recrystallized using hexanes to give an off-white solid. ¹H NMR (CDCl₃, 400 MHz): δ 8.47 (d, *J* = 8 Hz, 1H, α-py-*H*), 7.55 (dt, *J* = 8 Hz, 4 Hz, 1H, γ-py-*H*), 7.47 (dt, *J* = 8 Hz, 4 Hz, 1H, β-py-*H*), 7.45 (td, *J* = 8 Hz, 4 Hz, 2H, β-py-*H*), 7.31-7.23 (m, *J* = 8 Hz, 5H, Ph-*H*), 7.19 (dt, *J* = 8 Hz, 4 Hz, 1H, py-*H*), 7.09 (dt, *J* = 8 Hz, 4 Hz, 1H, py-*H*), 6.95 (d, *J* = 8 Hz, 2H, py-*H*), 3.73 (s, 4H, pyCH₂), 3.70 (s, 2H, PhCH₂), 3.58 (s, 2H, 6Me-py-CH₂), 2.71 (m, *J* = 8 Hz, 4H, en CH₂CH₂), 2.49 (s, 6H, 6Me-*H*). ¹³C NMR (101 MHz, CD₂Cl₂) δ 159.9, 158, 149.3, 136.88, 136.62, 129.3, 128.6, 127.3, 123.1, 122.2, 121.6, 120.0, 61.41, 61.04, 59.4, 52.7, 52.5, 24.7. An alternative synthesis route involves dissolving the amine in 20 mL of MeCN, followed by addition of 6-methyl-2-(chloromethyl)-pyridyl hydrochloride (2 eq). To this mixture, 6 equivalents of sodium hydroxide solution in 20 mL water is added, to give a 1:1 MeCN:H₂O mixture. This light grayish mixture is stirred under a nitrogen purge for 24 h, after which all the acetonitrile has evaporated, and light brown oily droplets are observed floating in the solution. To this mixture 5 mL of acetonitrile can be added and further stirring for 3 hours, and then 10 mL of water is added. The mixture is stirred for another 5 hours and at this point the ligand crashes out as an off-white solid in the solution. It can be filtered, washed with water, and dried under vacuum to give the title ligand.



Scheme 3.7 Synthesis of DQBnPEN

***N*-benzyl-*N*-(pyridin-2-ylmethyl)-*N',N'*-bis(quinolin-2-ylmethyl)ethane-1,2-**

diamine (DQBnPEN). 0.5 g (2.07 mmol) of **2-precursor** was dissolved in 30 mL of acetonitrile to which the 0.886 g (4.14 mmol) of (2-chloromethyl)-quinoline hydrochloride. Sodium hydroxide solution (25 mmol) was added to 30 mL water and the solution was then slowly added to the solution. The solution mixture was heated to 50 °C for 24 hours in air, and then extracted with dichloromethane (3 × 40 mL). The combined organic extracts were combined and dried with magnesium sulfate. Magnesium sulfate was filtered out and the filtrate was subject to rotary evaporation. The orange yellow solid that formed was recrystallized twice with hexanes to give 0.355 g of final ligand as a solid (35% yield). ¹H NMR (CDCl₃, 400 MHz): δ 8.41 (d, *J* = 8 Hz, 1H, α-py-*H*), 8.04 (d, *J* = 8 Hz, 2H, 4-Q-*H*), 8.01 (d, *J* = 8 Hz, 2H, 9-Q-*H*), 7.78 (d, *J* = 8 Hz, 2H, 6-Q-*H*), 7.68 (td, *J* = 4 Hz, 8 Hz 2H, 8-Q-*H*), 7.61 (d, *J* = 8 Hz, 2H, 3-Q-*H*), 7.50 (td, *J* = 8 Hz, 4 Hz, 2H, 7-Q-*H*), 7.41 (d, *J* = 8 Hz, 1H, 4-py-*H* (γ)), 7.36 (d, *J* = 8 Hz, 1H, 4-py-*H* (β)), 7.25-7.19 (m, 5H, Ph-*H*), 7.01 (td, *J* = 8 Hz, 4 Hz, 2H, 5-py-*H* (β)), 3.95 (s, 4H, QCH₂), 3.69 (s, 2H, pyCH₂), 3.56 (s, 2H, QCH₂), 2.76 (m, *J* = 8 Hz, 4H, en CH₂CH₂). ¹³C NMR (CD₂Cl₂) δ 160.6, 160.1, 148.64, 147.56, 139.4, 136.06, 136.04, 129.2, 128.94, 128.75, 128.04, 127.5, 127.4, 126.8, 126.0, 122.6, 121.7, 121.1, 61.6, 60.4, 58.9, 52.5, 51.9.

Syntheses of Trisubstituted Ligands

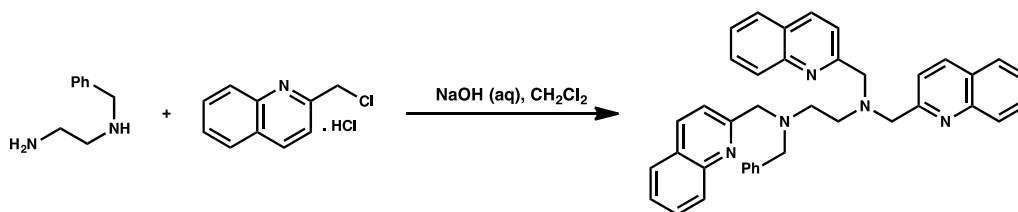
Syntheses of triply-substituted ligands for **3-6Me** and **3-Q** involved a single step reaction, using *N*-benzylethylenediamine and hydrochloride salts of 6-methyl-2-picolylchloride (for **6Me₃BnTPEN**), or (2-chloromethyl)-quinoline (for **BnTQEN**) in presence of excess base to carry out a nucleophilic substitution.



Scheme 3.8 Synthesis of 6Me₃BnTPEN

***N*-benzyl-*N,N',N'*-tris((6-methylpyridin-2-yl)methyl)ethane-1,2-diamine**

(6Me₃BnTPEN). 6-methyl-2-pyridinecarboxaldehyde (2 g, 16.5 mmol) was dissolved in 10 mL of 1,2-dichloroethane, followed by *N*-benzylethylenediamine (0.827 mL, 5.55 mmol) in 40 mL of DCE, followed by sodium triacetoxyborohydride (4 g, 18.8 mmol). The solution was stirred under argon for 3 hours. The reaction was quenched with 50 mL, 3 M NaOH solution, and then extracted with dichloromethane (3 × 50 mL). It was then dried with magnesium sulfate, and the decanted solution was subject to rotary evaporation to give a pale yellow oil, which solidified in air into an off-white solid. This solid was recrystallized using hexanes to yield 0.92 g of ligand in 67% yield. ¹H NMR (CD₂Cl₂, 400 MHz): δ 7.50 (dt, *J* = 8 Hz, 4 Hz 3H, 4-py-*H*), 7.50 (dt, *J* = 8 Hz, 4 Hz 3H, 4-py-*H*), 6.97 (d, *J* = 8 Hz, 3H, 5-py-*H*), 7.30 (overlapping d, *J* = 8 Hz, 3H, 3-py-*H*), 3.67 (s, 4H, pyCH₂), 3.63 (s, 2H, pyCH₂), 3.57 (s, 2H, PhCH₂), 2.68 (m, 4H, en CH₂CH₂), 2.45 (s, 9H, 6-Me-CH₃). ¹³C NMR (CDCl₃) δ 159.7, 159.3, 157.5, 157.3, 139.4, 136.58, 136.56, 128.7, 128.1, 126.8, 121.3, 121.2, 119.4, 119.4, 60.9, 60.7, 59.0, 52.2, 51.9, 24.4.



Scheme 3.9 Synthesis of BnTQEN.

***N*-benzyl-*N,N',N'*-tris(quinolin-2-ylmethyl)ethane-1,2-diamine (BnTQEN).** (2-chloromethyl)-quinoline hydrochloride (3.66 g, 17.1 mmol) was dissolved in 10 mL of water to give a brownish red solution. 50 mL of 3 M NaOH (60 mmol) in water was then added, followed by 10 mL of dichloromethane, to give a biphasic milky white and brown mixture. *N*-benzylethylenediamine (0.85 g, 5.65 mmol) in 5 mL of dichloromethane was then added to the solution to give an orange cloudy mixture. An additional 50 mL of 3 M NaOH was added to the solution over the course of 4 hours (which turned the solution lighter in color). The solution was allowed to stir under argon for 2 days, after which a white solid precipitated out of the solution, which was filtered off, and washed with acetone to give a pure white solid. ¹H NMR (CDCl₃, 400 MHz): δ 8.01 (d, *J* = 8 Hz, 2H, 4-*Q-H*), 7.98 (d, *J* = 8 Hz, 1H, 4-*Q-H*), 7.95 (d, *J* = 8 Hz, 2H, 9-*Q-H*), 7.84 (d, *J* = 8 Hz, 1H, 9-*Q-H*), 7.73 (d, *J* = 8 Hz 2H, 6-*Q-H*), 7.69 (d, *J* = 8 Hz 1H, 6-*Q-H*), 7.66 (dt, *J* = 8 Hz, 4 Hz 3H, 8-*Q-H*), 7.55 (d, *J* = 8 Hz, 2H, 3-*Q-H*), 7.49 (d, *J* = 8 Hz, 4 Hz, 3H, 7-*Q-H*), 4.00 (s, 4H, QCH₂), 3.86 (s, 2H, QCH₂), 3.6 (s, 2H, QCH₂), 2.82 (m, *J* = 8 Hz, 4H, en CH₂CH₂). ¹³C NMR (CDCl₃) δ 161.3, 160.9, 147.95, 147.86, 139.5, 136.63, 136.56, 129.77, 129.70, 129.46, 129.31, 128.6, 127.93, 127.75, 127.37, 126.5, 126.4, 121.43, 121.34, 62.2, 61.8, 59.7, 53.0, 52.7.

Deuteration of ligands 6MeBnTPEN, 6Me₂BnTPEN, and 6Me₃BnTPEN

An adapted procedure⁵³ was used to deuterate the benzylic positions of the ligands. There are 11, 14 and 17 benzylic protons in 6MeBnTPEN, 6Me₂BnTPEN, 6Me₃BnTPEN respectively, that were deuterated with over 80% deuterium incorporation. 5-10 mL of deuterated DMSO-d₆ was stirred under argon and heated to 80 °C for five minutes. Once oxygen was removed, the title ligand (0.5-0.6 mmol) was added and dissolved completely in this solvent. While still under argon, 0.05 mmol of potassium *tert*-butoxide was introduced into the solution. The solution turned dark pink in a minute, and was stirred for 1-2 h at 80 °C. The mixture was then cooled, and 10 mL of D₂O was added to yield a yellow murky solution, which was extracted with ethyl acetate (20 mL × 3). The combined organic layers

were then dried with magnesium sulfate and concentrated under high vacuum to give off-white crude ligand. This crude solid was recrystallized from hot hexanes to give the title ligands, which were characterized using ^1H NMR spectroscopy.

3.5.1.2 Syntheses of Iron(II) Complexes

Iron(II) complexes in this report are named with a prime letter (') after the name of the ferryl complex to distinguish them. The general procedure for the syntheses of iron(II) precursor complexes is as follows: equimolar amounts of $\text{Fe}(\text{OTf})_2(\text{CH}_3\text{CN})_2$ and ligands are stirred in dichloromethane for over 12 h under nitrogen and subsequently concentrated *in vacuo*. The resulting residue is stirred in diethyl ether for 1-2 hr and filtered to obtain a powder. Recrystallization of the powder from slow diffusion of diethyl ether into its dichloromethane or acetonitrile solutions gives the title compounds as crystalline materials, which are filtered and washed with diethyl ether, and dried under high vacuum. The specific syntheses of the precursor iron(II) complexes **1-Q'**, **1-6Me'**, **1-B'**, **2-Q'**, **2-6Me'**, **3-Q'**, and **3-6Me'** are shown below.

[Fe^{II}(6MeBnTPEN)(OTf)]OTf (1-6Me'):

This complex involved addition of 6MeBnTPEN (400 mg, 0.912 mmol) in dichloromethane (1 mL) to a stirred suspension of $\text{Fe}(\text{OTf})_2(\text{CH}_3\text{CN})_2$ (398 mg, 0.912 mmol) in dichloromethane (1 mL) under an inert atmosphere, to give a brown solution. The mixture was stirred overnight, and the solvent was then removed *in vacuo*. Stirring the resultant yellow precipitate in ether (8 mL) yielded a dark yellow powder, which was recrystallized from slow diffusion of diethyl ether in dichloromethane to give the title compound as light brown crystals in 89% yield. Anal. calculated for $\text{C}_{30}\text{H}_{31}\text{F}_6\text{FeN}_5\text{O}_6\text{S}_2\cdot\text{H}_2\text{O}$, $[\text{Fe}(\text{6Me-BnTPEN})\text{OTf}]\text{OTf}\cdot\text{H}_2\text{O}$: C, 44.51; H, 4.11; N, 8.65; F, 14.08. Found: C, 44.48; H, 3.83; N, 8.59; F, 14.20. A similar procedure was employed for the synthesis of the deuterated **1-6Me'**, and the corresponding salt $[\text{}^{57}\text{Fe}^{\text{II}}(\text{6MeBnTPEN})\text{OTf}](\text{OTf})$ was synthesized using $^{57}\text{Fe}(\text{OTf})_2(\text{CH}_3\text{CN})_2$.

[Fe^{II}(6Me₂BnTPEN)(OTf)]OTf (2-6Me')

6Me₂BnTPEN (375 mg, 0.83 mmol) in dichloromethane (1 mL) was transferred to a stirred suspension of Fe^{II}(OTf)₂•2CH₃CN (367 mg, 0.83 mmol) in dichloromethane (1 mL) under an inert atmosphere, to give a yellow solution. The mixture was stirred overnight, and the solvent was then removed *in vacuo*. Stirring the resultant light-yellow precipitate in ether (8 mL) yielded a dark yellow powder, which was recrystallized from slow diffusion of diethyl ether in dichloromethane to give the title compound as light yellowish green crystals in 68% yield. Anal. calculated for C₃₁H₃₃F₆FeN₅O₆S₂•H₂O, [Fe(6Me₂-BnTPEN)OTf]OTf•H₂O: C, 45.21; H, 4.28; N, 8.50; F, 13.84. Found: C, 45.25; H, 4.11; N, 8.52; F, 14.03. A similar procedure was employed for the synthesis of the deuterated **2-6Me'**, and the corresponding salt [⁵⁷Fe^{II}(6Me₂BnTPEN)OTf](OTf) was synthesized using ⁵⁷Fe(OTf)₂(CH₃CN)₂.

[Fe^{II}(6Me₃BnTPEN)(OTf)]OTf (3-6Me')

This synthesis of the complex involved addition of 6Me₃BnTPEN (247.5 mg, 0.532 mmol) in dichloromethane (1 mL) to a stirred suspension of Fe(OTf)₂(CH₃CN)₂ (232 mg, 0.532 mmol) in dichloromethane (1 mL) under an inert atmosphere, to give a yellow solution. The mixture was stirred overnight, and the solvent was then removed *in vacuo*. Stirring the resultant light-yellow precipitate in ether (8 mL) yielded a yellowish white powder, which was recrystallized from slow diffusion of diethyl ether in dichloromethane to give the title compound as white crystals in 68% yield. Anal. calculated for C₃₂H₃₅F₆FeN₅O₆S₂•H₂O, [Fe(6Me₃-BnTPEN)OTf]OTf•H₂O: C, 45.89; H, 4.45; N, 8.36; F, 13.61. Found: C, 46.31; H, 4.40; N, 8.41; F, 13.62. A similar procedure was employed for the synthesis of the deuterated **3-6Me'**, and the corresponding salt [⁵⁷Fe^{II}(6Me₃BnTPEN-*d*₁₇)OTf](OTf) was synthesized using ⁵⁷Fe(OTf)₂(CH₃CN)₂.

[Fe^{II}(BBnDPEN)(OTf)]OTf (1-B')

Under nitrogen atmosphere, the iron(II) salt $\text{Fe}(\text{OTf})_2(\text{CH}_3\text{CN})_2$ (92 mg, 0.211 mmol) was dissolved in 1 mL of dichloromethane and BBnDPEN (100 mg, 0.211 mmol) in 1 mL of dichloromethane was transferred slowly to the solution to give a brownish-red solution. The solution was removed using high vacuum, and the resulting solid was stirred in diethyl ether for fifteen minutes to give a muddy yellow slurry that was filtered to give a yellow solid; this slurry was recrystallized by slow diffusion of diethyl ether into a solution in dichloromethane to give greenish yellow crystals in 79% yield. Anal. calculated for $\text{C}_{32}\text{H}_{32}\text{F}_6\text{FeN}_6\text{O}_6\text{S}_2 \cdot 2\text{H}_2\text{O}$, $[\text{Fe}(\text{B-BnDPEN})\text{OTf}]\text{OTf} \cdot 2\text{H}_2\text{O}$: C, 44.35; H, 4.19; N, 9.70. Found: C, 44.28; H, 3.84; N, 9.46.

$[\text{Fe}^{\text{II}}(\text{QBnDPEN})\text{OTf}]\text{OTf}$ (1-Q'):

A 1 mL dichloromethane solution of iron(II) salt $\text{Fe}(\text{OTf})_2(\text{CH}_3\text{CN})_2$ (505 mg, 1.16 mmol) in O_2 -free atmosphere and QBnDPEN (549 mg, 1.16 mmol) solution in the same solvent were stirred together to give a red solution. The solvent was then evacuated, and the resulting solid was stirred in diethyl ether for fifteen minutes to give a muddy orange slurry, which was filtered to give a dull yellow solid. This solid was recrystallized twice by slowly diffusing diethyl ether into its dichloromethane solution to give orange-yellow crystals in 79% yield. Anal. calculated for $\text{C}_{33}\text{H}_{31}\text{F}_6\text{FeN}_5\text{O}_6\text{S}_2 \cdot 0.5\text{H}_2\text{O}$, $[\text{Fe}(\text{QBnDPEN})\text{OTf}]\text{OTf} \cdot 0.5\text{H}_2\text{O}$: C, 47.38; H, 3.86; N, 8.37. Found: C, 47.26; H, 3.79; N, 8.26. The corresponding salt $[\text{}^{57}\text{Fe}^{\text{II}}(\text{QBnDPEN})\text{OTf}](\text{OTf})$ was synthesized using $^{57}\text{Fe}(\text{OTf})_2(\text{CH}_3\text{CN})_2$.

$[\text{Fe}^{\text{II}}(\text{DQBnPEN})\text{OTf}]\text{OTf}$ (2-Q'):

To a suspension of iron(II) salt (295 mg, 0.68 mmol) in dichloromethane under the atmosphere of nitrogen, a yellow solution of the ligand DQBnPEN (355 mg, 0.68) in dichloromethane was added dropwise. This resulted in a dark green colored solution which was stirred overnight. The solvent was then removed, after which the addition of diethyl ether was carried out to leave behind a yellowish green solid. This solid was recrystallized from dichloromethane using slow diffusion of ether into the solution to give orange crystals. Anal. calculated for

$C_{37}H_{33}F_6FeN_5O_6S_2 \cdot 1.5H_2O$, $[Fe(DQBnPEN)OTf]OTf \cdot 1.5H_2O$: C, 48.16; H, 4.15; N, 7.59. Found: C, 48.06; H, 3.79; N, 7.52. The corresponding salt $[^{57}Fe^{II}(DQBnPEN)OTf](OTf)$ was synthesized using $^{57}Fe(OTf)_2(CH_3CN)_2$.

$[Fe^{III}(BnTQEN)(OTf)]OTf$ (3-Q'):

$Fe(OTf)_2(CH_3CN)_2$ (228 mg, 0.523 mmol) can be suspended tetrahydrofuran or dissolved in dichloromethane (1 mL), followed by slow addition of the insoluble white slurry of ligand BnTQEN (300 mg, 0.523 mmol) in the same solvent, to give a yellow colored suspension. It is stirred at room temperature overnight, to give a yellow precipitate in an orange solution. Diethyl ether is then added to precipitate out more solid from the solution which can be then filtered and washed with more diethyl ether, to give a bright yellow powder in 77% yield (371 mg). Anal. calc. for $C_{41}H_{35}F_6FeN_5O_6S_2 \cdot 1.5H_2O$, $[Fe(BnTQEN)OTf]OTf \cdot 1.5H_2O$: C, 51.58; H, 4.01; N, 7.34. Found: C, 51.87; H, 3.89; N, 7.33. The corresponding salt $[^{57}Fe^{II}(BnTQEN)OTf](OTf)$ was synthesized using $^{57}Fe(OTf)_2(CH_3CN)_2$.

3.5.1.3 Synthesis and Generation of Oxoiron(IV) Complexes

The iron(IV) complexes crystallographically characterized in this report were generated from their respective iron(II) precursors in a 1:3 mixture of acetonitrile and water, using 4 equivalents of ceric ammonium nitrate as oxidants. Once generated, excess sodium perchlorate salt provided the counterions to precipitate out the complex, which was then further used to obtain crystals for X-ray diffraction.⁵⁴ The remaining complexes were generated at given temperatures *in situ* from the corresponding iron(II) solutions in acetonitrile (1 mM, unless otherwise stated), using 2 equivalents of 1-(*tert*-butylsulfonyl)-2-iodosylbenzene dissolved in minimal amount of 2,2,2-trifluoroethanol.

$[Fe^{IV}(O)(BnTPEN)](ClO_4)_2$ (0):

$NaClO_4$ (314 mg, 2.57 mmol) and ceric ammonium nitrate (CAN) (133 mg, 0.243 mmol) were dissolved in 3 mL water to give a yellow solution. This solution was then transferred to a solution of $[Fe^{II}(BnTPEN)(OTf)]OTf$ (50 mg, 0.064 mmoles)

in 1 mL acetonitrile to yield a dark green solution which was kept at 2-8 °C overnight to yield dark green crystals in a yellowish green mother liquor. This solid was filtered, and washed with 2 mL water, and the resulting solid was dried overnight under high vacuum to yield a greenish black crystalline material (30 mg, 67% yield). The solid is stable for months as a crystalline material at room temperature. This crystalline material was also suitable for X-ray diffraction analysis. Anal. calcd. for $C_{27}H_{29}Cl_2FeN_5O_9$, $[Fe^{IV}(O)(BnTPEN)](ClO_4)_2$: C, 46.71; H, 4.21; N, 10.09. Found: C, 46.52; H, 4.27; N, 10.06.

$[Fe^{IV}(O)(B-BnDPEN)](ClO_4)_2$ (1-B):

$NaClO_4$ (314 mg, 2.57 mmol) and ceric ammonium nitrate (CAN) (133 mg, 0.243 mmol) were dissolved in 3 mL water to give a yellow solution. This mixture was then transferred to a solution of $[Fe^{II}(B-BnDPEN)(OTf)]OTf$ (50 mg, 0.060 mmoles) in 1 mL acetonitrile to yield a brown solution, which precipitated to give a burgundy solid. This mixture was kept for 2 h at 2-8 °C to allow further precipitation. The solution was then filtered, and washed with 2 mL water, and the resulting burgundy solid was dried overnight in high vacuum to yield a burgundy powder (30 mg, 62% yield). Crystals suitable for X-ray crystallography were grown by dissolving 10 mg of the solid in 0.2 mL acetonitrile and adding a water solution of $NaClO_4$ (50 mg in 1.8 mL). Slow evaporation of acetonitrile at 2-5 °C over the course of 8 h formed crystals suitable for X-ray diffraction. Anal. calcd. for $C_{30}H_{32}N_6O_9FeCl_2 \cdot 0.5H_2O$, $[Fe^{IV}(O)(B-BnDPEN)](ClO_4)_2 \cdot 0.5H_2O$: C, 47.64; H, 4.40; N, 11.11. Found: C, 47.54; H, 4.41; N, 11.48. About 30 mg of unlabeled solid was used for Mössbauer analysis.

3.5.2 Crystallographic Details for 0 and 1-B

Data collection and structure refinement details for complexes **0** and **1-B** are detailed below.

Complex 0:

A crystal (approximate dimensions: 0.150 x 0.120 x 0.100 mm) was placed onto the tip of a 0.5 mm MiTeGen loop and mounted on a Bruker photon-II CPAD diffractometer for a data collection at 123(2) K.⁵⁵ A preliminary set of cell constants was calculated from reflections harvested from three sets of 12 frames. These initial sets of frames were oriented such that orthogonal wedges of reciprocal space were surveyed. This produced initial orientation matrices determined from 258 reflections. The data collection was carried out using MoK α radiation (graphite monochromator) with a frame time of 30 seconds and a detector distance of 6.0 cm. A randomly oriented region of reciprocal space was surveyed to the extent of one sphere and to a resolution of 0.70 Å. Six major sections of frames were collected with 1° steps in ω at four different ϕ settings and a detector position of -28° in 2θ . The intensity data were corrected for absorption and decay.⁵⁶ Final cell constants were calculated from the xyz centroids of 9988 strong reflections from the actual data collection after integration.⁵⁷ Please refer to Table 3.6 for additional crystal and refinement information.

The structure was solved using SHELXS-97 (Sheldrick 2008)⁵⁸⁻⁵⁹ and refined using SHELXL-2018/3 (Sheldrick, 2018).⁶⁰ The space group P-1 was determined based on systematic absences and intensity statistics. A direct-methods solution was calculated which provided most non-hydrogen atoms from the E-map. Full-matrix least squares / difference Fourier cycles were performed which located the remaining non-hydrogen atoms. All non-hydrogen atoms were refined with anisotropic displacement parameters. All hydrogen atoms were placed in ideal positions and refined as riding atoms with relative isotropic displacement parameters. Two atoms of a perchlorate ion were disordered and modeled as individual atoms. A possible water atom is H-bonded to the non-disordered perchlorate counterion. This is common with perchlorate salts. In addition to better ellipsoids, modeling the disordered perchlorate helps make the water molecule visible on the difference map. Because it is on an inversion center, only one corner out of four corners in the unit cell has a water molecule. It is on/near an inversion center and it accounts for only about 0.125 (0.25 \times 0.5)

occupancy. The H-bonds to the perchlorate ion are reasonable and has been seen before with other ferryl complexes too, but it does not require extensive modeling. The final full matrix least squares refinement converged to $R1 = 0.0452$ and $wR2 = 0.1116$ (F^2 , all data).

Table 3.6 Crystal data and structure refinement for complex **0** and **1-B**.

Crystallographic details	0	1-B
CCDC Identification code	15247	18111
Empirical formula	$C_{27}H_{29}Cl_2FeN_5O_9$	$C_{30}H_{32}Cl_2FeN_6O_9$
Formula weight	694.30	747.36
Temperature	123(2) K	123(2) K
Wavelength	1.54178 Å	0.71073 Å
Crystal system	Triclinic	Triclinic
Space group	<i>P</i> -1	<i>P</i> -1
Unit cell dimensions	$a = 9.3710(2)$ Å $\alpha = 79.5650(10)^\circ$	$a = 9.489(7)$ Å $\alpha = 80.32(3)^\circ$
	$b = 10.3626(2)$ Å $\beta = 79.1540(10)^\circ$	$b = 10.496(10)$ Å $\beta = 79.83(3)^\circ$
	$c = 16.4140(3)$ Å $\gamma = 65.5000(10)^\circ$	$c = 16.943(10)$ Å $\gamma = 68.23(3)^\circ$
Volume	1415.00(5) Å ³	1533(2) Å ³
<i>Z</i>	2	2
Density (calculated)	1.630 Mg/m ³	1.619 Mg/m ³
Absorption coefficient	6.576 mm ⁻¹	0.734 mm ⁻¹
<i>F</i> (000)	716	772
Crystal color, morphology	Dark green, block	Brown, needle
Crystal size	0.20 x 0.10 x 0.10 mm ³	0.200 x 0.100 x 0.050 mm ³
Theta range for data collection	2.76 to 74.50°	2.313 to 26.324°
Index ranges	$-11 \leq h \leq 10$, $-12 \leq k \leq 12$, $-20 \leq l \leq 20$	$-11 \leq h \leq 11$, $-13 \leq k \leq 13$, $-21 \leq l \leq 21$

Crystallographic details	0	1-B
CCDC Identification code	15247	18111
Empirical formula	C ₂₇ H ₂₉ Cl ₂ FeN ₅ O ₉	C ₃₀ H ₃₂ Cl ₂ FeN ₆ O ₉
Formula weight	694.30	747.36
Temperature	123(2) K	123(2) K
Wavelength	1.54178 Å	0.71073 Å
Crystal system	Triclinic	Triclinic
Space group	<i>P</i> -1	<i>P</i> -1
Reflections collected	35216	23884
Independent reflections	5763 [<i>R</i> (int) = 0.0938]	6214 [<i>R</i> (int) = 0.0421]
Observed reflections	4881	5374
Completeness to theta = 74.50°	99.4%	99.90%
Absorption correction	None	Semi-empirical from equivalents
Refinement method	Full-matrix least-squares on <i>F</i> ²	Full-matrix least-squares on <i>F</i> ²
Data / restraints / parameters	5763 / 50 / 419	6214 / 0 / 434
Goodness-of-fit on <i>F</i> ²	1.034	1.057
Final <i>R</i> indices [<i>I</i> > 2σ(<i>I</i>)]	<i>R</i> 1 = 0.0452, <i>wR</i> 2 = 0.1045	<i>R</i> 1 = 0.0328, <i>wR</i> 2 = 0.0815
<i>R</i> indices (all data)	<i>R</i> 1 = 0.0597, <i>wR</i> 2 = 0.1116	<i>R</i> 1 = 0.0405, <i>wR</i> 2 = 0.0856
Largest diff. peak and hole	0.554 and -0.621 e.Å ⁻³	0.423 and -0.466 e.Å ⁻³

3.5.3 Oxidative Reactivity and Kinetics of Oxoiron(IV) Complexes

To examine the rates of reaction with substrates, the near-IR chromophores for all the complexes were followed against time when an excess concentration of a given substrate was introduced at any given temperature into 1-mM acetonitrile solutions of the complexes. The decay profiles were then followed for different concentrations of that substrate and used to obtain second-order rate constants. Because these oxoiron(IV) complexes were quite reactive, substrates with C–H BDE > 80 kcal/mol were used to measure HAT reactivity.

HAT reactivity of the complexes was examined at 298 K, except for **3-Q** and **3-6Me** which are too thermally unstable at room temperature. Even at 233 K, the HAT second-order rate constants could only be obtained for deuterated **3-6Me**,

which had a longer half-life than that of the parent complex. All OAT second-order rate constants are determined at 233 K. The plots for second-order rate constants for each of the complexes are shown below, and the second order rate constants are enlisted on Table 3.5 in the results section.

Complex 0:

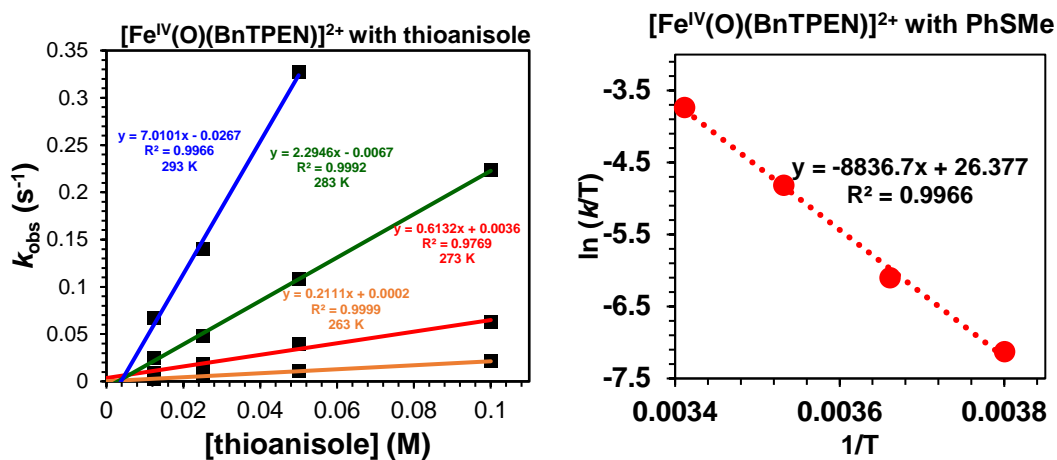
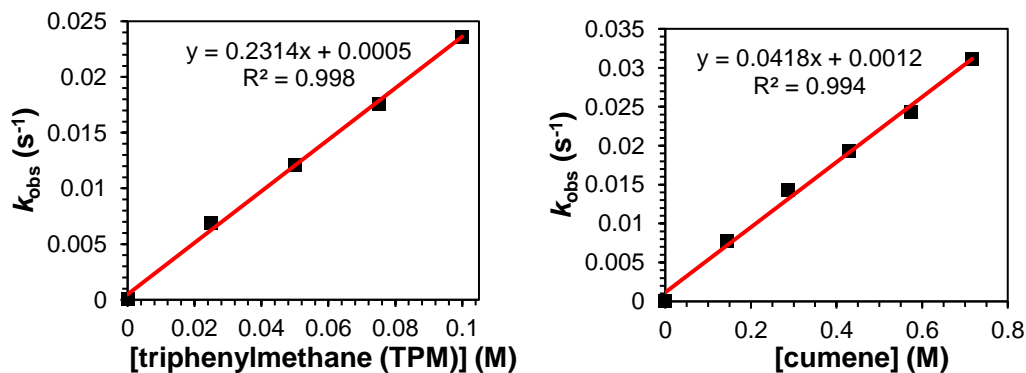


Figure 3.17 Second-order rate constants for the reaction of thioanisole with **0**, measured at different temperatures (left) and Eyring plot (right) for the reaction of **0** with thioanisole, from which the Eyring parameters listed in Table 3.7 were obtained.

Complex 1-B:



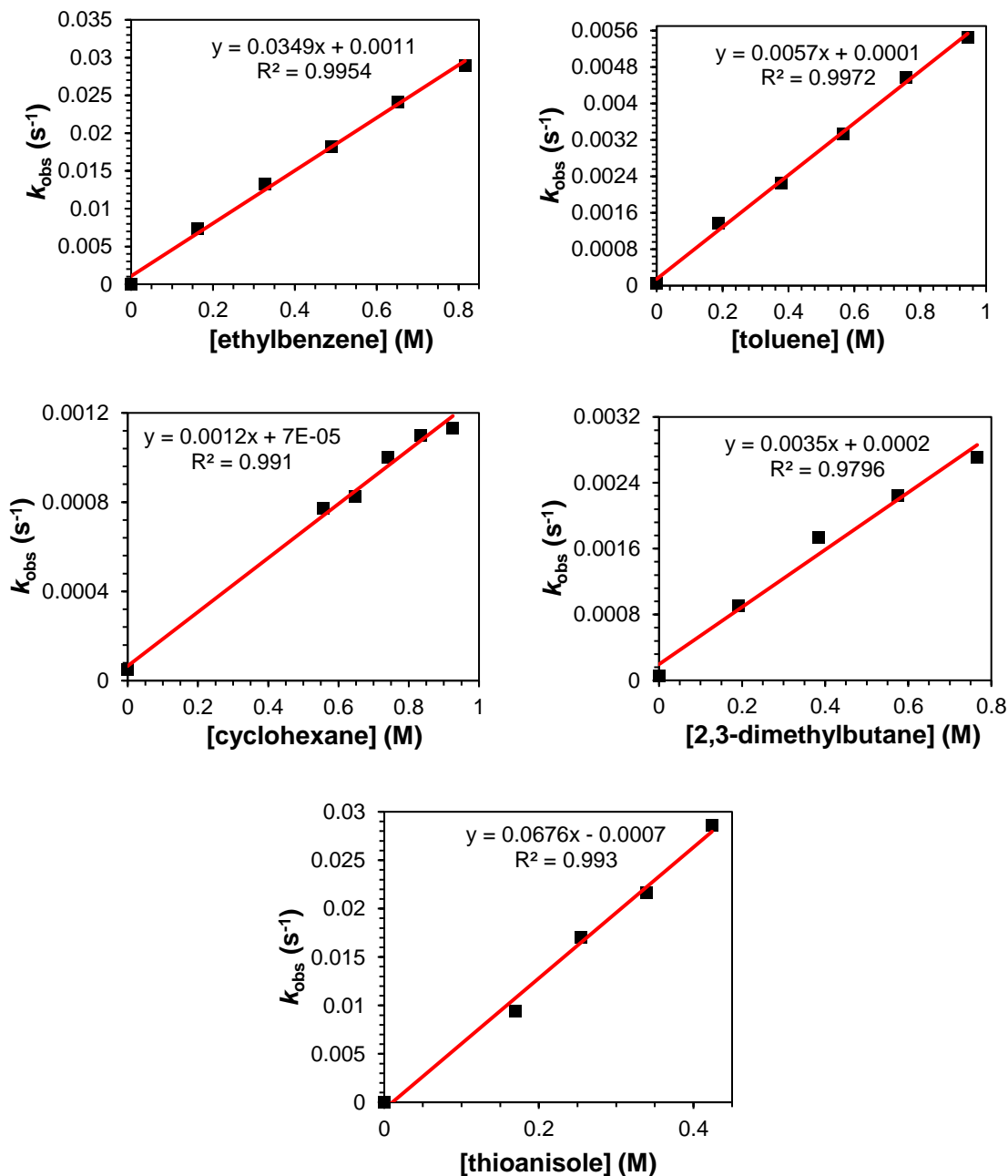
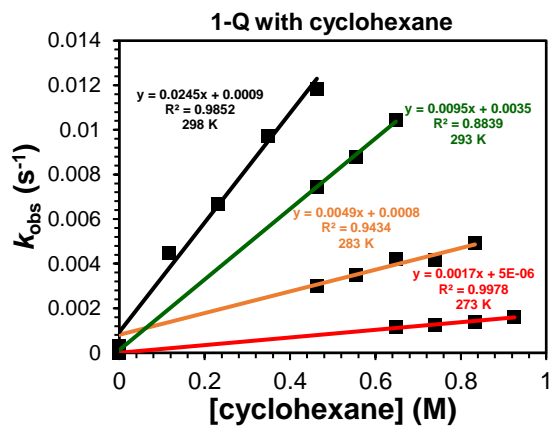
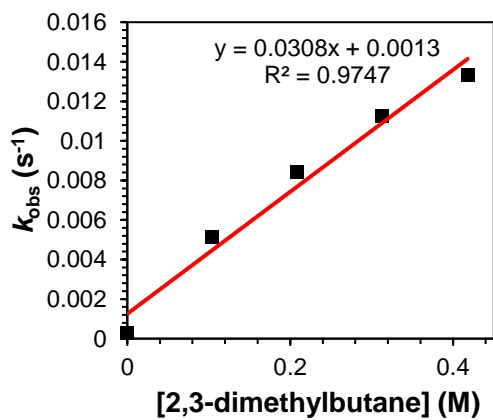
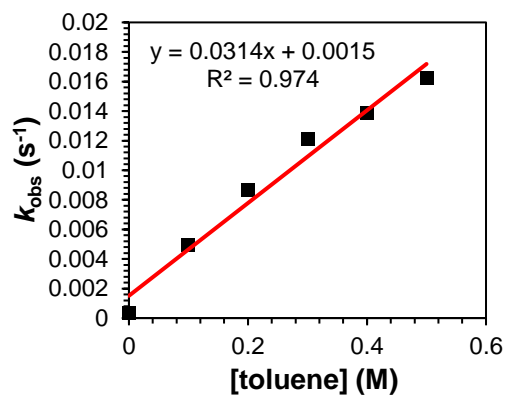
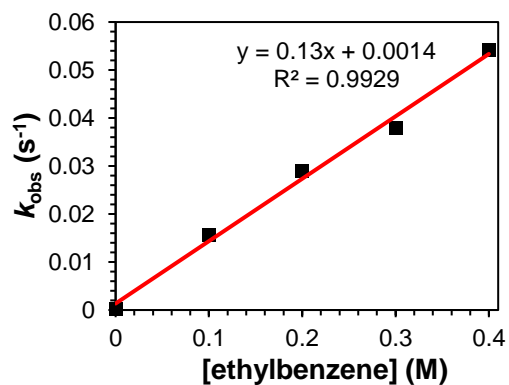
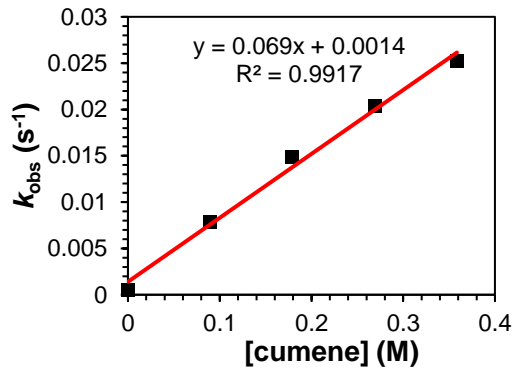
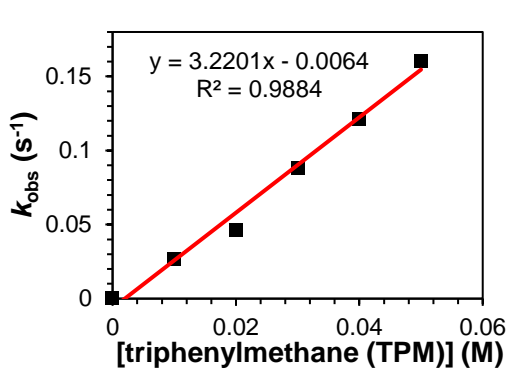


Figure 3.18 Second-order rate constants for reactions of HAT substrates at 298 K, and for thioanisole (OAT) at 233 K with complex **1-B**. Eyring plot of **1-B** with cyclohexane is also shown on the bottom right. The k_2 were obtained by reacting 0.8 M cyclohexane with acetonitrile solution of **1-B** at different temperatures.

Complex 1-Q:



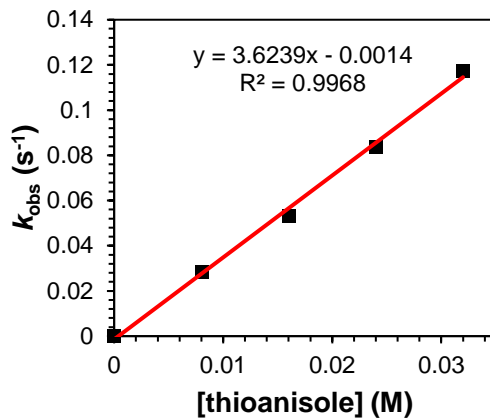
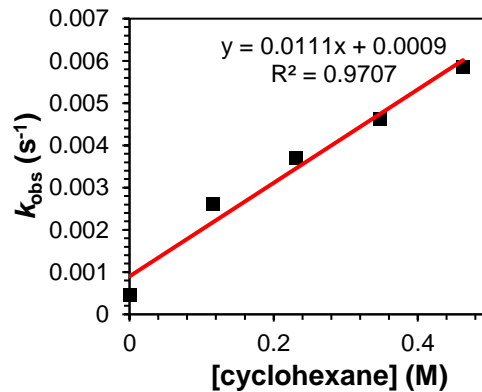
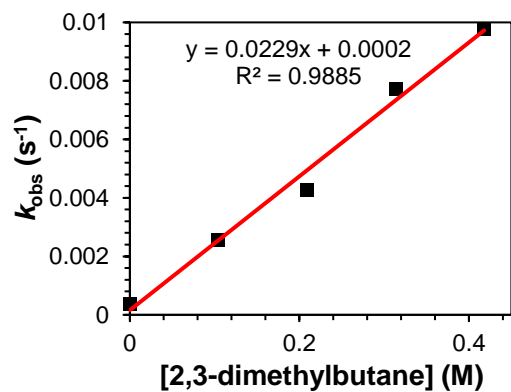
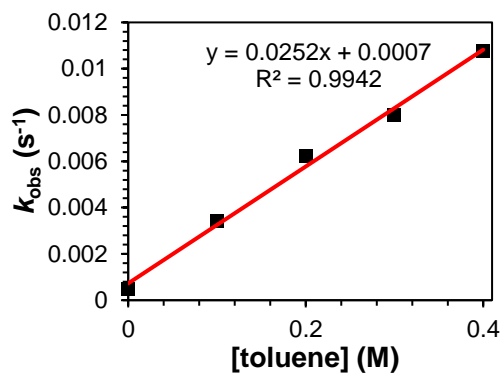
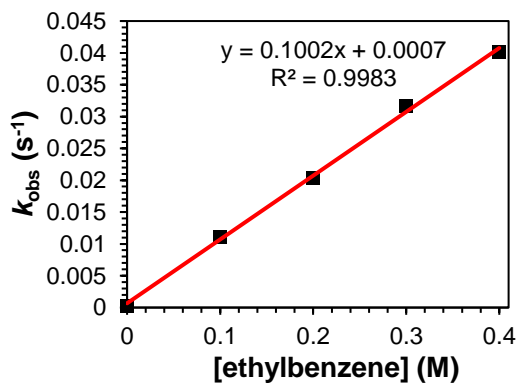
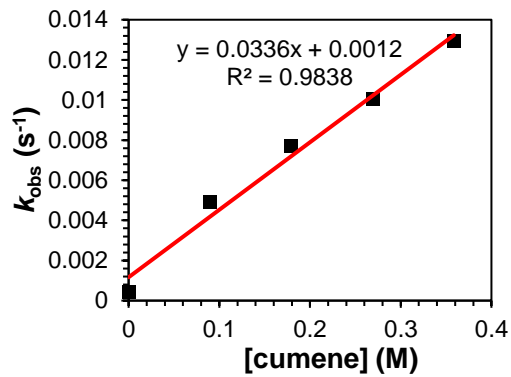
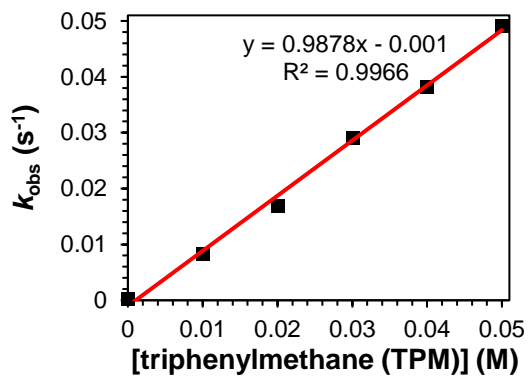


Figure 3.19 Second-order rate constants for reactions of HAT substrates at 298 K (except cyclohexane for which these rates were determined at more than one temperature), and for thioanisole (OAT) at 233 K with complex **1-Q**.

Complex 1-6Me:



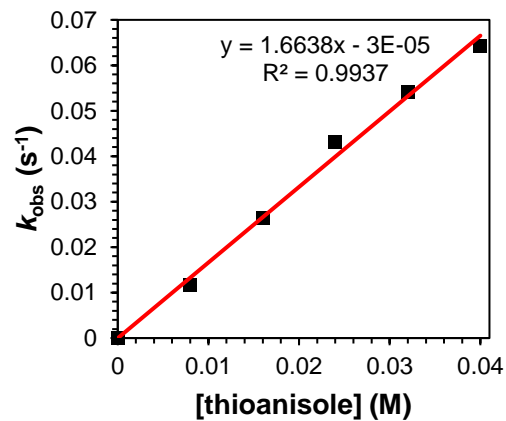
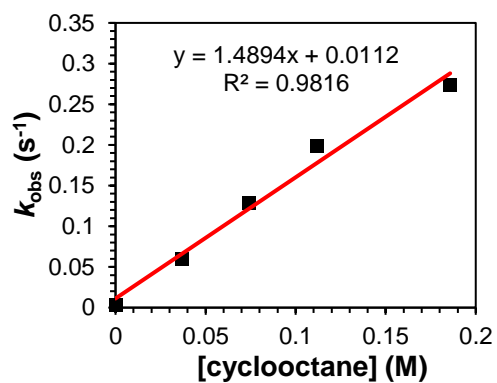
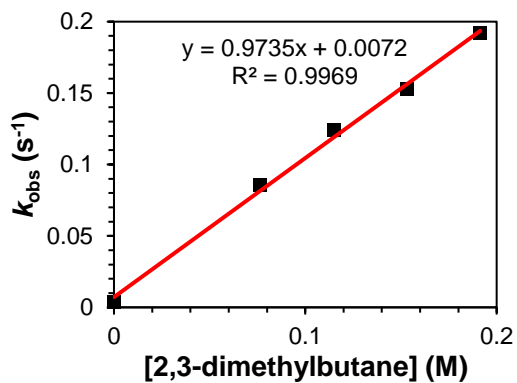
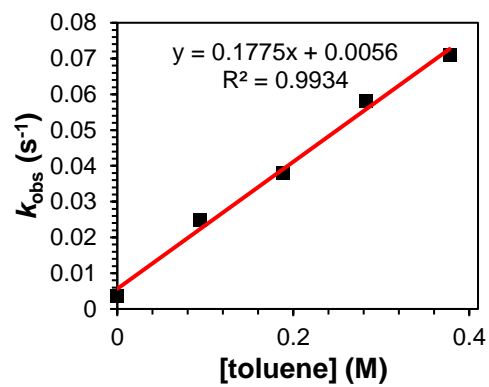
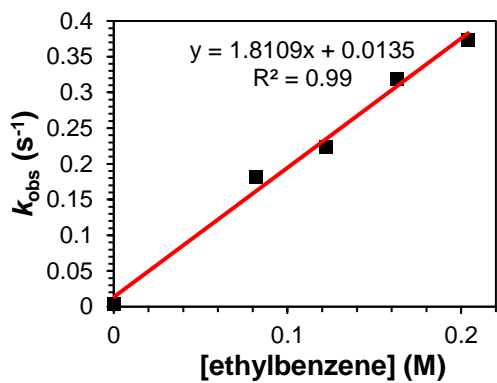
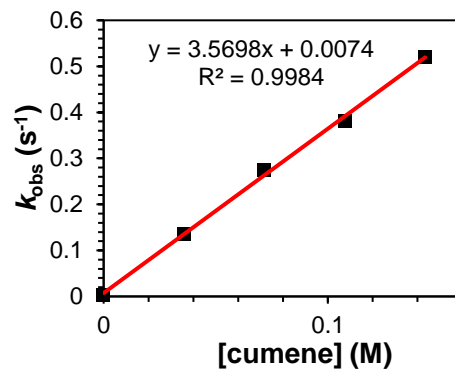
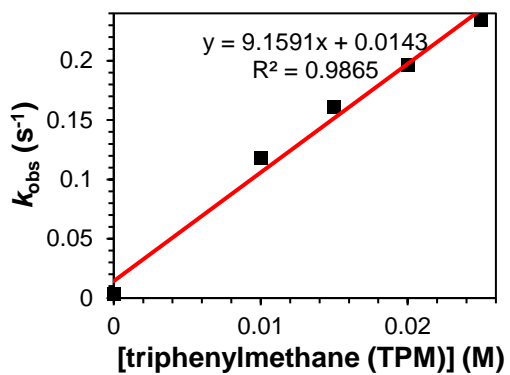


Figure 3.20 Second-order rate constants for reactions of HAT substrates at 298 K and for thioanisole (OAT) at 233 K with complex **1-6Me**.

Complex 2-Q:



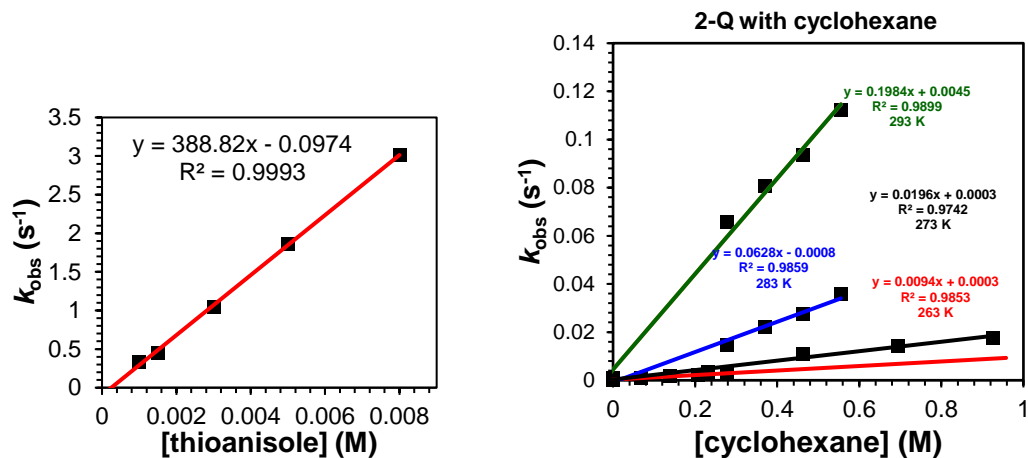
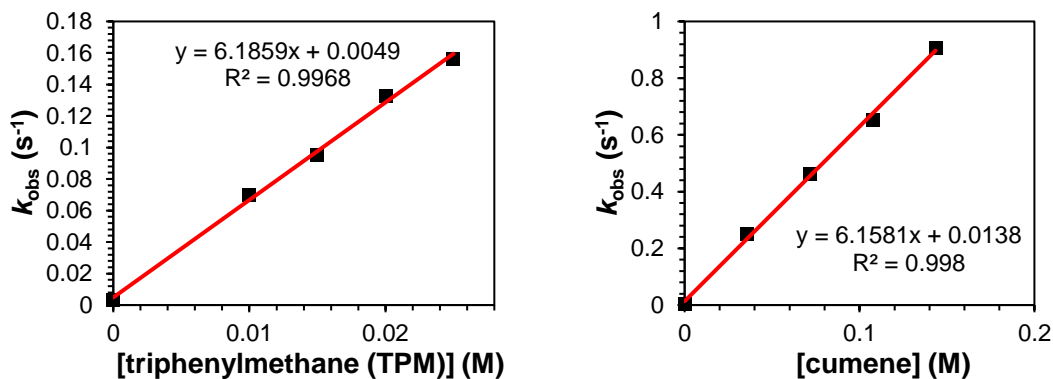


Figure 3.21 Second-order rate constants for reactions of HAT substrates at 298 K (except cyclohexane for which these rates were determined at more than one temperature), and for thioanisole (OAT) at 233 K with complex **2-Q**.

Complex 2-6Me-d:



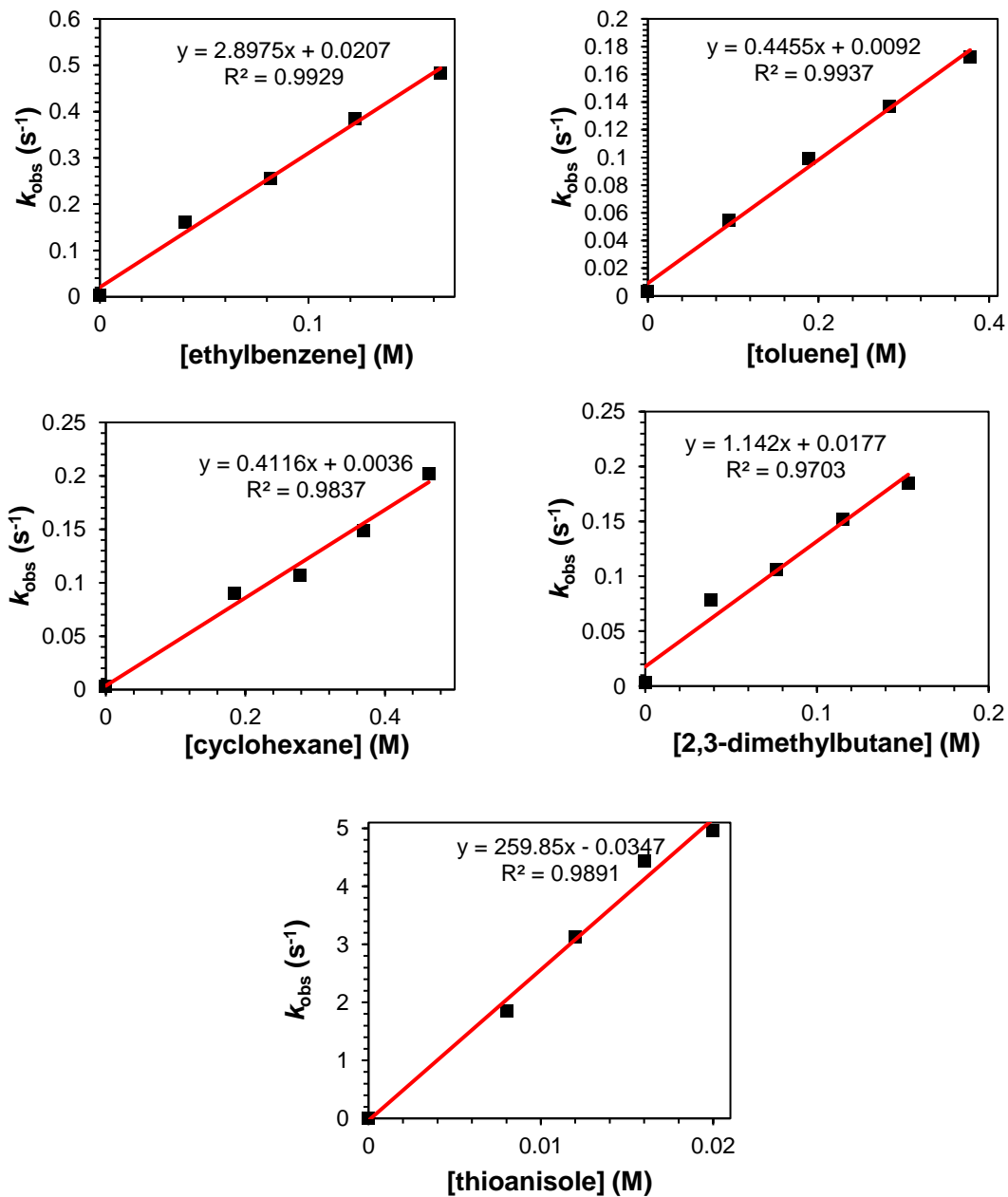


Figure 3.22 Second-order rate constants for reactions of HAT substrates at 298 K and for thioanisole (OAT) at 233 K with deuterated complex **2-6Me-d**.

Complex 3-6Me-d:

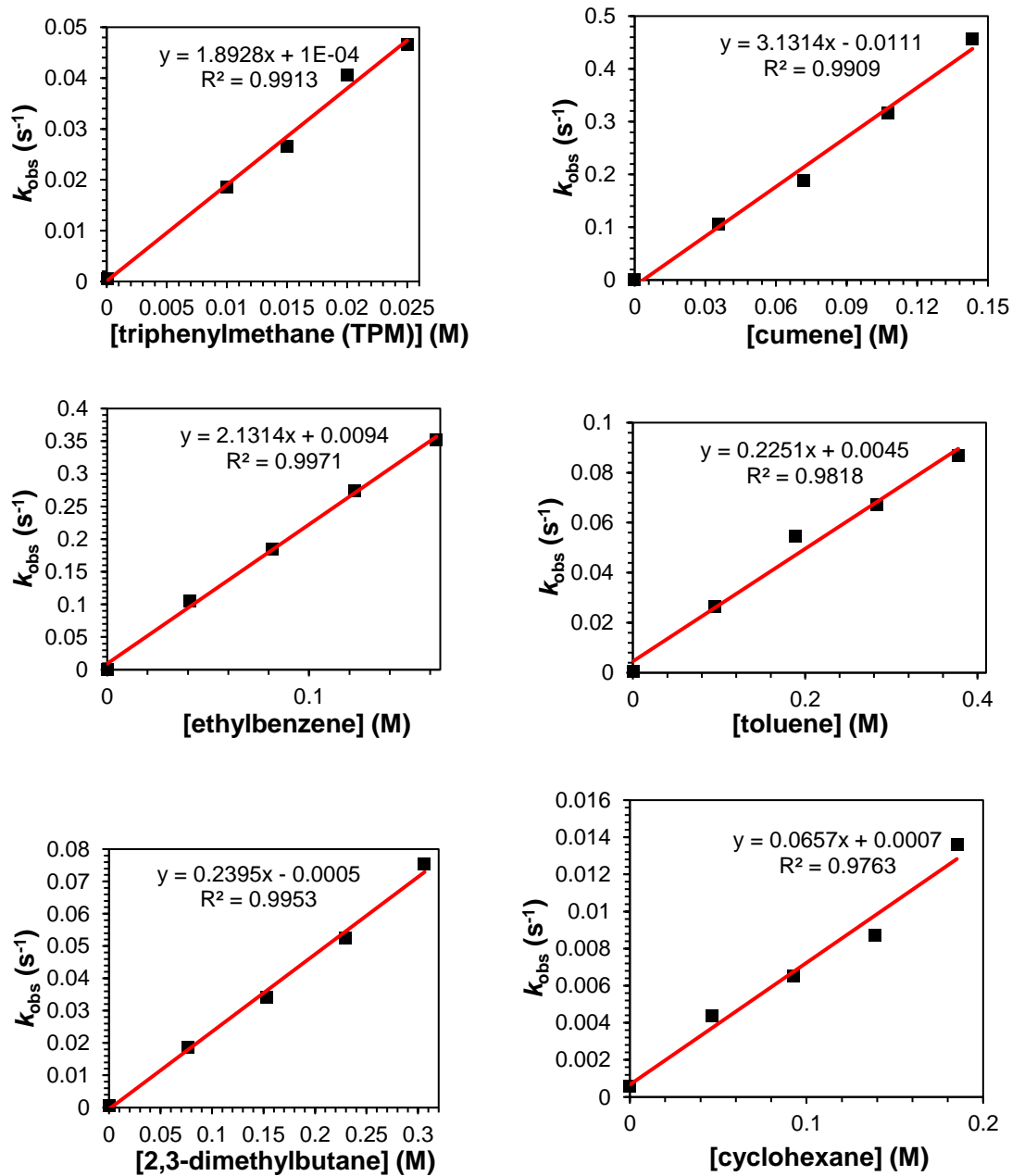


Figure 3.23 Second-order rate constants for reactions of HAT substrates and thioanisole (OAT) at 233 K with deuterated complex **3-6Me-d**.

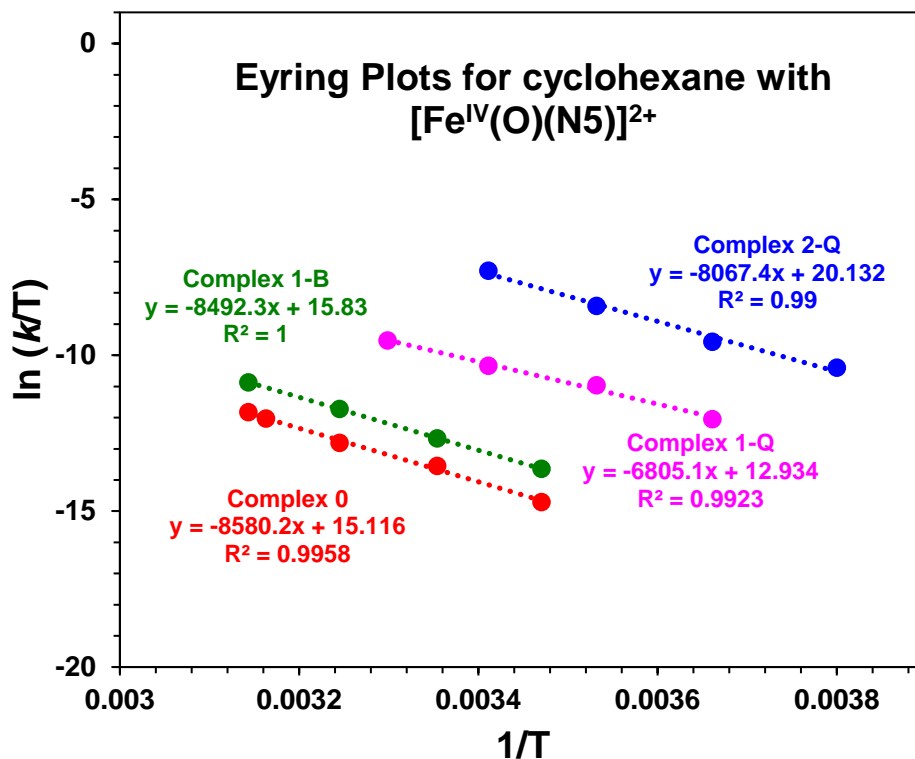


Figure 3.24 Eyring plots for the reactions of cyclohexane with different oxoiron(IV) complexes. Owing to the thermal instability or reactivity of different complexes, a temperature range of 263 K. to 318 K was used to get the rate constants.

The Table 3.7 shows the Eyring parameters for each of the reactions and their comparison with some data from Chapter 2.

Table 3.7 Eyring parameters for the reaction of different oxoiron(IV) complexes with cyclohexane and thioanisole.

Complex	ΔH^\ddagger (kJ mol ⁻¹)	ΔS^\ddagger (J mol ⁻¹ K ⁻¹)	Rate at 233 K (M ⁻¹ s ⁻¹)
Cyclohexane			
Fe ^{IV} (O)(N4Py)] ²⁺	68.1	-98.4	1.9 × 10 ⁻⁸
Fe ^{IV} (O)(N2Py2B)] ²⁺	68.1	-53.2	4.5 × 10 ⁻⁶
Fe ^{IV} (O)(N2Py2Q)] ²⁺	64.1	-61.3	1.3 × 10 ⁻⁵
0 , Fe ^{IV} (O)(BnTPEN)] ²⁺	71.3	-71.9	1.6 × 10 ⁻⁷
1-B , Fe ^{IV} (O)(BBnDPEN)] ²⁺	71.3	-65.9	2.30 × 10 ⁻⁷
1-Q , Fe ^{IV} (O)(QBnDPEN)] ²⁺	52.9	-102.3	3.0 × 10 ⁻⁵
2-Q , Fe ^{IV} (O)(DQBnPEN)] ²⁺	67.1	-30.2	1.2 × 10 ⁻⁴
Fe ^{IV} (O)(Py5Me ₂)] ²⁺	56.5	-119	8.20 × 10 ⁻⁷
Thioanisole			
Fe ^{IV} (O)(N4Py)] ²⁺	70.7	-10.8	2.0 × 10 ⁻⁴
0 , Fe ^{IV} (O)(BnTPEN)] ²⁺	73.5	+21.8	0.002
Fe ^{IV} (O)(Py5Me ₂)] ²⁺	67	-29	1.6 × 10 ⁻⁴

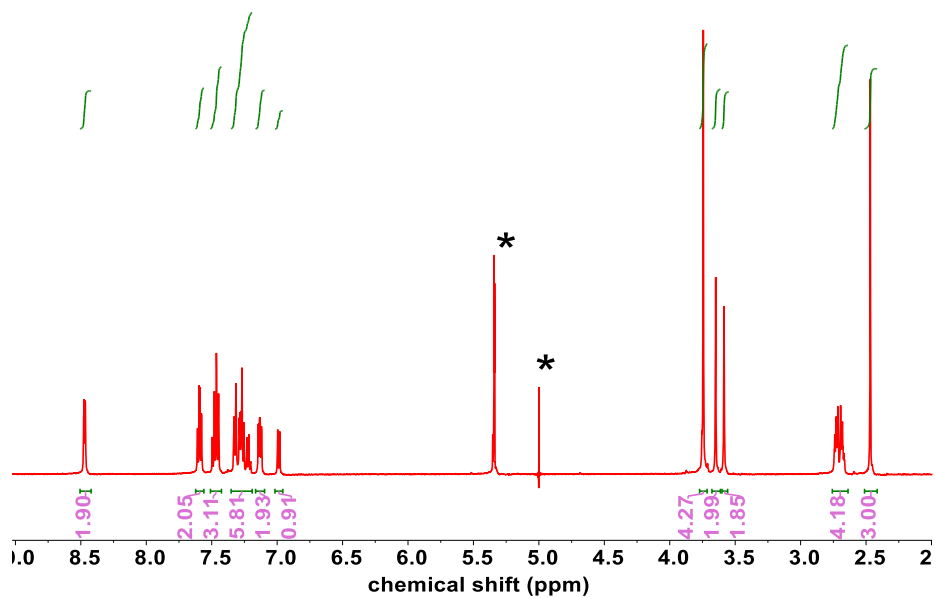
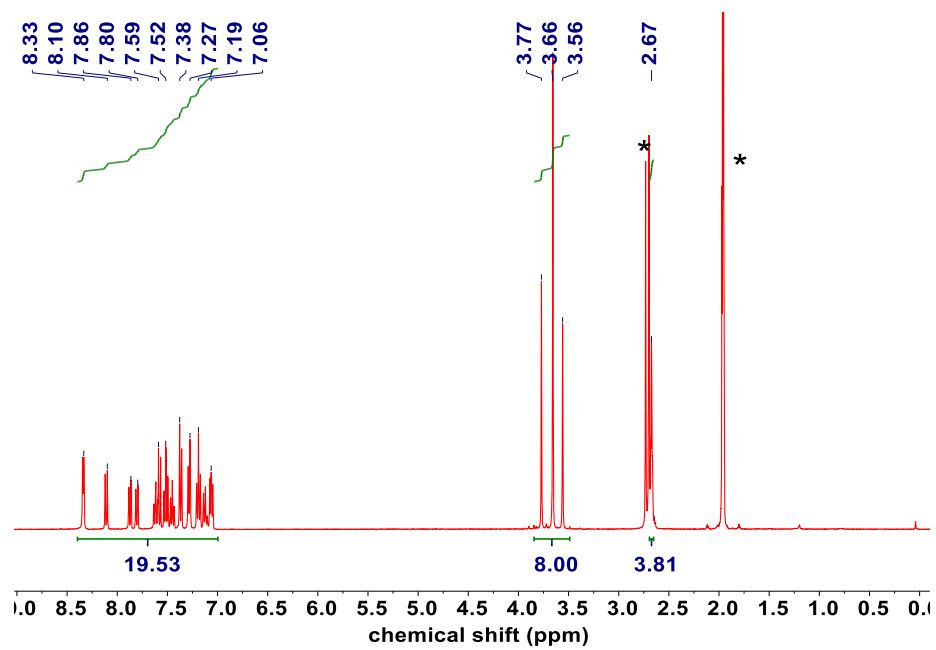


Figure 3.25 ^1H NMR spectra of Q-BnDPEN (top) in acetone- d_6 , and 6MeBnTPEN (bottom) in $\text{DCM-}d_2$ (* indicates either solvent or artifacts.)

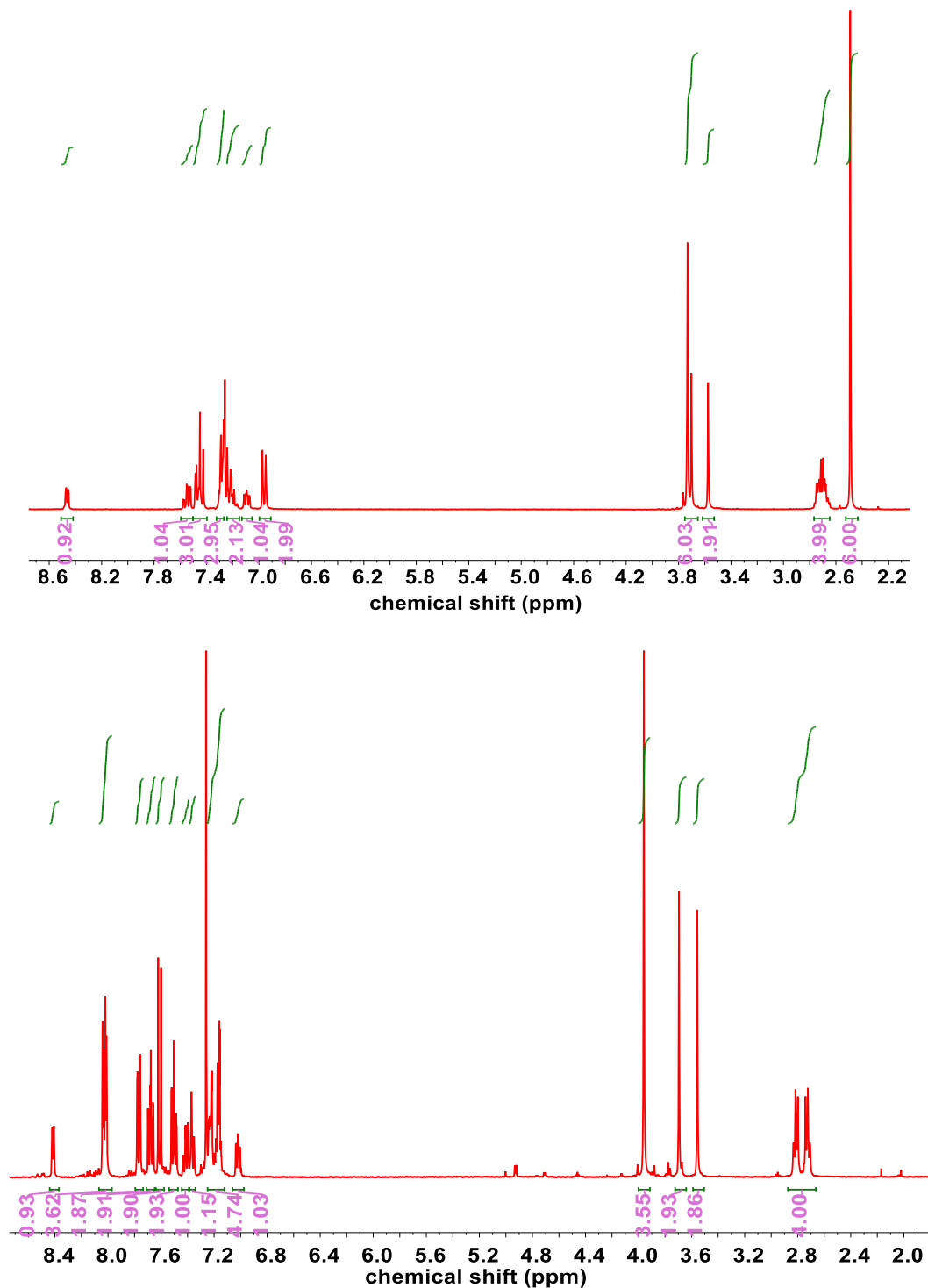


Figure 3.26 ¹H NMR spectra of 6Me₂BnTPEN (top) in acetone-*d*₆, and DQBnPEN (bottom) in DCM-*d*₂ (* indicates either solvent or artifacts.)

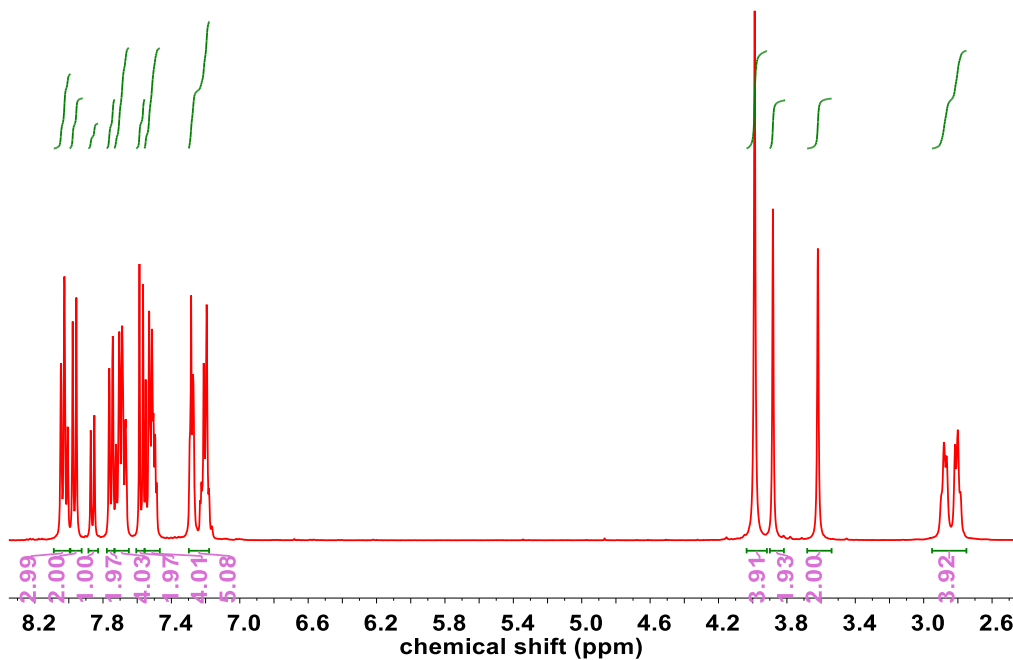
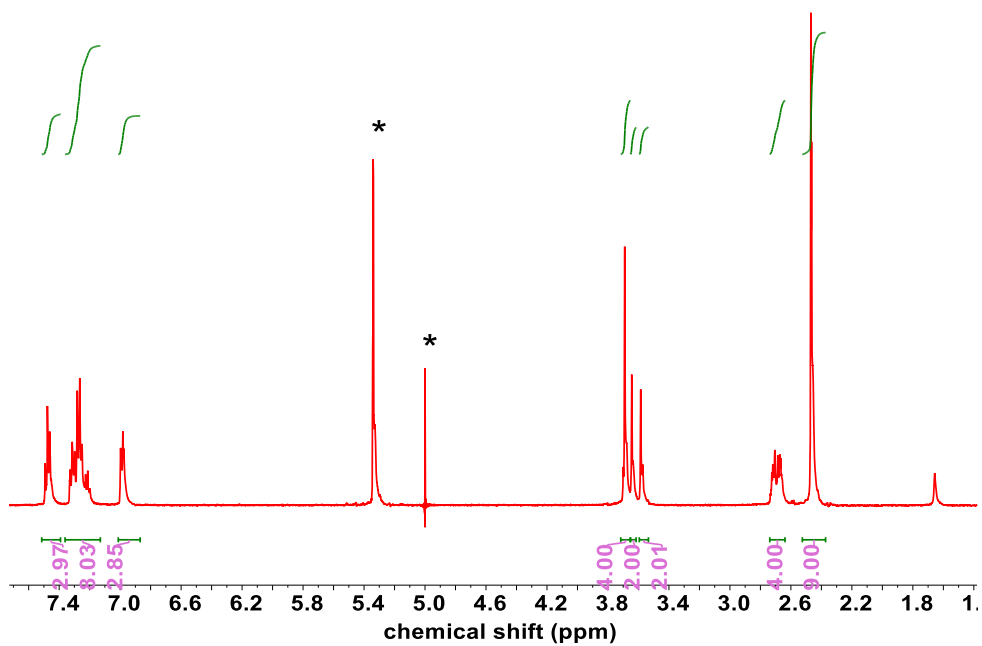


Figure 3.27 ¹H NMR spectra of 6Me₃BnTPEN (top) in DCM-d₂, and BnTQEN (bottom) in chloroform-d (* indicates either solvent or artifacts.)

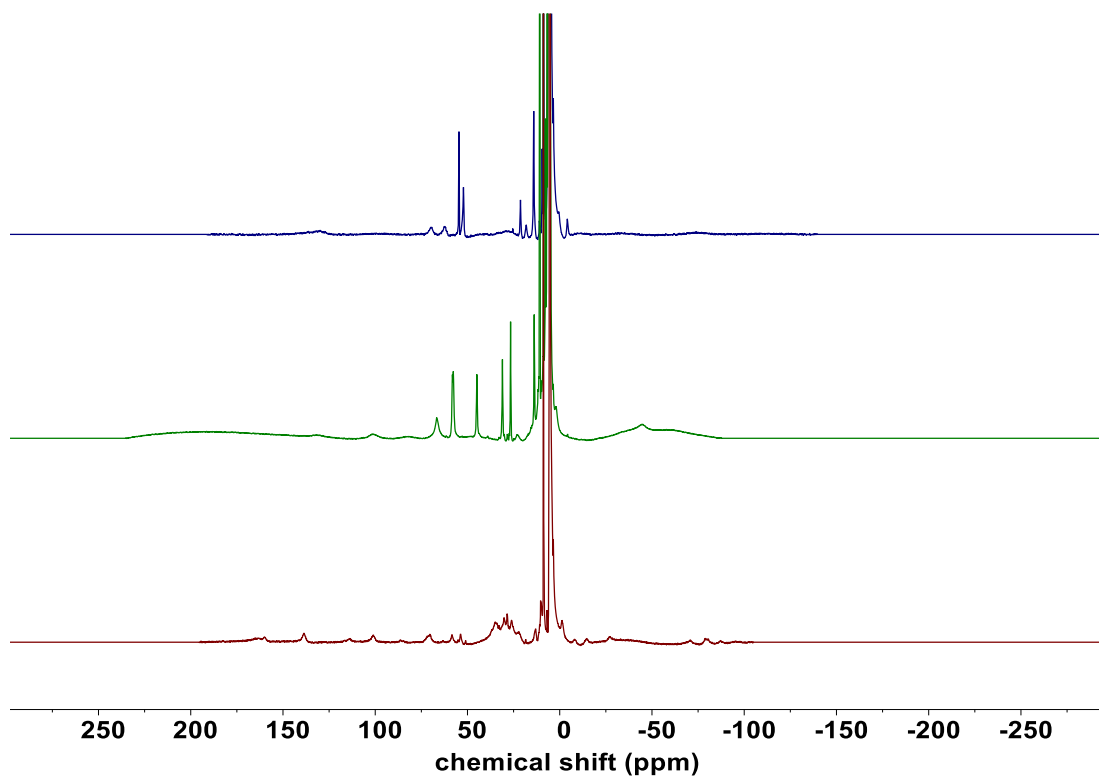


Figure 3.28 ¹H NMR spectra of iron(II) precursors with quinolines in CD₂Cl₂, [Fe^{II}(QBnDPEN)OTf]OTf (top), [Fe^{II}(DQBnPEN)OTf]OTf (middle) and [Fe^{II}(BnTQEN)OTf]OTf (bottom).

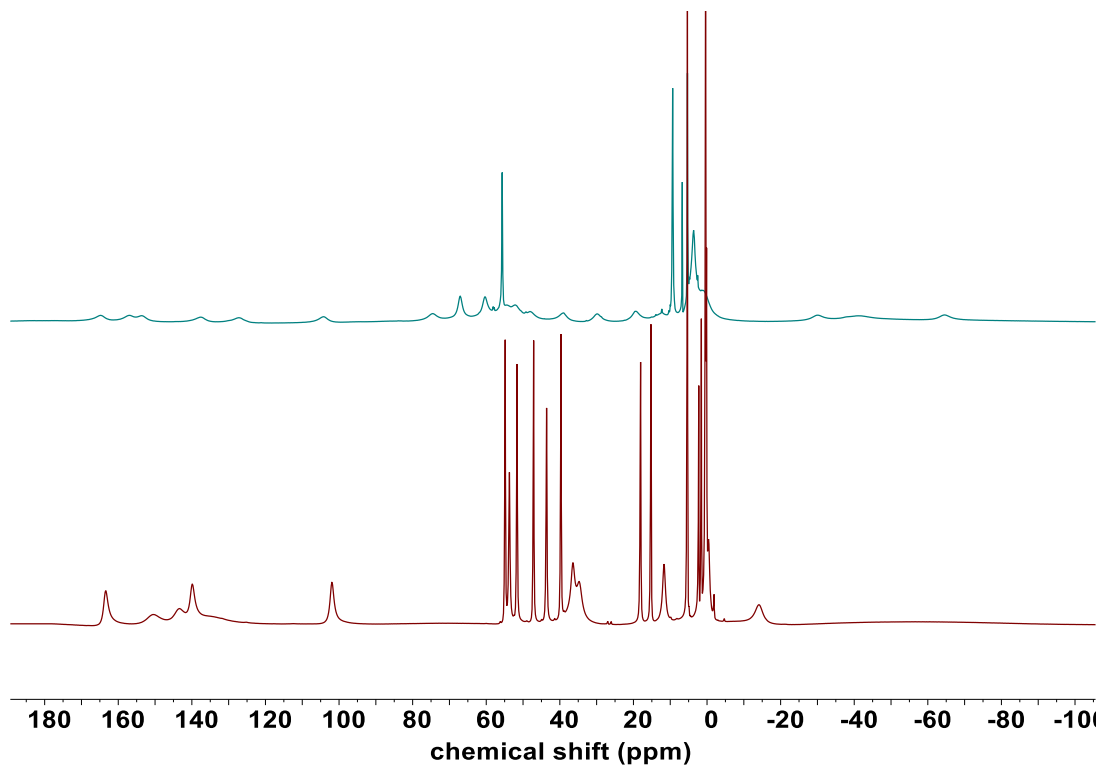


Figure 3.29 ¹H NMR spectra of [Fe^{II}(6MeBnTPEN)OTf]OTf (top) and [Fe^{II}(BnTPEN)OTf]OTf (bottom) in CD₂Cl₂.

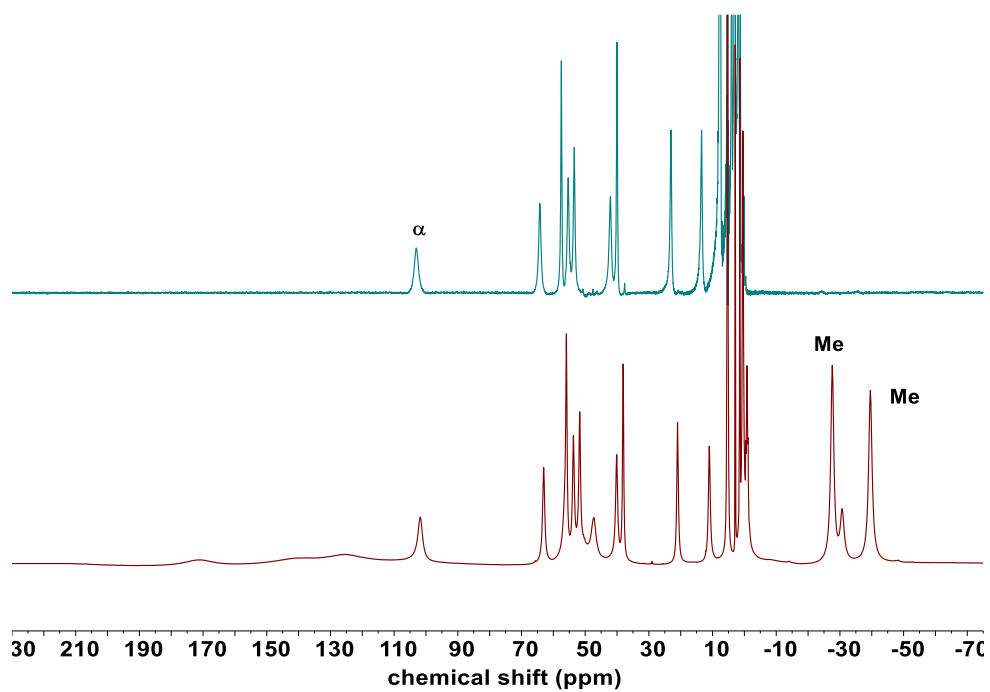


Figure 3.30 ^1H NMR spectra of $[\text{Fe}^{\text{II}}(6\text{Me}_2\text{BnTPEN})\text{OTf}]\text{OTf}$ in CD_2Cl_2 . The top spectrum has deuterated benzylic methylene and methyl protons.

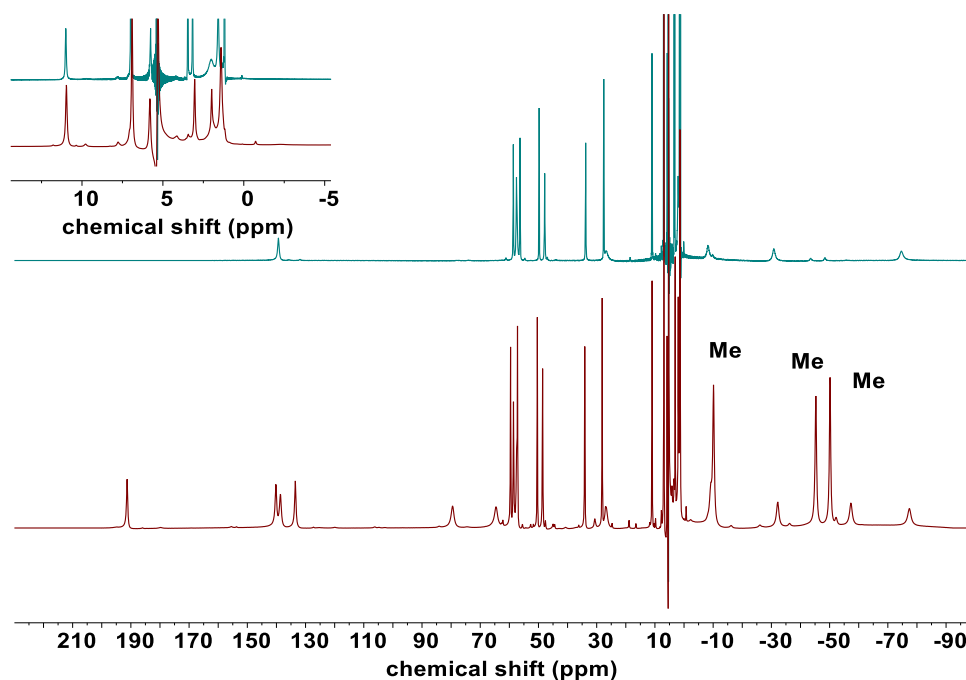


Figure 3.31 ^1H NMR spectra of $[\text{Fe}^{\text{II}}(6\text{Me}_3\text{BnTPEN})\text{OTf}]\text{OTf}$ in CD_2Cl_2 . The top spectrum has deuterated benzylic methylene and methyl protons.

3.7.1 XAS Analyses of 1-6Me, 2-6Me, 1-Q and 2-Q:

Because complexes **1-6Me-d** and **1-Q**, have short lifetimes with $t_{1/2} < 1$ h at 298 K for 1-mM MeCN solutions, growth of single crystals and structural analysis via XRD diffraction methods was not successful even at low temperatures. The doubly substituted complexes **2-Q** and **2-6Me-d** are even more unstable with 1-mM acetonitrile solutions of both complexes having half-lives of less than 5 minutes at room temperature! Therefore, structural information on these intermediates was obtained using X-ray absorption spectroscopy (XAS) experiments.

Preparation of XAS samples

Samples of the mononuclear oxoiron(IV) intermediates **1-Q** and **1-6Me-d** were generated by the addition of the appropriate oxidant (excess ArIO in 100 μ L of 2,2,2-trifluoroethanol) to a pre-cooled 5-mM acetonitrile solution of the appropriate iron(II) precursor complex at 243 K. Formation of the intermediate was followed by UV-visible spectroscopy (which yielded absorbance for its chromophore of $\lambda_{\text{max}} = 777$ nm, with over 80(5) % yields), and 1.5 mL of this solution was transferred using pre-cooled 9" pipettes, into a pre-cooled tandem XAS cup, covered with Kaptan tape. This solution was then frozen and submerged in liquid nitrogen. The 4-5 mM samples for **2-Q** and **2-6Me-d** were prepared at 263-273 K, as higher yields were obtained at higher temperatures for these complexes. The ligands of **2-6Me** and **1-6Me** were deuterated in their benzylic positions to increase their stability.

The lower yields and thermal instability of **3-Q** and **3-6Me** did not make them amenable for XAS analyses unfortunately.

XAS analyses for 1-Q and 1-6Me-d

The X-ray absorption near edge structure (XANES) of complexes **1-Q** and **1-6Me** reveal an Fe K-energy of 7123.9 eV, similar to that reported for **0** at 7123.7 eV.⁶¹ Both the complexes have a single pre-edge feature due to $1s \rightarrow 3d$ transitions at about 7114.2 eV, with a pre-edge energy for **1-Q** and **1-6Me-d** of 22.4 and 24.7 units respectively (Figure 3.32), suggesting that these complexes' environment deviates from centrosymmetry, likely due to the short $\text{Fe}^{\text{IV}}=\text{O}$ bond, as well as the asymmetric ligand environment. These areas are smaller than the 29.3(4) units reported for the parent complex **0**, but within range of a +4-oxidation state expected for ferryl complexes.

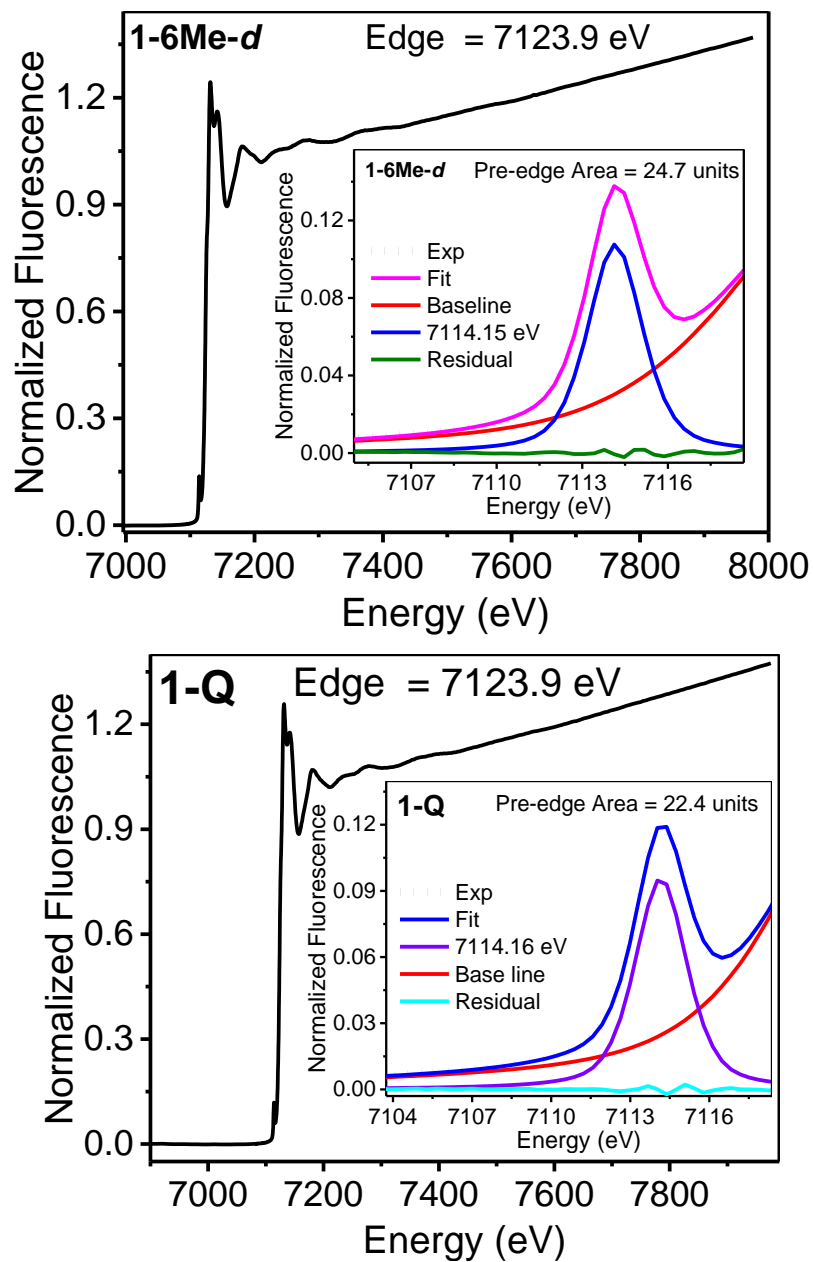


Figure 3.32 Fe K-edge X-ray absorption near-edge structures (XANES, fluorescence excitation) of iron(IV) complexes **1-6Me-d** (top) and **1-Q** (bottom)

The Fourier transformed EXAFS spectrum of the oxoiron(IV) complex **1-Q** in Figure 3.33 shows two prominent features at $R + \Delta \sim 1.5$ and 2.9 \AA . The first shell is best fit with 1 N/O scatterer at 1.66 \AA (arising from the Fe=O unit) and N/O

scatterers at 1.97 and 2.10 Å arising from the ligating atoms of polydentate ligand containing two pyridines, a quinoline and amines. The outer shell is best fit with C scatterers at 2.85 and 3.04 Å, which are associated with carbon atoms on the pyridine/quinoline rings, as also observed in the crystal structures of **0** and **1-B**.

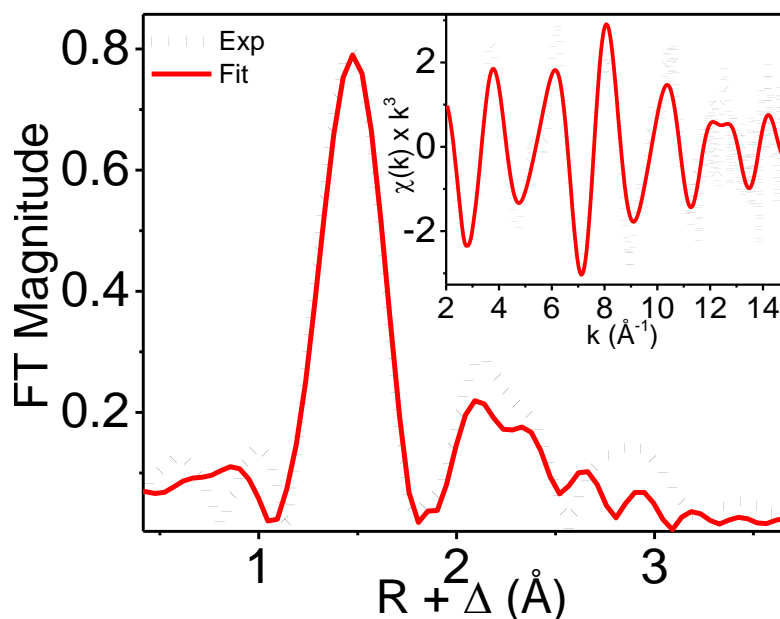


Figure 3.33 Fourier-transformed k-space EXAFS data of **1-Q** at 10 K. Inset shows the k-space spectrum.

3.7.2 Crystal structures of iron(II) complexes:

Crystal structures of 4 of the 7 new complexes reported in this chapter were obtained (Figure 3.34), by slowly diffusing diethyl ether into concentrated acetonitrile or dichloromethane solutions of iron(II) precursors to the ferryl complexes. In all cases, one triflate was found to be bound on the sixth coordination site. The unique heterocycles in the mono-substituted crystallographically characterized iron(II) complexes are a quinoline or 6-methylpyridine, and are found to be lifted partially above the plane defined by the equatorial ligands, so that quinoline H8 protons, and 6-methyl group's protons are about 2.21 and 2.31 angstroms away respectively, from the mean plane defining the pyridine parallel to the 6th coordination site. Their orientation prevents any significant steric

interactions with the sixth coordination site where the oxo is bound upon oxidation of the iron(II) center. However, the N-Fe-OTf angle is at 162°. But this angle is even smaller angle in the iron(II) crystal structure of the parent complex, and the effects of the single substitution on the parent complex are not clearly borne out in the iron(II) solid state structures supported by monosubstituted ligands.

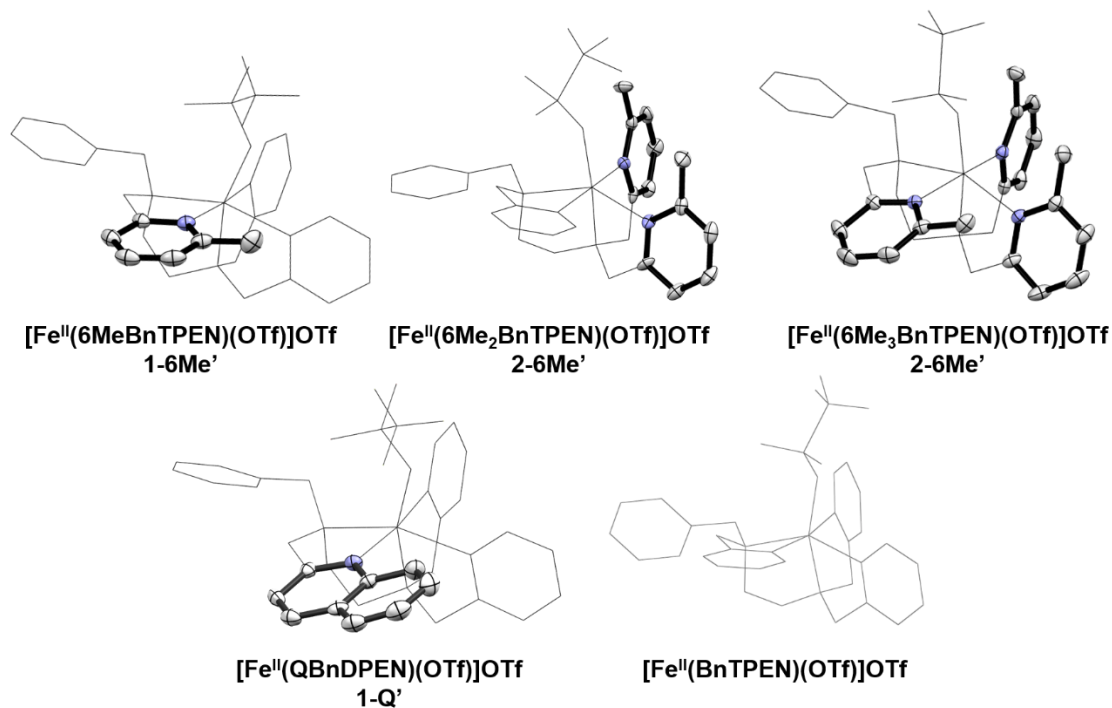


Figure 3.34 Crystal structures of iron(II) complexes supported by alpha-substituted BnTPEN framework. 50% probability ORTEPS were shown for the heterocycles that were modified, and the remaining part was shown as sticks for clarity, as was the removal of all H-atoms, solvent molecules and counterions.

When substitutions are made on the heterocycles parallel to the 6th coordination site, the N-Fe-OTf angles range from 170 to 173°. It is possible that the flexibility of the BnTPEN ligand framework mitigates the steric effects of the alpha-substitutions introduced.

Table 3.8 shows the bond lengths for the complexes. Interestingly, the typical Fe—N bond lengths are 2.2 Å. It isn't possible to discern trends in the bond lengths with increasing number of substitutions, because all of Fe—N bond lengths are equivalent within the error.

However, with introduction of each alpha-methyl substitution, there is a slight increase in the average Fe—N bond lengths going from parent complex to the complex with two substitutions. This trend however, breaks at the third methyl substitution, possibly because the compensating effects from the bends of heterocycles (which can be represented by torsion angles of the pyridine rings' plane with the Fe—O centers) also counter any steric effects imposed by the methyl groups.

Given the trends with the alpha-methyl substituted iron(II) complexes, one could expect similar patterns with the quinolyl-substituted iron(II) complexes. With the crystal structure of the [Fe(QBnTPEN)OTf]OTf, one can observe that the Fe—N bond lengths are not significantly different from [Fe(6MeBnTPEN)OTf]OTf, and there aren't many differences in the crystal structures. Owing to this observation, the iron(II) complexes for doubly and triply substituted quinolyl complexes were not examined through determination of their solid-state structures. The most important reason in lack of lengthened bond length can be attributed to the binding triflate counterion. If a solvent molecule such as acetonitrile replaced it, as has been reported the parent iron(II) complex,⁶² one can observe Fe—N_{py} bond lengths around 2.0 Å range, that are reflective of a low-spin iron(II) complexes. The binding of triflate however, enforces a high-spin state in the solid-state structures with all bond lengths being comparable with or without alpha-substitutions.

Table 3.8 Bond metrics (in Å) and angles (in °) of [Fe^{II}(BnTPEN)(X)]⁺ structures.

Bond Lengths	0' (X = MeCN)	0'	1-6Me'	2-6Me'	3-6Me'	1-Q'
Fe-N _⊥	1.994(4)	2.236(3)	2.221(2)	2.253/2.242	2.271(2)	2.197(3)
Fe-N	1.975(4)	2.189(3)	2.185(2)	2.323/2.300	2.235(2)	2.178(3)
Fe-N	1.971(4)	2.154(2)	2.225(2)	2.224/2.211	2.210(2)	2.235(3)
Fe-N _{trans-amine}	1.999(4)	2.215(3)	2.205(2)	2.197/2.205	2.203(2)	2.213(3)
Fe-N _{cis-amine}	2.077(4)	2.234(3)	2.267(1)	2.262/2.260	2.261(2)	2.275(3)
Fe-X	1.925(4)	2.032(3)	2.081(1)	2.084/2.104	2.091(1)	2.086(2)
average Fe-N _{py}	1.980(4)	2.193(2)	2.236(1)	2.244	2.240(2)	2.212(2)
average Fe-N	2.003	2.206	2.221	2.254/2.244	2.236	2.220
N-Fe-X, °	179.3	158.4	162.0	172.1/170.6	171.2	161.9
[Fe(BnTPEN)(X)] ⁺ , X = OTf unless otherwise indicated.						

3.6 Acknowledgments

The lessons learnt in this project were applied throughout my work in my time in Larry's lab. I am immensely grateful to my mentor Dr Mayank Puri, who initiated work on this project along with his undergraduate student Jaijei Chen. Mayank gave me full control on this project, not only in terms of help in syntheses, but also in terms of training on the instruments, not to mention his constant encouragement. This project has evolved with more than 4 collaborations from different universities and institutes. I would also like to acknowledge the help of Dr Andrew Jasniweski in letting me use their hood in my early days when the lab had fewer hoods than number of members. For help in obtaining the crystal structures and processing some of the XAS data, I would like to acknowledge Dr Apparao Draksharapu (now an assistant professor in IIT Kanpur). For Mössbauer and some parallel mode EPR spectroscopy that was carried out for this project, I would like to thank Dr Alex Guo and Ruixi Fan. Their help in figuring out the logistical details regarding handling samples and identifying the samples, not to mention their analysis of these complexes and their perspectives on the manuscripts was really useful. I also must

thank Dr Victor Young and Dr Gregory Rhode, for all their help in solving crystal structures in this chapter. This work would also not have been accomplished without help from Saikat Banerjee, who was my “benzimidazole” source in this project, and provided starting materials to synthesize **1-B**, and in measuring rate constants for other benzimidazole-containing complexes discussed in this work. I would also like to thank Marc C Piquette, a graduate student of Professor Rybak-Akimova, who determined some of the rate constants reported in this work. Finally I would like to thank Dr Jurek Krzystek, Dr Mike Ozerov, Dr Josh Telser for running HFEPR on some of the oxoiron(IV) complexes reported in this work.

3.7 References

1. Tamanaha, E.; Zhang, B.; Guo, Y.; Chang, W.-c.; Barr, E. W.; Xing, G.; St. Clair, J.; Ye, S.; Neese, F.; Bollinger, J. M.; Krebs, C., *J. Am. Chem. Soc.* **2016**, *138* (28), 8862-8874.
2. Wong, S. D.; Srnec, M.; Matthews, M. L.; Liu, L. V.; Kwak, Y.; Park, K.; Bell III, C. B.; Alp, E. E.; Zhao, J.; Yoda, Y.; Kitao, S.; Seto, M.; Krebs, C.; Bollinger, J. M.; Solomon, E. I., *Nature* **2013**, *499*, 320.
3. Sinnecker, S.; Svensen, N.; Barr, E. W.; Ye, S.; Bollinger, J. M.; Neese, F.; Krebs, C., *J. Am. Chem. Soc.* **2007**, *129* (19), 6168-6179.
4. Galonić Fujimori, D.; Barr, E. W.; Matthews, M. L.; Koch, G. M.; Yonce, J. R.; Walsh, C. T.; Bollinger, J. M.; Krebs, C.; Riggs-Gelasco, P. J., *J. Am. Chem. Soc.* **2007**, *129* (44), 13408-13409.
5. Eser, B. E.; Barr, E. W.; Frantom, P. A.; Saleh, L.; Bollinger, J. M.; Krebs, C.; Fitzpatrick, P. F., *J. Am. Chem. Soc.* **2007**, *129* (37), 11334-11335.
6. McDonald, A. R.; Que, L., Jr., *Coord. Chem. Rev.* **2013**, *257* (2), 414-428.
7. Krebs, C.; Galonić Fujimori, D.; Walsh, C. T.; Bollinger, J. M., *Acc. Chem. Res.* **2007**, *40* (7), 484-492.
8. Hausinger, R. P., *Critical Reviews in Biochemistry and Molecular Biology* **2004**, *39* (1), 21-68.

9. Klein, J. E. M. N.; Que, L., Biomimetic High-Valent Mononuclear Nonheme Iron-Oxo Chemistry. In *Encyclopedia of Inorganic and Bioinorganic Chemistry*, John Wiley & Sons, Ltd: 2016; p; DOI: 10.1002/9781119951438.eibc2344
10. Biswas, A. N.; Puri, M.; Meier, K. K.; Oloo, W. N.; Rohde, G. T.; Bominaar, E. L.; Münck, E.; Que, L., *J. Am. Chem. Soc.* **2015**, *137* (7), 2428-2431.
11. Rasheed, W.; Draksharapu, A.; Banerjee, S.; Young, V. G.; Fan, R.; Guo, Y.; Ozerov, M.; Nehr Korn, J.; Krzystek, J.; Telsler, J.; Que, L., *Angew. Chem. Int. Ed.* **2018**, *57* (30), 9387-9391.
12. Zang, Y.; Kim, J.; Dong, Y.; Wilkinson, E. C.; Appelman, E. H.; Que, L., Jr., *J. Am. Chem. Soc.* **1997**, *119*, 4197-4205.
13. Paine, T. K.; Costas, M.; Kaizer, J.; Que, L., Jr., *J. Biol. Inorg. Chem.* **2006**, *11* (11), 272-276.
14. Kaizer, J.; Klinker, E. J.; Oh, N. Y.; Rohde, J.-U.; Song, W. J.; Stubna, A.; Kim, J.; Münck, E.; Nam, W.; Que, L., Jr., *J. Am. Chem. Soc.* **2004**, *126* (2), 472-473.
15. Wang, D.; Ray, K.; Collins, M. J.; Farquhar, E. R.; Frisch, J. R.; Gómez, L.; Jackson, T. A.; Kerscher, M.; Waleska, A.; Comba, P.; Costas, M.; Que Jr, L., *Chem. Sci.* **2013**, *4* (1), 282-291.
16. Klinker, E. J.; Kaizer, J.; Brennessel, W. W.; Woodrum, N. L.; Cramer, C. J.; Que, L., Jr., *Angew. Chem. Int. Ed.* **2005**, *44* (24), 3690-3694.
17. Snider, V. G.; Pella, B. J.; Mukherjee, A., *Inorg. Chim. Acta* **2018**, *469*, 447-452.
18. Mitra, M.; Nimir, H.; Demeshko, S.; Bhat, S. S.; Malinkin, S. O.; Haukka, M.; Lloret-Fillol, J.; Lisensky, G. C.; Meyer, F.; Shteinman, A. A.; Browne, W. R.; Hrovat, D. A.; Richmond, M. G.; Costas, M.; Nordlander, E., *Inorg. Chem.* **2015**, *54* (15), 7152-7164.
19. Rana, S.; Dey, A.; Maiti, D., *Chem. Commun.* **2015**, *51* (77), 14469-14472.
20. Singh, R.; Ganguly, G.; Malinkin, S. O.; Demeshko, S.; Meyer, F.; Nordlander, E.; Paine, T. K., *Inorg. Chem.* **2019**.

21. de Visser, S.; Mukherjee, G.; Kumar, D.; Sastri, C.; Alili, A.; Barman, P., *Chem. Eur. J.* **2019**, 0 (Just Accepted).
22. Sahu, S.; Quesne, M. G.; Davies, C. G.; Dürr, M.; Ivanović-Burmazović, I.; Siegler, M. A.; Jameson, G. N. L.; de Visser, S. P.; Goldberg, D. P., *J. Am. Chem. Soc.* **2014**, 136 (39), 13542-13545.
23. Lőkóv, M.; Tshepelevitsh, S.; Heering, A.; Plieger, P. G.; Vianello, R.; Leito, I., *Eur. J. Org. Chem.* **2017**, 2017 (30), 4475-4489.
24. Decker, A.; Rohde, J.-U.; Que, L., Jr.; Solomon, E. I., *J. Am. Chem. Soc.* **2004**, 126 (17), 5378-5379.
25. Jackson, T. A.; Rohde, J.-U.; Seo, M. S.; Sastri, C. V.; DeHont, R.; Stubna, A.; Ohta, T.; Kitagawa, T.; Münck, E.; Nam, W.; Que, L., Jr., *J. Am. Chem. Soc.* **2008**, 130 (37), 12394-12407.
26. Bigelow, J. O.; England, J.; Klein, J. E. M. N.; Farquhar, E. R.; Frisch, J. R.; Martinho, M.; Mandal, D.; Münck, E.; Shaik, S.; Que, L., *Inorg. Chem.* **2017**, 56 (6), 3287-3301.
27. Kepp, K. P., *Inorg. Chem.* **2016**, 55 (6), 2717-2727.
28. Kepp, K. P., *Coord. Chem. Rev.* **2013**, 257 (1), 196-209.
29. Knizia, G., <http://www.iboview.org/>.
30. Knizia, G.; Klein, J. E. M. N., *Angew. Chem. Int. Ed.* **2015**, 54 (18), 5518-22.
31. Draksharapu, A.; Rasheed, W.; Klein, J. E. M. N.; Que, L., *Angew. Chem. Int. Ed.* **2017**, 56 (31), 9091-9095.
32. Ahlrichs, R.; Bär, M.; Häser, M.; Horn, H.; Kölmel, C., *Chem. Phys. Lett.* **1989**, 162 (3), 165-169.
33. Furche, F.; Ahlrichs, R.; Hättig, C.; Klopper, W.; Sierka, M.; Weigend, F., *WIREs Comput. Mol. Sci.* **2014**, 4 (2), 91-100.
34. Zhao, Y.; Truhlar, D. G., *J. Phys. Chem. A* **2005**, 109 (25), 5656-5667.
35. Weigend, F.; Ahlrichs, R., *Phys. Chem. Chem. Phys.* **2005**, 7 (18), 3297-3305.

36. Averkiev, B. B.; Truhlar, D. G., *Catal. Sci. Technol.* **2011**, *1* (8), 1526-1529.
37. Ribeiro, R. F.; Marenich, A. V.; Cramer, C. J.; Truhlar, D. G., *J. Phys. Chem. B* **2011**, *115* (49), 14556-14562.
38. Sierka, M.; Hogeckamp, A.; Ahlrichs, R., *J. Chem. Phys.* **2003**, *118* (20), 9136-9148.
39. Weigend, F., *Phys. Chem. Chem. Phys.* **2006**, *8* (9), 1057-1065.
40. Monte Pérez, I.; Engelmann, X.; Lee, Y.-M.; Yoo, M.; Kumaran, E.; Farquhar, E. R.; Bill, E.; England, J.; Nam, W.; Swart, M.; Ray, K., *Angew. Chem. Int. Ed.* **2017**, *56* (46), 14384-14388.
41. Seo, M. S.; Kim, N. H.; Cho, K.-B.; So, J. E.; Park, S. K.; Clémancey, M.; Garcia-Serres, R.; Latour, J.-M.; Shaik, S.; Nam, W., *Chem. Sci.* **2011**, *2* (6), 1039-1045.
42. England, J.; Guo, Y.; Farquhar, E. R.; Young Jr, V. G.; Münck, E.; Que Jr, L., *J. Am. Chem. Soc.* **2010**, *132* (25), 8635-8644.
43. Codolà, Z.; Gamba, I.; Acuña-Parés, F.; Casadevall, C.; Clémancey, M.; Latour, J.-M.; Luis, J. M.; Lloret-Fillol, J.; Costas, M., *J. Am. Chem. Soc.* **2019**, *141* (1), 323-333.
44. Klein Gebbink, R. J. M.; Chen, J., *ACS Catalysis* **2019**.
45. Banerjee, S.; Rasheed, W.; Fan, R.; Draksharapu, A.; Oloo, W. N.; Guo, Y.; Que Jr, L., *Angew. Chem. Int. Ed.* **2019**, *Submitted*.
46. Lee, N. Y.; Mandal, D.; Bae, S. H.; Seo, M. S.; Lee, Y.-M.; Shaik, S.; Cho, K.-B.; Nam, W., *Chem. Sci.* **2017**, *8* (8), 5460-5467.
47. Bae Seong, H.; Seo Mi, S.; Lee, Y. M.; Cho, K. B.; Kim, W. S.; Nam, W., *Angew. Chem. Int. Ed.* **2016**, *55* (28), 8027-8031.
48. Denler, M. C.; Massie, A. A.; Singh, R.; Stewart-Jones, E.; Sinha, A.; Day, V. W.; Nordlander, E.; Jackson, T. A., *Dalton Trans.* **2019**.
49. Hagen, K. S., *Inorg. Chem.* **2000**, *39*, 5867-5869.
50. Duelund, L.; Hazell, R.; McKenzie, C. J.; Preuss Nielsen, L.; Toftlund, H., *J. Chem. Soc., Dalton Trans.* **2001**, (2), 152-156.

51. Schatz, M.; Leibold, M.; Foxon, S. P.; Weitzer, M.; Heinemann, F. W.; Hampel, F.; Walter, O.; Schindler, S., *Dalton Trans.* **2003**, (8), 1480-1487.
52. Puri, M.; Company, A.; Sabenya, G.; Costas, M.; Que, L., *Inorg. Chem.* **2016**, 55 (12), 5818-5827.
53. Hu, Y.; Liang, L.; Wei, W.-t.; Sun, X.; Zhang, X.-j.; Yan, M., *Tetrahedron* **2015**, 71 (9), 1425-1430.
54. Rasheed, W.; Draksharapu, A.; Banerjee, S.; Young Victor, G.; Fan, R.; Guo, Y.; Ozerov, M.; Nehrkorn, J.; Krzystek, J.; Telser, J.; Que, L., *Angew. Chem. Int. Ed.* **2018**, (0), DOI: 10.1002/anie.201804836.
55. APEX3, Bruker Analytical X-ray Systems, Madison, WI (2016).
56. SADABS, Bruker Analytical X-ray Systems, Madison, WI (2016).
57. SAINT, Bruker Analytical X-ray Systems, Madison, WI (2016).
58. SHELXTL, Bruker Analytical X-Ray Systems, Madison, WI (2008).
59. Sheldrick, G. M., *Acta Cryst.* **A64**, 112-122 (2008).
60. Sheldrick, G. M., *Acta Cryst.* **C71**, 3-8 (2015).
61. Rohde, J.-U.; Torelli, S.; Shan, X.; Lim, M. H.; Klinker, E. J.; Kaizer, J.; Chen, K.; Nam, W.; Que, L., *J. Am. Chem. Soc.* **2004**, 126 (51), 16750-16761.
62. Norma Ortega-Villar; Víctor M. Ugalde-Saldívar; M. Carmen Muñoz; Luis A. Ortiz-Frade; José G. Alvarado-Rodríguez; José A. Real, a.; Rafael Moreno-Esparza*, **2007**.

Chapter 4:
Use of NMR Spectroscopy to Characterize Oxoiron(IV) Complexes

4.1 Introduction

In many non-heme oxygenases, oxoiron(IV) intermediates in the quintet ($S = 2$) spin state have been trapped as key species that oxidize strong C–H bonds.¹ A similarly reactive oxoiron(IV) species in the $S = 2$ spin state has been recently characterized in an iron-containing zeolite, and like soluble methane monooxygenase, it can also oxidize methane to methanol.² However, an overwhelming majority of the 90 or so synthetic molecular analogs of these intermediates contrasts the enzymatic and zeolitic intermediates with their triplet ($S = 1$) ground spin state and lower reactivity.³

Typically, characterization of oxoiron(IV) intermediates is done through the use of Mössbauer, XAS (X-ray Absorption Spectroscopy), X-ray crystallography, resonance Raman, IR, and UV-vis absorption spectroscopies. NMR-based studies that rely on differences in paramagnetic shifts to investigate spin states and spin-crossover behavior in solution state of molecules have only been recently applied to some coordination complexes of nickel, iron and cobalt.⁴ However, despite their relative accessibility, ¹H NMR studies have traditionally not been an important part of characterizations usually done for $S = 1$ oxoiron(IV) complexes, and not reported at all for any $S = 2$ oxoiron(IV) complexes.

This is likely owed to some non-trivial challenges associated with this technique that need to be addressed with this goal: 1) some of these intermediates are highly unstable and require low temperature NMR spectroscopy and careful handling to obtain such data; 2) complications in the interpretation of the NMR data prevent accurate assignments, and if line broadening is high due to slow electronic relaxation, these peaks are not even observable; and 3) presence of additives such as oxidants and solvents leads to complex mixtures of already short-lived intermediates, increasing uncertainty in the assignments.⁵⁻⁷ Although Evan's method can be successfully used to determine solution-state spin states of inorganic complexes at given temperatures (provided they're pure, have insignificant decay, and their exact concentrations are known), it is quite unreliable

and rarely carried out for unstable oxoiron(IV) intermediates and should be treated with caution.

Interestingly, over *half* of the oxoiron(IV) molecules reported so far incorporate heterocycles in their ligand structures. While many of these complexes have not been crystallographically characterized, their $S = 1$ iron(IV) centers possess electronic relaxation properties that give rise to relatively sharp and well-resolved, paramagnetically shifted peaks in their ^1H NMR spectra.⁸⁻¹⁰ Earlier studies have used NMR spectroscopy to study patterns of resonances displayed by pyridyl protons in oxoiron(IV) complexes to glean important structural insight into their liquid solution-state structures.¹⁰⁻¹¹ But its potential to provide additional information on spin states (typically determined through variable field and temperature Mössbauer spectroscopy) has not been realized. Therefore, it is critical to investigate the NMR properties of these complexes to provide the bioinorganic community a relatively more accessible tool in addition to Mössbauer spectroscopy that can help determine such information at higher temperatures.

Recently Borgogno *et al.* have successfully benchmarked DFT methods to address this potential opportunity, and their calculated NMR spectra for $S = 1$ oxoiron(IV) complexes supported by TPA (TPA = tris tris(pyridyl-2-methyl)-amine), TMC (TMC = 1,4,8,11-tetramethyl-1,4,8,11-tetraazacyclotetra-decane) and its variants are in agreement with some experimentally observed data.¹²⁻¹⁷ Despite reports of a few $S = 2$ oxoiron(IV) species supported by various ligands,¹⁸⁻²¹ none have been characterized by ^1H NMR spectroscopy.

The most reactive pair of oxoiron(IV) complexes reported thus far incorporate quinolines or benzimidazoles in their structures, and have different spin states. $[\text{Fe}^{\text{IV}}(\text{O})(\text{Me}_3\text{NTB})(\text{L})]^{2+}$ is one of these oxoiron(IV) complexes, where Me_3NTB (tris(*N*-methylbenzimidazolyl-2-methyl)amine) is a tripodal ligand (with three pendant *N*-methylbenzimidazoles).²² The high reactivity of this complex has been a subject of recent intense curiosity, and it has also been proposed to have different geometry and spin states at 233 K and at 4 K.²³⁻²⁴ NMR spectroscopy

may be useful in probing this proposed spin-crossover behavior, which has been shown for many ferrous and ferric complexes.²⁵ This example highlights a potential use of NMR spectroscopy as a convenient tool to not only assess liquid-solution state structure, but also assign spin states on these intermediates at different temperatures. However, thermal instability (few minutes at 233 K) of this complex has prevented any experimental information from being obtained.

In contrast to the pyridine and *N*-methylbenzimidazole donors, the steric effects of quinoline donors have been crystallographically shown to increase the Fe–N bond lengths in a ferryl complex (see Chapter 2).²⁶ In the $S = 1$ oxoiron(IV) complex supported by TPA (tris(2-pyridylmethyl)amine), namely $[\text{Fe}^{\text{IV}}(\text{O})(\text{TPA})(\text{L})]^{2+}$ (**0**), replacement of the three pendant pyridines with quinolines (or alpha-substituents) changes the spin state of the parent complex to $S = 2$, resulting in a very reactive complex, $[\text{Fe}^{\text{IV}}(\text{O})(\text{TQA})(\text{L})]^{2+}$ (**3**), where TQA = tris(2-quinolyl-methyl)amine.¹⁸ Our efforts to figure out the point at which this spin change occurs has led us to introduce alpha-substituents on pyridines and/or replace pyridines with quinolines systematically on the TPA framework, and study the resulting complexes with ^1H NMR spectroscopy and also probe their structure. Our findings, described herein, also highlight the potential of ^1H NMR spectroscopy as an alternative tool to Mössbauer spectroscopy, to determine the spin state for oxoiron(IV) complexes containing quinolines at higher temperature or in liquid solution state. We also use this technique to identify a spin-crossover behavior in one of the resulting complexes in liquid solution state.

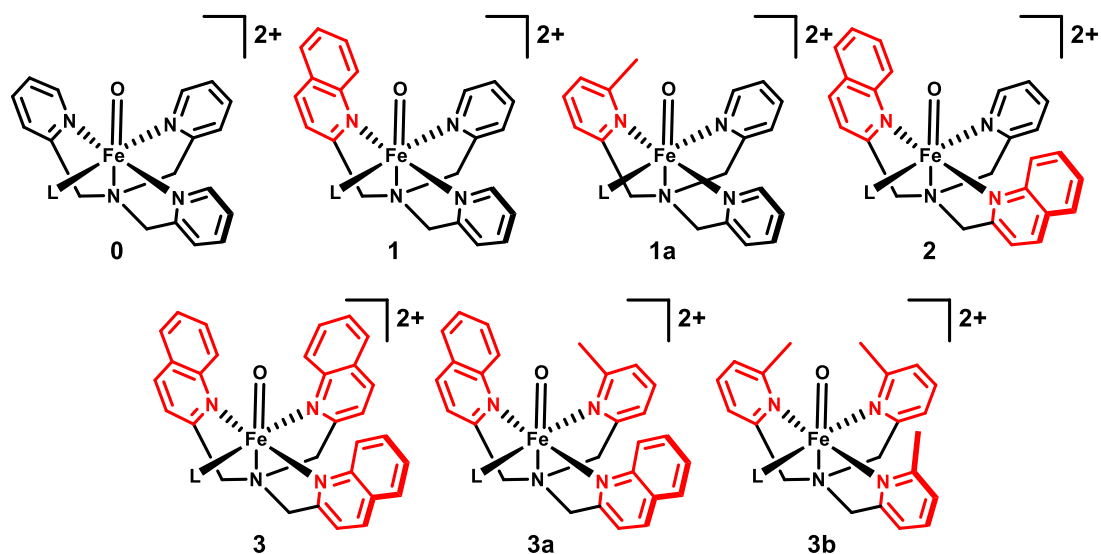


Figure 4.1 Oxoiron(IV) complexes examined in this work that contain increasing number of quinolines or pyridine donors with alpha-substituents.

The sequential introduction of alpha-methyl substituents on pyridines, or replacement of pyridines with quinolines in **0** results in newer mono-, di- and tri-substituted complexes, $[\text{Fe}^{\text{IV}}(\text{O})(\text{QBPA})(\text{L})]^{2+}$ (**1**) (QBPA = (2-quinolylmethyl)bis(2-pyridylmethyl)amine) and $[\text{Fe}^{\text{IV}}(\text{O})(6\text{MeTPA})(\text{L})]^{2+}$ (**1a**) (6MeTPA = (6-methyl-2-pyridylmethyl)bis(2-pyridylmethyl)amine), $[\text{Fe}^{\text{IV}}(\text{O})(\text{BQPA})(\text{L})]^{2+}$ (**2**) (BQPA = (2-pyridylmethyl)bis(2-quinolylmethyl)amine), $[\text{Fe}^{\text{IV}}(\text{O})(\text{TQA})(\text{L})]^{2+}$ (**3**). These modifications can generally be classified as alpha-substituents on pyridines. All complexes except **2** have been reported before.^{18, 27-28} The notations of the complexes indicate the number of quinolines or alpha-substituents in each complex (Figure 4.1). In order to gain better insight into the complexes, an additional variant of **2** is also examined, where the ferryl complex is only different from **2** in that it has an alpha-methyl substituent introduced on the lone pyridine donor (as represented by complex **3a**, $[\text{Fe}^{\text{IV}}(\text{O})(6\text{MeBQPA})(\text{L})]^{2+}$, where 6MeBQPA = (6-methylpyridyl-2-methyl)bis(2-quinolylmethyl)amine). A variant of **3** and **3a** which replaces all the quinolines with 6-methylpyridines is also examined, namely complex **3b**, $[\text{Fe}^{\text{IV}}(\text{O})(6\text{Me}_3\text{TPA})(\text{L})]^{2+}$, where 6Me₃TPA = tris(6-methylpyridyl-2-methyl)amine.

The complexes studied in this report were examined via ^1H NMR spectroscopy at 233 K to examine effects of their spin states on chemical shifts, and via Mössbauer spectroscopy at cryogenic temperatures to shed light on their spin state in frozen solution states. Our results, described below, lead us to identify **2** as the first oxoiron(IV) complex with spin-crossover behavior via NMR spectroscopy, and its variants **3a** and **3b** are characterized as $S = 2$ oxoiron(IV) complexes, similar to the triply substituted complex $[\text{Fe}^{\text{IV}}(\text{O})(\text{TQA})(\text{L})]^{2+}$ (**3**). **3a** and **3b** also represent the first characterized $S = 2$ complexes containing pyridines with alpha-methyl substituents.

4.2 Results

4.2.1 Generation of oxoiron(IV) complexes and their thermal stability

All complexes in this series can be generated from their ferrous precursors in acetonitrile at appropriate temperatures. Complexes **0**, **1** and **1a** are generated upon addition of 1-1.2 equivalents of either peracetic acid in acetonitrile,²⁷⁻²⁸ or 2-($t\text{BuSO}_2$)- $\text{C}_6\text{H}_4\text{IO}$ (ArIO) in 2,2,2-trifluoroethanol or dichloromethane- d_2 . The remaining complexes can only be generated upon addition of 2 equivalents of ArIO in 2,2,2-trifluoroethanol or CD_2Cl_2 .

Complexes **0**, **1** and **1a** are relatively stable at 233 K, with half-lives of at least a few hours depending on which oxidant is used to generate the complex. Complex **0** has a half-life of over 24 h at 233 K, but **1** and **1a** are stable for a few hours at 233 K (Table 4.1). The remaining complexes **2**, **3**, **3a** and **3b** are not particularly stable at 233 K with half-lives of only a 2, 15, 5, and 4 minutes respectively, which makes studies of their properties quite challenging at 233 K.

4.2.2 Mössbauer and Absorption Spectroscopy of Ferryl Complexes

UV-Visible Absorption Spectroscopy

Complexes **0**, **1**, **1a** and **2** exhibit near-IR absorption bands typical of $S = 1$ $\text{Fe}^{\text{IV}}(\text{O})$ complexes, which can be assigned to d-d transitions (Figure 4.2). For each

pyridine replacement with quinoline or each introduction of an alpha-methyl substituent on pyridine in this series of tetradentate oxoiron(IV) complexes, the characteristic ferryl bands red-shift by about 50-65 nm when an alpha-substituent is introduced on the pyridine. Similar but smaller red-shifts are observed on BnTPEN (see Chapter 3) and the N4Py (Chapter 2) ligand frameworks at about 30-40 nm per alpha-substituent.²⁹ So the λ_{\max} values for the near-IR features in complex **1** are at 775 nm (λ_{\max} value for complex **1a** is 770), and at 840 nm for complex **2**. This series of complexes shows a larger progressive weakening of the ligand field strength as pyridine donors are replaced with quinolines (or alpha-methyl substituents are introduced on pyridines) successively. The extinction coefficient of the bands at their respective λ_{\max} values in the cases of **0**, **1** and **1a** is $300 \text{ M}^{-1} \text{ cm}^{-1}$ but becomes smaller in **2** (about $200 \text{ M}^{-1} \text{ cm}^{-1}$). Lowered extinction coefficients are also seen in the oxoiron(IV) complexes supported by the BnTPEN framework, when a single alpha-substitution is introduced on its parent complex $[\text{Fe}^{\text{IV}}(\text{O})(\text{BnTPEN})]^{2+}$. The near-IR bands of **0** and **1**, and **1a** are typical for *bona fide* $S = 1$ complexes. While **2** represents near-IR bands and Mössbauer parameters that indicate an $S = 1$ oxoiron(IV) complex, it has high absorption features below 550 nm, in contrast to **0**, **1** and **1a**, which only have such absorption features below 450 nm.

The absorption features of the complexes **3**, **3a** and **3b** are very different from those seen in **0**, **1**, and **1a**. Complexes **3a** and **3b** have absorption features like those of **3** ($\lambda_{\max} = 650 \text{ nm}$) (Figure 4.2), with λ_{\max} of their bands at 640 nm and 630 nm respectively. The extinction coefficients of these complexes at their respective λ_{\max} values are $300 \text{ M}^{-1} \text{ cm}^{-1}$.

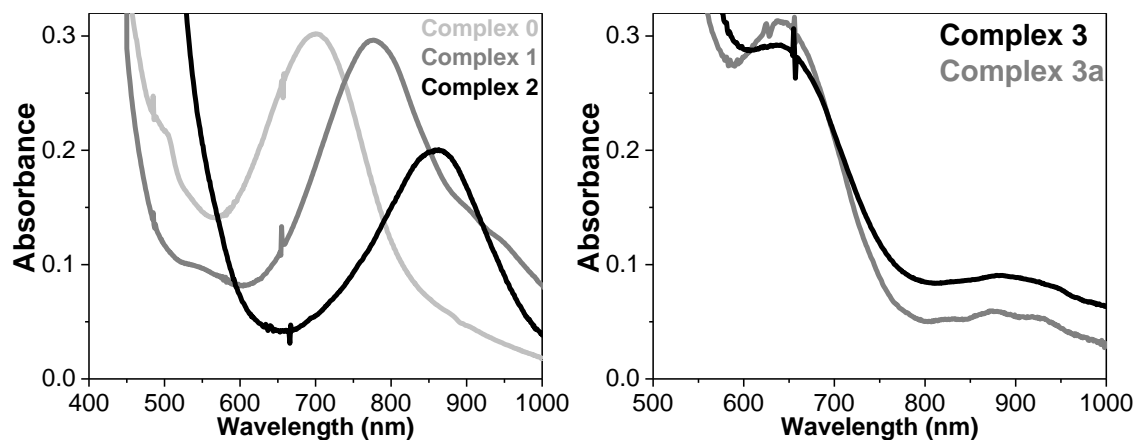


Figure 4.2 UV-visible spectra of 1-mM acetonitrile solutions of oxoiron(IV) complexes **0** (light gray), **1** (gray) and **2** (black) on the left; and **3** (light gray), **3a** (gray) and **3b** (black) on the right at 233 K.

Table 4.1 Properties of oxoiron(IV) complexes evaluated in this work.

Complexes	0	1	1a	2	3	3a	3b
λ_{\max} , nm (ϵ , $M^{-1} \text{ cm}^{-1}$)	720 (300)	775 (300)	770 (300)	850 (200)	650 (300) 900 (75)	640 900	630 (300) 900 (75)
δ , mm/s	0.01	0.02	-	0.04	0.24	0.22	0.24
ΔE_Q , mm/s	0.92	0.75	-	0.87	-1.05	0.94	
*S at 4 K	1	1	1	1	2	2	2
**S at 233 K	1	1	1	2	2	2	2
$t_{1/2}$, min (T in K)	> 1 day (233)	16 (283)	20 (283)	2 (233)	15 (233)	5 (233)	4 (233)
*based on Mössbauer spectroscopy. **based on NMR analysis.							

Mössbauer Spectroscopy:

Complexes **1** and **2** exhibit Mössbauer spectra obtained at 4 K with parameters like those of **0**, with isomer shifts at 0.01 to 0.04 mm/s, and quadrupole splitting in the range of 0.75 to 0.95 mm/s. Their behavior in applied magnetic fields also indicates an $S = 1$ spin-manifold, typical of most non-heme oxoiron(IV) complexes described in the past fifteen years. In contrast, complex **3**, **3a** and **3b** have much larger isomer shifts at 0.22 to 0.24 mm/s compared to those of **0**, **1** and **2**. This increase in isomer shift reflects a change in spin state to $S = 2$, as confirmed by

variable field and variable temperature Mössbauer studies. Their electronic properties are like those of the enzymatic intermediates.

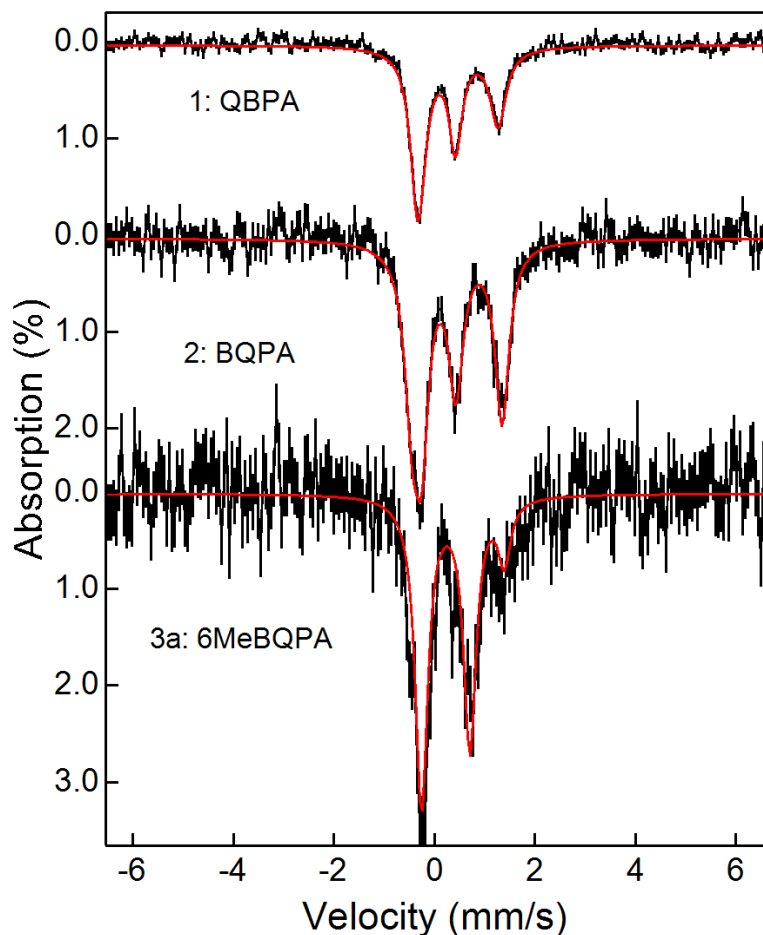


Figure 4.3 Mössbauer spectra of **1**, **2** and **3a**.

4.2.3 NMR spectroscopy of Oxoiron(IV) Complexes

4.2.3.1 NMR Assignment of $S = 1$ complexes **0**, **1** and **1a**

Complex 0:

The $S = 1$ complexes discussed in this series are relatively stable and have favorable relaxation properties for their heterocyclic protons. Figure 4.4 shows that the sharp resonances in the ^1H NMR spectrum of **0** at 233 K can be assigned by

comparison to $[\text{Fe}^{\text{IV}}(\text{O})(\text{N4Py})]^{2+}$ (where N4Py = *N,N*-bis(2-pyridylmethyl)-*N*-bis(2-pyridyl)methylamine). This is a *bona fide* $S = 1$ complex with an axial amine and four equatorial pyridines, each of which is aligned roughly parallel to the ferryl unit. The mirror symmetry in this complex (established from its solid-state structure) allows this complex to have two sets of paramagnetically shifted peaks, in which each set has a β , γ and β' resonance between 50 to -30 ppm at 298 K (Figure 4.4).

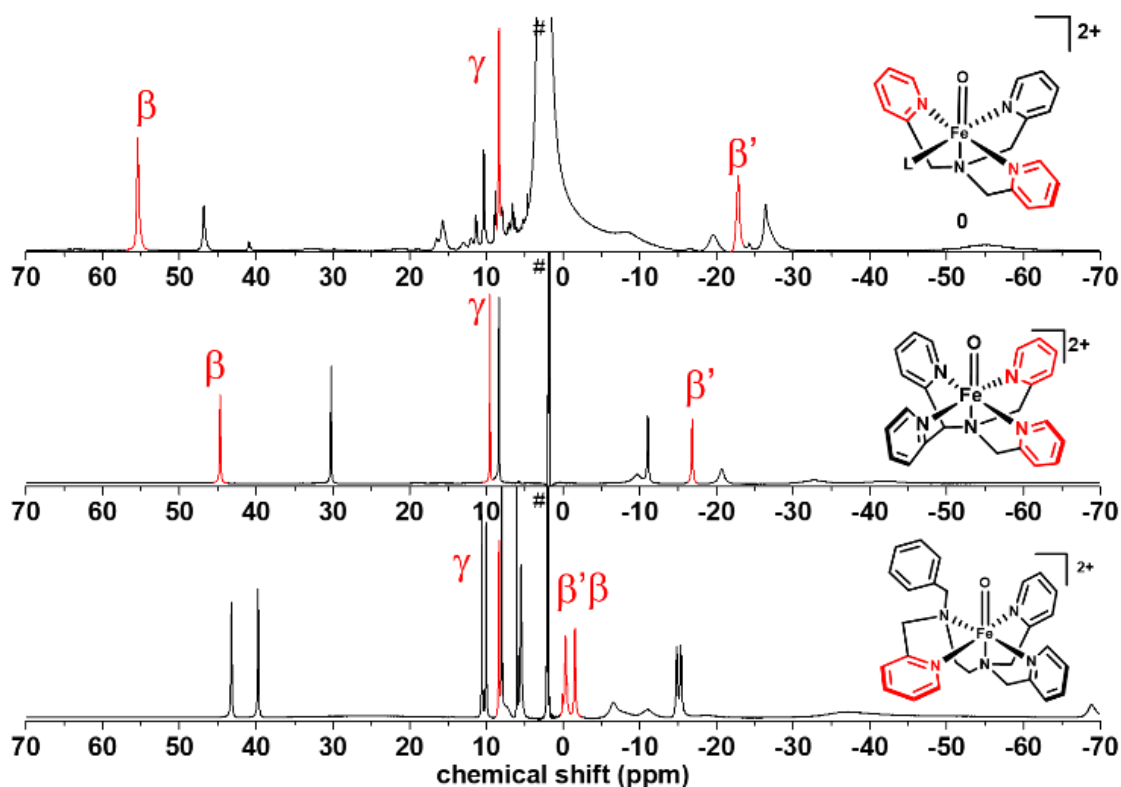


Figure 4.4 Stacked ^1H NMR spectra of **0** (top) at 233 K, $[\text{Fe}^{\text{IV}}(\text{O})(\text{N4Py})]^{2+}$ (middle) at 298 K and $[\text{Fe}^{\text{IV}}(\text{O})(\text{BnTPEN})]^{2+}$ (bottom) at 298 K, with pyridines and corresponding shifts highlighted in red.

The NMR spectrum of complex **0** resembles that of $[\text{Fe}^{\text{IV}}(\text{O})(\text{N4Py})]^{2+}$. A C_3 -symmetric trigonal bipyramidal $[\text{Fe}^{\text{IV}}(\text{O})(\text{TPA})]^{2+}$ complex **0** should exhibit only one set of pyridine ring proton peaks, while a six-coordinate complex with C_s symmetry should give rise to two sets of peaks with a 2:1 intensity ratio, arising from the two pyridines trans to each other and from the pyridines trans to the bound solvent.

The 233 K ^1H NMR spectrum of **0** reveals its C_s symmetric nature. The pyridines trans to each other have intensities of 2H each for the β -, γ -, and β' -H protons at 53, 8 and -21 ppm. The remaining sharp resonances at 45, 10 and -25 ppm correspond to the β -, γ -, and β' -H of the pyridine trans to the solvent, each with unit intensity. The α and CH_2 protons for all $S = 1$ complexes have broad linewidths and are not explicitly assigned, due to their proximity to the paramagnetic center. The assigned NMR spectrum of **0** also agrees with the DFT-calculated NMR spectrum reported for this isomer.¹⁷

There is a possible 6-coordinate isomer of **0** which would have two of its pyridines perpendicular to the $\text{Fe}^{\text{IV}}=\text{O}$ unit, and the remaining pyridine would be trans to the oxo atom instead of the amine. While ^1H NMR spectrum of this isomer has been predicted using DFT and the predicted shifts do not align with the spectrum observed¹⁷, we can additionally rule it out by using experimental data from the ^1H NMR spectrum of $[\text{Fe}^{\text{IV}}(\text{O})(\text{BnTPEN})]^{2+}$ complex (where BnTPEN is a pentadentate ligand abbreviated from *N*-benzyl-*N,N,N'*-tris(2-pyridylmethyl)-1,2-diaminoethane).¹⁰ This complex has an axial amine, and three equatorial pyridines, two of which are parallel and one perpendicular to the ferryl axis. The latter pyridine can help us in ruling out this isomer of **0**. The resonances of this “perpendicular” pyridine in $[\text{Fe}^{\text{IV}}(\text{O})(\text{BnTPEN})]^{2+}$ are distinct from those of the pyridines aligned parallel to the ferryl unit and exhibit smaller paramagnetic shifts (Figure 4.4). Its β and β' peaks are shifted upfield (below 0 ppm) and the γ peak is shifted slightly downfield in the diamagnetic region, a pattern of shifts quite different from that of the pyridines parallel to the ferryl axis. The different shift patterns reflect a different interaction between the pyridine π and π^* with the Fe d-orbitals that have differing amounts of unpaired spin density. The NMR spectrum of **0** does not show such a pattern of resonances, thus ruling out this possible six-coordinate isomer of **0** in solution.

Complex 1:

Our assignment of the resonances of complex **1** is significantly facilitated by the ^1H NMR spectrum of $[\text{Fe}^{\text{IV}}(\text{O})(\text{N}2\text{Py}2\text{Q})]^{2+}$, a ferryl complex supported by the pentadentate ligand N2Py2Q (N2Py2Q = 1,1-di(pyridin-2-yl)-N,N-bis(quinolin-2-ylmethyl)methanamine), which contains 2 quinolines and 2 pyridines parallel to the Fe=O unit that are held together by an amine trans to the oxo atom.²⁹ The ^1H NMR spectrum of the complex generated *in situ* from its iron(II) precursor has been previously reported but were not unequivocally assigned.^{6, 8} We have been able to confidently assign the peaks more accurately using the isolated sample, as it has a relatively clean diamagnetic region. This complex also has a mirror plane of symmetry that gives rise to a relatively simple ^1H -NMR spectrum with eight sharp peaks corresponding to protons on the heterocyclic ligands. All eight peaks have unit intensity, so that each represents a heterocyclic proton. At 298 K, the peaks at 31.3, 8.0 and -17.7 ppm can be assigned respectively to pyridine β -, γ -, and β' -protons by analogy to peaks in the spectrum of $[\text{Fe}^{\text{IV}}(\text{O})(\text{N}4\text{Py})]^{2+}$, as shown in Figure 4.5.

The remaining five peaks at 23.7, 20.8, 19.1, 14.6 and -19.1 ppm can thus be associated with quinoline C7-H, C5-H, C6-H, C4-H and C3-H protons respectively, by comparing their T_1 's and linewidths, which reflect their varying distances from the metal center as derived from its crystal structure. The quinoline C3-H and C4-H are also assigned based on their similarity to the pyridine β' and γ protons in terms of chemical shifts, distances from the ferryl center, their linewidths and T_1 's (see Table 4.2). Moreover, the assignments of C5-H and C6-H are supported by the cross peak between these two signals observed in the COSY spectrum of the complex (Figure 4.6). The quinoline C8-H and the pyridine α -H atoms likely have broader signals due to their increased proximity to the Fe=O unit, thus preventing conclusive assignments. So, it is possible to assign five of the six possible quinoline protons and three of the four pyridine protons.

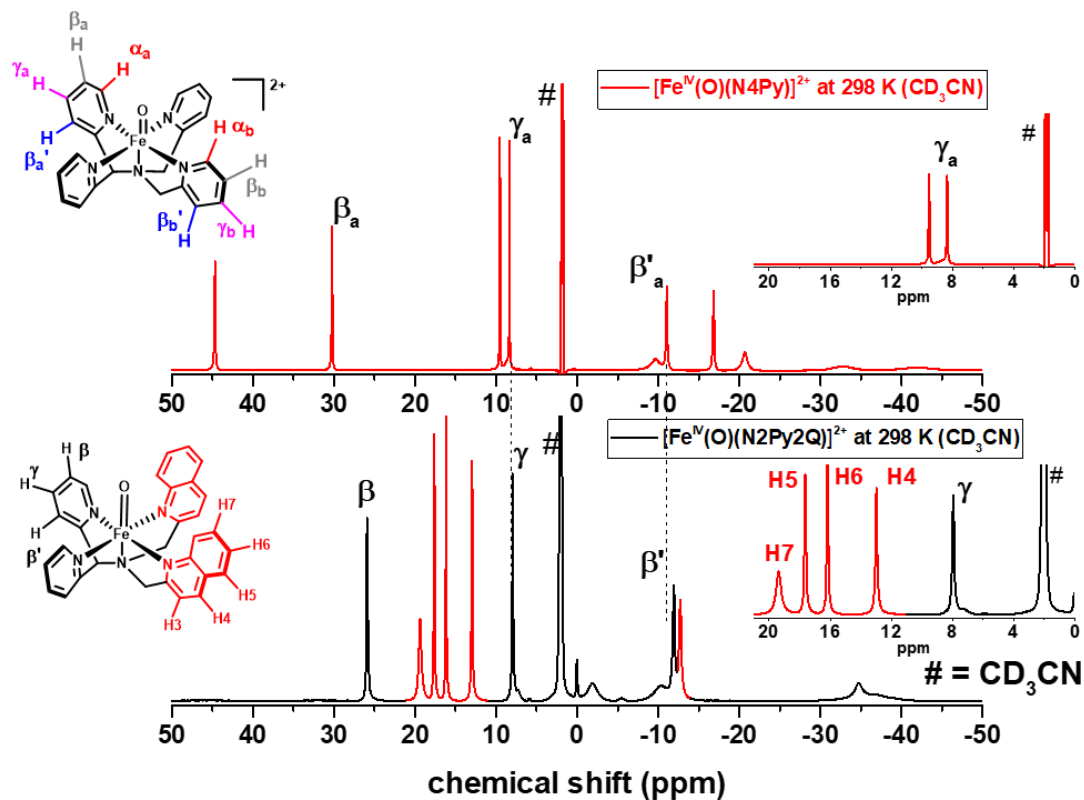
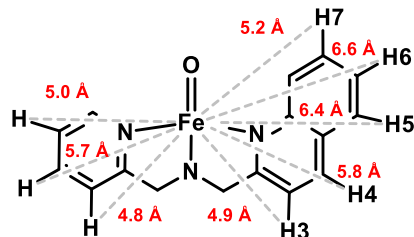


Figure 4.5 Stacked ^1H NMR spectra of $[\text{Fe}^{\text{IV}}(\text{O})(\text{N4Py})]^{2+}$ (top) and $[\text{Fe}^{\text{IV}}(\text{O})(\text{N2Py2Q})]^{2+}$ (bottom) at 298 K, with quinolines shifts in red. Inset shows the expanded region from 0 to 21 ppm. # = solvent. Corresponding structures of the complexes are shown along with the spectra.

Table 4.2 ^1H NMR spectroscopic properties for complex $[\text{Fe}^{\text{IV}}(\text{O})(\text{N}2\text{Py}2\text{Q})]^{2+}$ obtained in acetonitrile- d_3 at 298 K.

Legend	H3	H4	H5	H6	H7	py- γ	py- β'	py- β
δ (ppm)	-12.7	13	17.7	16.2	19.4	8	-11.9	25.9
FWHM (Hz)	140	30	25	20	190	58	117	46
T_1 (ms)	8	24	34	77	5	36	32	15
*d (Fe \cdots H) (\AA)	4.9	5.8	6.4	6.6	5.2	5.7	4.8	5.0

*Distance obtained from the crystal structure, shown from cross-section.²⁹



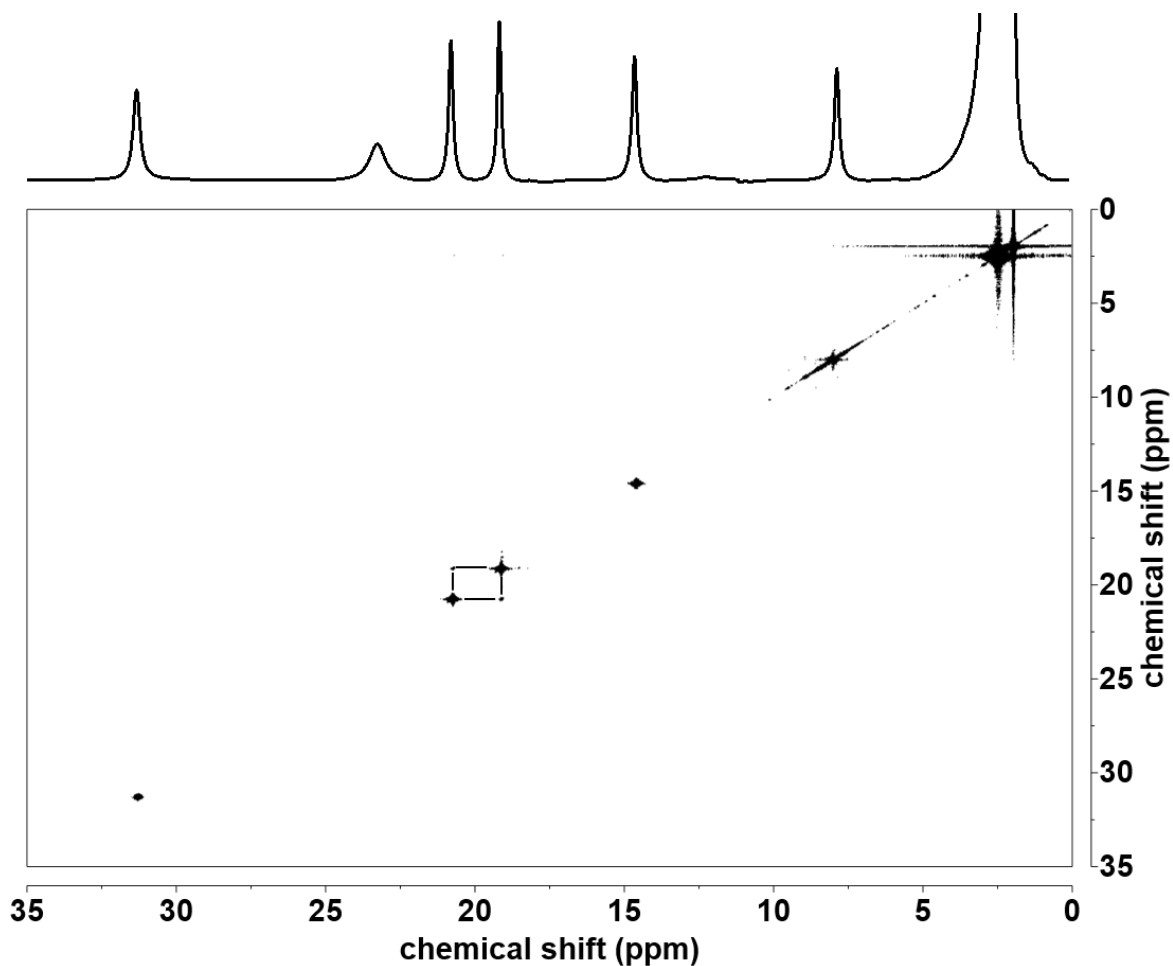


Figure 4.6 ^1H COSY NMR spectrum of complex $[\text{Fe}^{\text{IV}}(\text{O})(\text{N}_2\text{Py}_2\text{Q})]^{2+}$ in acetonitrile- d_3 at 233 K from 0 to 35 ppm. Only the peaks at 19 and 20.8 ppm are found to have relaxation properties at this temperature that allow them to talk with each other. The lower temperature was chosen to minimize the self-decay of $[\text{Fe}^{\text{IV}}(\text{O})(\text{N}_2\text{Py}_2\text{Q})]^{2+}$ over the course of data collection time (over 12 h) on a 10 mM sample.

The NMR spectrum of **1** shows two sets of pyridine protons, thereby excluding a C_s symmetric 5-coordinate or 6-coordinate structure, which would show a 2:1 intensity ratio of pyridine:quinoline protons (equivalent pyridines trans to each other and quinoline trans to the potentially solvent bound sixth-coordination site). Instead, two distinct β proton signals at 58 and 45 ppm and two distinct β' proton signals at -18 ppm and -26 (Figure 4.7) are observed in the spectrum of **1**. The γ protons are likely between 0 to 10 ppm but cannot be clearly assigned owing to

the interfering peaks from presence of additives like peracetic acid, water, acetic acid or ArIO or trifluoroethanol that can be all in the mixture for generating these complexes.

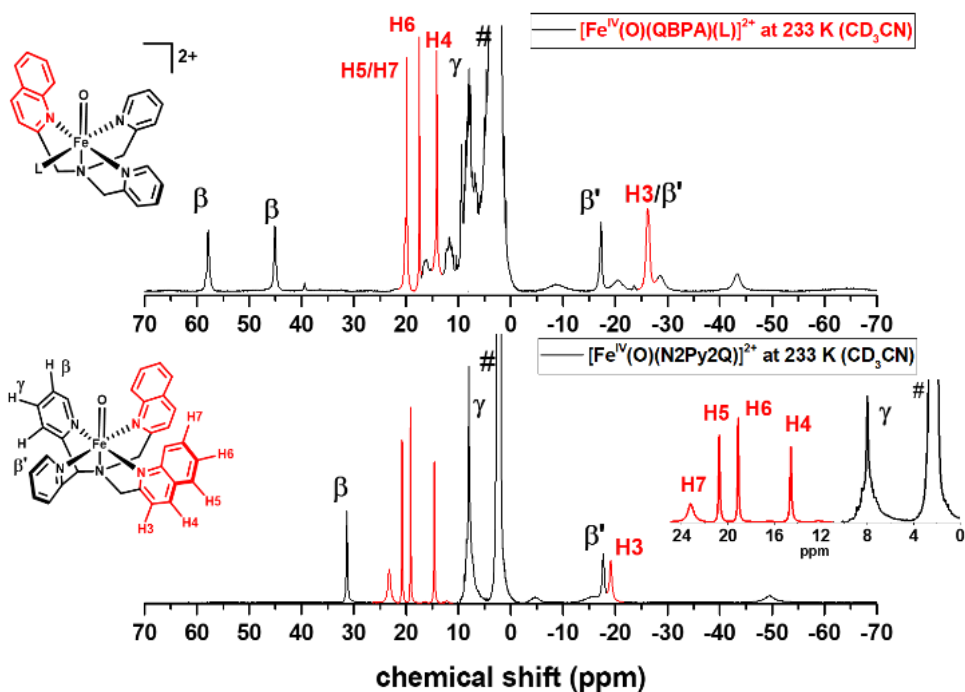


Figure 4.7 Stacked ¹H NMR spectra of $[\text{Fe}^{\text{IV}}(\text{O})(\text{QBPA})(\text{L})]^{2+}$ (**1**, top) and $[\text{Fe}^{\text{IV}}(\text{O})(\text{N2Py2Q})]^{2+}$ (bottom) at 233 K, with quinolines shifts in red. Inset shows the expanded region from 0 to 24 ppm.

The ¹H NMR spectrum of $[\text{Fe}^{\text{IV}}(\text{O})(\text{N2Py2Q})]^{2+}$ now defines our expectations for the quinoline protons of **1** (Figure 4.7). The quinoline signals in **1** can be distinguished from those of the pyridines as an even sharper set of resonances. The C5-H and C7-H resonances likely overlap at 20 ppm (with a relative integration of 2H), and peaks at 18 and 14 ppm correspond to C6-H and C4-H, respectively. The C3-H proton can then be assigned to the peak at -26 ppm, which integrates to 2Hs because of its overlap with a pyridine β' -H signal. $[\text{Fe}^{\text{IV}}(\text{O})(\text{N2Py2Q})]^{2+}$ and **1** have their quinoline heterocycles aligned parallel to the ferryl unit and have

observable resonances in the range of the –30 to 30 ppm regime for C3-H to C7-H protons, typical for $S = 1$ oxoiron(IV) complexes.

Complex 1a:

Complex **1a** is related to **1** by the substitution of quinoline with a 6-methylpyridine donor. The introduction of even one alpha-methyl substituted pyridine affects its ^1H NMR spectrum and shows proton signals that are distinct from those of the unsubstituted pyridines in **0**, **1a**, $[\text{Fe}^{\text{IV}}(\text{O})(\text{N4Py})]^{2+}$ and $[\text{Fe}^{\text{IV}}(\text{O})(\text{N2Py2Q})]^{2+}$. In order to interpret this complex **1a**'s spectrum, a clearer picture can be obtained by comparison with that of a recently reported complex, $[\text{Fe}^{\text{IV}}(\text{O})(6\text{Me}_2\text{N4Py})]^{2+}$, where $6\text{Me}_2\text{N4Py} = N,N\text{-bis(6-methylpyridin-2-methyl)-}N\text{-bis(2-pyridyl)methylamine}$.⁵ Unlike $[\text{Fe}^{\text{IV}}(\text{O})(\text{N2Py2Q})]^{2+}$, this complex is not isolable, because of its short half-life (30 minutes at 298 K). However, it can be generated from its starting iron(II) precursor using excess solid pentafluoriodosylbenzene (PFIB) and stabilized at low temperatures (Figure 4.8). The use of PFIB allows for eliminates signals from the added oxidant and gives rise to a clean diamagnetic region. Its spectrum is also further simplified by the mirror symmetry provided by the N4Py framework, so there are only six peaks corresponding to the unsubstituted and substituted pyridines, four of which have unit intensity, and two overlap with each other. At 233 K, the broad signals of the alpha-methyl protons can be clearly identified near 58 ppm. The β' , γ and β proton signals of the unsubstituted pyridines can be respectively assigned at –18, 9, and 30 ppm. The β' proton signals of the 6-methylpyridines overlap with the those of unsubstituted pyridine at –18 ppm, and the γ proton of the 6-methylpyridines can be identified as the sharp peak at 12 ppm. Finally, the β protons of the 6-methylpyridines are found in the diamagnetic region at 0.5 ppm, making the pattern of associated with the alpha-substituted pyridines clearly different from that of the unsubstituted pyridines. This is further verified by the COSY spectrum of this complex obtained at 233 K (Figure 4.9), which shows a cross peak between the γ and β signals, thus highlighting the effects of alpha-substituents on pyridines. Similar effects of alpha-

substituents were reported by Sahu *et al.*⁷ although the β signal was not identified in that case due to a relatively crowded diamagnetic region.

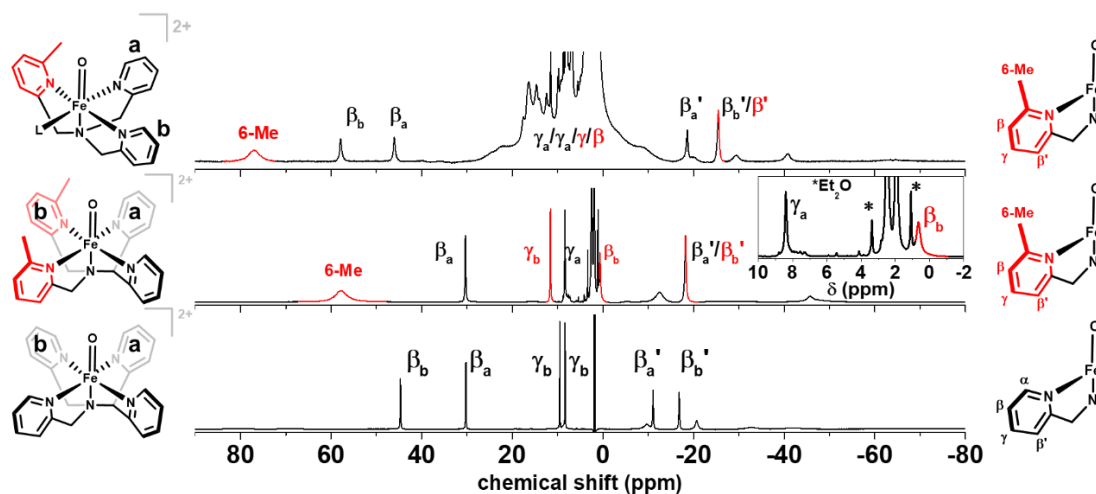


Figure 4.8 ^1H NMR spectra of **1a** (top, 233 K), $[\text{Fe}^{\text{IV}}(\text{O})(6\text{Me}_2\text{N}_4\text{Py})]^{2+}$ (middle, 233 K; inset zooms into diamagnetic region of spectrum to reveal the signals of β proton), and $[\text{Fe}^{\text{IV}}(\text{O})(\text{N}_4\text{Py})]^{2+}$ (bottom, 298 K).

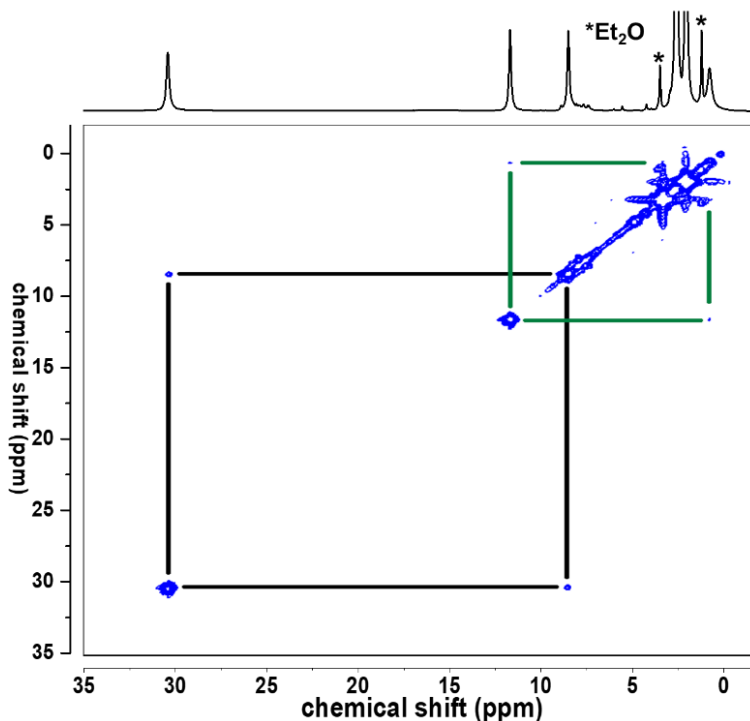


Figure 4.9a ^1H COSY NMR spectrum of complex $[\text{Fe}^{\text{IV}}(\text{O})(6\text{Me}_2\text{N}_4\text{Py})]^{2+}$ in acetonitrile- d_3 at 233 K from -2 to 35 ppm. T cross peaks, between the β and γ protons of two different pyridines are shown.

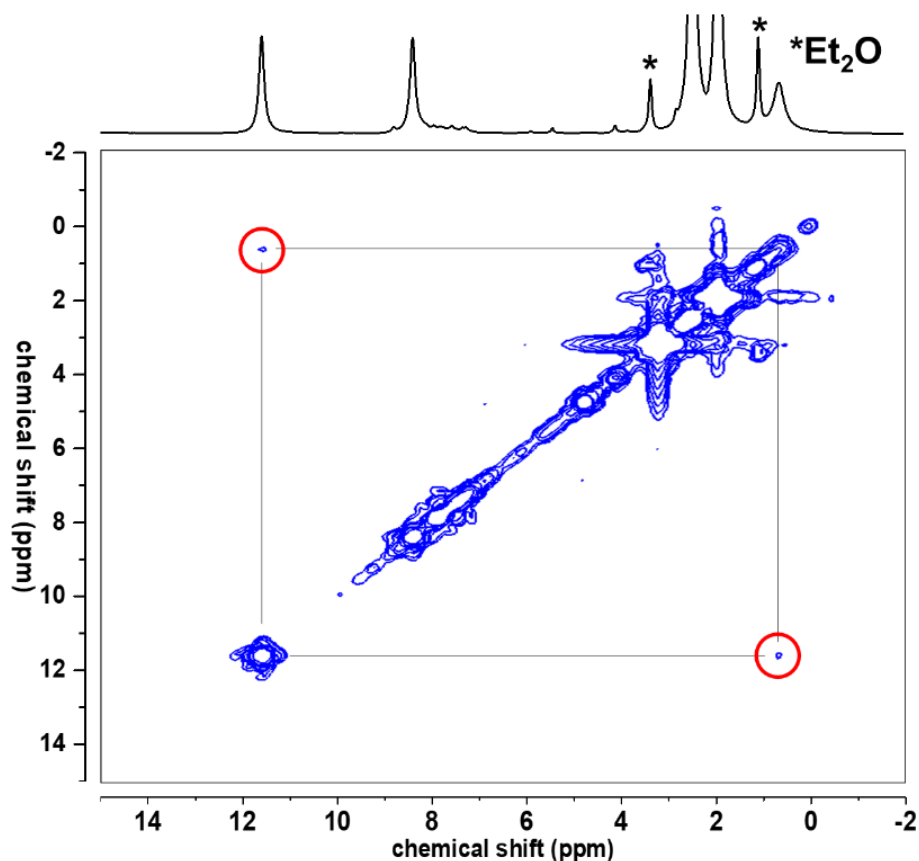


Figure 4.9b Zoomed ^1H COSY NMR spectrum of 10 mM $[\text{Fe}^{\text{IV}}(\text{O})(6\text{Me}_2\text{N}_4\text{Py})]^{2+}$ complex in acetonitrile- d_3 from -2 to 15 ppm at 233 K (lower temperature was chosen to minimize the self-decay over 12 h).

The assignments of peaks in the ^1H NMR spectrum of $[\text{Fe}^{\text{IV}}(\text{O})(6\text{Me}_2\text{N}_4\text{Py})]^{2+}$ can now be used to clarify the spectrum of **1a**. The alpha-methyl substituted pyridine is responsible for its C_1 symmetric nature in solution, as verified by its ^1H NMR spectrum. It shows two sets of unsubstituted pyridine protons, thereby excluding a C_s symmetric 5-coordinate or 6-coordinate structure, which would show a 2:1 ratio of pyridine:6-methylpyridine proton signals with equivalent unsubstituted pyridines trans to each other and a 6-methylpyridine trans to the sixth-coordination site bound to a solvent. Instead there are two distinct β proton signals at 58 and 46

ppm, and two distinct β' proton signals at -18 ppm and -26 (Figure 4.8) are observed in the spectrum of **1a**, arising from the unsubstituted pyridines, which we assign first in the spectrum of **1a**. The γ proton signals from all three pyridines in **1a** are likely between 0 to 10 ppm but cannot be clearly assigned owing to the presence of peaks from additives like peracetic acid, water, acetic acid or ArIO or trifluoroethanol that are part of the mixture used to generate **1a**. Now that the sharp signals from unsubstituted pyridines in this complex are assigned, we assign the only aromatic peak of a 6-methylpyridine at -26 ppm, which overlaps with the β' signal from 6-methylpyridine donor, as also observed in $[\text{Fe}^{\text{IV}}(\text{O})(6\text{Me}_2\text{N}4\text{Py})]^{2+}$. The signals of alpha-methyl group protons are paramagnetically shifted downfield to 70 ppm, just like in the case of $[\text{Fe}^{\text{IV}}(\text{O})(6\text{Me}_2\text{N}4\text{Py})]^{2+}$ where they are found near 58 ppm. The β and γ proton signals of the 6-methylpyridine donor are likely in the diamagnetic region and are not identifiable due to flooding of signals from additives in this region. Complexes **1a** and $[\text{Fe}^{\text{IV}}(\text{O})(6\text{Me}_2\text{N}4\text{Py})]^{2+}$ have their 6-methylpyridines aligned parallel to the ferryl unit and have observable resonances in the range of -30 to 12 ppm regime for γ , β and β' protons, and define the expectations for typical $S = 1$ oxoiron(IV) complexes with these alpha-substitutions.

4.2.3.2 NMR Peak Assignment for $S = 2$ complexes **3**, **3a**, **3b** and **2**

Doubling the number of unpaired electrons in going from $S = 1$ to $S = 2$ configuration in the iron(IV) center results in a threefold increase in its magnetic susceptibility, and the $S = 2$ complexes would be expected to exhibit significantly larger paramagnetic shifts. Unlike for $S = 1$ iron(IV) complexes, there are no ^1H NMR spectra of $S = 2$ iron(IV) complexes. Fortunately, like the $S = 1$ oxoiron(IV) complexes, the ligand protons of the $S = 2$ oxoiron(IV) complexes also exhibit generally favorable relaxation properties. However, these complexes are also very reactive and thermally unstable at 233 K with much shorter lifetimes than the $S = 1$ complexes. Thus we also investigate the NMR of the decayed species to ensure that we are correctly identifying the signals arising from the oxoiron(IV) center.

We have chosen to first discuss the NMR data of bona fide $S = 2$ complexes **3**, **3a** and **3b**, which can then help in the assignments of peaks in the NMR spectrum of **2**. This is because Mössbauer parameters of complex **2** at 4 K reveal characteristics of an $S = 1$ complex, but its ^1H NMR spectrum at 233 K shows peaks that are much more paramagnetically shifted than those of the quinolines and pyridines in **0**, **1**, $[\text{Fe}^{\text{IV}}(\text{O})(\text{N}2\text{Py}2\text{Q})]^{2+}$ and $[\text{Fe}^{\text{IV}}(\text{O})(6\text{Me}_2\text{N}4\text{Py})]^{2+}$, suggesting that spin crossover to an $S = 2$ state might occur for **2** at temperatures higher than the ones used for Mössbauer spectroscopy.

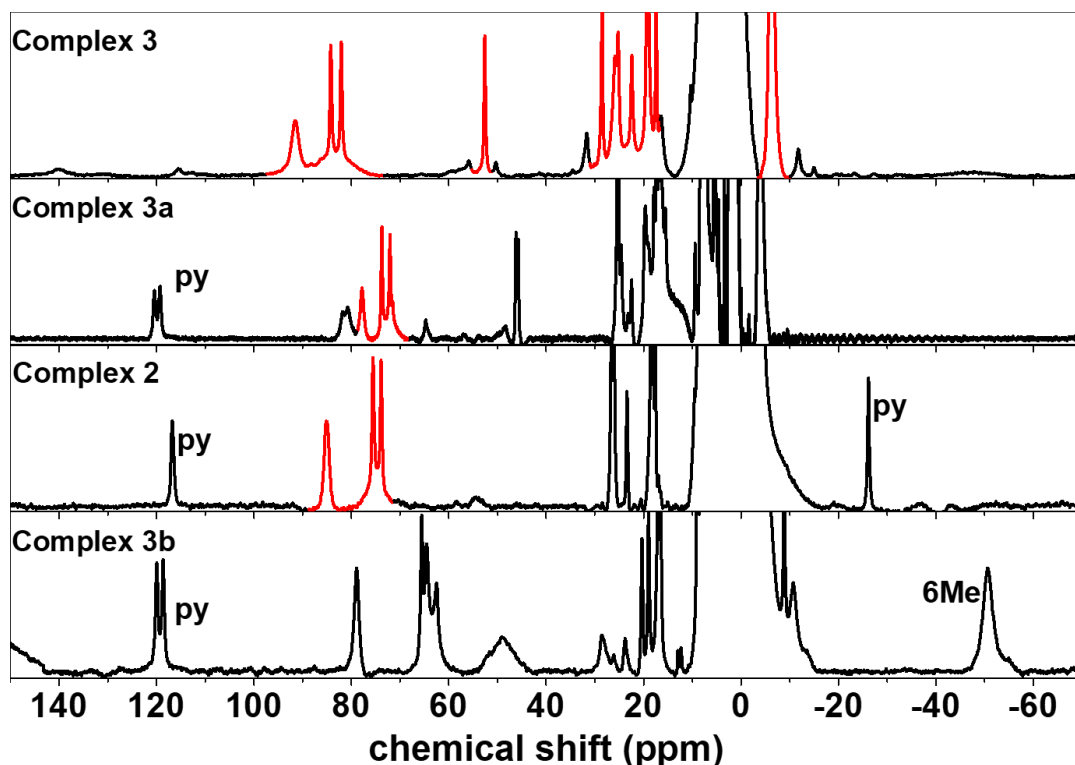


Figure 4.10 Stacked ^1H NMR spectra from top to bottom: **3**, **3a**, **2** and **3b** obtained at 233 K in CD_3CN . Quinoline signals are colored red.

Complex 3:

There are two possible isomeric forms of the complex **3**. A C_3 -symmetric isomer of **3** without any bound solvent would be expected to show six quinoline proton signals at 233 K (and two methylene protons) in its ^1H NMR spectrum. The other

isomer would be six-coordinate with a bound solvent, which would show at least 15 peaks (6 from the quinolines trans to each other and 6 from the quinolines trans to the solvent, in addition to methylene peaks). The C_3 -symmetric configuration can be discarded by the observation of more than 10 paramagnetically shifted peaks in its ^1H NMR spectrum, many of which have unit relative integrations. These peaks disappear upon decay, indicating that they most likely arise from the ferryl complex (Figure 4.11). This observation leads us to conclude that complex **3** is likely 6-coordinate at 233 K, which further disproves recent DFT-derived conclusions about its geometry.²⁴ Closer scrutiny of its spectrum in Figure 4.10 also shows that all quinolines are unique, likely because of a slight distortion of the six-coordinate $\text{Fe}^{\text{IV}}=\text{O}$ center by a twist of the two trans quinoline planes relative to each other along the N–Fe–N axis. The steric constraints provided by the quinoline protons may contribute to this asymmetric nature of **3**. Thus, the NMR data point to a six-coordinate C_1 -symmetric solution-state structure with a bound solvent as the dominant species for **3** at 233 K, with no detectable evidence for a C_3 -symmetric isomer.

The peaks in **3** are not conclusively assigned owing to its thermal instability. DFT methods can help to fill this knowledge gap and predict the paramagnetic shifts of **3** in the $S = 2$ state using a protocol that Borgogno *et al.* have successfully applied in reproducing the paramagnetic shifts observed for some $S = 1$ oxoiron(IV) complexes.¹⁷ The C8-H protons are likely too broad to be observed owing to their proximity to the $S = 2$ ferryl center. Using the DFT methods, we find that the most downfield shifted signals observable in **3** likely arise from C5-H at 92.6, 86 and 83.6 ppm, pending confirmation by using the C5-substituted quinoline variant of complex **3**.

While the complex can be stabilized at a much lower temperature of 193 K in acetone- d_6 , attempts to obtain COSY or selective TOCSY data at 193 K are not successful because of unfavorably fast relaxation times for the $S = 2$ species under these conditions. The ^1H NMR spectrum of obtained **3** in acetone at 193 K and in

acetonitrile at 233 K are not too different from one another, but the latter has more impurities at this temperature, further highlighting the challenges associated with accurately obtaining this data (Figure 4.19).

Complexes 3a and 3b

3a represents a “hybrid” version of alpha-substituted oxoiron(IV) complex containing two quinolines and a pyridine with an alpha-methyl substituent, whereas **3b** contains only pyridine donors with 6-methyl substituents. It makes more sense to describe the complexes **3a** and **3b** together and start analyzing the ^1H NMR spectrum of **3a** by pointing out its similarities and differences with **3** and **3b** (Figure 4.10). Therefore, the quinoline signals in **3a** can be identified by comparisons with the quinoline signals in the parent complex **3**, and absence of those signals in **3b**. Similarly, the two 6-methylpyridine protons (one pair of which is trans to each other and the other is trans to the solvent) in complex **3a** can be identified by comparisons with **3b** and their absence in **3** (because it has no 6-methylpyridines). The two 6-methylpyridine protons in **3a** are likely near 120 ppm, and are also found in **3b**; they are not found in **3** because it only has quinolines. The quinoline signals in **3a** are likely near 70-90 ppm, because that is where these signals are found in parent complex **3**, and they are not found in **3b**. However, we have not determined their identity as β , β' or γ protons.

Closer scrutiny of the spectrum of **3b** in Figure 4.10 reveals its six-coordinate C_s -symmetric solution-state structure with a bound solvent as the dominant species for **3b** at 233 K, which gives rise to 11 dominant peaks. No detectable evidence for a C_3 -symmetric isomer is found, which would give rise to only 5 peaks (one methylene peak, one methyl peak and three pyridyl proton peaks in the intensity ratio 2:3:1:1:1). The methyl groups of the 6-methylpyridines trans to each other are found paramagnetically shifted upfield to about -50 ppm in a C_s -symmetric structure. The geometry of **3a** is likely C_s geometry in solution, because quinoline proton signals between 70-90 ppm relative to a single pyridine proton signal near 120 ppm are in a 2:1 intensity ratio.

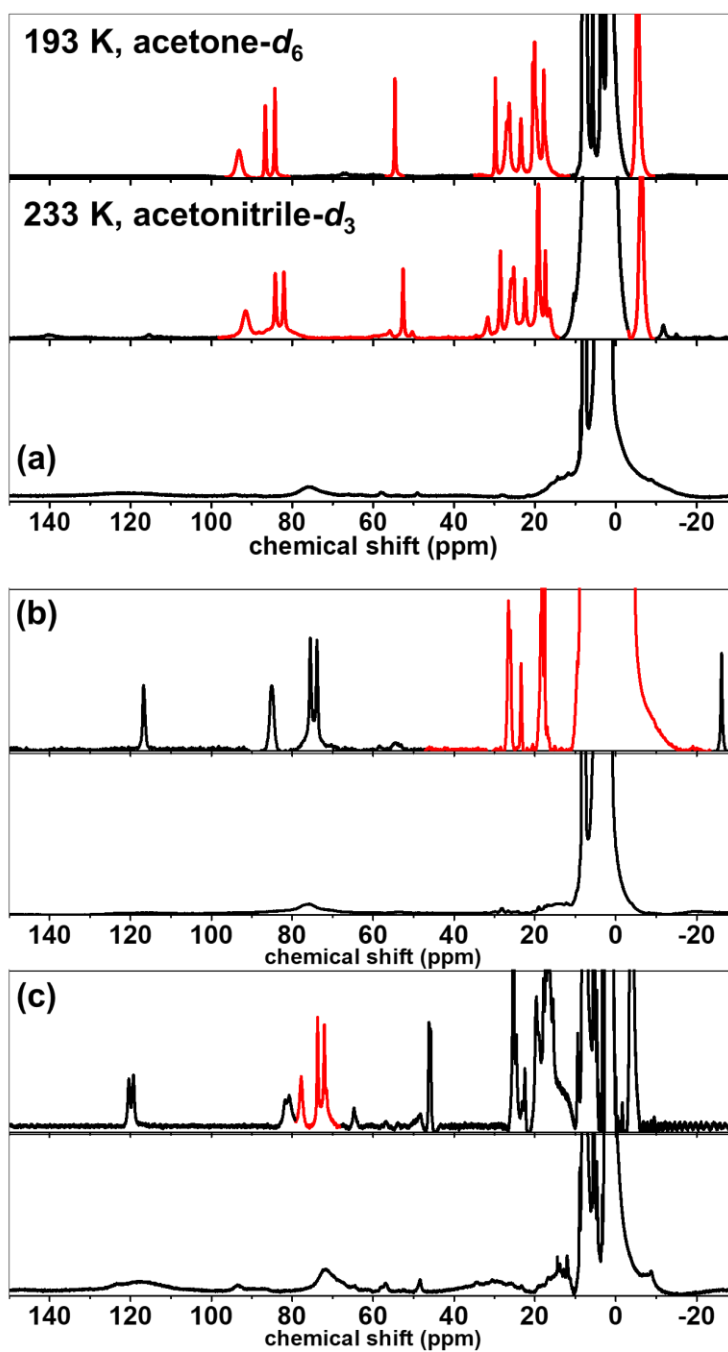


Figure 4.11 Stacked ^1H NMR spectra of oxoiron(IV) complexes and after it has decayed (bottom spectrum in each panel) for complexes **3** (a), **2** (b) and **3a** (c). Complex **3** ^1H NMR spectrum was obtained in two different solvents/temperatures.

Complex 2

Despite its Mössbauer parameters having parameters characteristic of $S = 1$ species, the ^1H NMR spectrum of **2** at 233 K more closely resembles the spectra of its $S = 2$ counterparts **3**, **3a** and **3b**. The three peaks observed in ^1H NMR spectrum of **2** at around 75-85 ppm are also found in the ^1H NMR spectrum of **3** and **3a**, and likely belong to quinolines. Complex **3a** is analogous to **2**, except that its pyridine contains an alpha-methyl substituent, which make it an unambiguously $S = 2$ complex based on Mössbauer spectroscopy. In complex **2** at 118 ppm, only one resonance is observed, in contrast with the two peaks observed near 120 ppm for **3a** and **3b**. This may be attributed to differences in alpha-substituted and unsubstituted pyridines in an $S = 2$ oxoiron(IV) complex, and how they experience the spin density of their respective paramagnetic centers. The missing pyridine signal is likely at -26 ppm and such a signal does not exist in **3a** and **3b**. Alpha-substituted and unsubstituted pyridines behave differently in the NMR spectra of $S = 1$ $\text{Fe}^{\text{IV}}(\text{O})$ complexes as well, as explained above using the NMR spectra of **1a** and $[\text{Fe}(\text{6Me}_2\text{N4Py})]^{2+}$, which contain both at least one alpha-substituted and unsubstituted pyridine.^{5, 7, 30}

Furthermore, if the patterns of quinoline and pyridine proton peaks in **2** and **3a** are compared with those of the pyridines in the $S = 1$ ferryl complexes, one can conclude that **2** may be $S = 2$ in nature at higher temperatures of 233 K which is where its NMR spectrum is obtained, and reactivity also determined (see a later section). This is also substantiated by its $S = 2$ analogs **3a** (which is unambiguously $S = 2$ at all temperatures), indicating much more paramagnetically shifted set of protons compared with $S = 1$ complexes discussed in this and related reports. **2** is also found to show fewer peaks than any of the other $S = 2$ complexes, which can be an indication that it might have C_s symmetry (which may or may not be bound by a solvent) at 233 K. Both 5- and 6-coordinate C_s symmetric **2** would be expected to show 2:1 ratio of peaks for quinolines:pyridines. Thus, pending a further absolute liquid-solution structural characterization, complex **2** exhibits an $S = 2$ character at 233 K.

4.2.3 Computed NMR Chemical Shifts for Oxoiron(IV) Complexes

Borgogno *et al.* have used DFT methods to predict NMR spectra for previously reported $S = 1$ complexes **0** and $[\text{Fe}^{\text{IV}}(\text{O})(\text{TMC})]^{2+}$ (TMC = 1,4,8,11-tetramethyl-1,4,8,11-tetraazacyclotetradecane).¹⁷ We have used these methods to predict the NMR shifts for complexes $[\text{Fe}^{\text{IV}}(\text{O})(\text{N}2\text{Py}2\text{Q})]^{2+}$, **2** and **3**. Our complexes serve as a direct way to validate the chemical shifts observed for $S = 1$ and $S = 2$ configuration of complexes **2** and **3**. Interestingly, the chemical shifts predicted for the $S = 1$ complex $[\text{Fe}^{\text{IV}}(\text{O})(\text{N}2\text{Py}2\text{Q})]^{2+}$ agree with the shifts observed experimentally, but its $S = 2$ isomer are predicted to have much more paramagnetically shifted peaks than those of the $S = 1$ counterpart (Table 4.3). Interestingly, for complex **2**, the chemical shifts predicted for an $S = 1$ isomer are similar to those for $[\text{Fe}^{\text{IV}}(\text{O})(\text{N}2\text{Py}2\text{Q})]^{2+}$, but for its $S = 2$ isomer (Table 4.4), these chemical shifts are closer in line with what is observed, further confirming our spin-state assignment at 233 K, at which all of these chemical shifts are calculated.

Table 4.3 Theoretical chemical shifts predicted for $[\text{Fe}^{\text{IV}}(\text{O})(\text{N}2\text{Py}2\text{Q})]^{2+}$ (in ppm) at 233 K.

H	exp. δ	calc. δ	
		S = 1	S = 2
α	≈ -50	-54	202
β	31.3 (1)	40	170
β'	-17.7 (1)	-18.3	82
γ	8 (1)	8.4	-4.1
H3	-19.1 (1)	-21.7	81
H4	14.6 (1)	14.2	-5
H5	20.7 (1)	24.2	89
H6	19.1 (1)	24.5	29
H7	23.2 (1)	33.6	41
H8	70	84	125

Table 4.4 Theoretical chemical shifts predicted for complexes **2** and **3** (in ppm) at 233 K.

H	exp. δ	calc. δ		H	exp. δ	calc. δ	
Complex 2		S = 2	S = 1	Complex 3		S = 2	S = 1
α	br*	201.6	-69.3	H3	54.1 (1)	52.3	-20.6
β	br*	197.1	48.8	H3	29.6	43.6	-21.3
β'	117 (1)	92.9	-25.6	H3	92.7	114.9	-17.8
γ	-26.3 (1)	-28.7	5.9	H4	br*	-33.5	12.3
H3	76 (2), 77	85.5	-20.4	H4	7.2 (1)	4.9	11.1
H3	(2), 83 (2)	87.3	-19.5	H4	-5.3 (8)	-6.5	8.5
H4	-8 (over- lapped)	-11.1	15.1	H5	83.6 (1)	74.5	11.9
H4		5.5	13.8	H5	86 (1)	102.5	7.4
H5	76 (2), 77	70.4	14.4	H5	19.9 (1)	26.5	23.4
H5	(2), 83 (2)	92.4	24.8	H6	20.3 (1)	24.2	23.5
H6	27 (2), 25	29.4	23.8	H6	23.3 (1)	35.4	29.9
H6	(1), 23 (1)	33.9	28.4	H6	17.7 (2)	28.7	17.3
H7	27 (2), 25	30.0	20.8	H7	26.7 (1)	40.5	33.0
H7	(1), 23 (1)	44.4	35.9	H7	-5.3 (8)	2.5	29.4
H8	br*	199.7	175.8	H7	26.3 (1)	42.4	6.2
H8		226.4	135.5	H8	br*	198	142.1
*br = broad, or not observed.				H8		172.6	177.3
				H8		281.6	115.3

4.2.4 Reactivity of Oxoiron(IV) Complexes

Complex **0** is inert towards strong C-H bonds at 233 K. At 273 K however, upon its generation with ArIO from starting iron(II) acetonitrile solution, it can abstract the C-H bonds of cyclohexane. Complex **1** is about an order of magnitude higher in its ability to abstract C-H bonds at this temperature. As can be seen from the plot of $\log(k_2')$ (where $k_2' = k_2/\text{number of equivalent substrate C-H bonds}$) versus C-H bond dissociation energies (BDE), the logarithms of the rate constants are found to decrease linearly with an increase in the C-H bond strength, indicating that HAT transfer is involved in the rate-determining step. This reasonably linear correlation has been shown for a number of oxoiron(IV) complexes.³¹⁻³² The thermal instability of **2** and **3** prevents us from obtaining reactivity data at 273 K, and thus we have resorted to 233 K to obtain this information.

Interestingly, complex **2** has rates higher than those of **0** and **1**, but very close to those of **3**. Note however, that rates for **0** and **1** are measured at 273 K. Typically, introduction of quinoline donors on ferryl complexes parallel to the ferryl unit, increases the C-H bond abstraction ability of the complexes by an order of magnitude. This is also seen from the case of **0** and **1**. The increased Fe-N bond lengths from the quinoline increases the electrophilicity of the ferryl center, thus resulting in higher rates of reaction. If one were to apply a typical temperature correction for 40 K difference in temperatures at which reactivity is measured between the pair of $S = 1$ (**0** and **1**), and $S = 2$ complexes (**2** and **3**), the rate would be expected to change by just over an order of magnitude. This difference already allows us to conclude that **2** and **3** have a much higher reactivity than **0** and **1**. The introduction of second quinoline in the TPA framework lends it some high-spin character, although it does not drastically increase its ability to react with C-H bonds, and the rate enhancement is just by over an order of magnitude. The rate differences among the three complexes become larger for substrates with stronger bonds, resulting in a decrease in the slopes of the Evans-Polanyi correlations shown in Figure 4.12, in going from **0** to **3**.

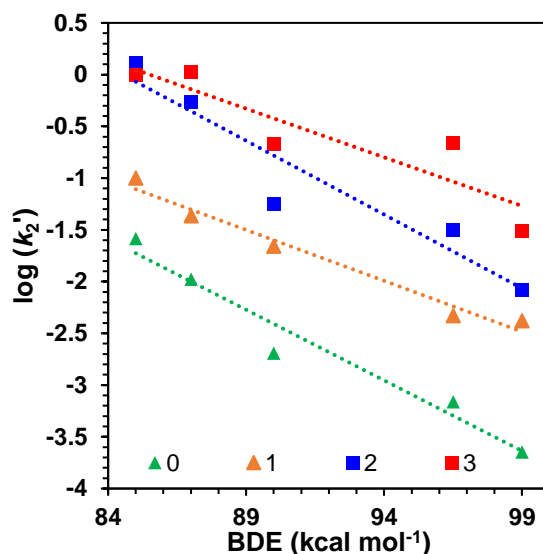


Figure 4.12 Evans-Polanyi plots for complexes **0** and **1** (rate constants obtained at 273 K), and **2** and **3** (rate constants obtained at 233 K).

4.3 Discussion

This work explores the effects of systematically introducing alpha-substituents on the tetradentate ligand frameworks supporting oxoiron(IV) complexes. While quinolines or alpha-substituents such as methyl group on the TPA framework can change the spin state of the oxoiron(IV) complexes, we wanted to explore at what point does this change occur. While introducing a single quinoline on the TPA framework retains the $S = 1$ spin state at all temperatures, introducing the second quinoline ends up imparting a potential “spin-crossover” behavior in complex **2**. Interestingly for oxoiron(IV) complexes supported by pentadentate ligands, incorporation of two alpha-substituents such as quinolines retains the triplet spin state. However, in the TPA framework examined in this work, introduction of the second quinoline results in a well-documented spin-crossover behavior, which has been shown only for iron(II) and iron(III) complexes,²⁵ and not for iron(IV) complexes, to the best of our knowledge.

We have used NMR spectroscopy in combination with Mössbauer spectroscopy to determine that the complex **2** likely possesses some spin crossover behavior. NMR spectra for $S = 1$ complexes has a much smaller range of peaks for identifiable resonances of heterocycles compared with that of $S = 2$ complexes. Additionally, while we are unable to

This has broad implications in terms of access to the quintet state for an oxoiron(IV) complex. The hydrogen-atom abstraction carried out by oxoiron(IV) complexes is often thought to proceed via access to a low-lying excited *quintet* transition state during the reaction with the substrate. However, observation of such a transition state is very challenging. This particular hypothesis is the foundation of two-state reactivity (TSR).³³ It is often postulated that non-heme enzymatic ferryl intermediates possess a ground quintet spin state because it is likely required for all hydrogen-atom abstraction reactivity. This is often used to explain why $S = 1$

complexes are typically less reactive, and to explain their reactivity, an access to $S = 2$ spin state must occur during the hydrogen-atom abstraction reactions. Unfortunately, transition states are not observable using any methods so far. Overall, a larger picture would also look at the thermodynamics of the HAT reaction whereby the energy difference between the reactants and products should also be taken into account.³⁴ But our work demonstrates that a ground spin state can be accessed at higher temperatures for reactive oxoiron(IV) complexes.

and therefore our work makes this oxoiron(IV) complex very unique.

4.4 Conclusion

In the process of examining the NMR properties, we have reported the NMR spectra of quintet oxoiron(IV) complexes for the first time, and their much more paramagnetically shifted peaks are in alignment with what is expected for the ferryl complexes. Interestingly the $S = 2$ iron(IV) complexes have an observable range of chemical shifts spanning about 200 ppm, and this is comparable to the NMR shifts in $S = 2$ iron(II) complexes, although the assignments of peaks to the protons are likely very different due to different propagation of spin as well as the d-orbital configuration. Our observation of an oxoiron(IV) complex which has different ground spin states at different temperatures is unprecedented, and was only recently proposed using DFT methods for one of the complexes (and later disproved by Banerjee *et al.*³⁵),

4.5 Experimental Section

Instrumentation and physical methods:

NMR (nuclear magnetic resonance) spectra for iron(II) complexes as well as iron(IV) complexes were recorded on a Bruker 400 or 500 MHz spectrometer at temperatures stated. NMR spectra to characterize the ligands were obtained at 298 K. 8" Wilmad-LabGlass 528-PP-7-5 NMR tubes were used to collect NMR spectra for iron(IV) and iron(II) complexes. For all the variable temperature spectra, the lower temperatures were calibrated using a sealed NMR tube containing a solution of tetramethylsilane (TMS) and methanol as a standard. For details on how the NMR spectra were obtained, see the NMR section outlined in a later section.

Elemental analyses were carried out by Atlantic Microlab (Norcross, GA).

UV-vis spectra were recorded on a HP8453A diode array spectrometer equipped with a cryostat from Unisoku Scientific Instruments (Osaka, Japan).

Mössbauer spectra were recorded with two spectrometers, using Janis Research (Wilmington, MA) SuperVaritemp dewars that allow studies in applied magnetic fields of up to 7.5 T in the temperature range from 1.5 to 200 K. A LakeShore Model 331A temperature controller was used to control the temperature in experiments. Mössbauer spectral simulations were performed using the WMOSS software package (SEE Co, Edina, Minnesota). Isomer shifts are quoted relative to α -Fe metal at 298 K. The spectra were plotted by SpinCount developed by Prof. Michael Hendrich at Carnegie Mellon University.

Materials:

All materials were bought from Sigma Aldrich, Fischer Scientific or TCI Chemicals, unless otherwise noted. The substrates cyclohexane, cyclooctane, 2,3-dimethylbutane, toluene, ethylbenzene, and cumene used in kinetic experiments were passed through a plug of silica before use; triphenylmethane was

recrystallized from ethanol, and its stock solutions were made in dichloromethane- d_2 in a nitrogen-filled glovebox.

All ligands and iron(II) complexes were synthesized as reported, except that iron(II) triflate was used exclusively to synthesize the iron(II) precursors, to avoid explosion risks associated with perchlorate salts.

4.5.1 Syntheses and Characterization

All ligands reported in this work were synthesized using reported methods. All iron(II) complexes except for the precursor for **3a** were prepared according to the methods reported here, except that iron(II) triflate was used to make the compounds to avoid explosion risks associated with perchlorates.

[Fe^{II}(6MeBQPA)(CH₃CN)(OTf)]OTf An equimolar acetonitrile solution of iron(II) triflate and 6MeBQPA ligand was combined and stirred to give a light yellow solution. This solution was stirred for a couple of hours, followed by a slow diffusion of diethyl ether, which gave yellow crystals of iron(II) salt. This solution was then filtered, and dried with ether. Anal. calculated for C₃₁H₂₇F₆FeN₅O₆S₂, [Fe^{II}(6MeBQPA)(CH₃CN)(OTf)]OTf: C, 46.57; H, 3.40; N, 8.76. Found: C, 46.41; H, 3.38; N, 8.57.

4.5.2 Preparation of NMR Samples and Characterization

Generation of the ferryl complexes for NMR spectroscopic analysis:

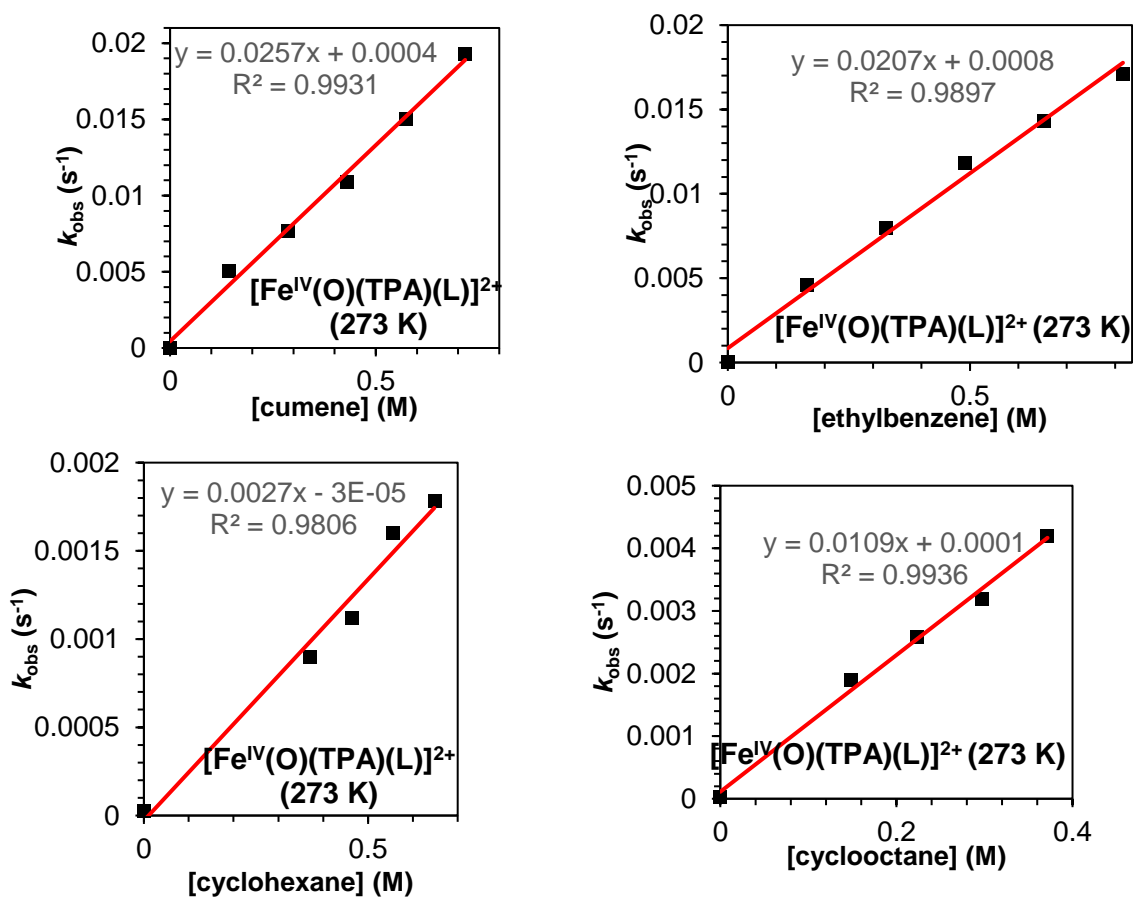
4-mM stock solutions of starting iron(II) precursors were made inside the air-free nitrogen-filled glovebox in acetonitrile- d_3 or acetone- d_6 . 0.5 mL of these 4-mM solutions was transferred into the NMR tube for each experiment. All oxoiron(IV) complexes were generated by first precooling 4-mM iron(II) starting solutions to a given temperature in the NMR instrument (where it was also locked to the deuterated solvent, tuned to the intended nucleus, and then shimmed to make the magnetic field uniform around the sample). Once the temperature had equilibrated, the ^1H NMR spectrum of the iron(II) was obtained at this point. The following three steps were then performed in quick succession: 1) the NMR tube was ejected from the instrument, 2) 2 equivalents of ArIO in either 2,2,2-trifluoroethanol (TFE) or $\text{DCM-}d_2$ were quickly injected to generate the oxoiron(IV) intermediate, the tube was capped with either a septum or its plastic cap, and (to minimize decay of the species) 3) the tube was immediately inserted back into the instrument for data collection. Because the instrument had been locked to the solvent as well as tuned to the nucleus of interest, only shimming was performed again before collection of NMR data for the oxoiron(IV) species. To obtain the spectrum of the decayed species, the complex was warmed to room temperature by ejecting the NMR tube from the instrument, and after the species had decayed, it was inserted back into the instrument and NMR data was obtained again at lowered temperature.

General parameters for data collection and processing:

The following parameters were used to acquire the ^1H NMR data for paramagnetic compounds: Acquisition time = 0.064 s; relaxation delay = 0.03 s; sweep width = 400 ppm offset (centered) at 6 ppm; line broadening factor = 10-30 Hz. Chemical shifts (ppm) were referenced to residual protic solvent peaks. The NMR spectra obtained were processed either using either the NMR processing software MestReNova 12.0 or through Bruker's Top-Spin 3.5p17.

4.5.3 Reactivity and Kinetics of Oxoiron(IV) Complexes

All experiments were conducted with 1 mL solutions of 1 mM iron(II) complexes in acetonitrile solutions at given temperatures for HAT (hydrogen-atom-transfer) substrates, unless otherwise stated. The oxoiron(IV) complexes were generated using 1-2 eq. ArIO in 2,2,2-trifluoroethanol or DCM- d_2 . The pseudo-first order decay curves from absorption-time profiles were obtained by monitoring the decrease in absorbance for the oxoiron(IV) complexes with time. These profiles at various concentrations were fit with an exponential decay. The rates (k_{obs}) were plotted against different concentrations of substrates, and their slopes represent 2nd order rate constants (k_2).



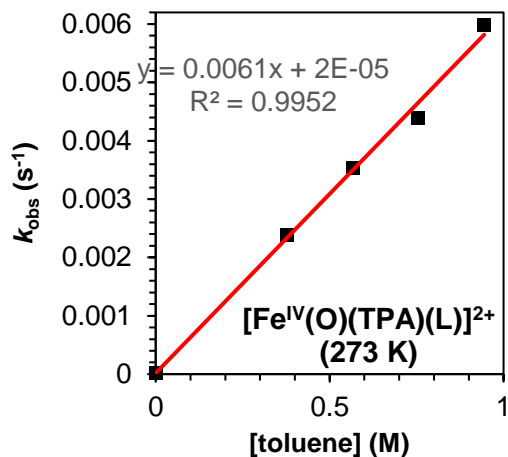
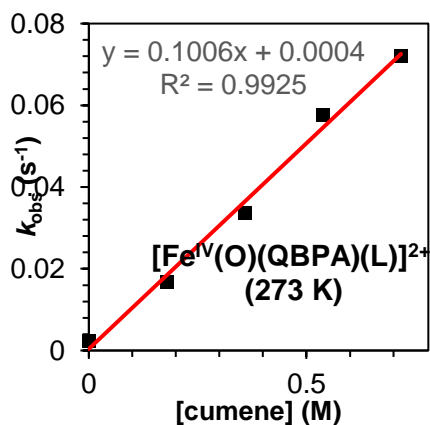
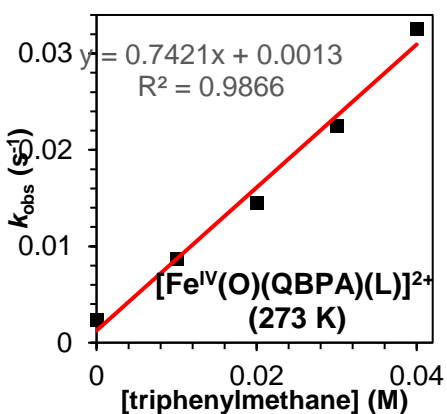


Figure 4.13 k_2 plots for the reactions of different HAT substrates with $[\text{Fe}^{\text{IV}}(\text{O})(\text{TPA})(\text{L})]^{2+}$. The slopes of the fitted red lines represent the second-order rate constants (k_2) at 273 K. The oxoiron(IV) complex was generated using 1.2 eq of ArIO in TFE, followed by addition of substrate.



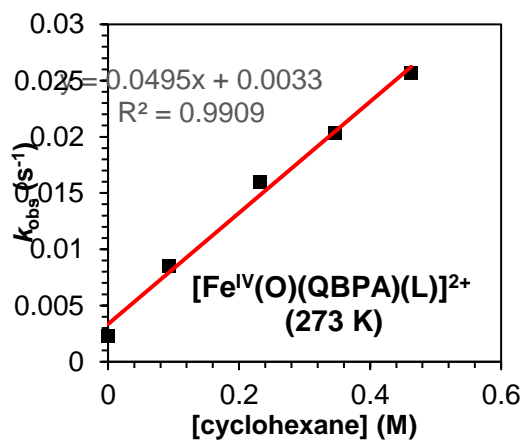
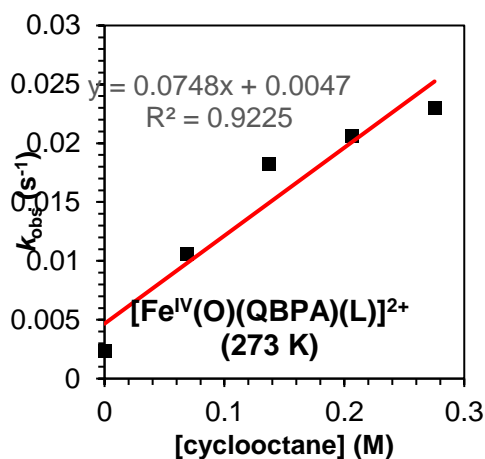
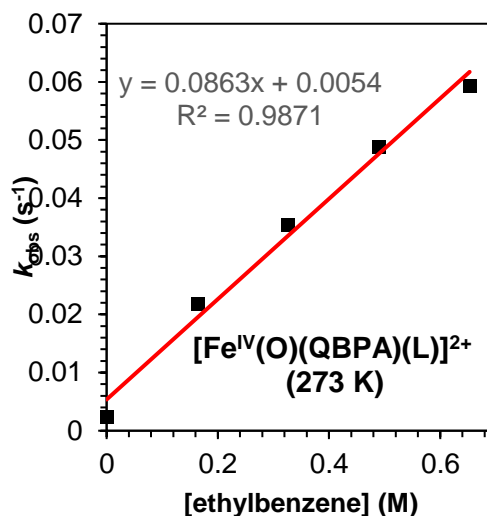
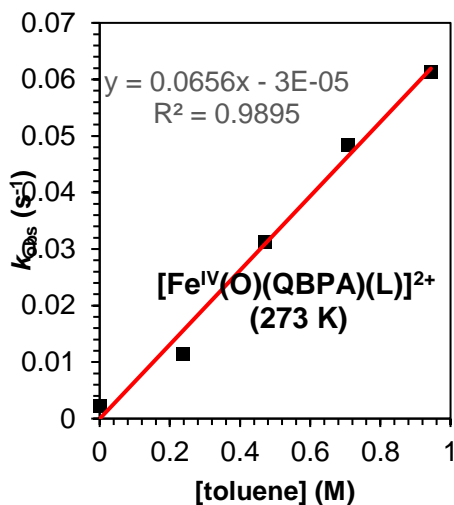
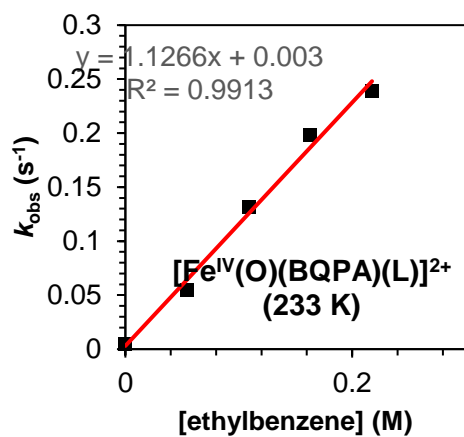
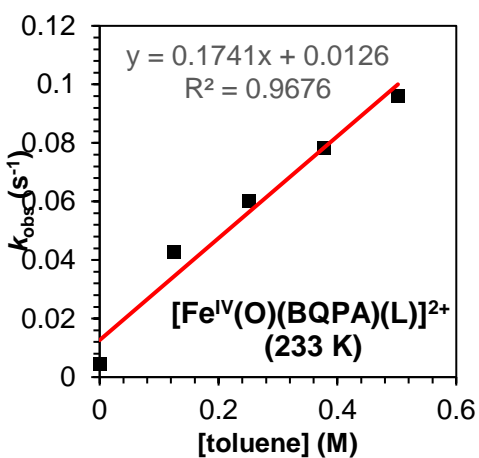
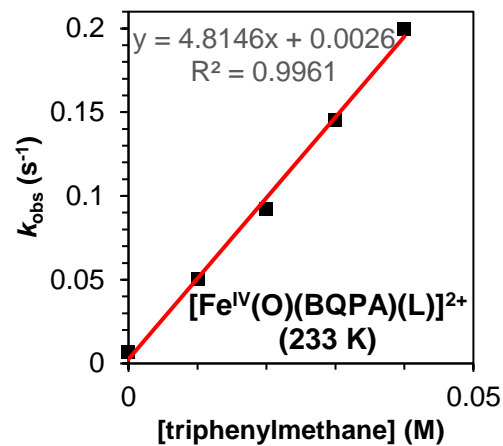
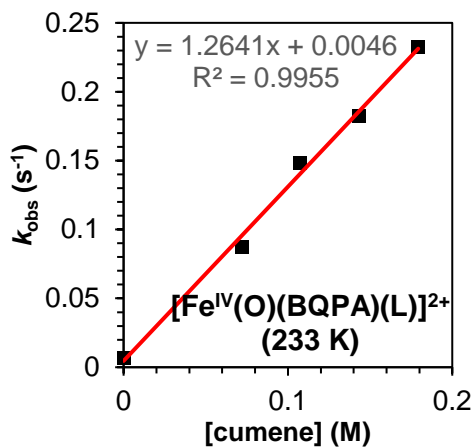


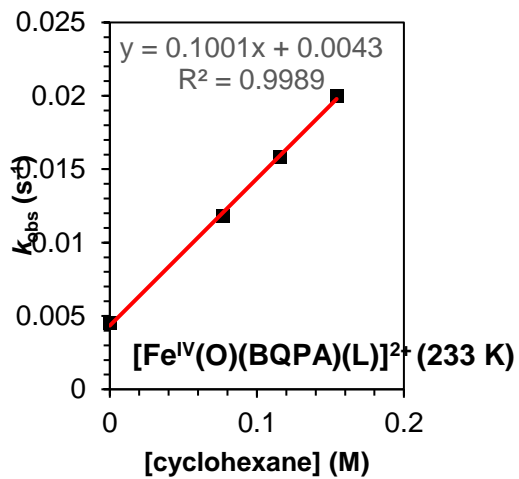
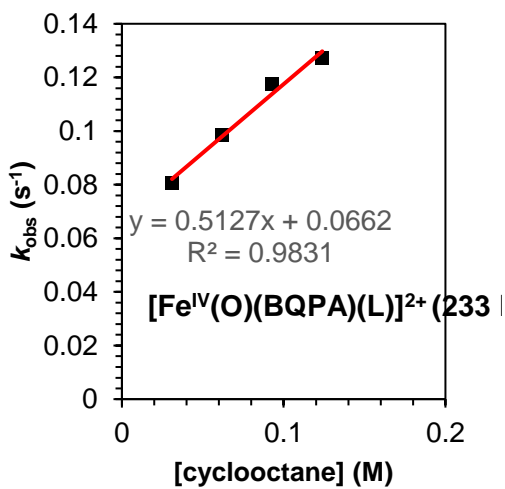
Figure 4.14 k_2 plots for the reactions of different HAT substrates with $[\text{Fe}^{\text{IV}}(\text{O})(\text{QBPA})(\text{L})]^{2+}$. The slopes of the fitted red lines represent the second-order rate constants (k_2) at 273 K. The oxoiron(IV) complex was generated using 1.2 eq of ArIO followed by addition of substrate.

Figure 4.15 k_2 plots for the reactions of different HAT substrates with $[\text{Fe}^{\text{IV}}(\text{O})(\text{BQPA})(\text{L})]^{2+}$. The slopes of the fitted red lines represent the second-order rate constants (k_2) at 233 K. The oxoiron(IV) complex was generated using 2 eq of ArIO followed by addition of substrate.



Needs to be repeated

Needs to be repeated



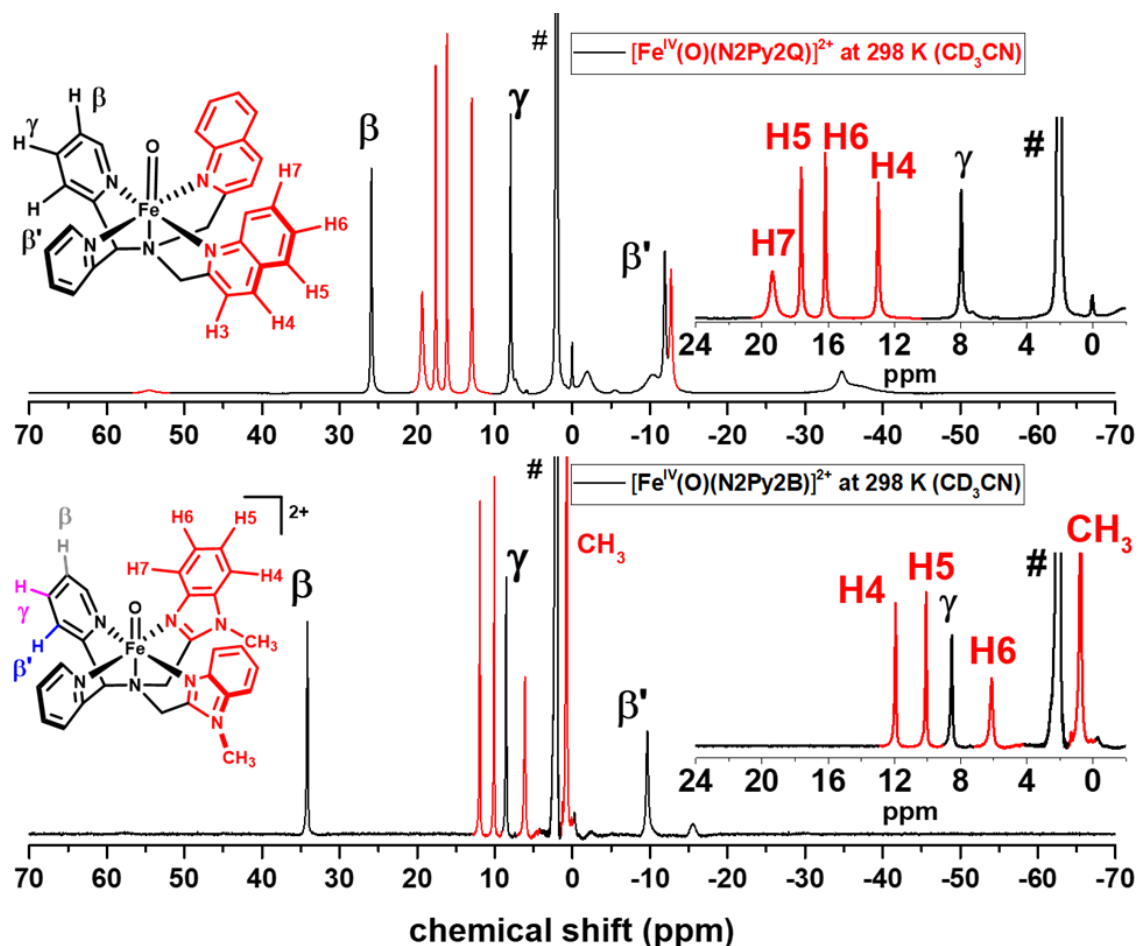


Figure 4.16 Stacked ^1H NMR spectrum of complexes (top) $[\text{Fe}^{\text{IV}}(\text{O})(\text{N}2\text{Py}2\text{Q})]^{2+}$ and (down) $[\text{Fe}^{\text{IV}}(\text{O})(\text{N}2\text{Py}2\text{B})]^{2+}$ in CD_3CN at 298 K from -70 to 70 ppm, along with assignments. Peaks for pyridines are in **black** and quinolines and benzimidazoles are in **red**.

Comparisons of complexes containing benzimidazoles and quinolines:

In these oxoiron(IV) complexes, quinolines' H3 and H4 protons appear at similar chemical shifts to pyridines' γ and β' protons, indicating that these sets of protons experience similar paramagnetism from the $S = 1$ Fe^{IV} center as pyridines. This is not surprising given that quinoline can be thought of as a pyridine having a fused phenyl ring.

H5/H6 in $[\text{Fe}^{\text{IV}}(\text{O})(\text{N}2\text{Py}2\text{Q})]^{2+}$ and H4/H5 in $[\text{Fe}^{\text{IV}}(\text{O})(\text{N}2\text{Py}2\text{B})]^{2+}$ belong to the fused phenyl ring on the respective heterocycles, and have the sharpest resonances, allowing for relaxation properties that make them amenable to COSY spectroscopy for these heterocycles so that their cross-peak can be observed at 233 K. The most broad and observable fused heterocyclic proton peaks in the NMR spectra of these ferryl complexes belong to H7 in $[\text{Fe}^{\text{IV}}(\text{O})(\text{N}2\text{Py}2\text{Q})]^{2+}$ and H6 in $[\text{Fe}^{\text{IV}}(\text{O})(\text{N}2\text{Py}2\text{B})]^{2+}$. However, H7 in $[\text{Fe}^{\text{IV}}(\text{O})(\text{N}2\text{Py}2\text{Q})]^{2+}$ is more downfield-shifted than H6 in $[\text{Fe}^{\text{IV}}(\text{O})(\text{N}2\text{Py}2\text{B})]^{2+}$. H6 in $[\text{Fe}^{\text{IV}}(\text{O})(\text{N}2\text{Py}2\text{B})]^{2+}$ is also 0.5 Å farther from the iron(IV) center than H7 in $[\text{Fe}^{\text{IV}}(\text{O})(\text{N}2\text{Py}2\text{Q})]^{2+}$ and may explain the differences observed in their paramagnetic shifts. When pyridines, benzimidazoles and quinolines are viewed together, assignment of quinoline protons in the $S = 1$ iron(IV) center is greatly facilitated, and parallels between pyridines, benzimidazoles and quinolines can be drawn, even though the heterocycles are not necessarily the same.

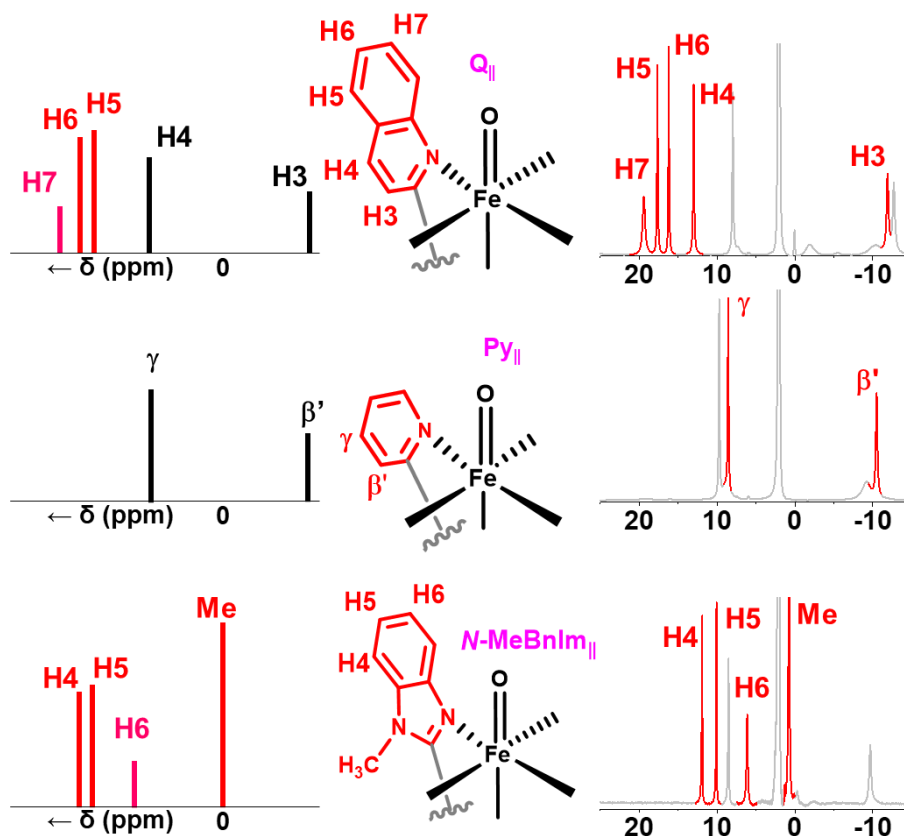


Figure 4.17 Similarities between NMR peaks of different heterocycles aligned parallel to the ferryl unit in oxoiron(IV) complexes.

Table 4.5 ^1H NMR spectroscopic properties for complexes containing benzimidazoles or quinolines in the N4Py framework, obtained at 298 K.

Legend	quinolines					benzimidazoles		
	H3	H4	H5	H6	H7	H4	H5	H6
δ (ppm)	-12.7	13	17.7	16.2	19.4	12	10	6.2
FWHM (Hz)	140	30	25	20	190	56	44	96
T_1 (ms)	8	24	34	77	5	36	59	13
**d (Fe \cdots H) (Å)	4.9	5.8	6.4	6.6	5.2	6.3	6.8	5.7

*Distance obtained from the crystal structures, shown from cross-section.²⁹

Assignments of NMR spectra on $S = 1$ oxoiron(IV) complexes with differently substituted pyridines:

The resonances of the pyridines:

The orientation of pyridines around the iron center can change the pattern of chemical shifts observed for protons of the pyridines. There are broadly three potential ways (Scheme 4.1) a bound pyridine can orient around the $\text{Fe}^{\text{IV}}=\text{O}$ unit: 1) axially on the iron center (*trans* to the oxo atom), and either aligned between, or with the equatorial ligands; 2) equatorially, perpendicular to axis of the $\text{Fe}^{\text{IV}}=\text{O}$ unit, (where the ring is) in the plane defined by the equatorial ligands; and 3) equatorially, with the pyridine ring parallel to the $\text{Fe}^{\text{IV}}=\text{O}$ unit.

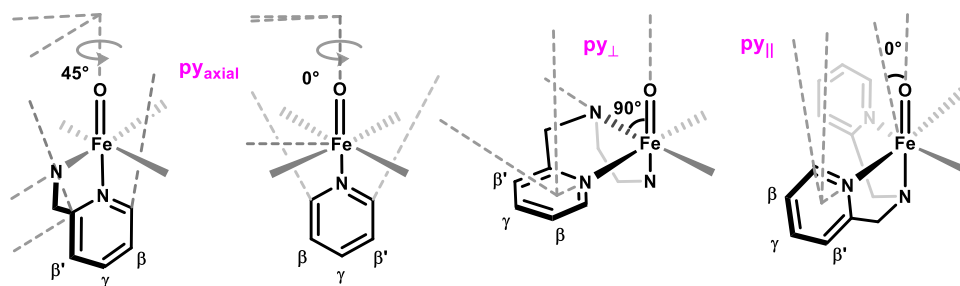


Figure 4.18 Possible orientations of the pyridine heterocycle around the $\text{Fe}^{\text{IV}}=\text{O}$ unit.

For the well-studied case of the “parent” complex $[\text{Fe}^{\text{IV}}(\text{O})(\text{N}4\text{Py})]^{2+}$ where pyridines are parallel to the oxoiron(IV) center, the β , γ and β' protons can be assigned using methyl and methoxy group substitutions on the pyridines, which results in disappearance of the signals from the parent complex with concomitant appearance of methyl signals in the diamagnetic region for the resulting newer complexes. These assignments have also been previously confirmed through ^1H COSY NMR spectroscopy on the parent complex with unsubstituted pyridines.¹⁰ (Figure 4.J) The resonances of α protons of pyridines are very broad owing to their proximity to the metal center. They can be assigned in two ways: 1) a unique complex called $[\text{Fe}^{\text{IV}}(\text{O})(\text{Py}5\text{Me}_2)]^{2+}$ has four pyridines roughly parallel to the $\text{Fe}^{\text{IV}}=\text{O}$ unit, with no methylene and methine protons which often give rise to broad signals (Figure 4.I). Therefore, most protons for this complex exhibit sharp resonances which are all assigned using integration, except one set of broad signals in the upfield region, likely from the α protons. 2) The broad α protons in the upfield region can also be assigned using substitutions to generate a new complex, which eliminates the corresponding broad signal in the upfield region. In this case, if a 6-methyl substitution is introduced on the parent complex, the 6-methyl protons’ chemical shifts are paramagnetically shifted to the downfield region (near 60 ppm) as a broad signal due to their proximity to the iron(IV) center. For all methyl or methoxy group substitutions made on the 5-, 4- and 3-H protons of the pyridines, the methyl groups appear in the diamagnetic region in resulting complexes.

Lastly the 6-methylpyridine parallel to the ferryl center is different from an unsubstituted pyridine parallel to the ferryl center. β (5-H) proton of the pyridine substituted with 6-Me substitution experiences a different spin from the metal, as has also been seen in cases where aryl substitutions are introduced on the pyridines on the 6th position.³⁶ γ (4-H) and β' (3-H) protons in this 6-methylpyridine appear in the same region as in the pyridine without any alpha-substituents. β proton's chemical shift deviates from the expected resonance in the downfield region near 30 to 50 ppm and is instead assigned using COSY spectroscopy to be closer to 1 ppm (Figure 4.D).

The patterns for each of the pyridines in different orientations for β and γ protons can be seen in the [figure](#) below. For the pyridine perpendicular to the oxoiron(IV) unit, the resonances were assigned using ¹H COSY spectroscopy as well as substitution on the β position of the corresponding proton. The protons on the pyridine bound trans to the oxo atom have been assigned using integrations in the case of $[\text{Fe}^{\text{IV}}(\text{O})(\text{Py5Me}_2)]^{2+}$.

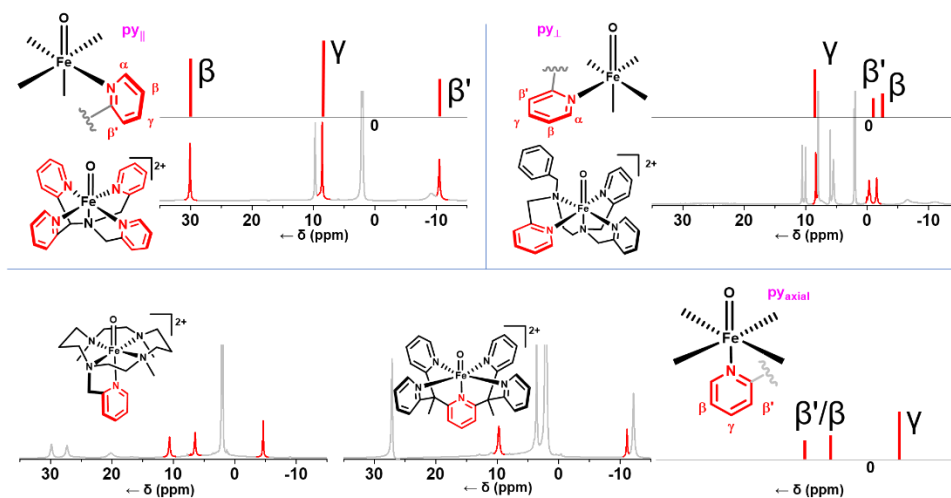


Figure 4.19 ¹H NMR resonances for an equatorial pyridine oriented parallel to the $S = 1$ $\text{Fe}^{\text{IV}}=\text{O}$ unit in $[\text{Fe}^{\text{IV}}(\text{O})(\text{N4Py})]^{2+}$ (top, left); an equatorial pyridine oriented perpendicular to the oxoiron(IV) unit in $[\text{Fe}^{\text{IV}}(\text{O})(\text{BnTPEN})]^{2+}$ (top, right); and an axial pyridine trans to the oxo atom in $[\text{Fe}^{\text{IV}}(\text{O})(\text{TMC-Py})]^{2+}$ (bottom, left) and

[Fe^{IV}(O)(Py5Me₂)]²⁺ (bottom, middle). All resonances are highlighted, along with respective pyridines of these complexes.

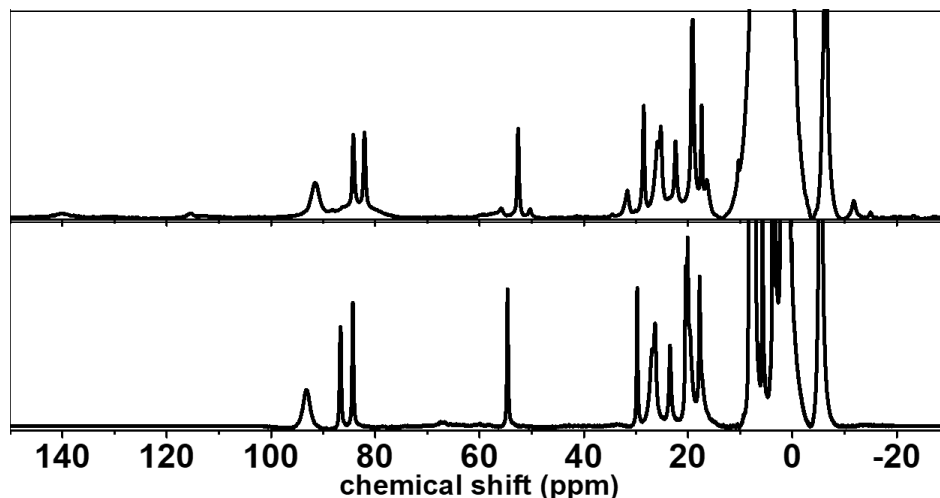


Figure 4.20 ¹H NMR spectra of complex **3** in acetonitrile-*d*₃ at 233 K (top), and in acetone-*d*₆ at 193 K (bottom).

4.2.1 Spin State Splitting Energies of Ferryl Complexes

For a series of oxoiron(IV) complexes based on the TPA ligand framework with varying number of quinoline substitutions (Figure 4.1), spin state splitting energies were computed for the $S = 1$ and $S = 2$ spin state gaps (Table 4.6). For complexes with one or two quinolone substituents, QBPA and BQPA, both C_1 and C_s conformations were considered. Notably, no geometrical constraints regarding symmetry were imposed during the geometry optimization and the labels C_1 and C_s therefore only reflect the relative orientation for the substituents.

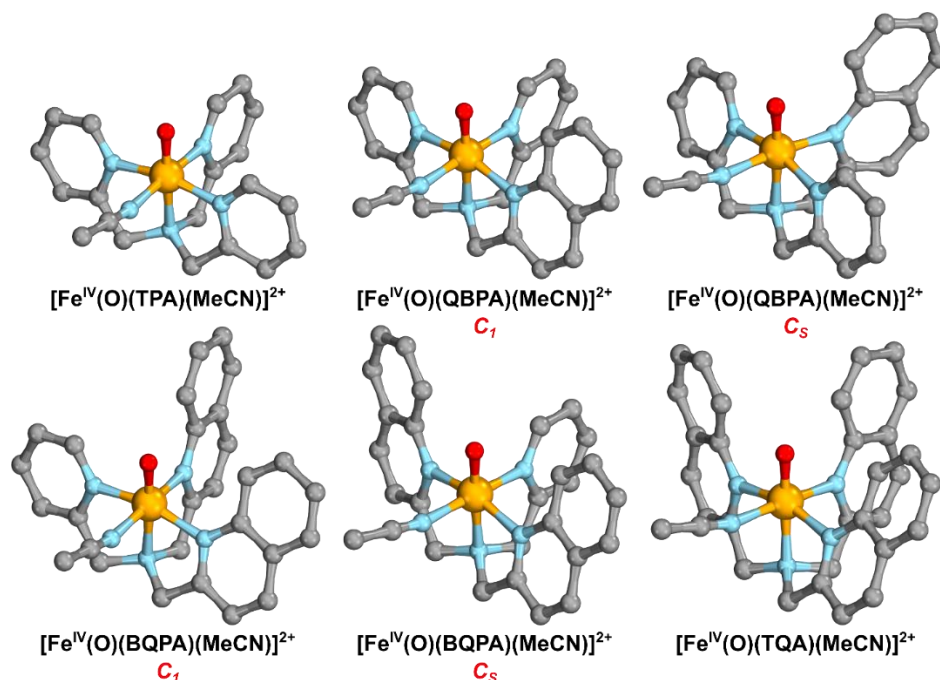


Figure 4.21 Structural depictions of the oxoiron(IV) complexes studied. Structures corresponding to the $S = 1$ spin state are shown. Geometries were obtained at the PW6B95/def2-TZVP level of theory in the gas phase. Depictions were made using IboView.³⁷⁻³⁸

Table 4.6 Computed spin state splitting energies at the PW6B95/def2-TZVP level of theory.

Complex	$\Delta E(Q-T)$ [kcal mol ⁻¹]	$\Delta E_{ZPE}(Q-T)$ [kcal mol ⁻¹]
0	4.9	3.5
1 (C_1)	3.4	2.3
1 (C_s)	1.4	0.5
2 (C_1)	0.2	-0.8
2 (C_s)	1.4	0.1
3	-1.5	-2.5

A plot of the computed spin state splitting energies reveals a direct correlation with the number of substitutions made and the spin state splitting energies (Figure 4.22, red dots). In a similar study on the effect of quinoline substitutions to the Bn-TPEN

framework such a trend was also observed. The data is also shown in **Figure 2** for comparison (black squares).

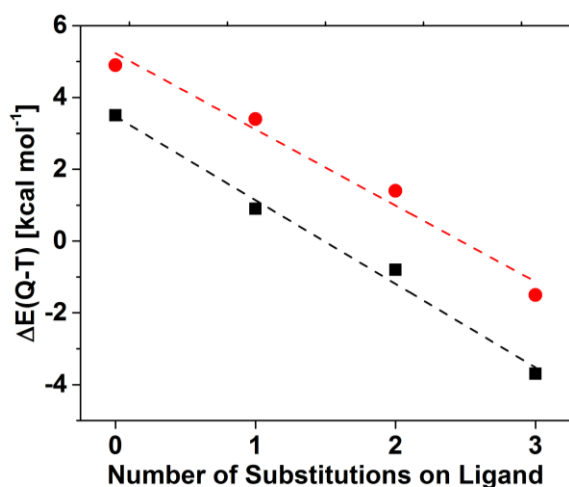


Figure 4.22 Plot of the computed spin state splitting energies at the PW6B95/def2-TZVP level of theory and the number of quinoline substitutions made. Red dots show data for the TPA ligand framework (C_1 and C_s symmetric structures were considered for QBPA and BQPA ligands, respectively). Data computed for an analogous series of quinoline substitutions to the BnTPEN ligand framework (black squares) are shown for comparison.

In case of the complex **1** the role of C_1 and C_s isomers is rather clear. Here the C_1 conformation is clearly favored (Table 4.7). For the isomers of the complex **2**, this analysis is less obvious, especially when comparing zero-point vibrational energy (ZPE) corrected electronic energies or free energies (298 K) these isomers are energetically very similar.

Table 4.7 Comparison of the relative energies of the C_1 and C_s isomers of complexes **1** and **2** at the PW6B95/def2-TZVP level of theory. All energetics are in kcal mol⁻¹.

Complex	Spin State	ΔE	ΔE_{ZPE}	ΔG_{298}
1 (C_1)	S = 1	0.0	0.0	0.0
1 (C_1)	S = 2	3.4	2.3	1.4
1 (C_s)	S = 1	2.9	2.7	2.7
1 (C_s)	S = 2	4.3	3.2	2.3

2 (C₁)	S = 1	1.1	0.7	0.5
2 (C₁)	S = 2	1.3	-0.1	-1.1
2 (C_s)	S = 1	0.0	0.0	0.0
2 (C_s)	S = 2	1.4	0.1	-0.8

Computational Experimental Details:

All calculations were performed using Turbomole v7.0.1.³⁹⁻⁴¹ The PW6B95 functional⁴² and the def2-TZVP basis set⁴³ were used in all calculations. All calculations were carried out in the gas phase and numerical second derivatives were computed to confirm that a minimum was reached, showing no imaginary frequencies. For ZPE corrections small frequencies (< 100 cm⁻¹) were raised to 100 cm⁻¹.⁴⁴⁻⁴⁵ Calculations were accelerated by the MARI-J approach⁴⁶ using Weigend's fitting basis sets.⁴⁷ Grid m5 was used throughout.

4.6 Acknowledgments

For this work I am thankful first to Saikat Banerjee's constant help. This work needed really two pair of hands to obtain data. I am also immensely grateful to Ruixi Fan on DFT calculations done on these complexes' NMR spectra, as well as numerous Mössbauer spectra that he collected for me in this project. I am also grateful to Dr Will Oloo, who first inspired me to work on this project from the aspect of 6Me substituents, which eventually turned out to be more complicated than expected but I could eventually understand at least some of the NMR spectra by using complexes I synthesized for other projects. I am also grateful to Dr Mayank Puri for his help and guidance and Dr Achintesh Biswas in helping me track some of the data, and his help in syntheses of some of the ligands.

4.7 References

1. Kal, S.; Que, L., *J. Biol. Inorg. Chem.* **2017**, *22* (2), 339-365.
2. Bols, M. L.; Hallaert, S. D.; Snyder, B. E. R.; Devos, J.; Plessers, D.; Rhoda, H. M.; Dusselier, M.; Schoonheydt, R. A.; Pierloot, K.; Solomon, E. I.; Sels, B. F., *J. Am. Chem. Soc.* **2018**, *140* (38), 12021-12032.
3. McDonald, A. R.; Que, L., Jr., *Coord. Chem. Rev.* **2013**, *257* (2), 414-428.
4. Pavlov, A. A.; Denisov, G. L.; Kiskin, M. A.; Nelyubina, Y. V.; Novikov, V. V., *Inorg. Chem.* **2017**, *56* (24), 14759-14762.
5. de Visser, S.; Mukherjee, G.; Kumar, D.; Sastri, C.; Alili, A.; Barman, P., *Chem. Eur. J.* **2019**, *0* (Just Accepted).
6. Mukherjee, G.; Lee, C. W. Z.; Nag, S. S.; Alili, A.; Cantú Reinhard, F. G.; Kumar, D.; Sastri, C. V.; de Visser, S. P., *Dalton Trans.* **2018**, *47* (42), 14945-14957.
7. Sahu, S.; Zhang, B.; Pollock, C. J.; Dürr, M.; Davies, C. G.; Confer, A. M.; Ivanović-Burmazović, I.; Siegler, M. A.; Jameson, G. N. L.; Krebs, C.; Goldberg, D. P., *J. Am. Chem. Soc.* **2016**, *138* (39), 12791-12802.
8. Rana, S.; Biswas, J. P.; Sen, A.; Clémancey, M.; Blondin, G.; Latour, J.-M.; Rajaraman, G.; Maiti, D., *Chem. Sci.* **2018**, *9* (40), 7843-7858.
9. Rana, S.; Dey, A.; Maiti, D., *Chem. Commun.* **2015**, *51* (77), 14469-14472.
10. Klinker, E. J.; Kaizer, J.; Brennessel, W. W.; Woodrum, N. L.; Cramer, C. J.; Que, L., Jr., *Angew. Chem. Int. Ed.* **2005**, *44* (24), 3690-3694.
11. Duban, E. A.; Bryliakov, K. P.; Talsi, E. P., *Eur. J. Inorg. Chem.* **2007**, *2007* (6), 852-857.
12. Monte Pérez, I.; Engelmann, X.; Lee, Y.-M.; Yoo, M.; Kumaran, E.; Farquhar, E. R.; Bill, E.; England, J.; Nam, W.; Swart, M.; Ray, K., *Angew. Chem. Int. Ed.* **2017**, *56* (46), 14384-14388.
13. Bigelow, J. O.; England, J.; Klein, J. E. M. N.; Farquhar, E. R.; Frisch, J. R.; Martinho, M.; Mandal, D.; Münck, E.; Shaik, S.; Que, L., *Inorg. Chem.* **2017**, *56* (6), 3287-3301.

14. England, J.; Prakash, J.; Cranswick, M. A.; Mandal, D.; Guo, Y.; Münck, E.; Shaik, S.; Que, L., *Inorg. Chem.* **2015**, *54* (16), 7828-7839.
15. Prakash, J.; Rohde, G. T.; Meier, K. K.; Münck, E.; Que, L., *Inorg. Chem.* **2015**, *54* (23), 11055-11057.
16. England, J.; Bigelow, J. O.; Van Heuvelen, K. M.; Farquhar, E. R.; Martinho, M.; Meier, K. K.; Frisch, J. R.; Münck, E.; Que, L., *Chem. Sci.* **2014**, *5* (3), 1204-1215.
17. Borgogno, A.; Rastrelli, F.; Bagnò, A., *Chem. Eur. J.* **2015**, *21* (37), 12960-12970.
18. Biswas, A. N.; Puri, M.; Meier, K. K.; Oloo, W. N.; Rohde, G. T.; Bominaar, E. L.; Münck, E.; Que, L., *J. Am. Chem. Soc.* **2015**, *137* (7), 2428-2431.
19. Pestovsky, O.; Stoian, S.; Bominaar, E. L.; Shan, X.; Münck, E.; Que Jr, L.; Bakac, A., *Angew. Chem. Int. Ed.* **2005**, *44* (42), 6871-6874.
20. Lacy, D. C.; Gupta, R.; Stone, K. L.; Greaves, J.; Ziller, J. W.; Hendrich, M. P.; Borovik, A. S., *J. Am. Chem. Soc.* **2010**, *132* (35), 12188-12190.
21. England, J.; Guo, Y.; Farquhar, E. R.; Young Jr, V. G.; Münck, E.; Que Jr, L., *J. Am. Chem. Soc.* **2010**, *132* (25), 8635-8644.
22. Seo, M. S.; Kim, N. H.; Cho, K.-B.; So, J. E.; Park, S. K.; Clémancey, M.; Garcia-Serres, R.; Latour, J.-M.; Shaik, S.; Nam, W., *Chem. Sci.* **2011**, *2* (6), 1039-1045.
23. Bae Seong, H.; Seo Mi, S.; Lee, Y. M.; Cho, K. B.; Kim, W. S.; Nam, W., *Angew. Chem. Int. Ed.* **2016**, *55* (28), 8027-8031.
24. Lee, N. Y.; Mandal, D.; Bae, S. H.; Seo, M. S.; Lee, Y.-M.; Shaik, S.; Cho, K.-B.; Nam, W., *Chem. Sci.* **2017**, *8* (8), 5460-5467.
25. Boillot, M.-L.; Weber, B., *C. R. Chim.* **2018**, *21* (12), 1196-1208.
26. Rasheed, W.; Draksharapu, A.; Banerjee, S.; Young, V. G.; Fan, R.; Guo, Y.; Ozerov, M.; Nehr Korn, J.; Krzystek, J.; Telsner, J.; Que, L., *Angew. Chem. Int. Ed.* **2018**, *57* (30), 9387-9391.
27. Lim, M. H.; Rohde, J.-U.; Stubna, A.; Bukowski, M. R.; Costas, M.; Ho, R. Y. N.; Münck, E.; Nam, W.; Que, L., *PNAS* **2003**, *100* (7), 3665.

28. Paine, T. K.; Costas, M.; Kaizer, J.; Que Jr, L., *J. Biol. Inorg. Chem.* **2006**, *11* (3), 272-276.
29. Rasheed, W.; Draksharapu, A.; Banerjee, S.; Young Victor, G.; Fan, R.; Guo, Y.; Ozerov, M.; Nehrkorn, J.; Krzystek, J.; Telser, J.; Que, L., *Angew. Chem. Int. Ed.* **2018**, (0), DOI: 10.1002/anie.201804836.
30. Singh, R.; Ganguly, G.; Malinkin, S. O.; Demeshko, S.; Meyer, F.; Nordlander, E.; Paine, T. K., *Inorg. Chem.* **2019**.
31. Kaizer, J.; Klinker, E. J.; Oh, N. Y.; Rohde, J.-U.; Song, W. J.; Stubna, A.; Kim, J.; Münck, E.; Nam, W.; Que, L., Jr., *J. Am. Chem. Soc.* **2004**, *126* (2), 472-473.
32. Mitra, M.; Nimir, H.; Demeshko, S.; Bhat, S. S.; Malinkin, S. O.; Haukka, M.; Lloret-Fillol, J.; Lisensky, G. C.; Meyer, F.; Shteinman, A. A.; Browne, W. R.; Hrovat, D. A.; Richmond, M. G.; Costas, M.; Nordlander, E., *Inorg. Chem.* **2015**, *54* (15), 7152-7164.
33. Klinker, E. J.; Shaik, S.; Hirao, H.; Que, L., Jr, *Angew. Chem. Int. Ed.* **2009**, *48* (7), 1291-1295.
34. Saouma, C. T.; Mayer, J. M., *Chem. Sci.* **2014**, *5* (1), 21-31.
35. Banerjee, S.; Rasheed, W.; Fan, R.; Draksharapu, A.; Oloo, W. N.; Guo, Y.; Que Jr, L., *Angew. Chem. Int. Ed.* **2019**, *Submitted*.
36. Sahu, S.; Quesne, M. G.; Davies, C. G.; Dürr, M.; Ivanović-Burmazović, I.; Siegler, M. A.; Jameson, G. N. L.; de Visser, S. P.; Goldberg, D. P., *J. Am. Chem. Soc.* **2014**, *136* (39), 13542-13545.
37. Knizia, G., <http://www.iboview.org/>.
38. Knizia, G.; Klein, J. E. M. N., *Angew. Chem. Int. Ed.* **2015**, *54* (18), 5518-22.
39. Draksharapu, A.; Rasheed, W.; Klein, J. E. M. N.; Que, L., *Angew. Chem. Int. Ed.* **2017**, *56* (31), 9091-9095.
40. Ahlrichs, R.; Bär, M.; Häser, M.; Horn, H.; Kölmel, C., *Chem. Phys. Lett.* **1989**, *162* (3), 165-169.

41. Furche, F.; Ahlrichs, R.; Hättig, C.; Klopper, W.; Sierka, M.; Weigend, F., *WIREs Comput. Mol. Sci.* **2014**, *4* (2), 91-100.
42. Zhao, Y.; Truhlar, D. G., *J. Phys. Chem. A* **2005**, *109* (25), 5656-5667.
43. Weigend, F.; Ahlrichs, R., *Phys. Chem. Chem. Phys.* **2005**, *7* (18), 3297-3305.
44. Averkiev, B. B.; Truhlar, D. G., *Catal. Sci. Technol.* **2011**, *1* (8), 1526-1529.
45. Ribeiro, R. F.; Marenich, A. V.; Cramer, C. J.; Truhlar, D. G., *J. Phys. Chem. B* **2011**, *115* (49), 14556-14562.
46. Sierka, M.; Hogeckamp, A.; Ahlrichs, R., *J. Chem. Phys.* **2003**, *118* (20), 9136-9148.
47. Weigend, F., *Phys. Chem. Chem. Phys.* **2006**, *8* (9), 1057-1065.

Chapter 5:
Conclusion and Perspectives

5.1 Introduction

This thesis has detailed work on the generation, characterization, and reactivity of a series of reactive high-valent nonheme oxoiron(IV) complexes. Well-known pyridine-rich ligand frameworks (which have been known to support oxoiron(IV) complexes since 2004) were chosen as starting points, namely BnTPEN, N4Py and TPA (Figure 5.1), and modified to support new oxoiron(IV) complexes with enhanced reactivity, bringing the total unofficial count of oxoiron(IV) complexes known to the Que lab from 92 to just past a 100!

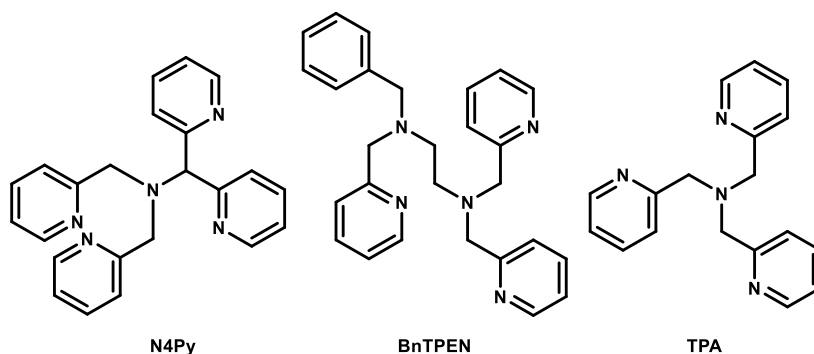


Figure 5.1 Ligand frameworks that were modified to form newer oxoiron(IV) complexes. N4Py: 1,1-di(pyridin-2-yl)-N,N-bis(pyridin-2-ylmethyl)methanamine, BnTPEN: *N*-benzyl-*N,N',N'*-tris(2-pyridylmethyl)ethylenediamine, TPA: tris(2-pyridylmethyl)amine.

However, the underlying goal of the pursuit to make new oxoiron(IV) complexes was driven by two motives that still piqued the interest of bioinorganic chemists with respect to oxoiron(IV) complexes. The first motive was to obtain structural information on oxoiron(IV) complexes that are very reactive in nature. The most successful attempt at making $S = 2$ oxoiron(IV) complexes, which functionally and electronically mimic enzymatic intermediates, is represented by $[\text{Fe}^{\text{IV}}(\text{O})(\text{TQA})(\text{L})]^{2+}$, which was reported over a decade after the first oxoiron(IV) complexes were reported.¹ This complex contains quinolines, and is the most reactive oxoiron(IV) complex reported. While the hypothesis that quinoline heterocycles are sterically encumbering is generally accepted, the best proof would come from structural information on oxoiron(IV) complexes containing

quinoline heterocycles that can be structurally characterized. Typically direct evidence of such interactions was only available for iron(II), manganese(II) and zinc(II) complexes supported by complexes containing quinolines or alpha-methyl substituents on pyridines.²⁻⁴ These first-row transition metal complexes show that introduction of alpha-substitutions on pyridines or replacement of pyridines with quinolines increased the M–N bond lengths, owing to increased steric interactions from the quinolyl or alpha-methyl protons.⁴⁻⁵ In this thesis, an oxoiron(IV) complex containing quinoline heterocycles was crystallographically characterized.⁶ While it retains its $S = 1$ spin state, it does show increased average Fe–N bond lengths compared with the parent complex that only contained pyridines, and the steric interactions additionally also tilt the oxoiron(IV) unit by about 10° off the z-axis. This is because the H8 protons of the quinolines encounter steric interactions with the ferryl unit, and this increases the distance of the quinoline donors from the iron center and forces the oxo unit to tilt sideways. This is the first time that we can experimentally show that these steric trends persist in the higher-oxidation state for a first-row transitional metal complex. Since the increased M–L bond lengths also increase the electrophilicity of the metal center, up to a 1000-fold increase in the reactivity of the resulting complexes is demonstrated compared with the parent pyridine-rich complex (Figure 5.2).

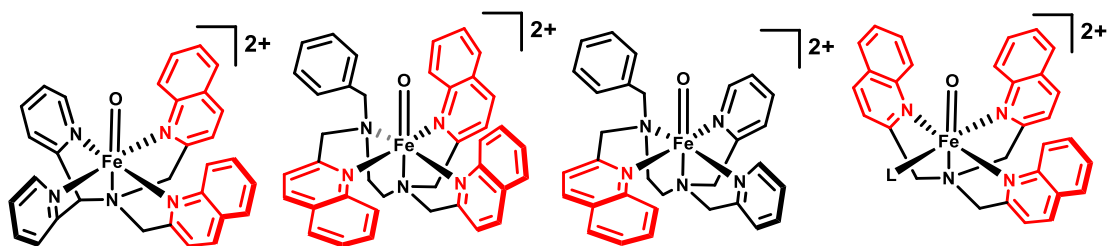


Figure 5.2 Some of the oxoiron(IV) complexes containing quinolines examined in this thesis. The complex on the left was structurally characterized.

The second motive was to develop structural and spectroscopic correlations with reactivity of oxoiron(IV) complexes. To pursue this goal, this thesis further expands on the BnTPEN ligand framework with similar substitutions that were made on N4Py, although in BnTPEN, one of the substituted pyridines is perpendicular to the

oxoiron(IV) unit, and would arguably have different steric interactions with the ferryl unit. In this process, crystallographic data on two oxoiron(IV) complexes was obtained, and we were able to characterize additional oxoiron(IV) complexes that are stable enough at room temperature to allow measurements of their rate constants, but not stable enough to be crystallized. In making these substituted complexes, we were also able to measure the fastest rates for reactions of cyclohexane with oxoiron(IV) complexes at room temperature, and this was achieved without having fully 'saturated' the ligand supporting the ferryl complex with alpha-substitutions. Overall, the examination of effects of the number of substitutions, the type of substituents and the orientation of the substituent was further enabled by BnTPEN framework.

This series of oxoiron(IV) complexes supported by these pentadentate ligands is shown to encompass reaction rates that span at least 7 orders of magnitude (with OAT at 233 K) and at least 5 orders of magnitude in the rates of reactions with HAT substrates both at 298 or 233 K. This has enabled development of reactivity correlations with structural features that are represented by average Fe-N bond lengths. This change in Fe-N bond lengths may help us define where to expect average Fe-N bond lengths for the thermally unstable $S = 2$ complex $[\text{Fe}^{\text{IV}}(\text{O})(\text{TQA})(\text{L})]^{2+}$ for which no structural data has been reported thus far (Figure 5.3)

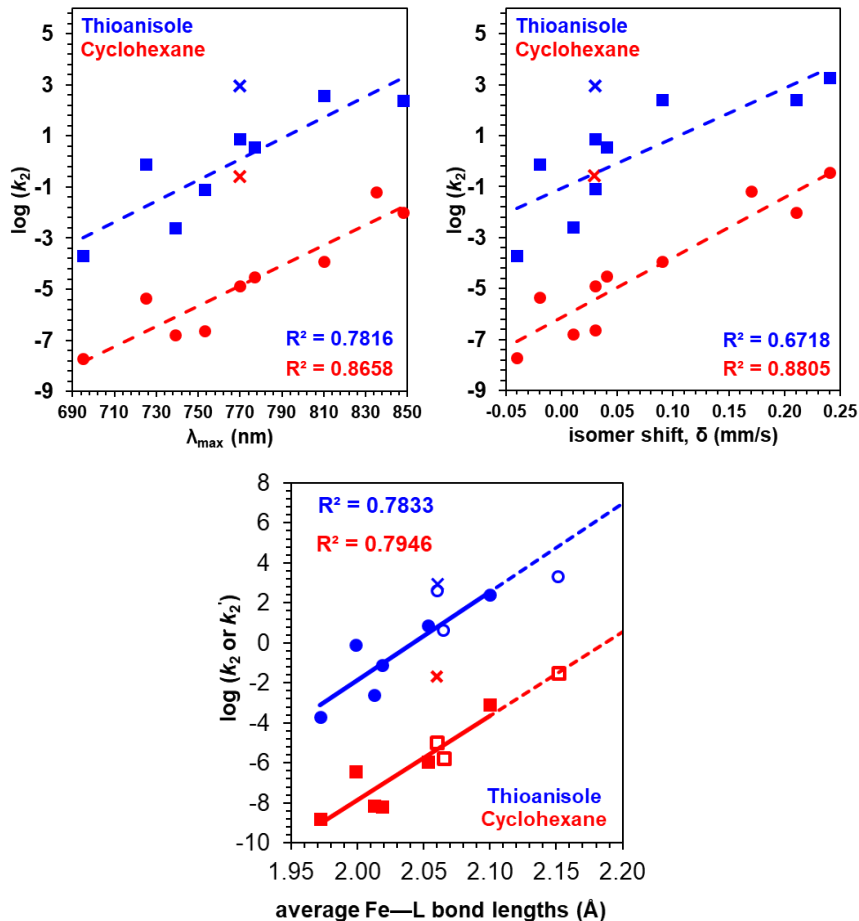


Figure 5.3 Spectroscopic (top) and structural (bottom) correlations of oxoiron(IV) complexes with reactivity measured by second-order rate constants at 233 K. The value represented by x represents the complex [Fe^{IV}(O)(Me₃NTB)(L)]²⁺.

We have also developed some unprecedented spectroscopic correlations with reactivity, as represented by isomer shift and absorption bands in Figure 5.3, both of which are measurements of electronics around the iron center. Interestingly isomer shifts and Fe-N bond lengths would be considered to have a role in defining the spin state of the oxoiron(IV) complexes, but would not be correlated linearly with the reactivity.

If a sufficient number of substitutions is made on oxoiron(IV) complexes, a ground spin state change of the complexes can result from $S = 1$ to $S = 2$ as demonstrated

by the complex $[\text{Fe}^{\text{IV}}(\text{O})(\text{TQA})(\text{L})]^{2+}$. In the process of sequentially introducing these substitutions, we were able to identify a unique oxoiron(IV) complex with properties of $S = 1$ and $S = 2$ complexes at different temperatures, thus showing for the first time experimentally that an oxoiron(IV) species can have temperature-dependent spin states, which is formally a spin-crossover behavior.

Lastly this thesis examines the NMR properties of complexes, and reports spectra of quintet oxoiron(IV) complexes for the first time, and their much more paramagnetically shifted peaks are in alignment with what is expected for the ferryl complexes with more unpaired spin. Interestingly the $S = 2$ iron(IV) complexes have an observable range of chemical shifts spanning about 200 ppm, and this is comparable to the NMR shifts in $S = 2$ iron(II) complexes, although the assignments of peaks to the protons are likely very different due to different pathways for unpaired spin propagation as well as the d-orbital configuration.

5.2 Future Challenges

Oxoiron(IV) complexes containing alpha-methyl substituents generally have lower stability compared with their quinoline containing counterparts. If one can deuterate the benzylic positions, it might be possible for us to stabilize reactive species for longer periods, and obtain structural information on oxoiron(IV) complexes containing alpha-methyl substituents, just like the case where structural information is available on complexes containing quinolines.

While the two tetragonal oxoiron(IV) complexes in the quintet spin state reported so far are found to be very reactive,^{1, 7} there is a striking exception of a tetragonal complex in the triplet spin state, namely $[\text{Fe}^{\text{IV}}(\text{O})(\text{Me}_3\text{NTB})(\text{L})]^{2+}$,⁸⁻¹¹ that has somewhat comparable reactivity to that of the most reactive oxoiron(IV) complex, namely $[\text{Fe}^{\text{IV}}(\text{O})(\text{TQA})(\text{L})]^{2+}$. While most complexes that we have reported in this thesis exhibit reactivity trends that are in line with their observed isomer shift and absorption features, we have found that this complex is an exception to the rule.

This highlights some challenges and need for more perspectives on reactivity of oxoiron(IV) complexes.

When the isomer shift (0.03 mm/s), absorption features ($\lambda_{\text{max}} = 770 \text{ nm}$), and averaged Fe-N bond lengths (2.06 Å) of the complex $[\text{Fe}^{\text{IV}}(\text{O})(\text{Me}_3\text{NTB})(\text{L})]^{2+}$ are plotted on the correlations, the correlations predict a much lower reactivity than what is observed. This complex contains benzimidazole donors which actually have higher basicity than pyridines, and the trends observed in reactivity indicate that we should consider other factors in addition to the structural and spectroscopic properties of oxoiron(IV) complexes in determining the reactivity of complexes.

The typical explanation for reactive $S = 1$ oxoiron(IV) complexes relies on a theoretical model that cannot be directly experimentally verified, namely two-state reactivity, as first postulated by Shaik.¹² This idea was applied to $[\text{Fe}^{\text{IV}}(\text{O})(\text{Me}_3\text{NTB})(\text{L})]^{2+}$ when it was first reported, and suggests that during the hydrogen atom abstraction reaction, a spin crossover to a more reactive and excited $S = 2$ reaction surface occurs as the $\text{Fe}^{\text{IV}}=\text{O}$ unit interacts with a substrate's C-H bond along the reaction coordinate. As these are events postulated to occur in the transition state, experimental confirmation is not possible. The only indirect way to measure this excited spin state's contribution into the $S = 1$ ground spin state is to measure the zero-field splitting parameter of the complexes. A higher value reflects a greater contribution of excited spin state into the ground spin state. While a higher zfs parameter can be used to explain the high reactivity of the complex, it does not verify TSR directly because this model only talks about access during a transition state. Furthermore, the accurate measurement of this parameter requires access to the solid samples, which are not accessible for unstable intermediates like this one. We can estimate this value using Mössbauer spectroscopy however, and for this complex, we do find that this value is among the highest ZFS parameters determined for any complex. Still, zfs parameters do not directly probe the HAT reaction, and are likely only part of a kinetic argument. Potentially thermodynamic factors should also be considered, as favoured by

Mayer in comparing HAT reactivity.¹³ A correlation between the HAT reactivity of a metal-oxo species with the strength of the MO–H bond formed has been demonstrated based on ideas developed by Bordwell and Mayer for which the MO–H bond strength would reflect the driving force for the HAT reaction.¹⁴⁻¹⁷ To obtain this number, one needs to have access to be able to measure reduction potential of the oxidized metal oxo species, as well as pKa of the reduced MO–H bond. This value has been successfully measured for Cu(III) hydroxides, but only in one case has this value been measured for iron(III) hydroxides.¹⁸

This is why future approaches to explain reactivity of oxoiron(IV) complexes should also look at thermodynamic driving forces that drive the reaction rates, in addition to spectroscopic and structural correlations.

Lastly, all synthetic non-heme oxoiron(IV) complexes reported so far are either supported by pyridines, quinolines and/or amines,¹⁹ with some exceptions of ligands supported by carboxylates in addition to pyridines/amines.²⁰ Many enzymatic non-heme mononuclear oxoiron(IV) intermediates are supported by 2-His-1-carboxylate facial triad, and are thus not directly represented by the synthetic model complexes. The closest we get to histidine in synthetic model complexes are benzimidazole groups which were employed by Nam on the tripodal ligand that supports the complex $[\text{Fe}^{\text{IV}}(\text{O})(\text{Me}_3\text{NTB})(\text{L})]^{2+}$, and subsequently by others.²¹ There is one possible variant of this ligand that contains 2-histidines and 1-carboxylate center, but formation of oxoiron(IV) complex with this ligand has not been attempted.²²

Below are two possible examples of oxoiron(IV) complexes that can be supported by BnTPEN-like framework. The ligands for these are easily accessible using the same synthetic routes that are employed to make substitutions on BnTPEN frameworks (Figure 5.4).

Good luck to aspiring bioinorganic chemists who pursue these ventures.

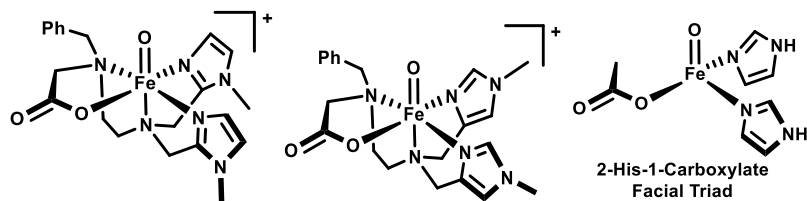


Figure 5.4 Oxoiron(IV) complexes containing a facial-triad like ligand framework.

5.3 References

1. Biswas, A. N.; Puri, M.; Meier, K. K.; Oloo, W. N.; Rohde, G. T.; Bominaar, E. L.; Münck, E.; Que, L., *J. Am. Chem. Soc.* **2015**, *137* (7), 2428-2431.
2. Lo, W. K. C.; McAdam, C. J.; Blackman, A. G.; Crowley, J. D.; McMorran, D. A., *Inorg. Chim. Acta* **2015**, *426*, 183-194.
3. Massie, A. A.; Denler, M. C.; Cardoso, L. T.; Walker, A. N.; Hossain, M. K.; Day, V. W.; Nordlander, E.; Jackson, T. A., *Angew. Chem. Int. Ed.* **2017**, *56* (15), 4178-4182.
4. de Visser, S.; Mukherjee, G.; Kumar, D.; Sastri, C.; Alili, A.; Barman, P., *Chem. Eur. J.* **2019**, *0* (Just Accepted).
5. Zang, Y.; Kim, J.; Dong, Y.; Wilkinson, E. C.; Appelman, E. H.; Que, L., Jr., *J. Am. Chem. Soc.* **1997**, *119*, 4197-4205.
6. Rasheed, W.; Draksharapu, A.; Banerjee, S.; Young, V. G.; Fan, R.; Guo, Y.; Ozerov, M.; Nehr Korn, J.; Krzystek, J.; Telser, J.; Que, L., *Angew. Chem. Int. Ed.* **2018**, *57* (30), 9387-9391.
7. Pestovsky, O.; Stoian, S.; Bominaar, E. L.; Shan, X.; Münck, E.; Que Jr, L.; Bakac, A., *Angew. Chem. Int. Ed.* **2005**, *44* (42), 6871-6874.
8. Seo, M. S.; Kim, N. H.; Cho, K.-B.; So, J. E.; Park, S. K.; Clémancey, M.; Garcia-Serres, R.; Latour, J.-M.; Shaik, S.; Nam, W., *Chem. Sci.* **2011**, *2* (6), 1039-1045.
9. Bae Seong, H.; Seo Mi, S.; Lee, Y. M.; Cho, K. B.; Kim, W. S.; Nam, W., *Angew. Chem. Int. Ed.* **2016**, *55* (28), 8027-8031.
10. Lee, N. Y.; Mandal, D.; Bae, S. H.; Seo, M. S.; Lee, Y.-M.; Shaik, S.; Cho, K.-B.; Nam, W., *Chem. Sci.* **2017**, *8* (8), 5460-5467.

11. Banerjee, S.; Rasheed, W.; Fan, R.; Draksharapu, A.; Oloo, W. N.; Guo, Y.; Que Jr, L., *Angew. Chem. Int. Ed.* **2019**, *Submitted*.
12. Klinker, E. J.; Shaik, S.; Hirao, H.; Que, L., Jr, *Angew. Chem. Int. Ed.* **2009**, *48* (7), 1291-1295.
13. Saouma, C. T.; Mayer, J. M., *Chem. Sci.* **2014**, *5* (1), 21-31.
14. Mayer, J. M., *Accounts of Chemical Research* **2011**, *44* (1), 36-46.
15. Roth, J. P.; Yoder, J. C.; Won, T.-J.; Mayer, J. M., *Science* **2001**, *294* (5551), 2524.
16. Mayer, J. M., *Accounts of Chemical Research* **1998**, *31* (8), 441-450.
17. Gardner, K. A.; Mayer, J. M., *Science* **1995**, *269* (5232), 1849.
18. Usharani, D.; Lacy, D. C.; Borovik, A. S.; Shaik, S., *J. Am. Chem. Soc.* **2013**, *135* (45), 17090-17104.
19. McDonald, A. R.; Que, L., Jr., *Coord. Chem. Rev.* **2013**, *257* (2), 414-428.
20. McDonald, A. R.; Guo, Y.; Vu, V. V.; Bominaar, E. L.; Münck, E.; Que, L., Jr., *Chem. Sci.* **2012**, *3*, 1680-1693.
21. Browne; David, M. M.; Hassan, N.; Serhiy, D.; Satish, S. B.; Sergey, O. M.; Matti, H.; Julio, L.-F.; George, C. L.; Franc, M.; Albert, A. S.; Wesley, R., **2015**.
22. Rodriguez, M.-C.; Morgenstern-Badarau, I.; Cesario, M.; Guilhem, J.; Keita, B.; Nadjo, L., *Inorg. Chem.* **1996**, *35* (26), 7804-781

Bibliography

1. Borgogno, A.; Rastrelli, F.; Bagno, A., *Chem. Eur. J.* **2015**, *21* (37), 12960-12970.
2. Knizia, G., <http://www.iboview.org/>.
3. Knizia, G.; Klein, J. E. M. N., *Angew. Chem. Int. Ed.* **2015**, *54* (18), 5518-22.
4. Banerjee, R.; Proshlyakov, Y.; Lipscomb, J. D.; Proshlyakov, D. A., *Nature* **2015**, *518*, 431.
5. Bols, M. L.; Hallaert, S. D.; Snyder, B. E. R.; Devos, J.; Plessers, D.; Rhoda, H. M.; Dusselier, M.; Schoonheydt, R. A.; Pierloot, K.; Solomon, E. I.; Sels, B. F., *J. Am. Chem. Soc.* **2018**, *140* (38), 12021-12032.
6. Price, J. C.; Barr, E. W.; Tirupati, B.; Bollinger, J. M.; Krebs, C., *Biochemistry* **2003**, *42* (24), 7497-7508.
7. van der Ploeg, J. R.; Weiss, M. A.; Saller, E.; Nashimoto, H.; Saito, N.; Kertesz, M. A.; Leisinger, T., *J. Bacteriol.* **1996**, *178* (18), 5438.
8. Hegg, E. L.; Jr, L. Q., *Eur. J. Biochem.* **1997**, *250* (3), 625-629.
9. Koehntop, K. D.; Emerson, J. P.; Que, L., *J. Biol. Inorg. Chem.* **2005**, *10* (2), 87-93.
10. Kal, S.; Que, L., *J. Biol. Inorg. Chem.* **2017**, *22* (2), 339-365.
11. Bollinger Jr, J. M.; Price, J. C.; Hoffart, L. M.; Barr, E. W.; Krebs, C., *Eur. J. Inorg. Chem.* **2005**, *2005* (21), 4245-4254.
12. Tamanaha, E.; Zhang, B.; Guo, Y.; Chang, W.-c.; Barr, E. W.; Xing, G.; St. Clair, J.; Ye, S.; Neese, F.; Bollinger, J. M.; Krebs, C., *J. Am. Chem. Soc.* **2016**, *138* (28), 8862-8874.
13. Wong, S. D.; Srnec, M.; Matthews, M. L.; Liu, L. V.; Kwak, Y.; Park, K.; Bell lii, C. B.; Alp, E. E.; Zhao, J.; Yoda, Y.; Kitao, S.; Seto, M.; Krebs, C.; Bollinger, J. M.; Solomon, E. I., *Nature* **2013**, *499*, 320.
14. Sinnecker, S.; Svensen, N.; Barr, E. W.; Ye, S.; Bollinger, J. M.; Neese, F.; Krebs, C., *J. Am. Chem. Soc.* **2007**, *129* (19), 6168-6179.
15. Galonić Fujimori, D.; Barr, E. W.; Matthews, M. L.; Koch, G. M.; Yonce, J. R.; Walsh, C. T.; Bollinger, J. M.; Krebs, C.; Riggs-Gelasco, P. J., *J. Am. Chem. Soc.* **2007**, *129* (44), 13408-13409.
16. Eser, B. E.; Barr, E. W.; Frantom, P. A.; Saleh, L.; Bollinger, J. M.; Krebs, C.; Fitzpatrick, P. F., *J. Am. Chem. Soc.* **2007**, *129* (37), 11334-11335.
17. Panay, A. J.; Lee, M.; Krebs, C.; Bollinger, J. M.; Fitzpatrick, P. F., *Biochemistry* **2011**, *50* (11), 1928-1933.

18. Yu, C.-P.; Tang, Y.; Cha, L.; Milikisiyants, S.; Smirnova, T. I.; Smirnov, A. I.; Guo, Y.; Chang, W.-c., *J. Am. Chem. Soc.* **2018**, *140* (45), 15190-15193.
19. Rohde, J.-U.; In, J.-H.; Lim, M. H.; Brennessel, W. W.; Bukowski, M. R.; Stubna, A.; Münck, E.; Nam, W.; Que, L., *Science* **2003**, *299* (5609), 1037.
20. McDonald, A. R.; Que, L., Jr., *Coord. Chem. Rev.* **2013**, *257* (2), 414-428.
21. Klein, J. E. M. N.; Que, L., Biomimetic High-Valent Mononuclear Nonheme Iron-Oxo Chemistry. In *Encyclopedia of Inorganic and Bioinorganic Chemistry*, John Wiley & Sons, Ltd: 2016; p; DOI: 10.1002/9781119951438.eibc2344
22. Puri, M.; Que, L., *Acc. Chem. Res.* **2015**, *48* (8), 2443-2452.
23. Lim, M. H.; Rohde, J.-U.; Stubna, A.; Bukowski, M. R.; Costas, M.; Ho, R. Y. N.; Münck, E.; Nam, W.; Que, L., *PNAS* **2003**, *100* (7), 3665.
24. Zang, Y.; Kim, J.; Dong, Y.; Wilkinson, E. C.; Appelman, E. H.; Que, L., Jr., *J. Am. Chem. Soc.* **1997**, *119*, 4197-4205.
25. Rasheed, W.; Draksharapu, A.; Banerjee, S.; Young, V. G.; Fan, R.; Guo, Y.; Ozerov, M.; Nehrkorn, J.; Krzystek, J.; Telsler, J.; Que, L., *Angew. Chem. Int. Ed.* **2018**, *57* (30), 9387-9391.
26. Lubben, M.; Meetsma, A.; Wilkinson, E. C.; Feringa, B.; Que Jr, L., *Angew. Chem. Int. Ed.* **1995**, *34* (13-14), 1512-1514.
27. Lo, W. K. C.; Huff, G. S.; Preston, D.; McMorran, D. A.; Giles, G. I.; Gordon, K. C.; Crowley, J. D., *Inorganic Chemistry* **2015**, *54* (14), 6671-6673.
28. Kaizer, J.; Klinker, E. J.; Oh, N. Y.; Rohde, J.-U.; Song, W. J.; Stubna, A.; Kim, J.; Münck, E.; Nam, W.; Que, L., Jr., *J. Am. Chem. Soc.* **2004**, *126* (2), 472-473.
29. Xue, G.; De Hont, R.; Münck, E.; Que Jr, L., *Nature Chemistry* **2010**, *2*, 400.
30. Paine, T. K.; Costas, M.; Kaizer, J.; Que Jr, L., *J. Biol. Inorg. Chem.* **2006**, *11* (3), 272-276.
31. Klinker, E. J.; Kaizer, J.; Brennessel, W. W.; Woodrum, N. L.; Cramer, C. J.; Que, L., Jr., *Angew. Chem. Int. Ed.* **2005**, *44* (24), 3690-3694.
32. Massie, A. A.; Denler, M. C.; Cardoso, L. T.; Walker, A. N.; Hossain, M. K.; Day, V. W.; Nordlander, E.; Jackson, T. A., *Angew. Chem. Int. Ed.* **2017**, *56* (15), 4178-4182.
33. Duelund, L.; Hazell, R.; McKenzie, C. J.; Preuss Nielsen, L.; Toftlund, H., *J. Chem. Soc., Dalton Trans.* **2001**, (2), 152-156.
34. Ortega-Villar, N.; Ugalde-Saldívar, V. M.; Muñoz, M. C.; Ortiz-Frade, L. A.; Alvarado-Rodríguez, J. G.; Real, J. A.; Moreno-Esparza, R., *Inorg. Chem.* **2007**, *46* (18), 7285-7293.

35. Cheaib, K.; Mubarak, M. Q. E.; Sénéchal-David, K.; Herrero, C.; Guillot, R.; Clémancey, M.; Latour, J.-M.; de Visser, S. P.; Mahy, J.-P.; Banse, F.; Avenier, F., *Angew. Chem. Int. Ed.* **2019**, *58* (3), 854-858.
36. Lennartson, A.; McKenzie, C. J., *Angew. Chem. Int. Ed.* **2012**, *51* (27), 6767-6770.
37. Kang, Y.; Li, X.-X.; Cho, K.-B.; Sun, W.; Xia, C.; Nam, W.; Wang, Y., *J. Am. Chem. Soc.* **2017**, *139* (22), 7444-7447.
38. Duban, E. A.; Bryliakov, K. P.; Talsi, E. P., *Eur. J. Inorg. Chem.* **2007**, *2007* (6), 852-857.
39. Mukherjee, G.; Lee, C. W. Z.; Nag, S. S.; Alili, A.; Cantú Reinhard, F. G.; Kumar, D.; Sastri, C. V.; de Visser, S. P., *Dalton Trans.* **2018**, *47* (42), 14945-14957.
40. Singh, R.; Ganguly, G.; Malinkin, S. O.; Demeshko, S.; Meyer, F.; Nordlander, E.; Paine, T. K., *Inorg. Chem.* **2019**.
41. Sahu, S.; Zhang, B.; Pollock, C. J.; Dürr, M.; Davies, C. G.; Confer, A. M.; Ivanović-Burmazović, I.; Siegler, M. A.; Jameson, G. N. L.; Krebs, C.; Goldberg, D. P., *J. Am. Chem. Soc.* **2016**, *138* (39), 12791-12802.
42. Rana, S.; Biswas, J. P.; Sen, A.; Clémancey, M.; Blondin, G.; Latour, J.-M.; Rajaraman, G.; Maiti, D., *Chem. Sci.* **2018**, *9* (40), 7843-7858.
43. Bigi, J. P.; Harman, W. H.; Lassalle-Kaiser, B.; Robles, D. M.; Stich, T. A.; Yano, J.; Britt, R. D.; Chang, C. J., *J. Am. Chem. Soc.* **2012**, *134* (3), 1536-1542.
44. Krebs, C.; Galonić Fujimori, D.; Walsh, C. T.; Bollinger, J. M., *Acc. Chem. Res.* **2007**, *40* (7), 484-492.
45. Engelmann, X.; Monte-Pérez, I.; Ray, K., *Angew. Chem. Int. Ed.* **2016**, *55* (27), 7632-7649.
46. Nam, W.; Lee, Y.-M.; Fukuzumi, S., *Acc. Chem. Res.* **2014**, *47* (4), 1146-1154.
47. England, J.; Guo, Y.; Farquhar, E. R.; Young Jr, V. G.; Münck, E.; Que Jr, L., *J. Am. Chem. Soc.* **2010**, *132* (25), 8635-8644.
48. Lacy, D. C.; Gupta, R.; Stone, K. L.; Greaves, J.; Ziller, J. W.; Hendrich, M. P.; Borovik, A. S., *J. Am. Chem. Soc.* **2010**, *132* (35), 12188-12190.
49. Pestovsky, O.; Stoian, S.; Bominaar, E. L.; Shan, X.; Münck, E.; Que Jr, L.; Bakac, A., *Angew. Chem. Int. Ed.* **2005**, *44* (42), 6871-6874.
50. Biswas, A. N.; Puri, M.; Meier, K. K.; Oloo, W. N.; Rohde, G. T.; Bominaar, E. L.; Münck, E.; Que, L., *J. Am. Chem. Soc.* **2015**, *137* (7), 2428-2431.

51. Seo, M. S.; Kim, N. H.; Cho, K.-B.; So, J. E.; Park, S. K.; Clémancey, M.; Garcia-Serres, R.; Latour, J.-M.; Shaik, S.; Nam, W., *Chem. Sci.* **2011**, 2 (6), 1039-1045.
52. Mitra, M.; Nimir, H.; Demeshko, S.; Bhat, S. S.; Malinkin, S. O.; Haukka, M.; Lloret-Fillol, J.; Lisensky, G. C.; Meyer, F.; Shteinman, A. A.; Browne, W. R.; Hrovat, D. A.; Richmond, M. G.; Costas, M.; Nordlander, E., *Inorg. Chem.* **2015**, 54 (15), 7152-7164.
53. Rana, S.; Dey, A.; Maiti, D., *Chem. Commun.* **2015**, 51 (77), 14469-14472.
54. Sahu, S.; Quesne, M. G.; Davies, C. G.; Dürr, M.; Ivanović-Burmazović, I.; Siegler, M. A.; Jameson, G. N. L.; de Visser, S. P.; Goldberg, D. P., *J. Am. Chem. Soc.* **2014**, 136 (39), 13542-13545.
55. Massie, A. A.; Sinha, A.; Parham, J. D.; Nordlander, E.; Jackson, T. A., *Inorg. Chem.* **2018**, 57 (14), 8253-8263.
56. Denler, M. C.; Massie, A. A.; Singh, R.; Stewart-Jones, E.; Sinha, A.; Day, V. W.; Nordlander, E.; Jackson, T. A., *Dalton Trans.* **2019**.
57. McDonald, A. R.; Guo, Y.; Vu, V. V.; Bominaar, E. L.; Münck, E.; Que, L., *Chem. Sci.* **2012**, 3 (5), 1680-1693.
58. de Visser, S.; Mukherjee, G.; Kumar, D.; Sastri, C.; Alili, A.; Barman, P., *Chem. Eur. J.* **2019**, 0 (Just Accepted).
59. Hagen, K. S., *Inorg. Chem.* **2000**, 39, 5867-5869.
60. Petasis, D. T.; Hendrich, M. P., Chapter Eight - Quantitative Interpretation of Multifrequency Multimode EPR Spectra of Metal Containing Proteins, Enzymes, and Biomimetic Complexes. In *Methods in Enzymology*, Qin, P. Z.; Warncke, K., Eds. Academic Press: 2015; Vol. 563, pp 171-208.
61. Hassan, A. K.; Pardi, L. A.; Krzystek, J.; Sienkiewicz, A.; Goy, P.; Rohrer, M.; Brunel, L. C., *J. Magn. Reson.* **2000**, 142 (2), 300-312.
62. Ludwig, J.; Vasilyev, Y. B.; Mikhailov, N. N.; Poumirol, J. M.; Jiang, Z.; Vafek, O.; Smirnov, D., *Phys. Rev. B* **2014**, 89 (24), 241406.
63. Spek, A. L.; Schoondergang, M. F. J.; Feringa, B. L., *CSD Communication* **2004**, CCDC 232796.
64. Decker, A.; Rohde, J.-U.; Que, L., Jr.; Solomon, E. I., *J. Am. Chem. Soc.* **2004**, 126 (17), 5378-5379.
65. Jackson, T. A.; Rohde, J.-U.; Seo, M. S.; Sastri, C. V.; DeHont, R.; Stubna, A.; Ohta, T.; Kitagawa, T.; Münck, E.; Nam, W.; Que, L., Jr., *J. Am. Chem. Soc.* **2008**, 130 (37), 12394-12407.

66. Draksharapu, A.; Angelone, D.; Quesne, M. G.; Padamati, S. K.; Gómez, L.; Hage, R.; Costas, M.; Browne, W. R.; de Visser, S. P., *Angew. Chem. Int. Ed.* **2015**, *54* (14), 4357-4361.
67. Draksharapu, A.; Rasheed, W.; Klein, J. E. M. N.; Que, L., *Angew. Chem. Int. Ed.* **2017**, *56* (31), 9091-9095.
68. Lee, Y.-M.; Dhuri, S. N.; Sawant, S. C.; Cho, J.; Kubo, M.; Ogura, T.; Fukuzumi, S.; Nam, W., *Angew. Chem. Int. Ed.* **2009**, *48* (10), 1803-1806.
69. Chanda, A.; Shan, X.; Chakrabarti, M.; Ellis, W. C.; Popescu, D. L.; Tiago de Oliveira, F.; Wang, D.; Que, L., Jr.; Collins, T. J.; Münck, E.; Bominaar, E. L., *Inorg. Chem.* **2008**, *47* (9), 3669-3678.
70. Krzystek, J.; England, J.; Ray, K.; Ozarowski, A.; Smirnov, D.; Que, L., Jr.; Telser, J., *Inorg. Chem.* **2008**, *47* (9), 3483-3485.
71. Telser, J.; Krzystek, J.; Ozarowski, A., *J. Biol. Inorg. Chem.* **2014**, *19* (3), 297-318.
72. Bucinsky, L.; Breza, M.; Lee, W.-T.; Hickey, A. K.; Dickie, D. A.; Nieto, I.; DeGayner, J. A.; Harris, T. D.; Meyer, K.; Krzystek, J.; Ozarowski, A.; Nehrkorn, J.; Schnegg, A.; Holldack, K.; Herber, R. H.; Telser, J.; Smith, J. M., *Inorg. Chem.* **2017**, *56* (8), 4751-4768.
73. Bucinsky, L.; Rohde, G. T.; Que, L.; Ozarowski, A.; Krzystek, J.; Breza, M.; Telser, J., *Inorg. Chem.* **2016**, *55* (8), 3933-3945.
74. APEX3, Bruker Analytical X-ray Systems, Madison, WI (2016).
75. SADABS, Bruker Analytical X-ray Systems, Madison, WI (2016).
76. SAINT, Bruker Analytical X-ray Systems, Madison, WI (2016).
77. SHELXTL, Bruker Analytical X-Ray Systems, Madison, WI (2008).
78. Sheldrick, G. M., *Acta Cryst.* **A64**, 112-122 (2008).
79. Sheldrick, G. M., *Acta Cryst.* **C71**, 3-8 (2015).
80. Rowland, R. S.; Taylor, R., *J. of Phys. Chem.* **1996**, *100* (18), 7384-7391.
81. Lee, N. Y.; Mandal, D.; Bae, S. H.; Seo, M. S.; Lee, Y.-M.; Shaik, S.; Cho, K.-B.; Nam, W., *Chem. Sci.* **2017**, *8* (8), 5460-5467.
82. Jensen, M. P.; Costas, M.; Ho, R. Y. N.; Kaizer, J.; Mairata i Payeras, A.; Münck, E.; Que, L., Jr.; Rohde, J.-U.; Stubna, A., *J. Am. Chem. Soc.* **2005**, *127* (30), 10512-10525.
83. Lőkóv, M.; Tshepelevitsh, S.; Heering, A.; Plieger, P. G.; Vianello, R.; Leito, I., *Eur. J. Org. Chem.* **2017**, *2017* (30), 4475-4489.

84. Wang, D.; Ray, K.; Collins, M. J.; Farquhar, E. R.; Frisch, J. R.; Gómez, L.; Jackson, T. A.; Kerscher, M.; Waleska, A.; Comba, P.; Costas, M.; Que, L., *Chem. Sci.* **2013**, *4* (1), 282-291.
85. Klinker, E. J.; Shaik, S.; Hirao, H.; Que, L., Jr, *Angew. Chem. Int. Ed.* **2009**, *48* (7), 1291-1295.
86. Mandal, D.; Mallick, D.; Shaik, S., *Acc. Chem. Res.* **2018**, *51* (1), 107-117.
87. Bae Seong, H.; Seo Mi, S.; Lee, Y. M.; Cho, K. B.; Kim, W. S.; Nam, W., *Angew. Chem. Int. Ed.* **2016**, *55* (28), 8027-8031.
88. Saouma, C. T.; Mayer, J. M., *Chem. Sci.* **2014**, *5* (1), 21-31.
89. Neidig, M. L.; Decker, A.; Choroba, O. W.; Huang, F.; Kavana, M.; Moran, G. R.; Spencer, J. B.; Solomon, E. I., *PNAS* **2006**, *103* (35), 12966-12973.
90. Srnec, M.; Wong, S. D.; Matthews, M. L.; Krebs, C.; Bollinger, J. M.; Solomon, E. I., *J. Am. Chem. Soc.* **2016**, *138* (15), 5110-5122.
91. Hausinger, R. P., *Critical Reviews in Biochemistry and Molecular Biology* **2004**, *39* (1), 21-68.
92. Paine, T. K.; Costas, M.; Kaizer, J.; Que, L., Jr., *J. Biol. Inorg. Chem.* **2006**, *11* (11), 272-276.
93. Wang, D.; Ray, K.; Collins, M. J.; Farquhar, E. R.; Frisch, J. R.; Gómez, L.; Jackson, T. A.; Kerscher, M.; Waleska, A.; Comba, P.; Costas, M.; Que Jr, L., *Chem. Sci.* **2013**, *4* (1), 282-291.
94. Snider, V. G.; Pella, B. J.; Mukherjee, A., *Inorg. Chim. Acta* **2018**, *469*, 447-452.
95. Bigelow, J. O.; England, J.; Klein, J. E. M. N.; Farquhar, E. R.; Frisch, J. R.; Martinho, M.; Mandal, D.; Münck, E.; Shaik, S.; Que, L., *Inorg. Chem.* **2017**, *56* (6), 3287-3301.
96. Kepp, K. P., *Inorg. Chem.* **2016**, *55* (6), 2717-2727.
97. Kepp, K. P., *Coord. Chem. Rev.* **2013**, *257* (1), 196-209.
98. Ahlrichs, R.; Bär, M.; Häser, M.; Horn, H.; Kölmel, C., *Chem. Phys. Lett.* **1989**, *162* (3), 165-169.
99. Furche, F.; Ahlrichs, R.; Hättig, C.; Klopper, W.; Sierka, M.; Weigend, F., *WIREs Comput. Mol. Sci.* **2014**, *4* (2), 91-100.
100. Zhao, Y.; Truhlar, D. G., *J. Phys. Chem. A* **2005**, *109* (25), 5656-5667.
101. Weigend, F.; Ahlrichs, R., *Phys. Chem. Chem. Phys.* **2005**, *7* (18), 3297-3305.

102. Averkiev, B. B.; Truhlar, D. G., *Catal. Sci. Technol.* **2011**, *1* (8), 1526-1529.
103. Ribeiro, R. F.; Marenich, A. V.; Cramer, C. J.; Truhlar, D. G., *J. Phys. Chem. B* **2011**, *115* (49), 14556-14562.
104. Sierka, M.; Hogeckamp, A.; Ahlrichs, R., *J. Chem. Phys.* **2003**, *118* (20), 9136-9148.
105. Weigend, F., *Phys. Chem. Chem. Phys.* **2006**, *8* (9), 1057-1065.
106. Monte Pérez, I.; Engelmann, X.; Lee, Y.-M.; Yoo, M.; Kumaran, E.; Farquhar, E. R.; Bill, E.; England, J.; Nam, W.; Swart, M.; Ray, K., *Angew. Chem. Int. Ed.* **2017**, *56* (46), 14384-14388.
107. Codolà, Z.; Gamba, I.; Acuña-Parés, F.; Casadevall, C.; Clémancey, M.; Latour, J.-M.; Luis, J. M.; Lloret-Fillol, J.; Costas, M., *J. Am. Chem. Soc.* **2019**, *141* (1), 323-333.
108. Klein Gebbink, R. J. M.; Chen, J., *ACS Catalysis* **2019**.
109. Banerjee, S.; Rasheed, W.; Fan, R.; Draksharapu, A.; Oloo, W. N.; Guo, Y.; Que Jr, L., *Chem. Eur. J.* **2019**, <http://dx.doi.org/10.1002/chem.201902048>.
110. Schatz, M.; Leibold, M.; Foxon, S. P.; Weitzer, M.; Heinemann, F. W.; Hampel, F.; Walter, O.; Schindler, S., *Dalton Trans.* **2003**, (8), 1480-1487.
111. Puri, M.; Company, A.; Sabenya, G.; Costas, M.; Que, L., *Inorg. Chem.* **2016**, *55* (12), 5818-5827.
112. Hu, Y.; Liang, L.; Wei, W.-t.; Sun, X.; Zhang, X.-j.; Yan, M., *Tetrahedron* **2015**, *71* (9), 1425-1430.
113. Rasheed, W.; Draksharapu, A.; Banerjee, S.; Young Victor, G.; Fan, R.; Guo, Y.; Ozerov, M.; Nehr Korn, J.; Krzystek, J.; Telsler, J.; Que, L., *Angew. Chem. Int. Ed.* **2018**, (0), DOI: 10.1002/anie.201804836.
114. Rohde, J.-U.; Torelli, S.; Shan, X.; Lim, M. H.; Klinker, E. J.; Kaizer, J.; Chen, K.; Nam, W.; Que, L., *J. Am. Chem. Soc.* **2004**, *126* (51), 16750-16761.
115. Norma Ortega-Villar; Víctor M. Ugalde-Saldívar; M. Carmen Muñoz; Luis A. Ortiz-Frade; José G. Alvarado-Rodríguez; José A. Real, a.; Rafael Moreno-Esparza*, **2007**.
116. Pavlov, A. A.; Denisov, G. L.; Kiskin, M. A.; Nelyubina, Y. V.; Novikov, V. V., *Inorg. Chem.* **2017**, *56* (24), 14759-14762.
117. England, J.; Prakash, J.; Cranswick, M. A.; Mandal, D.; Guo, Y.; Münck, E.; Shaik, S.; Que, L., *Inorg. Chem.* **2015**, *54* (16), 7828-7839.
118. Prakash, J.; Rohde, G. T.; Meier, K. K.; Münck, E.; Que, L., *Inorg. Chem.* **2015**, *54* (23), 11055-11057.

119. England, J.; Bigelow, J. O.; Van Heuvelen, K. M.; Farquhar, E. R.; Martinho, M.; Meier, K. K.; Frisch, J. R.; Münck, E.; Que, L., *Chem. Sci.* **2014**, 5 (3), 1204-1215.
120. Boillot, M.-L.; Weber, B., *C. R. Chim.* **2018**, 21 (12), 1196-1208.
121. Lo, W. K. C.; McAdam, C. J.; Blackman, A. G.; Crowley, J. D.; McMorran, D. A., *Inorg. Chim. Acta* **2015**, 426, 183-194.
122. Mayer, J. M., *Accounts of Chemical Research* **2011**, 44 (1), 36-46.
123. Roth, J. P.; Yoder, J. C.; Won, T.-J.; Mayer, J. M., *Science* **2001**, 294 (5551), 2524.
124. Mayer, J. M., *Accounts of Chemical Research* **1998**, 31 (8), 441-450.
125. Gardner, K. A.; Mayer, J. M., *Science* **1995**, 269 (5232), 1849.
126. Usharani, D.; Lacy, D. C.; Borovik, A. S.; Shaik, S., *J. Am. Chem. Soc.* **2013**, 135 (45), 17090-17104.
127. McDonald, A. R.; Guo, Y.; Vu, V. V.; Bominaar, E. L.; Münck, E.; Que, L., Jr., *Chem. Sci.* **2012**, 3, 1680-1693.
128. Browne; David, M. M.; Hassan, N.; Serhiy, D.; Satish, S. B.; Sergey, O. M.; Matti, H.; Julio, L.-F.; George, C. L.; Franc, M.; Albert, A. S.; Wesley, R., **2015**.
129. Rodriguez, M.-C.; Morgenstern-Badarau, I.; Cesario, M.; Guilhem, J.; Keita, B.; Nadjio, L., *Inorg. Chem.* **1996**, 35 (26), 7804-7810.

Appendix

The following pages include the curriculum vitae of Waqas Rasheed.

Summary of Qualifications

- PhD Candidate in chemistry, with collaborative research projects with over 4 different institutes
- Experienced in syntheses of inorganic and organic compounds, and use of various spectroscopic techniques such as UV-Vis, XRD and vibrational spectroscopies and mass spectrometry, and in mechanistic and kinetic studies
- Organized active lab member with a focus on advancing lab safety, and operation/design of experiments/equipment
- Led and co-authored publications in high-impact peer-reviewed journals such as *Angew. Chem. Int. Ed.* with two more in preparation
- Presented work to technical and non-technical audience, at university symposia and national conference

Education

Ph.D. Chemistry

Sep 2013 – May 2019

University of Minnesota, Minneapolis, MN

B.S. Chemistry

Sep 2009 – Jun 2013

Lahore University of Management Sciences, Lahore, Pakistan

Academic Research Experience

Research Assistant, Que Research Group

Sep 2015 – Present

Department of Chemistry, University of Minnesota

- Synthesized diverse new inorganic compounds, with up to 1,000,000-fold improved ability to break C—H bonds
- Characterized unstable ($t_{1/2} < 2$ min) and unique inorganic intermediates with advanced spectroscopic techniques
- Used X-ray crystallography to characterize several thermally unstable and air-sensitive inorganic compounds
- Employed low-temperature NMR spectroscopy as a useful technique to benchmark expensive Mössbauer studies

- Directly mentored an undergraduate student, 2 international visiting scholars from Korea, and an incoming grad student. Two of my mentees are now pursuing PhD at Princeton University and in the Netherlands.
- Initiated an improved glove box management of my lab, wrote several safety operating procedures regarding inert glove box maintenance, and handling of inert gas cylinders and cryogenic dewars
- Created and scripted the group's internal website management system to consolidate group inventory, waste manifestation, group calendars to book instrumentation, safety operating procedures, and exit checklists

Technical Skills

Laboratory: Organic and inorganic syntheses, inert environment handling (Schlenk-line, glove box), analytical techniques (multinuclear and variable temperature NMR, EPR, IR, Raman, Mössbauer, X-ray absorption, UV-visible spectroscopies, ESI mass spectrometry (ESI-MS), gas chromatography (GC/GC-MS), X-ray crystallography (XRD), cyclic voltammetry)

Computer: SHELX (XRD), MestReNova and TopSpin Bruker (NMR), ChemDraw, Origin Graphing, Adobe Suite (Dreamweaver, Flash, Photoshop), Drupal Lite, Weebly, Pixelmator, Microsoft Office Suite, Web- and graphic design

Coding: Basic HTML, ActionScript, Basic Python, Matlab, Google Script

Professional Development

Equity and Diversity Certificate, U of Minn.

Nov 2017 – Present

Participated in 36/48 h of workshops geared to improve equity and diversity in all aspects of professional and personal lives

Joint Safety Team, U of Minn. & The Dow Chemical Company

Aug 2017 – Present

Public Relations Committee Member. Wrote monthly newsletters for safety practices, and designed posters and stall wall moments pasted throughout the chemistry and chemical engineering department

SciMentors, U of Minn. and Open-Door Learning Center

Jan 2015 – Present

Head of Web Development, taught and trained for GED classes, designed logo and experiments to teach topics covering concepts like heredity to acid-base chemistry to mechanics and kinetics and graphing

Community of Chemistry Graduate Students, U of Minn.

Sep 2016 – Present

Designed logo of the organization and mental health posters for the chemistry department

Pakistani Student Association, U of Minn.

Sep 2013 – May 2018

Co-founder, head of website design, advisor, organizer of events to promote awareness about Pakistani traditions and cultural values, in addition to holding sessions to promote dialogues, and writing many resources at psaumn.weebly.com

Publications and Presentations

Journals:

- ***VIP: Rasheed, W.;** Draksharapu, A.; **Banerjee, S.;** Young, V. G.; Fan, R.; Guo, Y.; Ozerov, M.; Nehrkorn, J.; Krzystek, J.; Telser, J.; Que, L., Jr. *Angew. Chem. Int. Ed.* **2018**, 57, 9387

“Crystallographic Evidence for a Sterically Induced Ferryl tilt in a Nonheme Oxoiron(IV) Complex”

- ***VIP: Draksharapu, A.;** **Rasheed, W.;** Klein, J. E. M. N.; Que, L., Jr. *Angew. Chem. Int. Ed.*, **2017**, 56, 9091

“Facile and Reversible Formation of Iron(III)–Oxo–Cerium(IV) Adducts from Nonheme Oxoiron(IV) Complexes and Cerium(III)”

- Chen, J.; Draksharapu, A.; Harvey, E.; **Rasheed, W.;** Que, L., Jr.; Browne, W. R. *Chem. Commun.*, **2017**, 53, 12357

“Direct Photochemical Activation of Nonheme Fe^{IV}=O Complexes”

- **Rasheed, W.;** Fan, R.; Abelson, C. A.; Peterson, O. P.; Ching, W-M.; Guo, Y.; Que, L., Jr. *Chem. Eur. J.*, **2019**, *Just Accepted (not online)*

- Banerjee, S.; **Rasheed, W.;** Fan, R.; Draksharapu, A.; Oloo, W. N.; Guo, Y.; Que, L., Jr. *J. Biol. Inorg. Chem.*, **2019**, *Just Accepted (DOI: 10.1002/chem.201902048)*

***VIP (Very Important Publication) designation is given to < 5% articles in this journal.**

Presentations:

- **Oral: Rasheed, W.;** Que, L. Jr. *Structural Insight into the Reactivity and Spin State of Oxoiron(IV) Complexes.* UMN Metalloprotein Interest Group (MPIG) – Invited Lecture, Minneapolis, MN, May 2018
- **Poster: Rasheed, W.;** Puri, M.; Klein, J. E. M. N.; Que, L. Jr. *Using Steric Bulk to Improve Reactivity of Oxoiron(IV) Complexes.* International Student Research Showcase, University of Minnesota, Minneapolis, MN, Sep 10th, 2017
- **Poster: Rasheed, W.;** Puri, M.; Draksharapu, A.; Klein, J. E. M. N.; Que, L. Jr *Tuning the C-H Bond Cleavage Ability of an Oxoiron(IV) Complex.* 253rd American Chemical Society National Meeting, San Francisco, CA., April 3rd, 2017
- **Poster:** Puri M.; **Rasheed, W.;** Que, L. Jr., *Ligand Dependence on the Reactivity of Synthetic Non-Heme Fe^{IV}(O) Complexes.* Bioinorganic Headwaters Symposium, University of Minnesota, Minneapolis, MN. Aug 1st, 2014

Teaching Experience

Teaching Assistant, Organic Chemistry Lab

Sep 2013 – Jun 2015

Department of Chemistry, University of Minnesota

- Recipient of Honorable Mention for Excellence in Teaching Chemistry award
- Created pairing system in the labs to allow unique pairings, and created online tools for the lab to help students keep tab of their performance, and developed a mechanism for students to get self-driven anonymous feedback

Head Teaching Assistant, General and Organic Chemistry

Sep 2011 – Sep 2013

Department of Chemistry, Lahore University of Management Sciences

- Used embedded animations and online forums on the learning management systems, in addition to conducting live demonstrations as an undergraduate TA, and taught an online organic chemistry course with UIUC, and organic lab

Volunteering

Chemists in the Library, Minnesota Section of American Chemical Society

2013 – Present

Demonstrating science experiments to children aged 4-16 in libraries throughout Twin Cities and Hennepin county suburbs

Volunteering with the Association of Multicultural Scientists

2014 – 2018

Showcasing chemistry experiments and creating interest in science amongst children

2nd Twin Cities Science Fair

Feb 2017

Judged and scored over 10 high-school science projects

3M Visiting Wizards Super Science Saturday, 3M

Oct 2014 – Oct 2016

Managed booths demonstrating science experiments to more than 200 children at 3M campus